

DISSERTATION

FUNDAMENTAL AND APPLIED STUDIES OF POLYMERIC PHOTONIC CRYSTALS:
THE ROLE OF POLYMER ARCHITECTURE AND 3D PRINTING

Submitted by

Bret Michael Boyle

Department of Chemistry

In partial fulfillment of the requirements

For the Degree of Doctor of Philosophy

Colorado State University

Fort Collins, Colorado

Spring 2020

Doctoral Committee:

Advisor: Garret Miyake

Andrew McNally
Carmen Menoni
David Prawel

Copyright by Bret Michael Boyle 2020

All Rights Reserved

ABSTRACT

FUNDAMENTAL AND APPLIED STUDIES OF POLYMERIC PHOTONIC CRYSTALS: THE ROLE OF POLYMER ARCHITECTURE AND 3D PRINTING

Block copolymers (BCP) provide a bottom-up, economical approach to synthesizing polymeric photonic crystals (PC) through the process of self-assembly. Photonic crystals (PC) are defined as periodic, dielectric nanostructures able to reflect certain wavelengths of light within a photonic band gap. The ability to directly tailor the synthesis, conformation, and self-assembly of a BCP to affect the properties of the resulting PC material creates a modular platform for PC materials design. Even though this platform exists for polymeric PC materials, the direct result of modulating the polymer architecture on the dynamics, self-assembly, and application of PC materials remains relatively unexplored. To help close this gap, this dissertation presents the polymer synthesis, characterization, and self-assembly of macromolecules within two unique classes of polymer architecture, dendritic block copolymers (DBCPC) and bottlebrush block copolymers (BBCPC). DBCPCs were shown to possess many characteristics similar to those of bottlebrush polymers such as a rod-like conformation, a reduced capability for chain entanglement, and lower glassy moduli compared to non-rigid, linear polymers. Further, DBCPCs possess high free energy parameters, as well as glass transition temperatures below melt extrusion 3D printing operating conditions, and were shown to self-assemble into PCs during the process of 3D printing. DBCPC PCs represented the first example of 3D printing structural color. For BBCPCs, the backbone composition's effect on the global BBCPC

conformation and in modulating self-assembly processes was examined. The backbone composition was shown to dramatically shift the wavelength of reflection of the PC material at similar molecular weights as well as improve the fidelity of the nanostructure morphology as the molecular weight increases from 50,000 g/mol to 2 million g/mol. The structure-property relationships illuminated herein have laid the groundwork for new research efforts into engineering BCPs for novel PC applications.

ACKNOWLEDGEMENTS

This dissertation would not have been possible without contributions from many different people. These people include my many mentors, graduate committee members (Prof. Andy McNally, Prof. Carmen Menoni, and Prof. David Prawel), peers, mentees, family, and friends. Thank you very much to each and every one of you.

I would like to expressly thank my graduate advisor, Prof. Garret Miyake, for the scientific training and mentorship that he has provided me throughout my graduate career. The values and lessons that I learned in the Miyake lab as well as the expectation of excellence will be a cornerstone I rely on throughout my future career. Additionally, I greatly appreciate Garret's friendship and dedication to my personal growth as a human being. "Ganbatte!"

Another significant guiding influence on my development as a scientist came from Prof. Yifu Ding of the University of Colorado – Boulder. I am eternally grateful for the mentorship Yifu offered me, especially as I am not a part of his own research group. This guidance allowed me the opportunity to expand my horizons into another realm of science and engineering that I would not have been able to do without Yifu. Not to mention, it also allowed me to round out more than a few of the gaps in knowledge I had when I was only using a chemist's lens to solve problems.

To my colleagues, both graduate students and post-doctoral fellows, that I have had the wonderful opportunity of working with, thank you for insightful discussions, collaborations, trainings, and all of the adventures that we shared. You all have shaped my graduate school experience in significant ways and I am extremely grateful for that!

To the undergraduate researchers who have worked tirelessly alongside me over the years: Tara Mensch, Joseph Collins, Touzong Xiong, and Timothy Werder. Thank you very much for all of the hard work, dedication, and eagerness to try new things. A large part of this dissertation is due to you all and your hard work. I have learned many lessons and insights from you all. I hope you will carry some of what you have learned in your time here on to your next adventure. Your futures are extremely bright and exciting – thank you for letting me be a part of your journey.

To my family, perhaps the biggest thank you is required to appreciate the great amount of support and encouragement I received from each of you along this journey. This dissertation would not have been possible without you all, in particular my parents, Janice and Michael Boyle, my brothers, Jacob and Timothy, and my wife, Marcia. To my parents and my brothers, thank you for consistently showing me the value of hard work, raising the standards, and your dedicated and constant support. To Marcia, I cannot express the amount of gratitude I feel for your never-ending encouragement, compassion, support, and love. Thanks for standing steadfast by my side throughout this journey.

Chapter 2: This dissertation chapter contains the manuscript of an article [Boyle, B. M.*; French, T. A.*; Pearson, R. M.; McCarthy, B. G.; Miyake, G. M. Structural Color for Additive Manufacturing: 3D-Printed Photonic Crystals from Block Copolymers *ACS Nano* **2017**, *11*, 3052-3058. *Denotes co-first authors]. This work was supported by the University of Colorado Boulder, the National Science Foundation (CMMI-1634941), the Advanced Research Projects Agency-Energy (DE- AR0000683), the National Institute of General Medical Sciences of the National Institutes of Health under award number R35GM119702, and an IBM Students for a Smarter Planet Award. B.G.M. is grateful for support from the Marian Sharrah Fellowship from

the CU Boulder Department of Chemistry and Biochemistry and a Graduate Assistance in Areas of National Need Fellowship. We thank Materia Inc. for the generous gift of (H2IMes) (PPh₃) (Cl)₂RuCHPh. The authors would like to thank Mr. Steven M. Sartor for his assistance in the light source emission measurements.

Chapter 3: This dissertation chapter contains the manuscript of an article [Boyle, B. M.*; Xiong, P. T.*; Mensch, T. E.; Werder, T. J.; Miyake, G. M. 3D Printing Using Powder Melt Extrusion *Addit. Manuf.* **2019**, 29, 100811. *Denotes co-first authors]. We would like to acknowledge the Colorado State University, the National Science Foundation (CMMI-1634941) and the National Institute of General Medical Sciences of the National Institutes of Health under Award Number R35GM119702 for funding. The content is solely the responsibility of the authors and does not necessarily represent the official views of the National Institutes of Health. We thank Prof. Mark A Ganter, Prof. Andrew J. Boydston, and Johanna J. Schwartz from the University of Washington for the gift of the MPCNC printer and help with its assembly. We would also like to thank Brian Reifsnnyder of Reifsnnyder Precision Works for machining expertise and helpful discussions. Further, the authors would like to thank Pat McCurdy for his SEM expertise, as well as Kyle Foster and Max Kudisch for enlightening discussions and photography contributions.

Chapter 4: This dissertation chapter contains the manuscript of an article [Boyle, B. M.*; Heinz, O.*; Miyake, G. M.; Ding, Y. Impact of the Pendant Group on the Chain Conformation and Bulk Properties of Norbornene Imide-Based Polymers *Macromolecules* **2019**, 52, 3426-3434. *Denotes co-first authors]. B.M.B. and G.M.M. would like to thank the Colorado State University, the National Science Foundation (CMMI- 1634941), the Advanced Research Projects Agency-Energy (DEAR0000683), and the National Institute of General Medical

Sciences of the National Institutes of Health under Award Number R35GM119702. The content is solely the responsibility of the authors and does not necessarily represent the official views of the National Institutes of Health. O.H. and Y.D. gratefully acknowledge the National Science Foundation (NSF) Industry/University Cooperative Research Center for Membrane Science, Engineering and Technology (MAST) at the University of Colorado at Boulder (CU-B) for support of this research via NSF Award IIP 1624602.

Chapter 5: This dissertation chapter contains the manuscript of an article to be submitted for publication [Boyle, B. M.; Collins, J. L.; Mensch, T. E.; Ryan, M. D.; Newell, B. S.; Miyake, G. M. Impact of Backbone Structure on Polymer Dynamics and Brush Block Copolymer Self-Assembly *In Preparation* **2020**.] B.M.B. and G.M.M. would like to thank the Colorado State University, the National Science Foundation (CMMI- 1634941), and the National Institute of General Medical Sciences of the National Institutes of Health under Award Number R35GM119702. The content is solely the responsibility of the authors and does not necessarily represent the official views of the National Institutes of Health. The authors would also like to sincerely thank J. Cole, R. Pearson, and B. McCarthy for insightful discussions, as well as, M. Kudisch for his photography expertise and time.

TABLE OF CONTENTS

ABSTRACT.....	ii
ACKNOWLEDGEMENTS.....	iv
CHAPTER 1 – INTRODUCTION.....	1
CHAPTER 2 – STRUCTURAL COLOR FOR ADDITIVE MANUFACTURING: 3D PRINTED PHOTONIC CRYSTALS FROM BLOCK COPOLYMERS	5
Overview.....	5
Introduction.....	5
Results and Discussion	8
Conclusions.....	13
Experimental Methods	14
References.....	41
CHAPTER 3 – 3D PRINTING USING POWDER MELT EXTRUSION	49
Overview.....	49
Introduction.....	50
Printer Head Design and Modifications.....	52
Print Results and Discussion.....	61
Conclusions.....	69
Experimental Method.....	70
References.....	99
CHAPTER 4 – IMPACT OF THE PENDANT GROUP ON THE CHAIN CONFORMATION AND BULK PROPERTIES OF NORBORNENE IMIDE-BASED POLYMERS.....	104

Overview.....	104
Introduction.....	104
Results and Discussion	106
Conclusions.....	121
Experimental Methods	122
References.....	166
CHAPTER 5 – IMPACT OF BACKBONE STRUCTURE ON POLYMER DYNAMICS AND BRUSH BLOCK COPOLYMER SELF-ASSEMBLY	175
Overview.....	175
Introduction.....	175
Results and Discussion	178
Conclusions.....	191
Experimental Methods	192
References.....	289
CHAPTER 6 – SUMMARY.....	297
References.....	298
APPENDIX I	299

CHAPTER 1 – INTRODUCTION

This dissertation is written to follow the Journals Format as accepted by the Graduate School at Colorado State University and is based on three peer-reviewed first-authored publications that have appeared in *ACS Nano*, *Additive Manufacturing*, and *Macromolecules*, as well as one manuscript submitted for peer-review publication. The principal theme of this dissertation is to synthesize, characterize, engineer, and employ dendritic block copolymers (DBCPs) and brush block copolymers (BBCPs) in polymeric PC applications. The following topics are discussed in detail in the proceeding chapters:

2. Structural Color for Additive Manufacturing: 3D Printed Photonic Crystals from Block Copolymers
3. 3D Printing Using Powder Melt Extrusion
4. Impact of the Pendant Group on the Chain Conformation and Bulk Properties of Norbornene Imide-Based Polymers
5. Impact of Backbone Structure on Polymer Dynamics and Brush Block Copolymer Self-Assembly

In Chapter 2, the first example of incorporation of structural color (color derived from light's interaction with a material's nanostructure morphology) into 3D printed parts is reported. DBCPs were designed, synthesized, and used to additively manufacture plastic parts exhibiting structural color. The reflection properties of the photonic crystals arose from the periodic nanostructure formed through block copolymer self-assembly during polymer processing. The wavelength of reflected light could be tuned across the visible spectrum by synthetically

controlling the block copolymer molecular weight. This molecular weight polymer series was then used to manufacture parts that reflected violet, green, or orange light.

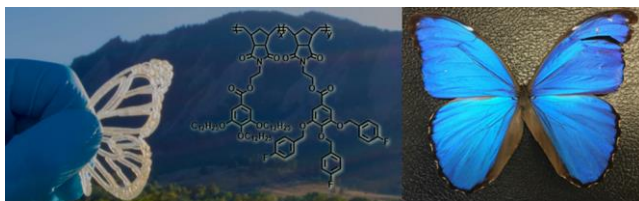


Figure 1.1. A visual representation of 3D printed structural color intended to recreate the structural color seen in the wings of a Morpho butterfly.

In Chapter 3, a bench-top powder melt extrusion (PME) 3D printer head was designed and fabricated to print parts directly from powder-based materials rather than filament. The final design of the PME printer head evolved from the Rich Rap Universal Pellet Extruder (RRUPE) design and was realized through an iterative approach. To facilitate a quicker cycle time from the laboratory bench-top to a 3D printed object with structural color, it was necessary to provide a 3D printing system able to better process the DBCPs than what was currently available and what was used in Chapter 2. The resulting prototype of this study was the first example of a PME 3D printer for novel thermoplastic material printing.

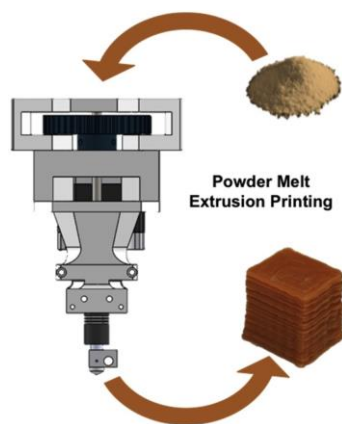


Figure 1.2. A schematic of how the PME 3D printer head processes thermoplastic powder into 3D printed objects.

In Chapter 4, three series of well-defined norbornene imide-based polymers with different pendant groups were synthesized to investigate and characterize the effect of the

pendant group on the polymer conformation in solution and bulk melt properties. These pendant groups consisted of the wedge pendant groups that compose the dendritic polymer architecture. Sterically bulky pendant wedge groups modestly increase the rodlike conformation of the norbornene-imide polymer. In contrast, the different side groups significantly impacted the bulk viscoelastic and thermal properties. By increasing the pendant group size, the chain diameter of the polymer increases and lowers the entanglement modulus, while the segmental relaxation time and the fragility index of these norbornene-based polymers are decreased. By analyzing the effect that the pendant groups have on dendritic homopolymer polymers, insights into how to modulate the properties and dynamics of the dendritic polymers will allow for a more targeted molecular design of polymers with properties ideal for PC applications or manufacturing.

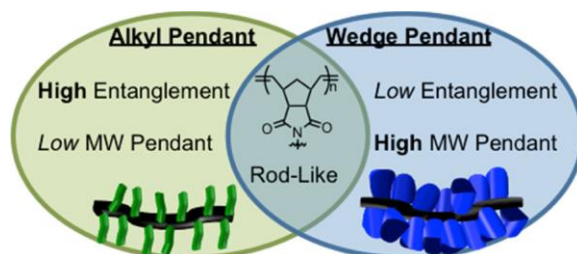


Figure 1.3. A diagram comparing the impacts that an alkyl pendant or a wedge pendant group has on the norbornene imide-based polymer dynamics.

In Chapter 5, four series of well-defined BBCPs with near identical side chain compositions but varying backbone structures were synthesized to investigate the effect of backbone structure on the process of thermal BBCP self-assembly to photonic crystals (PC). The structure of the backbone within a BBCP has a dramatic effect on the ability of the BBCP to self-assemble into ordered nanostructures and on the ability to retain the ordering of the nanostructure morphology in higher molecular weight BBCPs. Further, by analyzing the melt rheological responses of the backbone structure both as linear polymers and homobrush polymers, it was

observed that the inherent stiffness of the backbone promotes enhanced local ordering in the nanostructure morphology and larger domain sizes in the resulting PC materials.

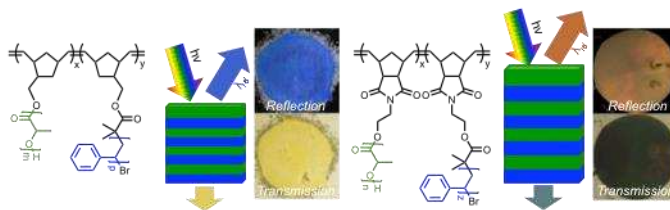


Figure 1.4. A schematic showing the impact of the brush backbone structure on the nanostructure morphology and the resulting PC material reflection.

Chapter 6 contains a brief summary of the work presented within this dissertation. The majority of the work conducted by the author during the course of graduate school has been included in this dissertation. Additional work by the author that has been published, but does not directly pertain to the principal theme of this dissertation has not been included in the proceeding chapters. All work that has resulted in publication during the author's graduate studies has been incorporated into a list within Appendix I.

CHAPTER 2 – STRUCTURAL COLOR FOR ADDITIVE MANUFACTURING: 3D PRINTED PHOTONIC CRYSTALS FROM BLOCK COPOLYMERS

Overview

The incorporation of structural color into 3D printed parts is reported, presenting an alternative to the need for pigments or dyes for colored parts produced through additive manufacturing. Thermoplastic build materials composed of dendritic block copolymers were designed, synthesized, and used to additively manufacture plastic parts exhibiting structural color. The reflection properties of the photonic crystals arise from the periodic nanostructure formed through block copolymer self-assembly during polymer processing. The wavelength of reflected light could be tuned across the visible spectrum by synthetically controlling the block copolymer molecular weight and manufacture parts that reflected violet, green, or orange light with the capacity to serve as selective optical filters and light guides.

Introduction

The importance of color broadly ranges from aesthetics to communications, and although a vast array of brilliant colors can be displayed using dyes or pigments, many such colorants are based on toxic molecules or heavy metals.¹ In contrast, nature presents an inspirational approach to sustainable color that is exemplified in butterflies, beetles, peacocks, and opals.²⁻⁴ The color visualized in these objects arises from their nanostructure and is termed a photonic crystal (PC). PCs are periodic dielectric materials possessing a photonic band gap inhibiting the propagation of specific frequencies of light.⁵ As the color of a PC arises from the nanostructure of the material, embedded structural color has been suggested as a more environmentally friendly

alternative to pigments and dyes.¹ Thus, the ability to mimic the structural color observed in nature represents a sustainable approach to integrate color into objects because it doesn't photo-bleach or require the use of toxic chemicals as pigments and dyes do.

Although several routes to visible-light PCs have been developed, access to an intermediate size regime of the periodic dielectric presents limitations. Synthetic PCs have been implemented as light guides, optical filters, and reflective coatings, with the potential to enable smaller and faster optical computing devices.⁶⁻¹³ Lithography can yield precise PCs, but requires specialized apparatus.¹⁴⁻¹⁶ Co-extrusion, fiber pulling, or layer-by-layer deposition of multiple materials are typically restricted by geometry,¹⁷⁻²³ while the self-assembly of colloidal crystals requires uniform particles and controlled self-assembly conditions.²⁴⁻²⁶ In sum, the development of a versatile technology for the economical and scalable production of PCs is required for broad incorporation of sustainable structural color.

Additive manufacturing (AM) promises to revolutionize the future of manufacturing and has enabled the rapid production of parts and prototypes composed of designer materials with tailored chemical, mechanical, or thermal properties;²⁷⁻³¹ however, the incorporation of optical properties into such objects is less developed.^{32,33} Recognizing the potential of AM, we were motivated to explore the feasibility of integrating structural color into 3D printed parts for the incorporation of objects possessing structural color. Furthermore, due to the light reflecting capability of PCs, such 3D printed objects could have the potential to serve as selective optical filters or guides. Herein, we report the 3D printing of block copolymers (BCPs) using fused deposition modeling (FDM). PC objects with 3D geometries of centimeter sizes (Figures 2.19–2.25) were manufactured and reflect specific frequencies of light across the visible

spectrum by controlling the domain size of the nanostructure through modulation of the BCP molecular weight (Figure 2.1).

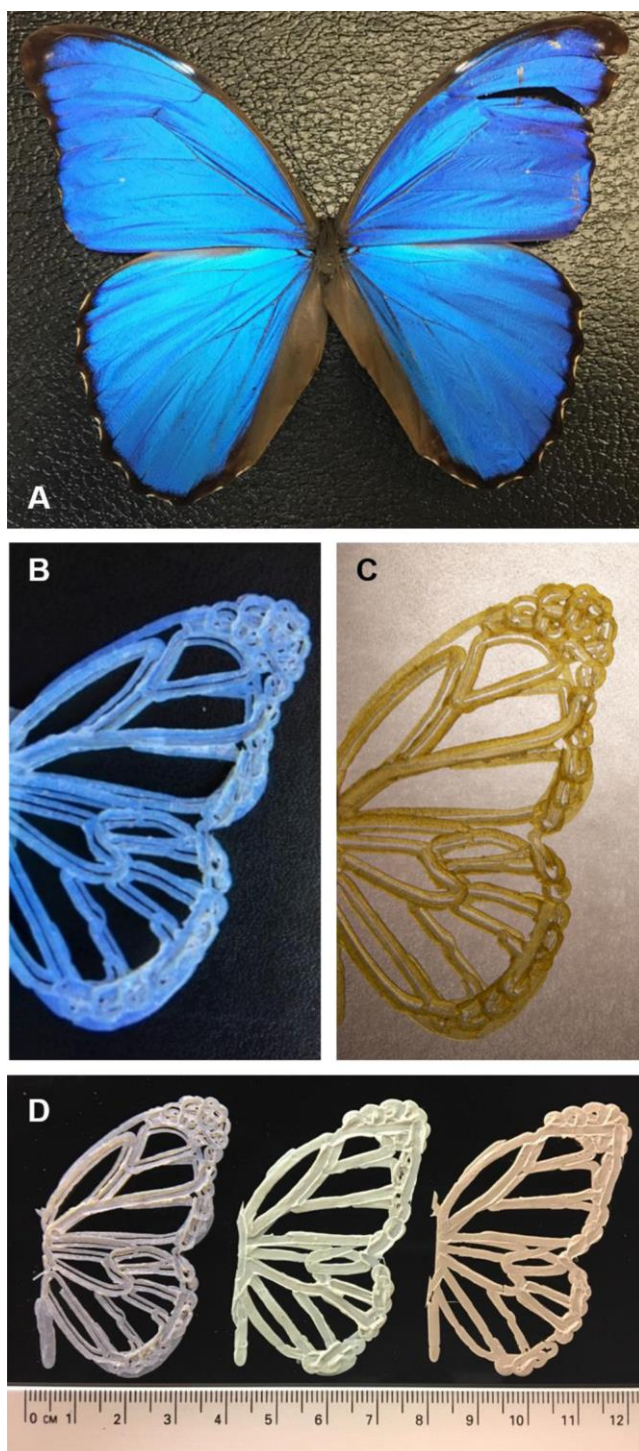


Figure 2.1. Photographs of PC butterflies. Photograph of a morpo butterfly (A). Photograph of a 3D printed butterfly wing in reflection (B) and transmission (C). Photograph of 3D printed PC butterfly wings from BCPs-1, -2, and -3 reflecting violet, green, and red light, respectively (D).

Results and Discussion

The self-assembly of BCPs to nanostructured materials possessing a photonic bandgap provides the potential for an economical and scalable solution through the bottom-up self-assembly of commodity materials.^{34–38} However, the self-assembly of BCPs to nanostructured materials with periodicity within the intermediate size regime needed to yield a photonic bandgap in the visible spectrum is challenging.^{39,40} Domain size swelling coupled with extended self-assembly conditions can overcome this challenge, but are not broadly amendable to the time-scale and standard operating conditions of FDM 3D printers.^{41–50} The inherent characteristic of macromolecular chain entanglement introduces an energetic barrier for the self-assembly to ordered nanostructures, preventing facile access to visible-light PCs.^{51,52} To circumvent this fundamental property, the design and synthesis of macromolecules with rigid-rod characteristics and reduced capability for chain entanglement allow for rapid self-assembly to PCs, reflecting light across the visible and into the near-IR spectrum.^{53–59} Molecular brush and dendritic copolymers composed of sterically bulky repeat units limit the potential for chain entanglement⁶⁰ and have been successfully synthesized via a grafting through approach using ruthenium-mediated ring-opening metathesis polymerization (ROMP).⁶¹ ROMP is a robust and efficient methodology for the synthesis of such high molecular weight (MW) polymers with low dispersity (\mathcal{D}).^{62–66} As such, we hypothesized that dendritic BCPs possessed the potential to self-assemble to visible-light reflecting PCs under the conditions of FDM for the production of 3D-metamaterial objects.

To investigate if dendritic BCPs could self-assemble to PCs via filament extrusion and FDM en route to 3D printing of PC objects, a dendritic BCP composed of a benzyl and alkyl wedge-type monomer was synthesized. The BCP possessed a weight-average molecular weight (M_w) of 484 kDa and $D = 1.10$ (Figure 2.2). The rapid self-assembly of this dendronized BCP was highlighted during filament extrusion at 200 °C, yielding a PC filament in the time scale of minutes. The as-isolated, unassembled, BCP was colorless due to a lack of ordered nanostructured periodicity; however, during filament extrusion, the BCP self-assembled to a nanostructured material possessing photonic properties, reflecting violet light (yellow-transmitting) (Figure 2.2). Examination of the material located in the extruder nozzle revealed the most intense color was located at the heated barrel metal interface. As such, although shear forces during the extrusion process are imposed on the BCP, we propose the self-assembly mechanism is strongly thermally induced.⁶⁷

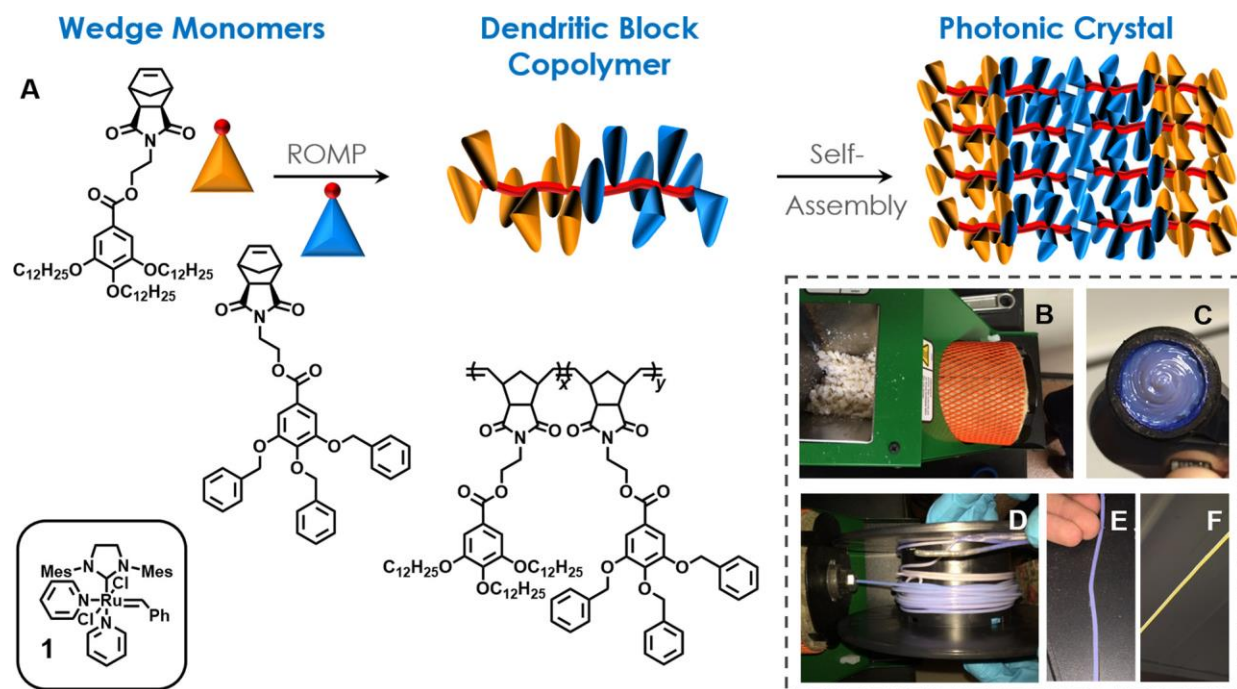


Figure 2.2. Synthetic approach to rigid-rod dendritic BCPs and schematic representation of the self-assembly of BCPs to PCs (A). Photographs of the unassembled, colorless BCP loaded in the extruder hopper (B), self-assembly to a PC during filament extrusion in the extruder nozzle (C),

to yield a filament reflecting violet (D, E) and transmitting yellow light (F).

Previous studies revealed modulating the BCP MW directly controlled the domain size of the resulting nanostructure, and the wavelength of reflected light of the PC could be tuned from the UV, through the visible, and into the near IR.^{6-13,34} However, with this BCP composition, the wavelength of reflected light of the PC only gradually increased with increasing BCP MW. The highest MW BCP in this series ($M_w = 909$ kDa) only reflected green light ($\lambda_{max} = 480$ nm) (Figure 2.26, Table 2.7). As such, extremely high MW BCPs of this chemical composition would be required for the production of PC objects able to reflect longer wavelengths of light, which raised concern about the processability during extrusion and 3D printing with high MW BCPs.

Therefore, a BCP was designed and synthesized from a combination of a dodecyl and fluorobenzyl wedge-type monomers with the motivation to access longer wavelength- reflecting PCs from a lower MW BCP. This combination of monomers was designed to minimize chain entanglement with sterically bulky monomer repeat units and to encourage rapid self-assembly by chemically distinct blocks. Investigating the effects of BCP MW on the wavelength of reflected light revealed this composition could assemble to PCs reflecting across the visible spectrum, where the maximum peak wavelength (λ_{max}) was linearly related to the BCP MW (Figure 2.27, Table 2.8). Three BCP samples were subsequently synthesized on multigram scale through the sequential ROMP of equal molar ratios of the two monomers to produce BCPs with M_{ws} of 581 (BCP-1), 876 (BCP-2), and 1130 (BCP-3) kDa. The bulk BCPs were then extruded into filaments for 3D printing using FDM.

For all three BCPs, the as-isolated materials are colorless. PC thin films of the three BCPs were fabricated through thermal annealing and reflected violet ($\lambda_{\text{max}} = 412 \text{ nm}$), green ($\lambda_{\text{max}} = 530 \text{ nm}$), and orange ($\lambda_{\text{max}} = 610 \text{ nm}$) light for BCP-1, -2, and -3, respectively (Figure 2.3G–I). Scanning electron microscopy (SEM) was used to visualize the nanostructured morphology of the cross sections of these films after freeze fracturing and staining with RuO₄ (Figure 2.3A–C). For films made from BCP- 2 and -3, lamellar morphologies were observed with periodicities correlating to the observed reflection of the films. Interestingly, although the film from BCP-1 efficiently reflected violet light, the observed morphology was not a lamellar morphology, but a spherical morphology reminiscent of kinetically trapped morphologies observed in similar dendronized BCPs.⁵⁴ Regardless, for all three BCPs possessing the same empirical formula, the observed color was a result of the nanostructured periodicity of the BCP. The observed structural color of both the BCP derived films and 3D printed objects has been stable for at least one year under ambient conditions.

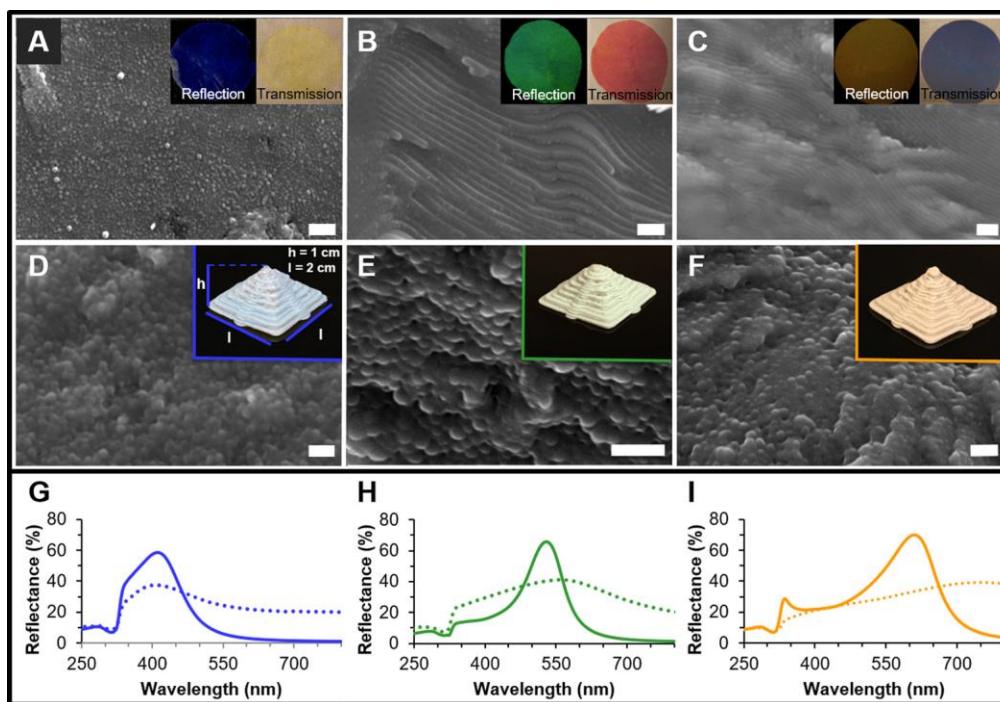


Figure 2.3. SEM images of freeze-fractured cross sections of thin films of poly(DDW-b-FBnW)

BCP-1 (A), BCP-2 (B), and BCP-3 (C) and photographs of the films in reflection and transmission (insets). SEM images of the freeze-fractured cross sections and photographs of the 3D printed pyramids ($2 \times 2 \times 1.0$ cm) using BCP-1 (D), BCP-2 (E), and BCP-3 (F). Reflectance spectrum of thin films (solid line) and 3D printed object (dashed line) for BCP-1 (G), BCP-2 (H), and BCP-3 (I). Scale bars in SEM images are 1 μm .

Filaments from each BCP were drawn using a benchtop extruder. The filament produced from BCP-1 reflected a slightly higher energy wavelength ($\lambda_{\text{max}} = 387$ nm) than when assembled to the thin film, although both processing methods yielded PC materials with relatively similar reflection profiles (Figure 2.28, Table 2.8). In contrast, the filaments produced from BCP-2 and -3 reflected longer wavelengths of light ($\lambda_{\text{max}} = 552$ and 737 nm, respectively), and the reflection profiles of the filaments became broader. As such, the filament from BCP-1 transmitted light well, while the filaments from BCP-2 and -3 were not visually transparent. SEM was used to visualize the morphology of these materials (Figure 2.32). In the case of all three filaments, spherical morphologies were observed, similar to the PC thin film produced from BCP-1.

The filaments were printed using FDM to manufacture 3D cuboids ($1.0 \times 1.0 \times 0.6$ cm; Figure 2.4), cylinders (diameter = 1.6 cm; Figure 2.4), or pyramids ($2.0 \times 2.0 \times 1.0$ cm) possessing photonic properties and reflecting violet ($\lambda_{\text{max}} = 412$ nm), green ($\lambda_{\text{max}} = 560$ nm), or red ($\lambda_{\text{max}} = 743$ nm) light when using BCP- 1, -2, or -3, respectively (Figure 2.3). FDM did not appear to alter the photonic properties or the self-assembly of the nanostructure as compared to the filaments. The λ_{max} , reflection profiles, and morphologies of the printed objects remained nearly the same as the filaments they were printed from. Thin objects printed using BCP-1 could transmit light with the potential to serve as optical filters (Figure 2.1B.), yet thicker objects were not visually transparent. Objects printed from BCP-2 and -3 reflected green or red light, respectively, but were not transparent (Figures 2.3 and 2.4).

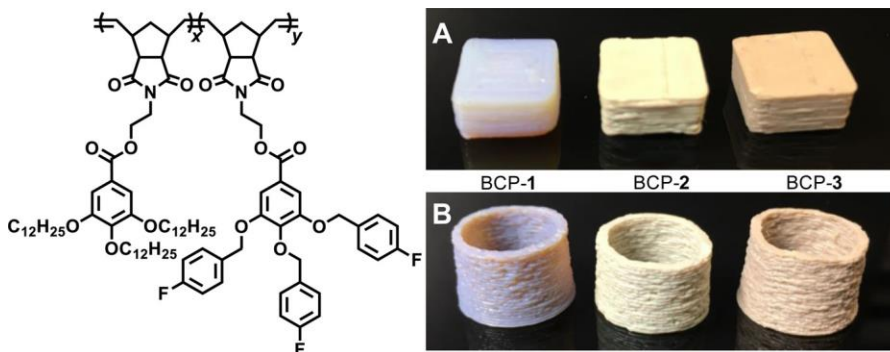


Figure 2.4. Structure of the BCP used for 3D printing (left). Cuboids ($1.0 \times 1.0 \times 0.6$ cm; A) and cylinders (diameter = 1.6 cm; B) 3D printed using BCP-1, -2, or -3 reflecting violet, green, and orange light.

To demonstrate further application potential of objects printed from these BCPs, a hollow U-shaped tube was printed from BCP-2 (Figure 2.5). We envisioned this geometry would serve as a frequency selective light-guide around a curved geometry. In fact, when white light (emission spectrum, Figure 2.31) was introduced into one opening of the object, only green light exited the other opening. This experiment demonstrated the feasibility of using such 3D printed PC objects in more advanced optical devices or circuits and will be the focus of our future work.



Figure 2.5. Model of object and concept of a polymer-based PC acting as a light guide (A). Photograph of the 3D printed object with an outer diameter of 0.5 cm (B) that, when irradiated with a white flashlight from one opening, can guide green light to exit the other opening (C).

Conclusions

Dendritic BCPs were designed and synthesized to act as PCs able to reflect across the visible spectrum. These polymeric PCs were then processed via 3D printing to create geometrically unrestricted objects possessing photonic properties. The rapid self-assembly of these polymers to nanostructured photonic materials was thermally induced during filament

extrusion, yielding filaments reflecting across the visible spectrum and printed to 3D objects exhibiting structural color. This proof of concept represents an approach for the direct additive manufacturing of complex parts with tailored optical properties, without the use of pigments or dyes. In addition to introducing materials possessing photonic stop bands to 3D printing, the ability to control the flow of light with such materials was demonstrated, where printed photonic objects could filter light or even guide specified light frequencies around a curved geometry.

Experimental Methods

(H₂IMes)(PPh₃)(Cl)₂RuCHPh was received as a research gift from Materia Inc. and was converted to (H₂IMes)(py)₂(Cl)₂RuCHPh (1) via literature procedure.⁶⁸ N-(hydroxyethyl)-cis-5-norbornene-exo-2,3-dicarboximide (2) was prepared according to literature procedure.⁶⁹ All other chemicals were purchased from Sigma-Aldrich and VWR. All polymerizations were performed in a nitrogen-filled glovebox. NMR spectra were recorded on a Varian INOVA 400 MHz spectrometer (¹H/¹³C/¹⁹F). Chemical shifts were referenced to internal solvent resonances using CDCl₃ (¹H: 7.26 ppm; ¹³C: 77.16 ppm) and d₆-DMSO (¹H: 2.50 ppm ; ¹³C: 39.52 ppm) and are reported as parts per million relative to tetramethylsilane. High-resolution mass spectra were provided by the University of Colorado – Boulder Central Analytical Mass Spectrometry Facility using a Waters Synapt G2 HDMS Qtof with acetonitrile as the solvent. Polymer molecular weights were determined by multi-angle light-scattering (MALS) gel permeation chromatography (GPC), with THF as the eluent, using a miniDAWN TREOS light-scattering detector and a TrEX differential refractometer, all from Wyatt Technology. An Agilent 1200 UV-vis detector was also present in the detector stack. Absolute molecular weights were determined using dn/dc values calculated by assuming 100% mass recovery of the polymer

sample injection into the GPC. Batches of polymer of consistent molecular weight were thoroughly mixed by dissolving in methylene chloride to ensure homogeneity of the samples. After the removal of solvent, polymer batch mixtures were sufficiently dried in a VWR vacuum oven at 50 °C to a constant weight before extrusion. Differential scanning calorimetry (DSC) was conducted using a Mettler Toledo DSC823e. To reset thermal history, an initial sweep ramped from 25 °C to 250 °C (10 °C/min), where it was held constant for two minutes before cooled to 25 °C (-10 C/min). Thermal data was collected from the second sweep after holding at 25 °C for two minutes, ramping to 250 °C (5 °C/min), holding for two minutes, then returned to 25 °C (-5 °C/min). Polymer thin films were prepared by compressing polymer sample between two glass slides (rinsed with methanol, hexanes, and methylene chloride then dried) and annealed in a VWR vacuum oven at 100 °C for 24 h. Polymer filaments were extruded using a Filabot EX2 extruder from 125-145 °C. Objects were printed using a FlashForge Creator Pro Dual Extrusion 3D Printer (print temperature: 200 °C, nozzle diameter: 1.0 mm, layer height: 0.5 mm, object infill: 0%, 1 Shell, print-bed temperature: 40 °C, feed-rate: 10 mm/s, travel feed-rate: 10 mm/s). 3D-models were obtained from FlashForge pre-loaded calibration models, 3D-modeling in SketchUp Make software, and from the open-source website www.thingiverse.com. All 3D-models were visualized, sliced, and made into G-code using the Replicator G 0040r24-Sailfish software in tandem with the Skeinforge 50 slicing program. SEM images were taken on a JEOL JSM-6480LV scanning electron microscope after staining films with RuO₄. Reflection measurements were performed on a Cary 5000 UV/vis/NIR spectrophotometer, equipped with an integrating sphere diffuse reflectance accessory (DRA) (Internal DRA-2500) using the standard wide-open aperture. The samples were scanned at a rate of 1.0 nm/s with a 1.0 nm data interval, from 1100 to 200 nm, with a detector crossover (PbS to PMT) at 850 nm.

Monomer Synthesis

Methyl 3,4,5-tris(4-fluorobenzyloxy)benzoate (3a)

A 250 mL round-bottom flask was charged with DMF (75 mL) and a stir bar. The solution was sparged with nitrogen for 30 minutes. Once sufficiently deoxygenated, the flask was charged with methyl gallate (3.63 g, 19.7 mmol, 1 equiv) and potassium carbonate (12.5 g, 118.2 mmol, 6 equiv). While stirring, 4-fluorobenzyl chloride (14.2 mL, 118.2 mmol, 6 equiv) was slowly added to the mixture over a few minutes. A reflux condenser was attached to the flask and the mixture was heated to 80 °C for 12 hours. The reaction mixture was allowed to cool to room temperature then diluted with water (150 mL) and extracted with methylene chloride (2 × 150 mL). The organic phases were combined, washed with water (150 mL) followed by brine (150 mL), then dried over anhydrous magnesium sulfate. The organic phase was passed through basic alumina to purify. Solvent was removed in vacuo to yield the product 3a as a white solid (8.44 g, 16.6 mmol, 84.3%). ¹H NMR (400 MHz, CDCl₃) δ 7.39 (m, 4H), 7.38 (s, 2H), 7.30 (m, 2H), 7.07 (m, 4H), 6.92 (m, 2H), 5.08 (s, 4H), 5.03 (s, 2H), 3.90 (s, 3H). ¹³C NMR (100 MHz, CDCl₃) δ 166.6, 163.9, 161.5, 152.5, 142.1, 133.3, 133.2, 132.4, 132.4, 130.5, 130.4, 129.6, 129.6, 125.5, 115.7, 115.5, 115.3, 115.0, 109.1, 74.48, 70.67, 52.43. ¹⁹F NMR (376 MHz, CDCl₃) δ -113.9, -114.1. HRMS (ESI): calculated for M⁺ C₂₉H₂₃F₃O₅, 508.1498; observed 508.1576.

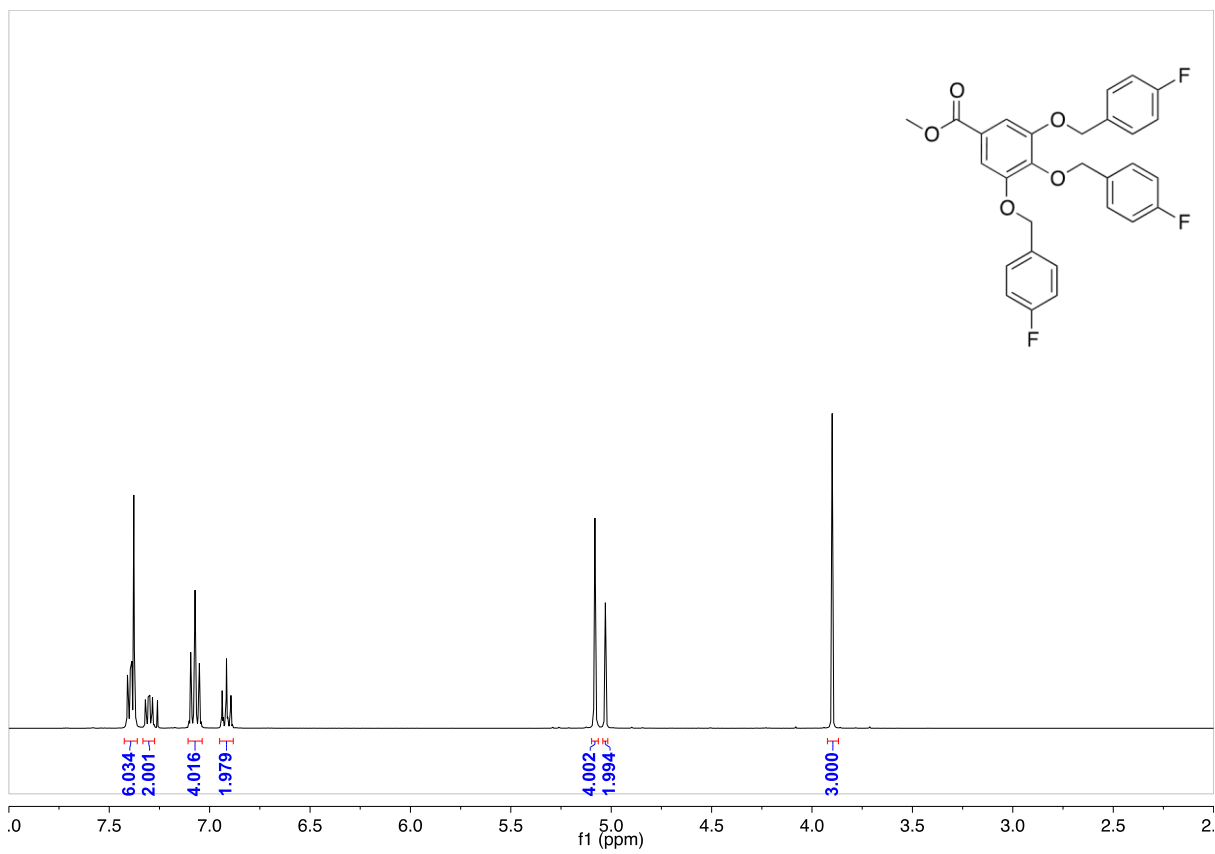


Figure 2.6. ¹H NMR of methyl 3,4,5-tris(4-fluorobenzyloxy)benzoate in CDCl₃.

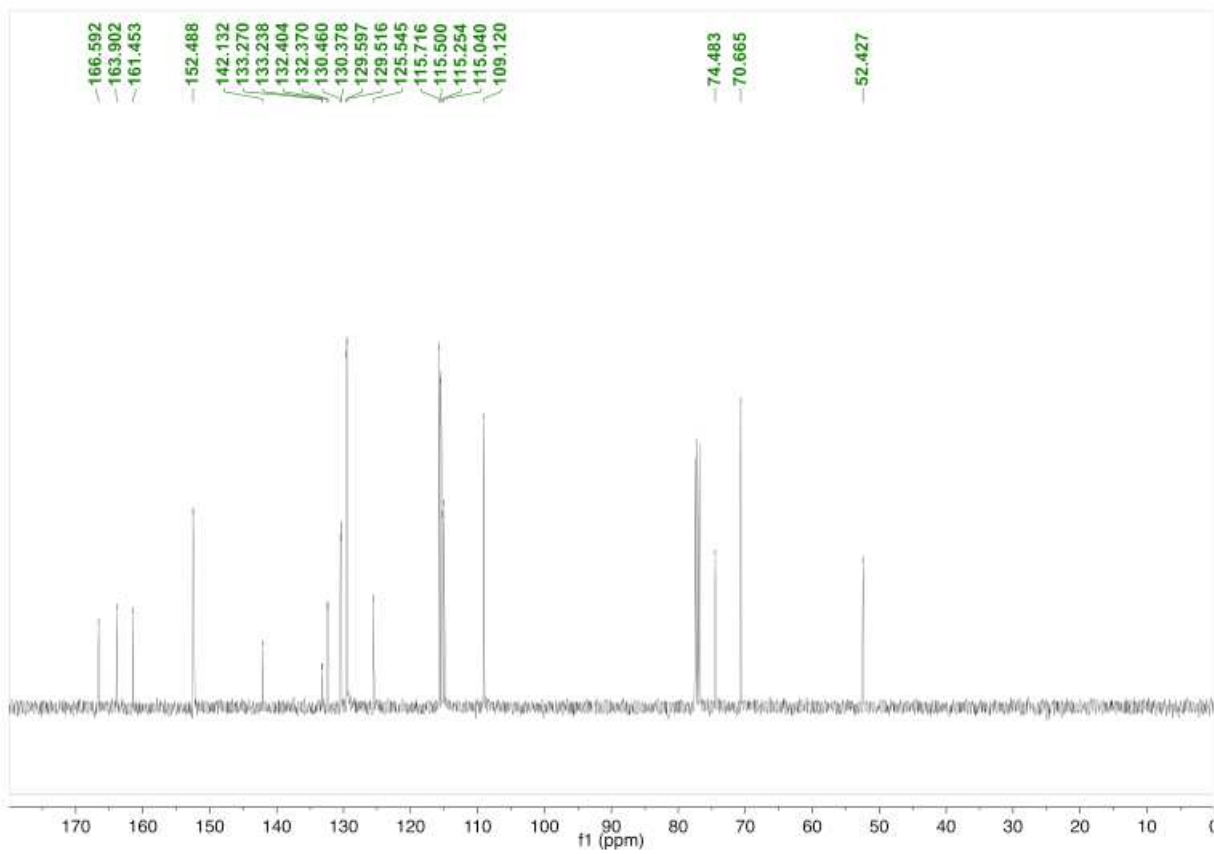


Figure 2.7. ^{13}C NMR of methyl 3,4,5-tris(4-fluorbenzyloxy)benzoate in CDCl_3 .

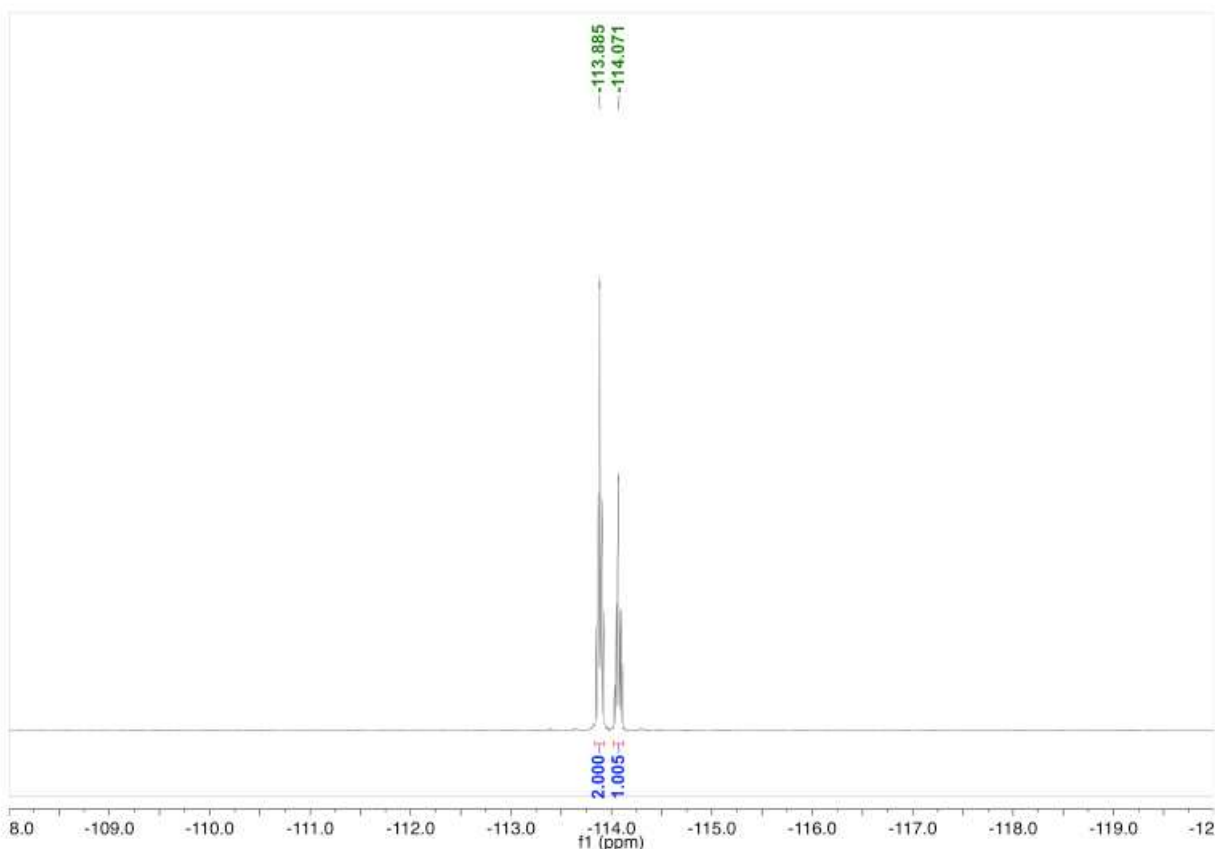


Figure 2.8. ^{19}F NMR of methyl 3,4,5-tris(4-fluorbenzyloxy)benzoate in CDCl_3 .

3,4,5-tris(4-fluorbenzyloxy)benzoic acid (3b)

A 250 mL round-bottom flask was charged with 3a (8.39 g, 16.5 mmol, 1 equiv), potassium hydroxide (9.26 g, 165 mmol, 10 equiv), 95% ethanol (90 mL) and a stir bar. A water-cooled reflux condenser was attached to the flask and the mixture was refluxed at 85 °C for 4 hours. The reaction mixture was allowed to cool to room temperature. Solvent was removed in vacuo yield a pale-yellow solid. The solid was washed with diethyl ether then suspended in 200 mL of diethyl ether with a stir bar. The suspension was acidified via slow addition of concentrated HCl, causing the precipitation of potassium chloride. The suspension was filtered and washed with excess water. The solid was dissolved in acetone and dried over anhydrous

magnesium sulfate. After filtering, solvent was removed in vacuo to yield 3b as a white solid (4.90 g, 9.91 mmol, 60.1%). ¹H NMR (400 MHz, d₆-DMSO) δ 7.50 (m, 4H), 7.38 (m, 2H), 7.35 (s, 2H), 7.24 (m, 4H), 7.08 (m, 2H), 5.15 (s, 4H), 5.00 (s, 2H). ¹³C NMR (100 MHz, d₆-DMSO) δ 166.9, 163.1, 160.6, 151.9, 140.8, 133.7, 133.7, 133.1, 133.1, 130.4, 130.4, 129.9, 129.9, 126.2, 115.4, 115.2, 115.0, 114.8, 108.2, 73.5, 69.5. ¹⁹F NMR (376 MHz, d₆-DMSO) δ -114.4. HRMS (ESI): calculated for M⁺ C₂₈H₂₁F₃O₅, 494.1341; observed 494.1263.

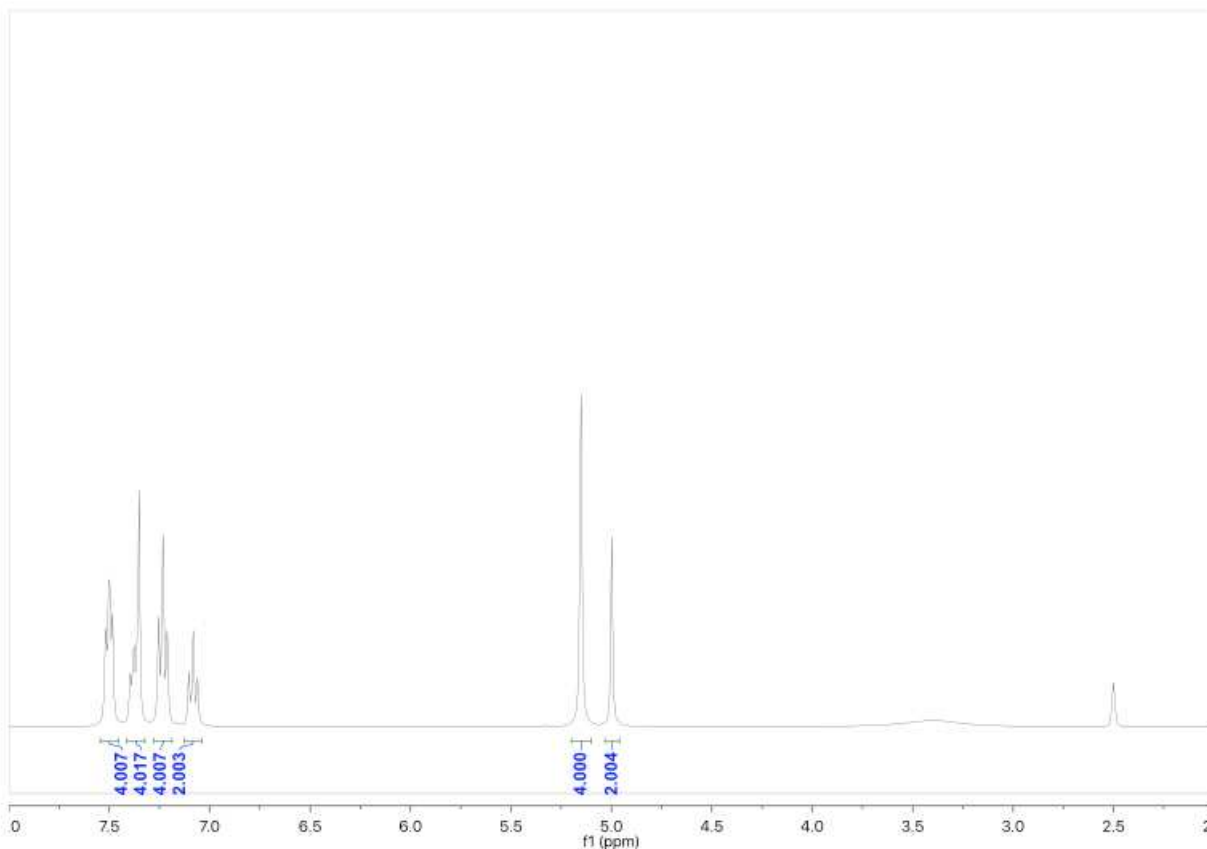


Figure 2.9. ¹H NMR of 3,4,5-tris(4-fluorbenzyloxy)benzoic acid in d₆-DMSO.

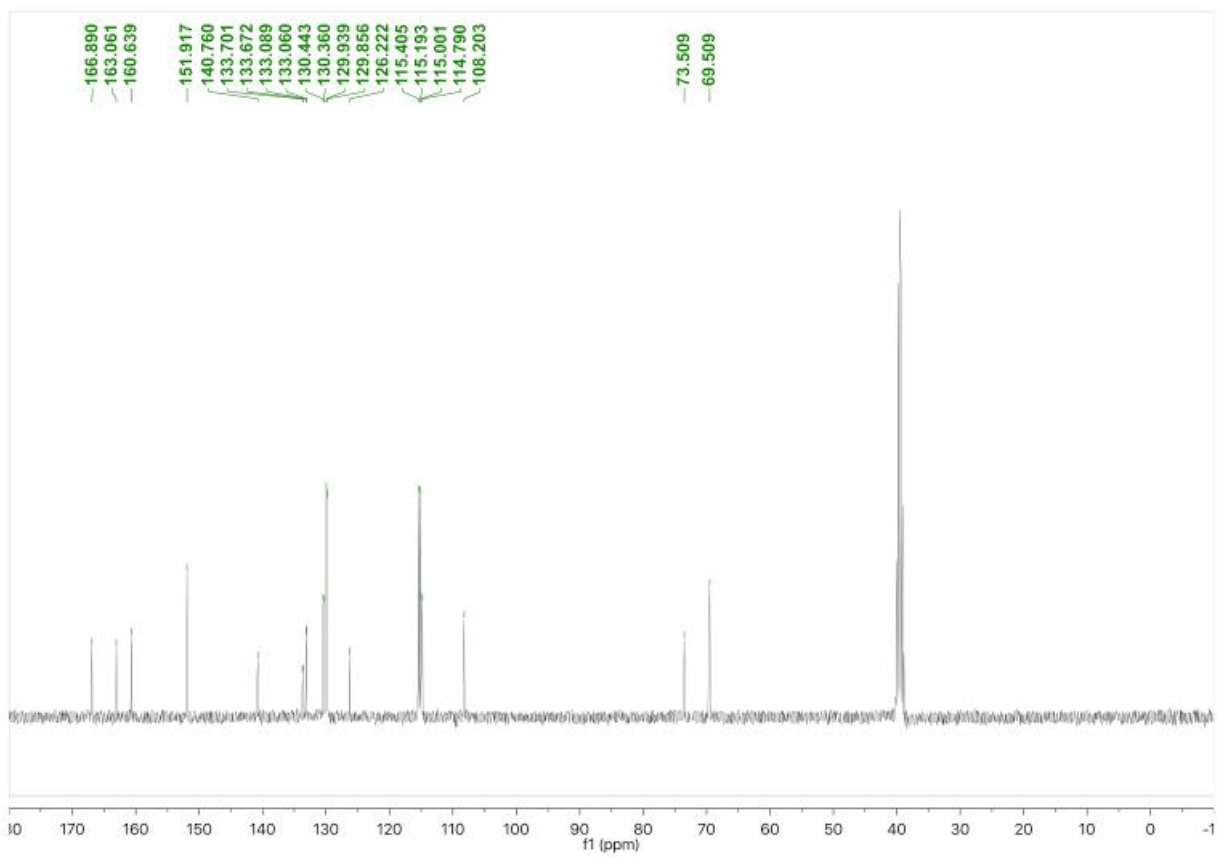


Figure 2.10. ¹³C NMR of 3,4,5-tris(4-fluorbenzyloxy)benzoic acid in d₆-DMSO.

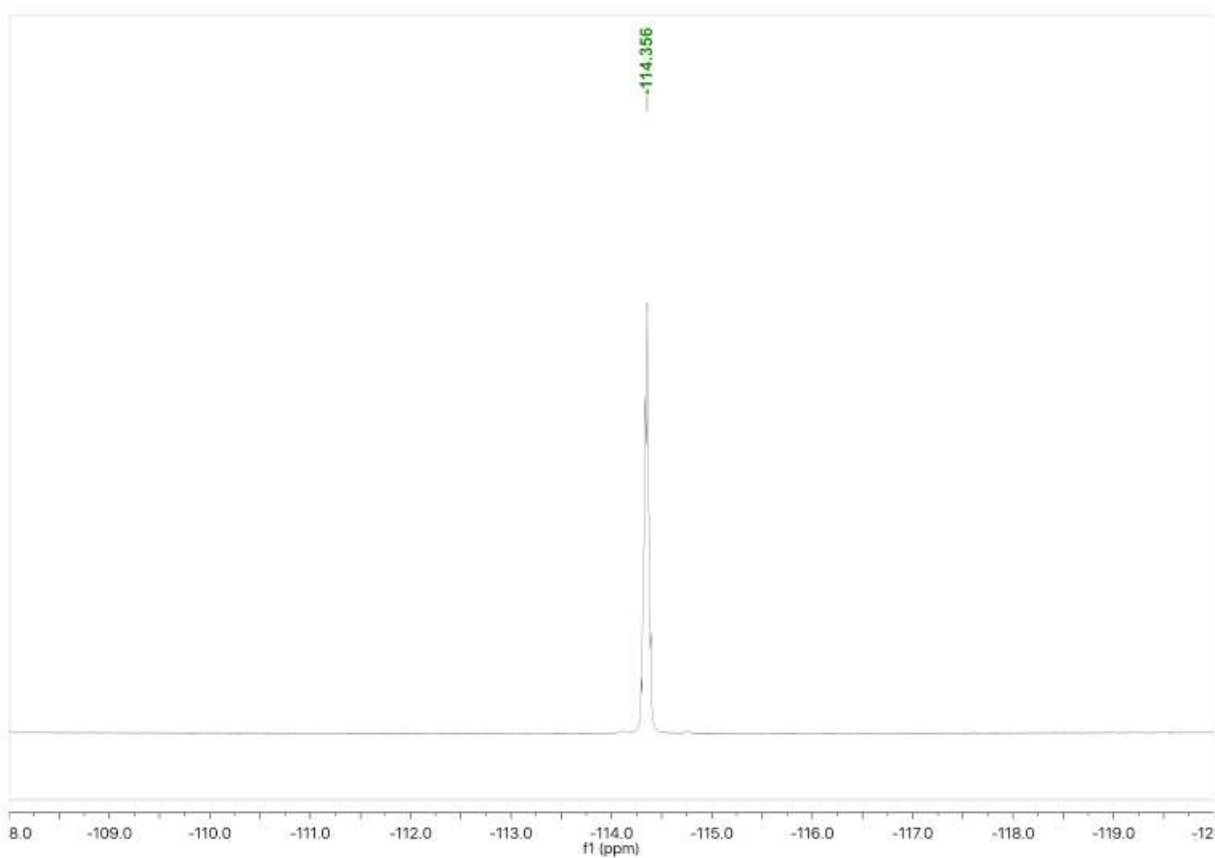


Figure 2.11. ^{19}F NMR of 3,4,5-tris(4-fluorobenzyloxy)benzoic acid in d_6 -DMSO.

Fluorobenzyl Wedge Monomer (FBnW)

A 200 mL Schlenk flask was equipped with a stir bar and flame-dried under vacuum. Once cool, the flask was backfilled with nitrogen then charged with 3b (4.84 g, 9.79 mmol, 1 equiv), alcohol 2 (2.24 g, 10.8 mmol, 1.1 equiv), 4-dimethylaminopyridine (120 mg, 0.979 mmol, 0.1 equiv), and methylene chloride (60 mL). The solution was cooled in an ice bath then charged with dicyclohexylcarbodiimide (2.23 g, 10.8 mmol, 1.1 equiv) and stirred at 0 °C for 1 h. The reaction mixture was allowed to warm to room temperature and stirred for 18 h. The resulting suspension was filtered and the solid was washed with minimal methylene chloride (50 mL). Solvent was removed from the filtrate in vacuo to yield a viscous, pale yellow oil. 95%

ethanol (250 mL) was added to the oil and stirred for 3 hours to precipitate the desired product. The solid was filtered, washed with 95% ethanol, and then dried in vacuo. The solid was then recrystallized out of DCM/hexanes and dried in vacuo to yield the monomer 3c as a white solid (5.38 g, 7.87 mmol, 80.4%). ^1H NMR (400 MHz, CDCl_3) δ 7.41 (4H, m), 7.34 (2H, s), 7.30 (2H, m), 7.07 (4H, m), 6.91 (2H, m), 6.27 (2H, t, $J = 1.9$ Hz), 5.10 (4H, s), 5.03 (2H, s), 4.41 (2H, t, $J = 4.9$ Hz), 3.92 (2H, t, $J = 5.3$ Hz), 3.21 (2H, s), 2.69 (2H, s), 1.39 (1H, d, $J = 9.8$ Hz), 1.22 (1H, d, $J = 9.7$ Hz). ^{13}C NMR (100 MHz, CDCl_3) δ 177.9, 165.7, 163.9, 161.4, 152.5, 142.2, 137.9, 133.3, 133.2, 132.5, 132.4, 130.4, 130.3, 129.6, 129.5, 124.9, 115.7, 115.5, 115.2, 115.0, 109.05, 74.4, 70.5, 62.1, 47.9, 45.3, 42.8, 37.6. ^{19}F NMR (376 MHz, CDCl_3) -113.9, -114.1. HRMS (ESI): calculated for M^+ $\text{C}_{39}\text{H}_{32}\text{F}_3\text{NO}_7$, 683.2131; observed 683.2209.

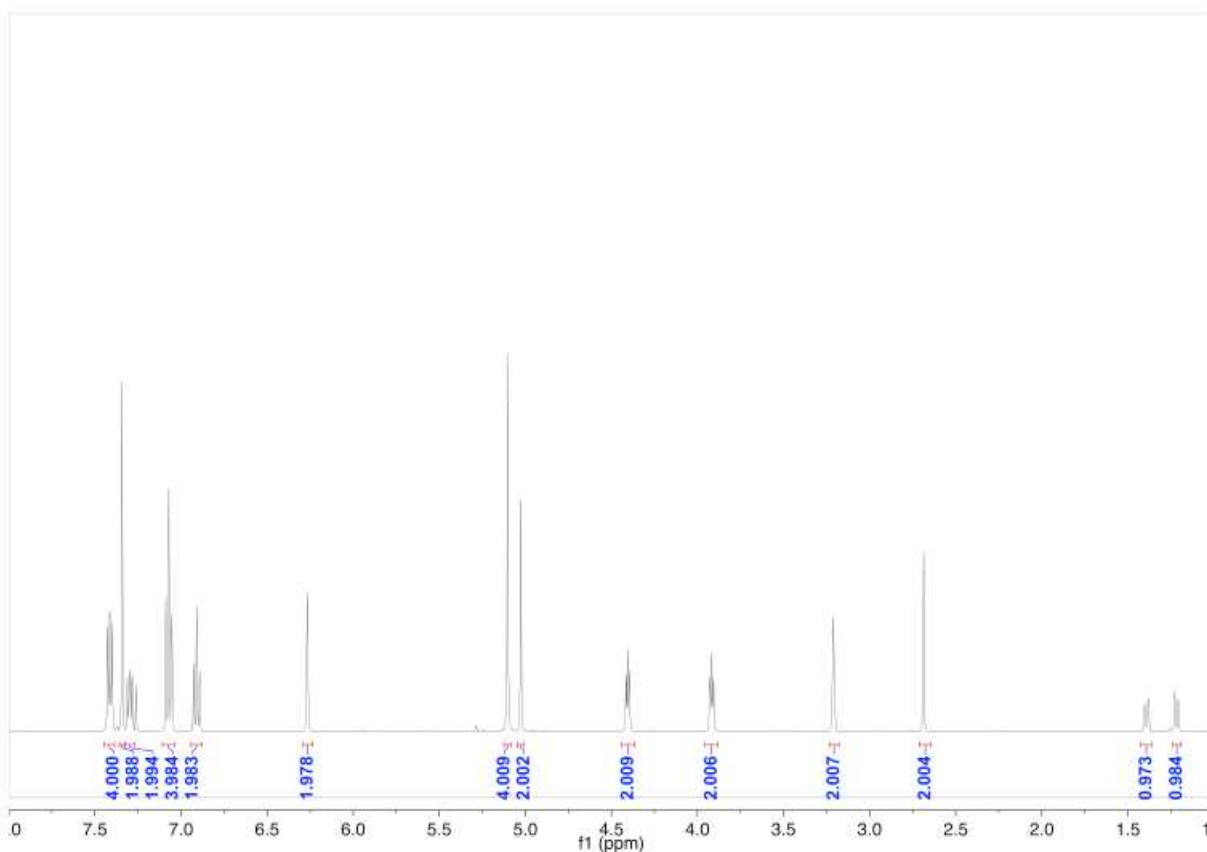


Figure 2.12. ^1H NMR of fluorobenzyl wedge (FBnW) monomer in CDCl_3 .

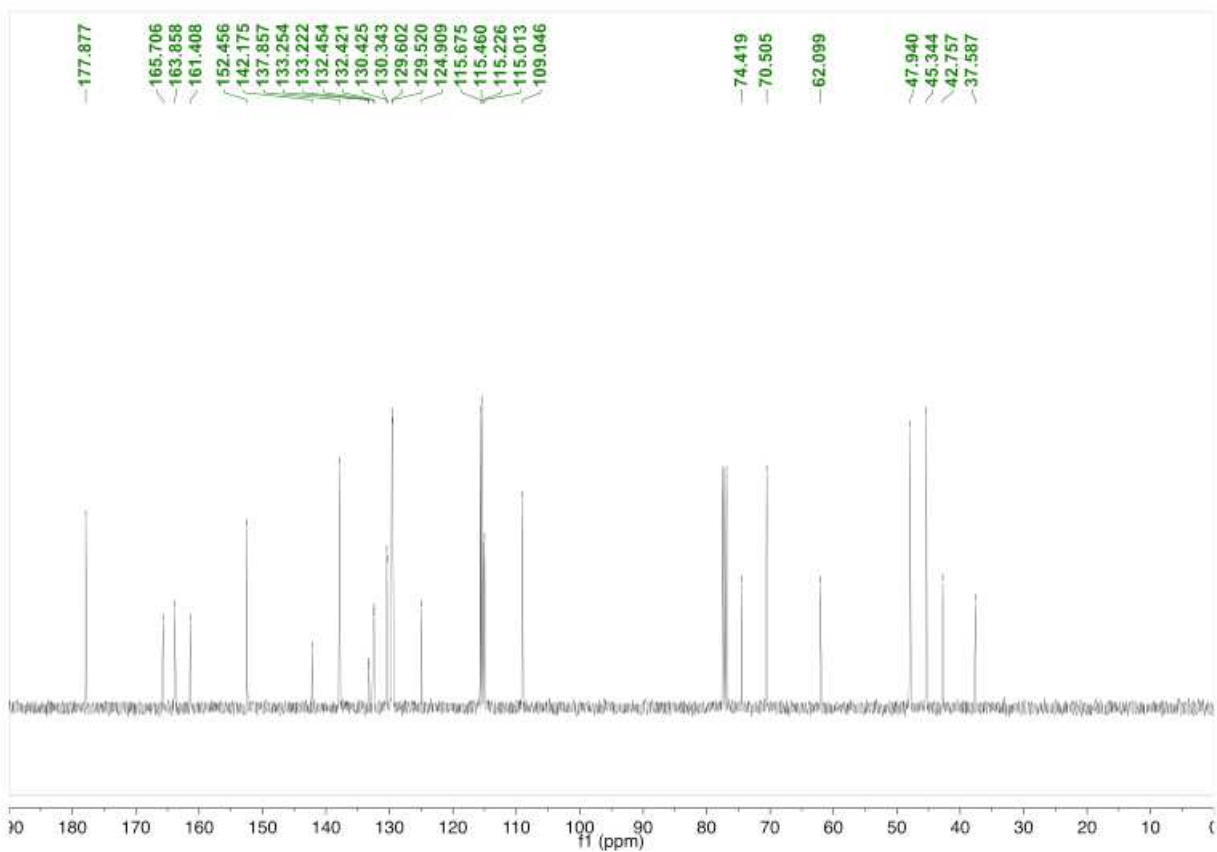


Figure 2.13. ^{13}C NMR of fluorobenzyl wedge (**FBnW**) monomer in CDCl_3 .

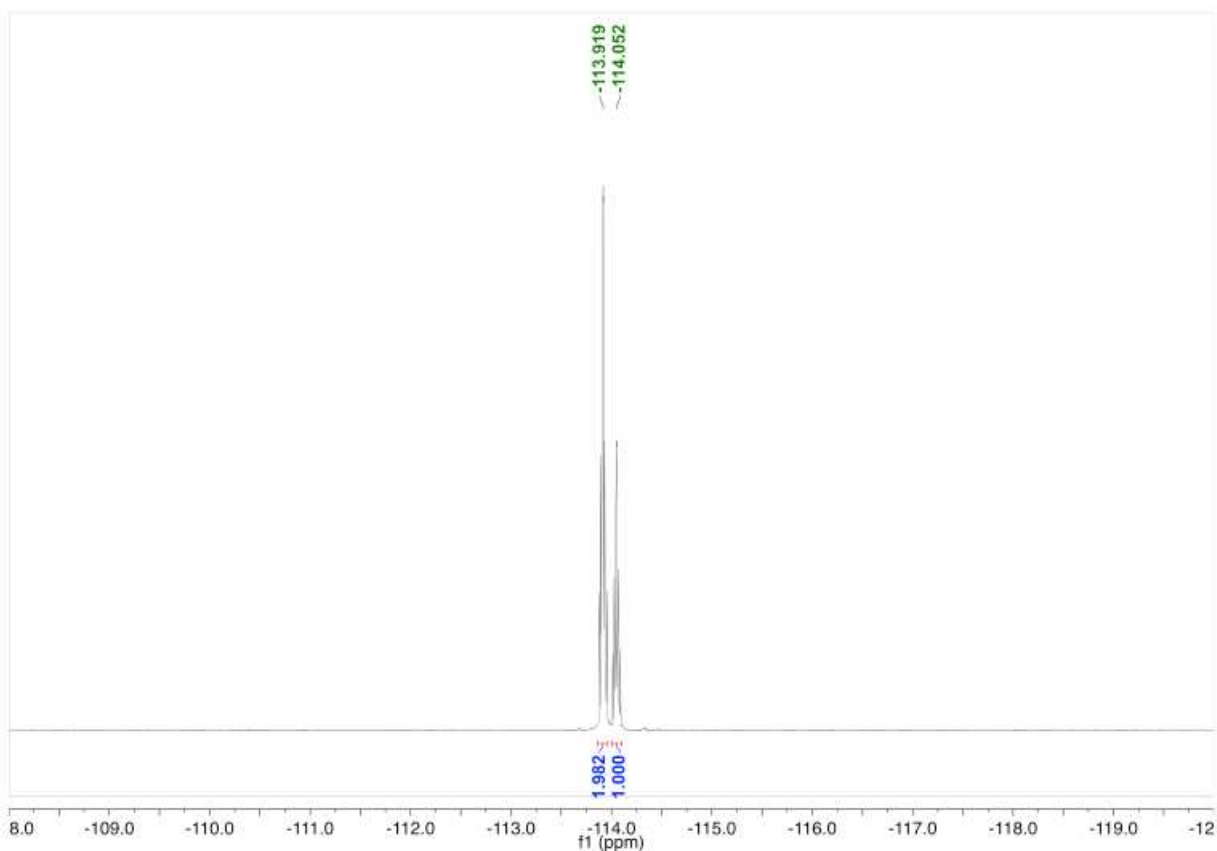


Figure 2.14. ^{19}F NMR of fluorobenzyl wedge (**FBnW**) monomer in CDCl_3 .

Dodecyl Wedge Monomer (DDW)

The dodecyl wedge monomer was prepared according to a previously reported literature procedure.⁷⁰

Benzyl Wedge Monomer (BnW)

The benzyl wedge monomer was prepared according to a previously reported literature procedure.⁵⁴

Synthesis of Block Copolymers

*Poly(DDW-*b*-BnW)*

Molecular Weight Series

In a nitrogen-filled glovebox, a 20 mL vial was charged with a stir bar, 50.0 mg (57.9 μmol) of **DDW** monomer and 1.0 mL of THF. With rapid stirring, 10 μL of an appropriate concentration of catalyst **1** in THF was quickly added via syringe. After one hour, 36.4 mg (57.9 μmol) of **BnW** monomer was added as a solid and allowed to react for 90 minutes. The polymerization was quenched by the addition of 0.1 mL of ethyl vinyl ether. The polymer was precipitated out into 15 mL of methanol and allowed to stir overnight, after which the polymer was isolated, washed with excess methanol, and dried under reduced pressure at 50 °C to a constant weight.

Scale-Up for Printing

In a nitrogen-filled glovebox, a 250 mL flat-bottom flask was charged with a stir bar, 6.00 g (6.94 mmol) of **DDW** monomer and 100 mL of THF. With rapid stirring, 300 μL of an appropriate concentration of catalyst **1** in THF was quickly added via a micropipette. After one hour, 4.37 g (6.94 mmol) of **BnW** monomer was added as a solid and allowed to react for 90 minutes. The polymerization was quenched by the addition of 2.0 mL of ethyl vinyl ether. The polymer was precipitated out into 500 mL of methanol and allowed to stir overnight, after which the polymer was isolated, washed with excess methanol, and dried under reduced pressure at 50 °C to a constant weight.

Isolated poly(DDW-b-BnW) ^1H NMR (400 MHz, CDCl_3): δ 7.43-7.14 (m), 5.41 (bs), 5.06 (t), 4.37 (bs), 3.98 (m), 3.80 (bs), 2.97 (bs), 2.65 (bs), 2.36 (bs), 2.05 (bs), 1.75 (m), 1.46 (s), 1.25 (s), 0.87 (t).

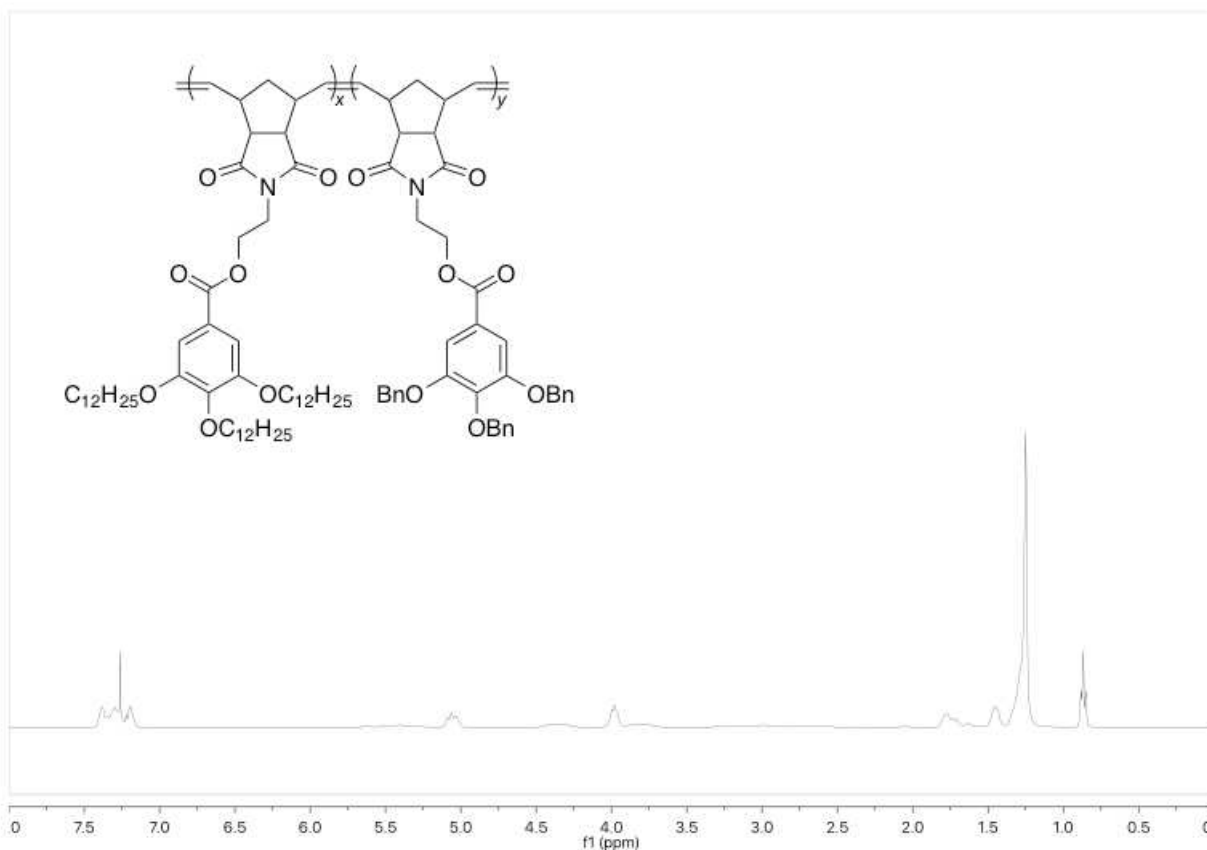


Figure 2.15. ^1H NMR of poly(DDW-b-BnW) in CDCl_3 .

Poly(DDW-b-FBnW)

In a nitrogen-filled glovebox, a 250 mL flat-bottom flask was charged with a stir bar, 6.00 g (6.94 mmol) of **DDW** monomer and 100 mL of THF. With rapid stirring, 300 μL of an appropriate concentration of catalyst **1** in THF was quickly added via a micropipette. After one hour, 6.00 g (6.94 mmol) of **FBnW** monomer was added as a solid and allowed to react for 90 minutes. The polymerization was quenched by the addition of 2.0 mL of ethyl vinyl ether. The

polymer was precipitated out into 500 mL of methanol and allowed to stir overnight, after which the polymer was isolated, washed with excess methanol, and dried under reduced pressure at 50 °C to a constant weight. This process was conducted in multiplet for each desired molecular weight. Polymers with consistent molecular weight were combined and dissolved in DCM to ensure a homogenous mixture. Once dissolved, the combined polymers were reprecipitated into methanol, filtered, and dried under reduced pressure at 50 °C to a constant weight.

Isolated poly(DDW-b-FBnW) ^1H NMR (400 MHz, CDCl_3): δ 7.35 (m), 7.21 (m), 7.00 (m), 6.86 (m), 5.45 (bs), 4.99 (m), 4.73 (bs), 3.98 (m), 3.82 (bs), 2.91 (bs), 2.39 (bs), 2.04 (bs), 1.77 (m), 1.45 (s), 1.25 (s), 0.87 (t).

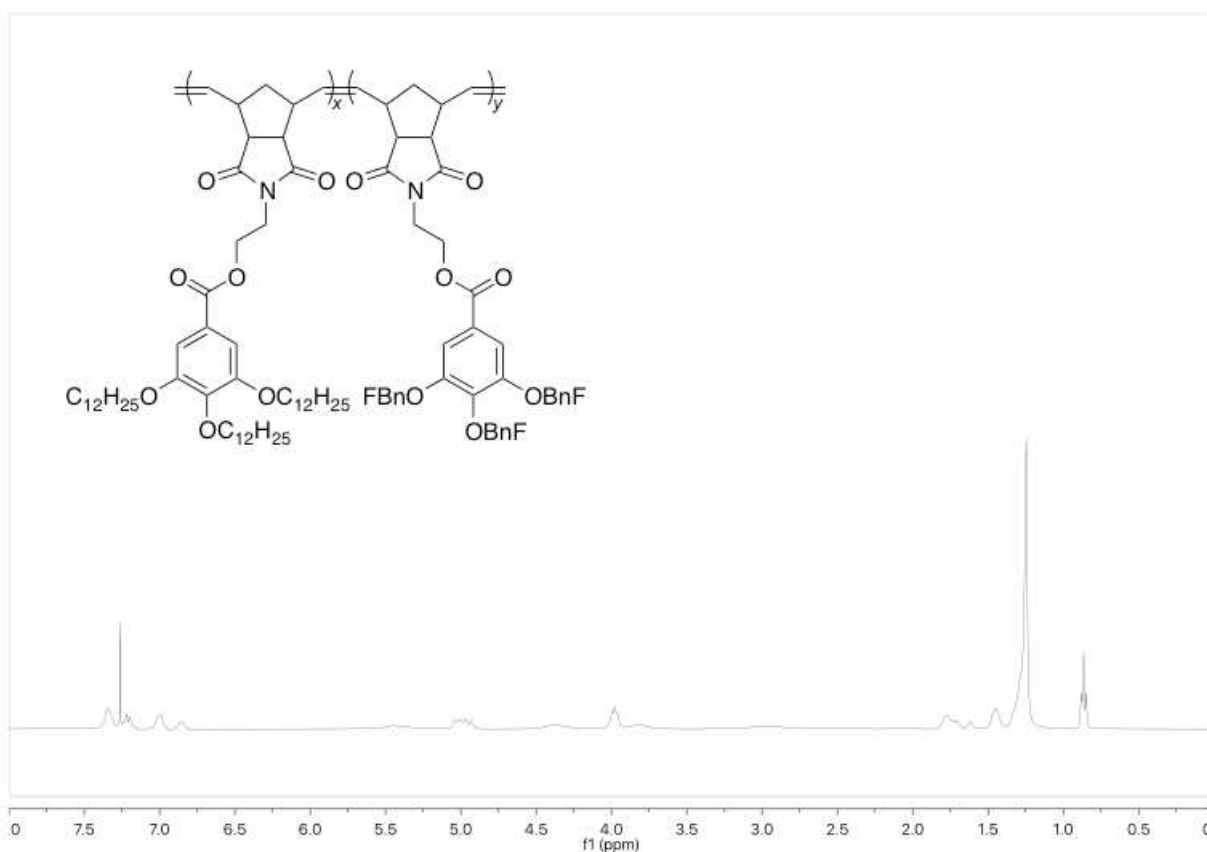


Figure 2.16. ^1H NMR of poly(DDW-b-FBnW) in CDCl_3

Characterization of Polymer Samples

GPC Analysis

Table 2.1. GPC analysis data of poly(DDW-b-BnW) molecular weight series and yields.

Sample	Feed Ratio	M_n (kDa)	M_w (kDa)	\bar{D} (M_w/M_n)	Yield (mg)	Yield (%)
1	[300]:[300]:[1]	488	507	1.04	73.5	85.1
2	[350]:[350]:[1]	554	574	1.04	72.0	83.3
3	[400]:[400]:[1]	641	689	1.08	77.4	89.6
4	[450]:[450]:[1]	713	754	1.06	69.2	80.1
5	[500]:[500]:[1]	740	828	1.12	76.4	88.4
6	[550]:[550]:[1]	814	875	1.08	80.3	92.9
7	[600]:[600]:[1]	841	902	1.07	77.8	90.0

Table 2.2. GPC analysis data of poly(DDW-b-BnW) scale-up for 3D printing and yields.

Sample	M_n (kDa)	M_w (kDa)	\bar{D} (M_w/M_n)	Yield (g)	Yield (%)
1	487	516	1.06	10.1	97.5
2	365	372	1.02	10.3	99.4
3	453	462	1.02	10.1	97.5
4	413	429	1.04	10.1	97.5
Mixture	440	484	1.10		

Table 2.3. GPC analysis data of **BCP-1** and yields.

Sample	M_n (kDa)	M_w (kDa)	$\mathcal{D} (M_w/M_n)$	Yield (g)	Yield (%)
1	570	582	1.02	10.3	95.9
2	516	548	1.06	10.3	95.9
3	553	569	1.03	10.3	95.9
4	552	563	1.02	10.4	96.8
5	561	574	1.02	10.3	95.9
6	534	550	1.03	10.4	96.8
7	526	552	1.05	10.3	95.9
8	550	568	1.03	10.5	97.8
9	545	562	1.03	10.4	96.8
10	530	547	1.03	10.3	95.9
11	554	568	1.03	10.3	95.9
12	488	530	1.09	10.3	95.9
13	504	551	1.09	10.7	99.6
14	478	525	1.10	10.4	96.8
15	472	523	1.11	10.4	96.8
Mixture (BCP-1)	564	581	1.03		

Table 2.4. GPC analysis data of **BCP-2** and yields

Sample	M_n (kDa)	M_w (kDa)	$\mathcal{D} (M_w/M_n)$	Yield (g)	Yield (%)
1	822	838	1.02	10.6	98.7
2	810	832	1.03	10.6	98.7
3	831	859	1.03	10.6	98.7
4	841	861	1.03	10.6	98.7
5	808	833	1.03	10.5	97.8
6	829	856	1.03	10.6	98.7
7	780	811	1.04	10.6	98.7
Mixture (BCP-2)	822	876	1.07		

Table 2.5. GPC analysis data of **BCP-3** and yields.

Sample	M_n (kDa)	M_w (kDa)	$\bar{D} (M_w/M_n)$	Yield (g)	Yield (%)
1	1050	1080	1.02	10.4	96.8
2	1040	1080	1.03	10.5	97.8
3	1050	1080	1.03	10.4	96.8
4	1040	1080	1.04	10.5	97.8
5	1050	1080	1.03	10.4	96.8
6	1050	1080	1.03	10.5	97.8
7	1060	1090	1.03	10.4	96.8
Mixture (BCP-3)	1040	1130	1.09		

Table 2.6. Measured dn/dc values of block copolymer samples used to estimate molecular weight.

Sample	dn/dc
poly(DDW-b-BnW)	0.116
BCP-1	0.119
BCP-2	0.119
BCP-3	0.122

DSC Analysis

T_g of **BCP-1** = 81-84 °C

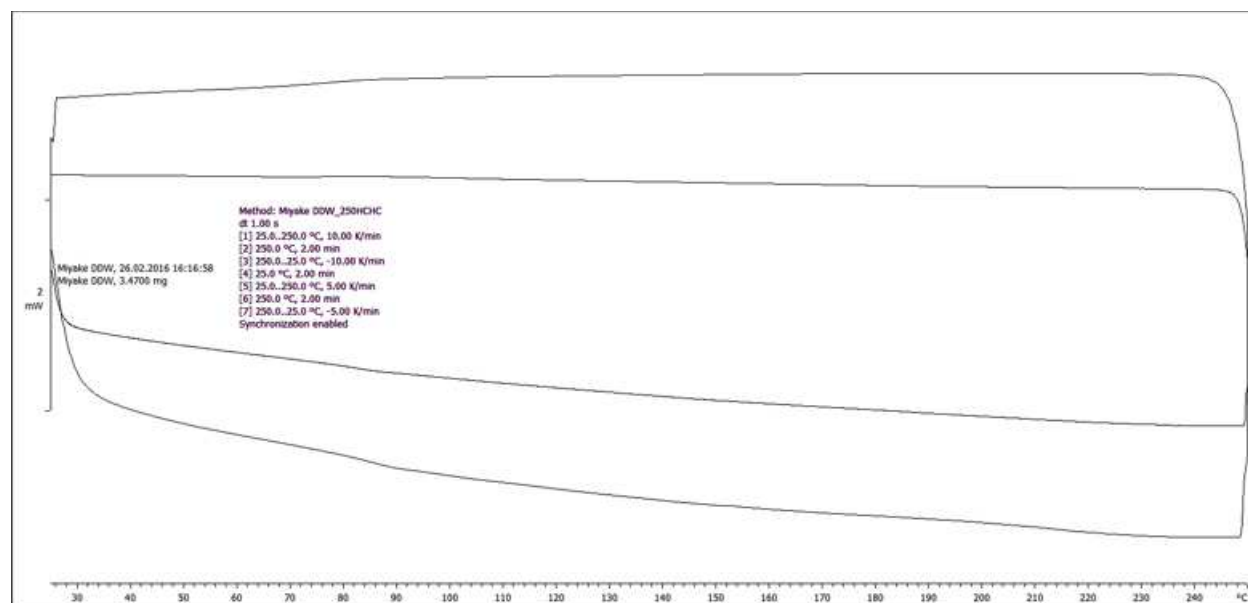


Figure 2.17. DSC analysis trace of **BCP-1**.

Characterization of Block Copolymer Photonic Crystal Thin Films, Filaments, and 3D Printed Objects

Images of Thin Films

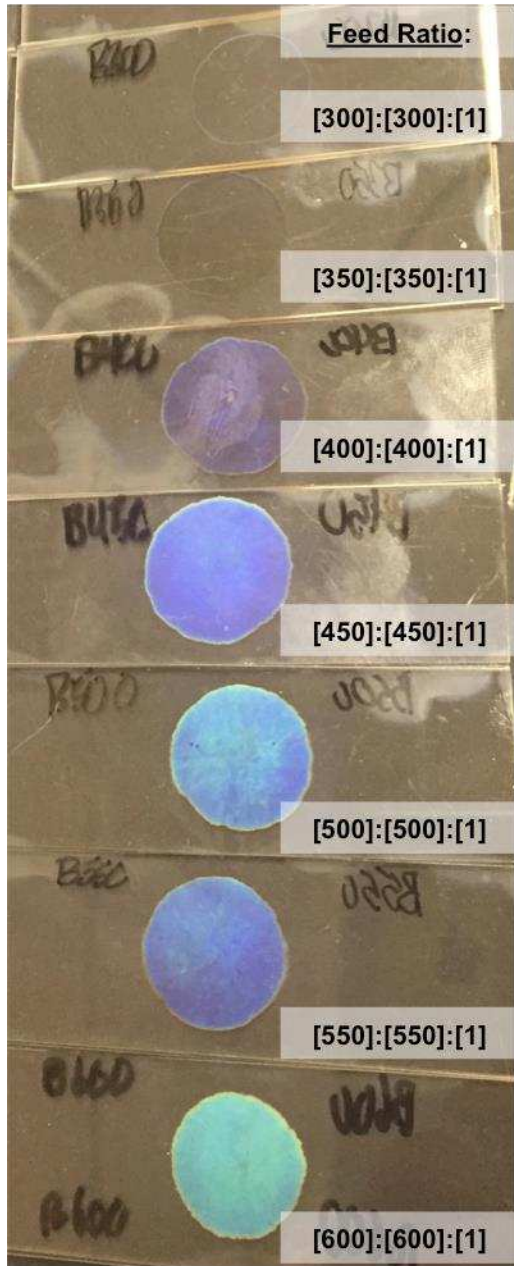


Figure 2.18. Photo of self-assembled poly(DDW-b-BnW) block copolymer photonic crystal thin films. Molecular weight increases descending from top of image.

Images of 3D Printed Objects

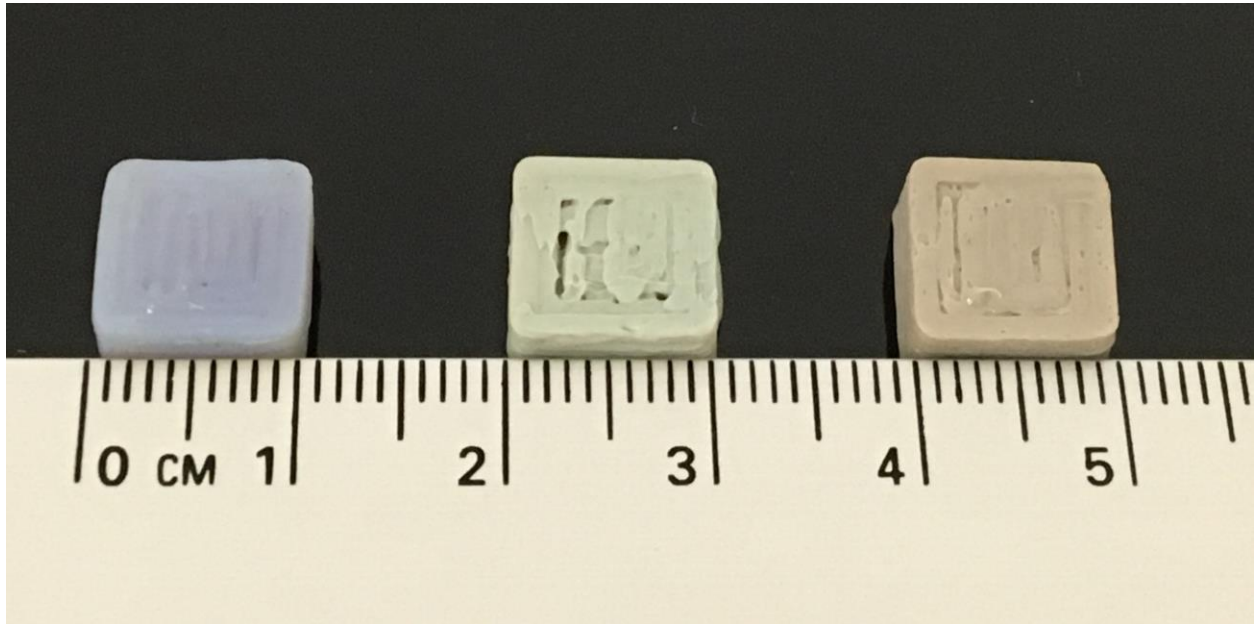


Figure 2.19. 3D printed cubes of **BCP-1**, **BCP-2**, and **BCP-3**.

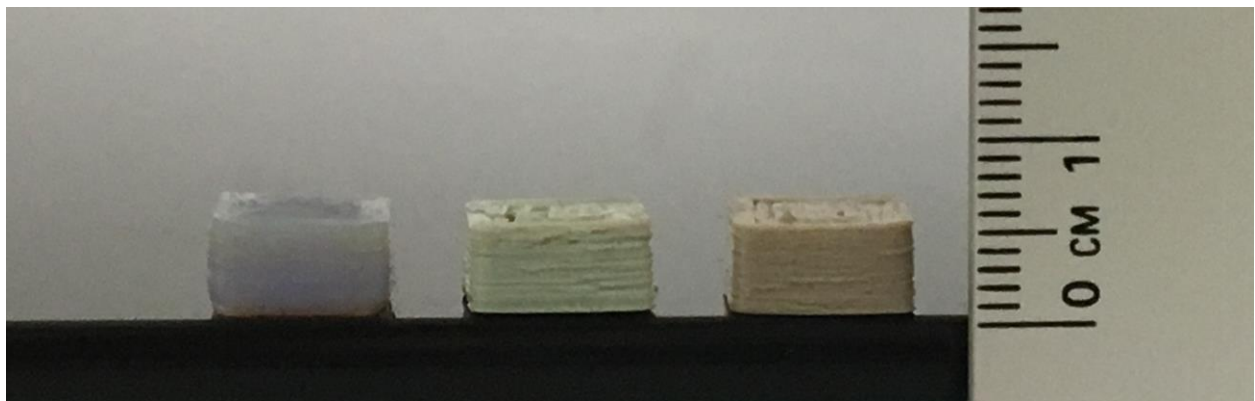


Figure 2.20. 3D printed cubes of **BCP-1**, **BCP-2**, and **BCP-3**.



Figure 2.21. 3D printed butterfly wings of **BCP-1**, **BCP-2**, and **BCP-3**.

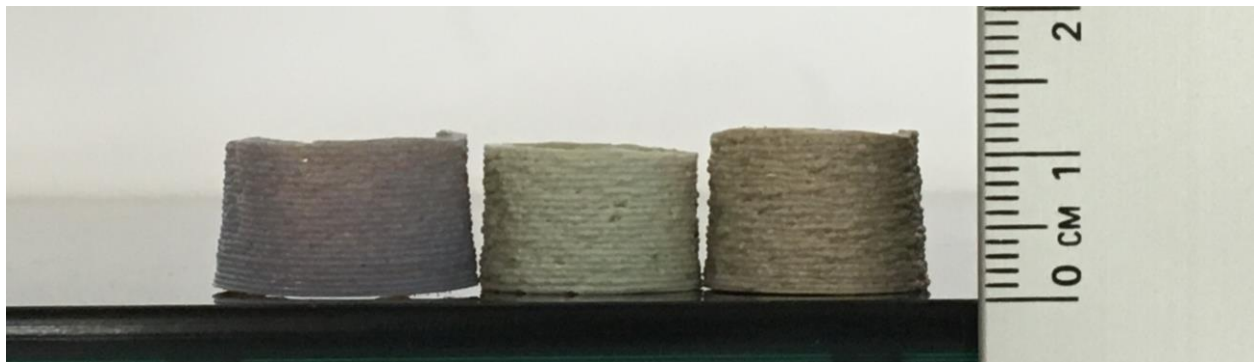


Figure 2.22. 3D printed cylinder of **BCP-1**, **BCP-2**, **BCP-3**.

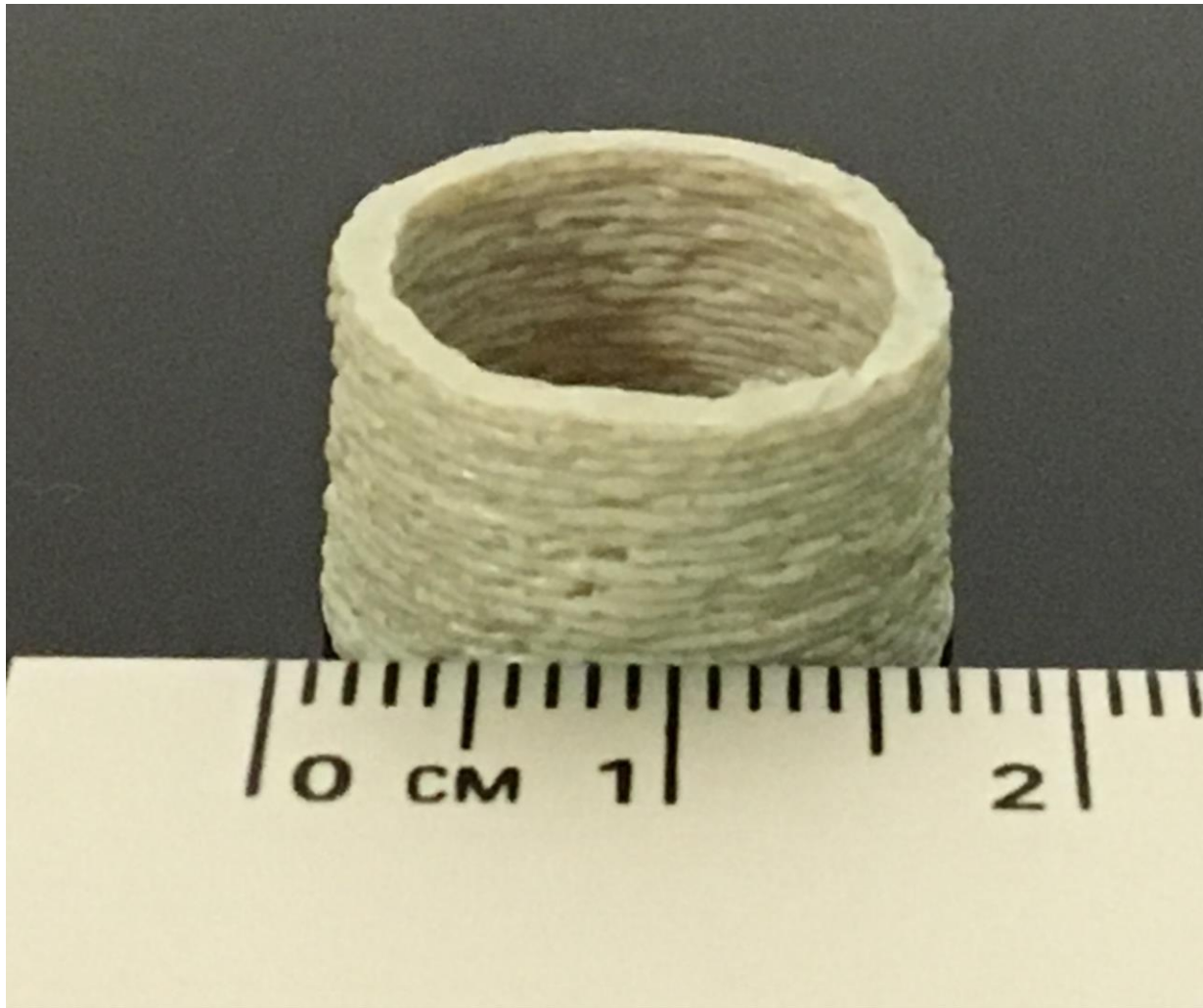


Figure 2.23. 3D printed cylinder of BCP-2.

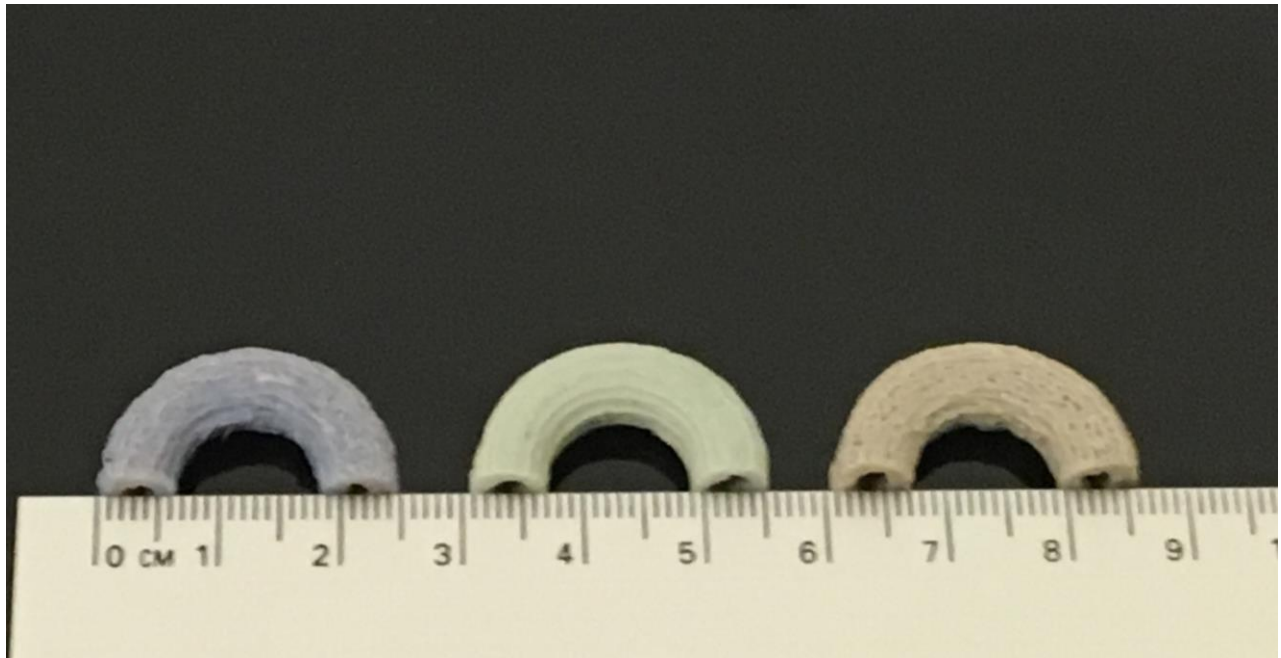


Figure 2.24. 3D printed U-shaped tube of **BCP-1, BCP-2, BCP-3.**

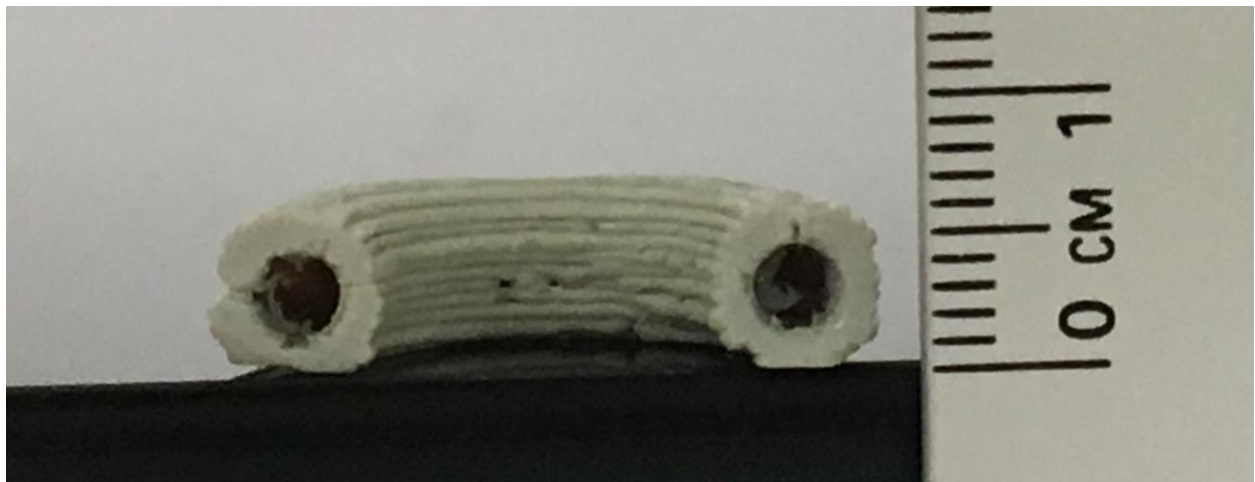


Figure 2.25. 3D printed U-shaped tube of **BCP-1**

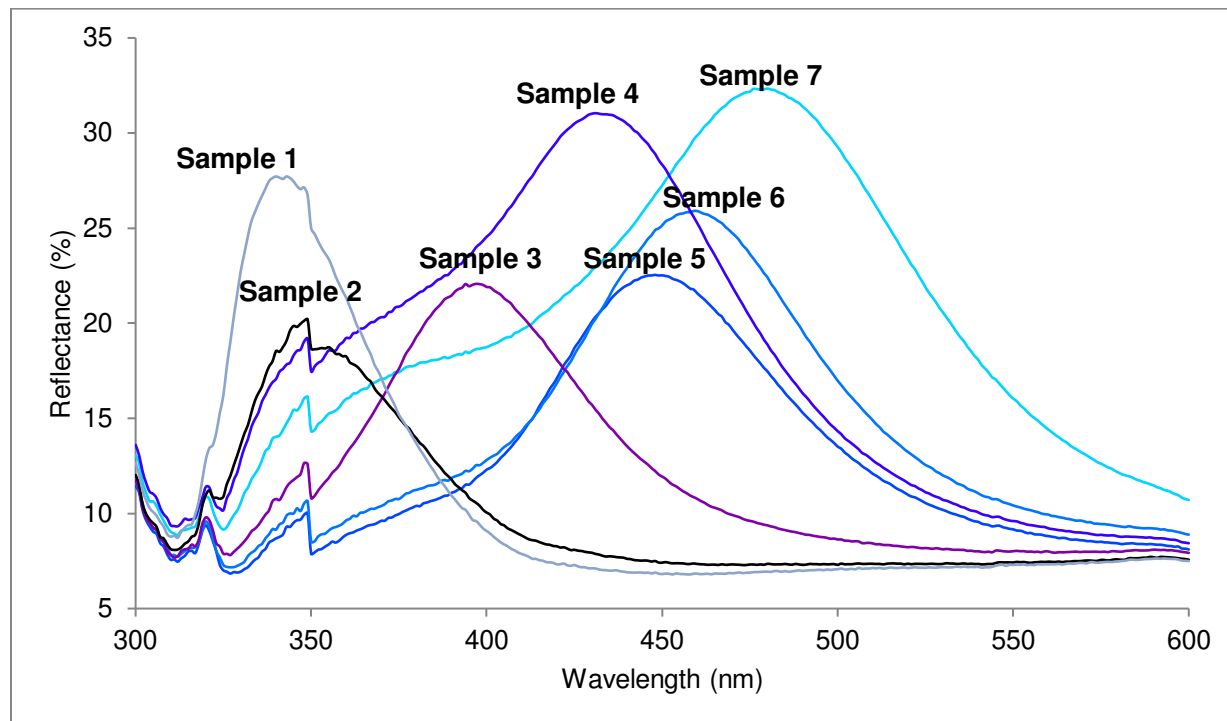


Figure 2.26. Plot of reflectance vs wavelength of self-assembled poly(DDW-b-BnW) block copolymer photonic crystal thin films.

Table 2.7. Peak reflection wavelengths of self-assembled poly(DDW-b-BnW) block copolymer photonic crystal thin films.

Sample	Peak Reflectance (nm)
1	343
2	349
3	397
4	431
5	450
6	459
7	480

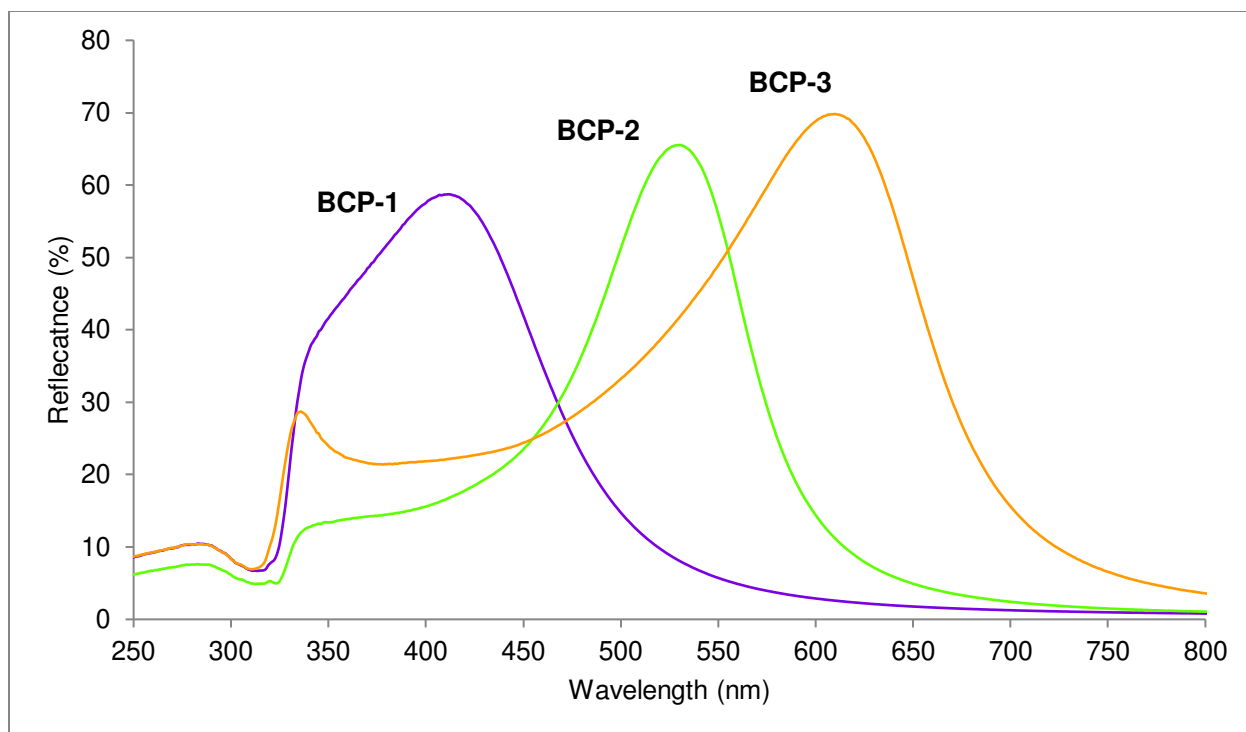


Figure 2.27. Plot of reflectance vs wavelength of self-assembled poly(DDW-b-FBnW) block copolymer photonic crystal thin films.

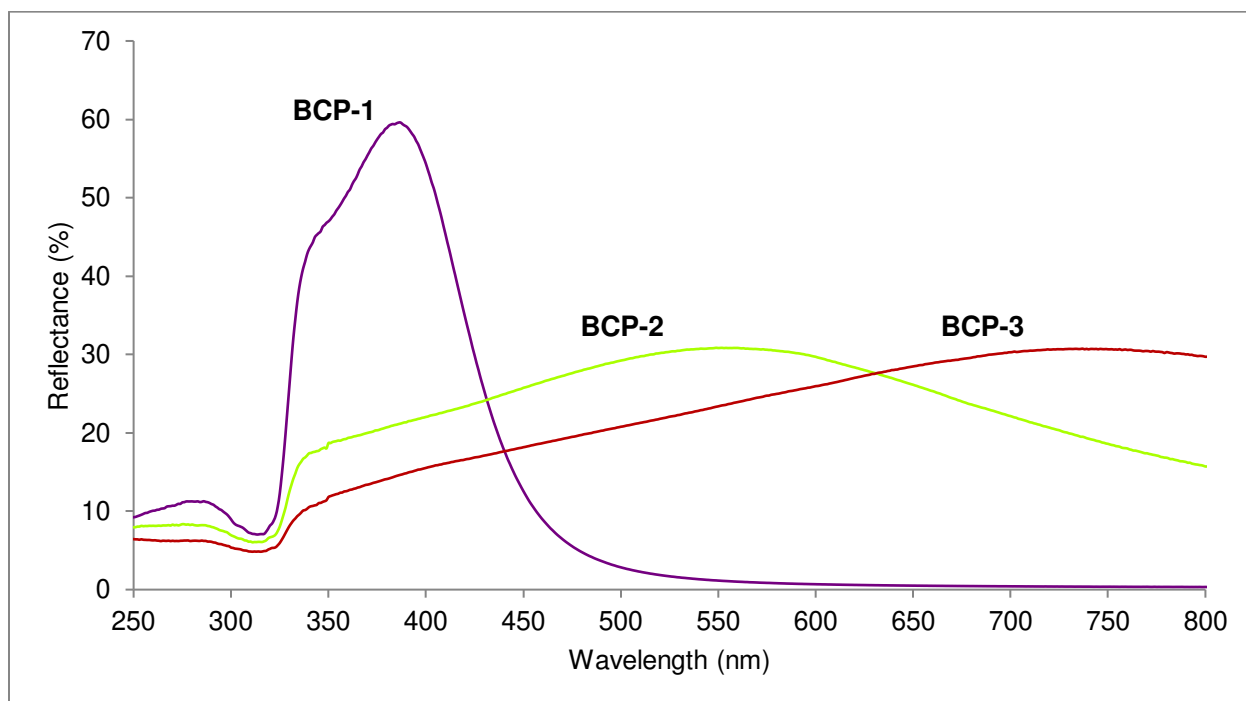


Figure 2.28. Plot of reflectance vs wavelength of self-assembled poly(DDW-b-FBnW) block copolymer photonic crystal filaments.

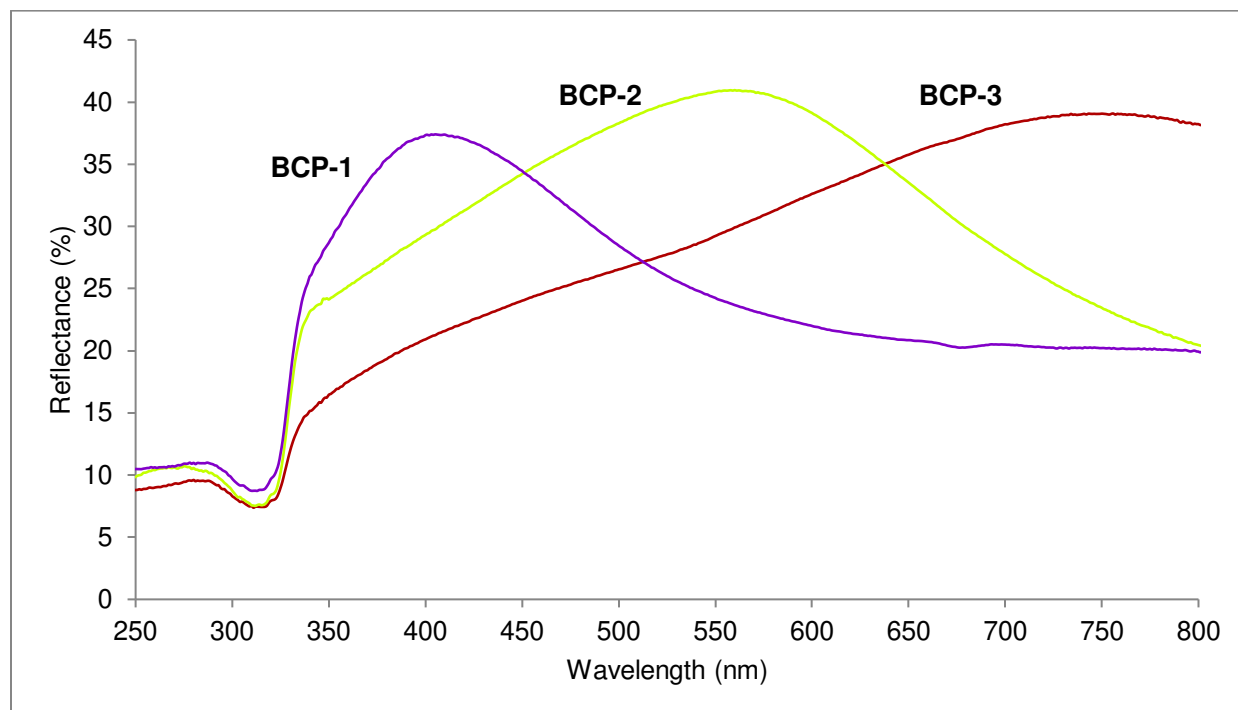


Figure 2.29. Plot of reflectance vs wavelength of self-assembled poly(DDW-b-FBnW) block copolymer photonic crystal 3D printed cubes.

Table 2.8. Peak reflection wavelengths of self-assembled poly(DDW-b-FBnW) block copolymer photonic crystal thin films, filaments, and 3D printed objects.

Sample	Film (nm)	Filament (nm)	Object - Pyramid (nm)
BCP-1	412	387	405
BCP-2	530	552	560
BCP-3	610	737	743

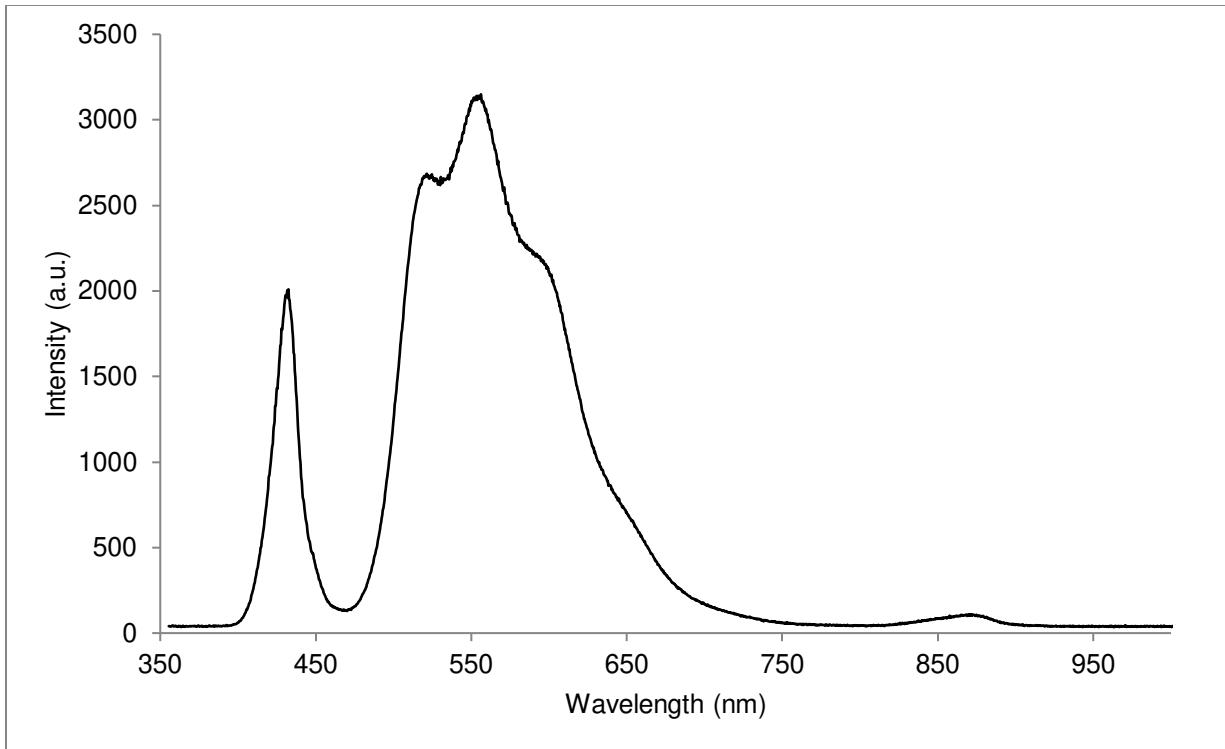


Figure 2.30. Emission spectrum of an iPhone 6S LED flashlight.

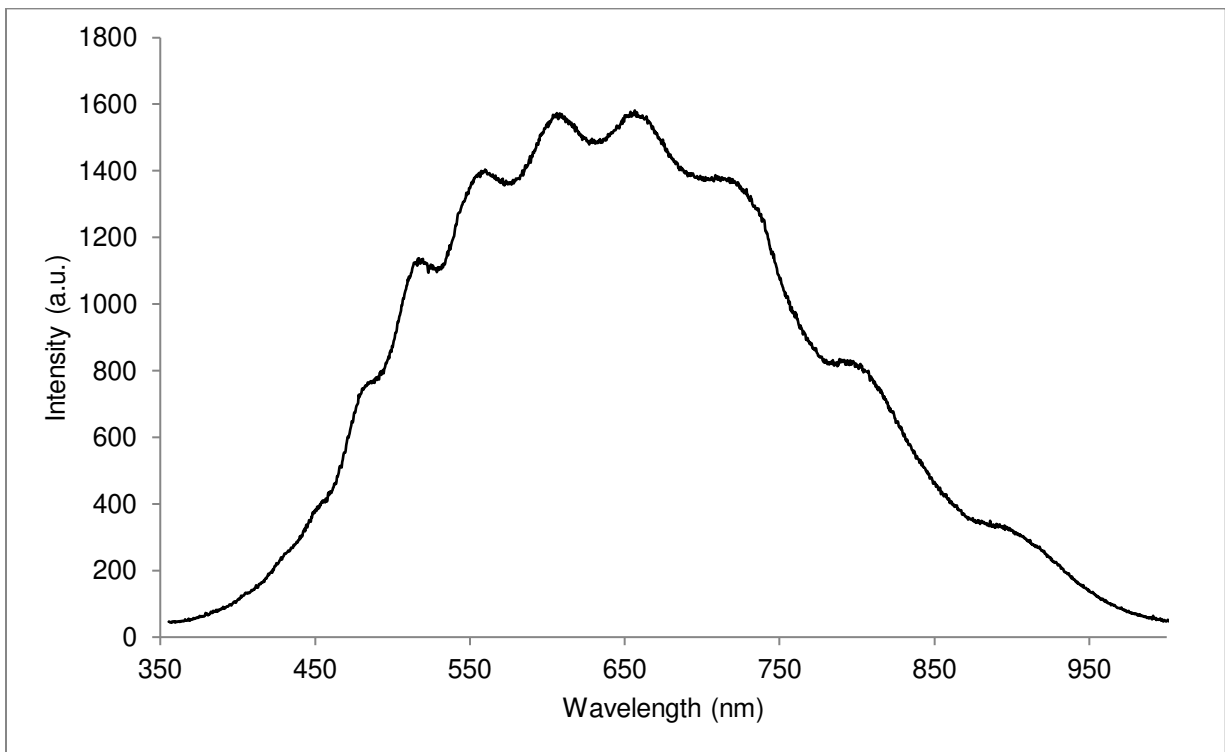


Figure 2.31. Emission spectrum of a Mini Maglite AAA flashlight

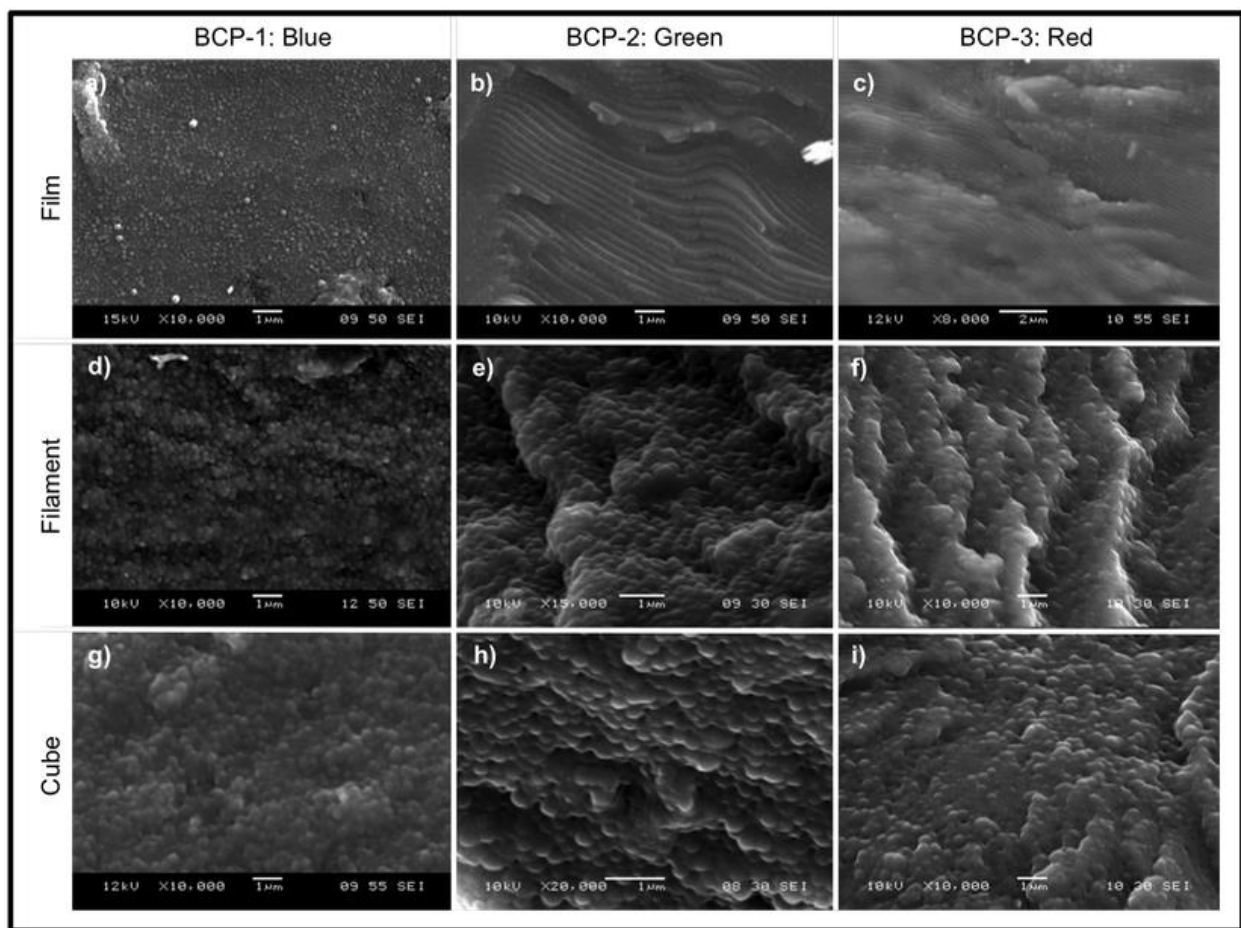


Figure 2.32. SEM images of self-assembled photonic crystal thin film, filament, and 3D printed cube: a) BCP-1 photonic crystal thin film b) BCP-2 photonic crystal thin film c) BCP-3 photonic crystal thin film d) BCP-1 photonic crystal filament e) BCP-2 photonic crystal filament f) BCP-3 photonic crystal filament g) BCP-1 3D printed photonic crystal cube h) BCP-2 3D printed photonic crystal cube i) BCP-3 3D printed photonic crystal cube.

References

- (1) McDonough, W.; Braungart, M. *The Upcycle: Beyond Sustainability—Designing for Abundance*; North Point Press: New York, **2013**.
- (2) Zi, J.; Yu, X.; Li, Y.; Hu, X.; Xu, C.; Wang, X.; Liu, X.; Fu, F. Coloration Strategies in Peacock Feathers. *Proc. Natl. Acad. Sci. U. S. A.* **2003**, 100, 12576–12578.
- (3) Sun, J.; Bhushan, B.; Tong, J. Structural Coloration in Nature. *RSC Adv.* **2013**, 3,

- 14862–14889.
- (4) Mason, C. W. Structural Colors in Insects. I. *J. Phys. Chem.* **1926**, 30, 383–395.
 - (5) Joannopoulos, J. D.; Johnson, S. G.; Winn, J. N.; Meade, R. D. *Photonic Crystals: Molding the Flow of Light*, 2nd ed.; Princeton University Press: Princeton, NJ, **2008**.
 - (6) Sorin, F.; Abouraddy, A. F.; Orf, N.; Shapira, O.; Viens, J.; Arnold, J.; Joannopoulos, J. D.; Fink, Y. Multimaterial Photodetecting Fibers: A Geometric and Structural Study. *Adv. Mater.* **2007**, 19, 3872–3877.
 - (7) Abouraddy, A. F.; Bayindir, M.; Benoit, G.; Hart, S. D.; Kuriki, K.; Orf, N.; Shapira, O.; Sorin, F.; Temelkuran, B.; Fink, Y. Towards Multimaterial Multifunctional Fibres that See, Hear, Sense and Communicate. *Nat. Mater.* **2007**, 6, 336–347.
 - (8) Ge, J.; Hu, Y.; Yin, Y. Highly Tunable Superparamagnetic Colloidal Photonic Crystals. *Angew. Chem., Int. Ed.* **2007**, 46, 7428–7431.
 - (9) Russell, P.; St, J. Photonic Crystal Fibers. *J. Lightwave Technol.* **2006**, 24, 4729–4749.
 - (10) Russell, P. Photonic Crystal Fibers. *Science* **2003**, 299, 358–362.
 - (11) Yablonovitch, E. Photonic Crystals: Semiconductors of Light. *Sci. Am.* **2001**, 285, 46–55.
 - (12) Schrenk, W. J.; Wheatley, J. A.; Lewis, R. A.; Arends, C. B. Nanolayer Polymeric Optical Films. *Tappi J.* **1992**, 169.
 - (13) Schrenk, W. J.; Lewis, R. A.; Wheatley, J. A.; Arends, C. B. Coextruded Infrared Reflecting Films. *Int. Polym. Process.* **1991**, 6, 255–256.
 - (14) Miyake, M.; Chen, Y.-C.; Braun, P. V.; Wiltzius, P. Fabrication of Three-Dimensional Photonic Crystals Using Multibeam Interference Lithography and Electrodeposition. *Adv. Mater.* **2009**, 21, 3012–3015.
 - (15) Bang, J.; Bae, J.; Löwenhielm, P.; Spiessberger, C.; Given-Beck, S. A.; Russell, T. P.;

- Hawker, C. J. Facile Routes to Patterned Surface Neutralization Layers for Block Copolymer Lithography. *Adv. Mater.* **2007**, *19*, 4552–4557.
- (16) Campbell, M.; Sharp, D. N.; Harrison, M. T.; Denning, R. G.; Turberfield, A. J. Fabrication of Photonic Crystals for the Visible Spectrum by Holographic Lithography. *Nature* **2000**, *404*, 53–56.
- (17) Beaulieu, M. R.; Hendricks, N. R.; Watkins, J. J. Large-Area Printing of Optical Gratings and 3D Photonic Crystals Using Solution- Processable Nanoparticle/Polymer Composites. *ACS Photonics* **2014**, *1*, 799–805.
- (18) Cui, L.; Li, Y.; Wang, J.; Tian, E.; Zhang, X.; Zhang, Y.; Song, Y.; Jiang, L. Fabrication of Large-Area Patterned Photonic Crystals by Ink- Jet Printing. *J. Mater. Chem.* **2009**, *19*, 5499–5502.
- (19) Kazmierczak, T.; Song, H.; Hiltner, H.; Baer, E. Polymeric One- Dimensional Photonic Crystals by Continuous Coextrusion. *Macro- mol. Rapid Commun.* **2007**, *28*, 2210–2216.
- (20) Liu, N.; Guo, H. C.; Fu, L. W.; Kaiser, S.; Schweizer, H.; Giessen, H. Three-Dimensional Photonic Metamaterials at Optical Frequencies. *Nat. Mater.* **2008**, *7*, 31–37.
- (21) Knight, J. C. Photonic Crystal Fibres. *Nature* **2003**, *424*, 847– 851.
- (22) Hart, S. D.; Maskaly, G. R.; Temelkuran, B.; Prideau, P. H.; Joannopoulos, J. D.; Fink, Y. External Reflection from Omnidirectional Dielectric Mirror Fibers. *Science* **2002**, *296*, 510–513.
- (23) Ozin, G. A.; Yang, S. M. The Race for the photonic Chip: Colloidal Crystal Assembly in Silicon Wafers. *Adv. Funct. Mater.* **2001**, *11*, 95–104.
- (24) Wang, J.; Zhang, Y.; Wang, S.; Song, Y.; Jiang, L. Bioinspired Colloidal Photonic Crystals with Controllable Wettability. *Acc. Chem. Res.* **2011**, *44*, 405–415.

- (25) Aguirre, C. I.; Reguera, E.; Stein, A. Tunable Colors in Opals and Inverse Opal Photonic Crystals. *Adv. Funct. Mater.* **2010**, *20*, 2565–2578.
- (26) Moon, J. H.; Yang, S. Chemical Aspects of Three-Dimensional Photonic Crystals. *Chem. Rev.* **2010**, *110*, 547–574.
- (27) Tumbleston, J. R.; Shirvanyants, D.; Ermoshikin, N.; Januszewicz, R.; Johnson, A. R.; Kelly, D.; Chen, K.; Pinschmidt, R.; Rolland, J. P.; Ermoshikin, A.; Samulski, E. T.; DeSimone, J. M. Continuous Liquid Interface Production of 3D Objects. *Science* **2015**, *347*, 1349–1352.
- (28) Bakarich, S. E.; Gorkin, R., III; in het Panhuis, M.; Spinks, G. M. Three-Dimensional Printing Fiber Reinforced Hydrogel Composites. *ACS Appl. Mater. Interfaces* **2014**, *6*, 15998–16006.
- (29) Conner, B. P.; Manogharan, G. P.; Martof, A. N.; Rodomsky, L. M.; Rodomsky, C. M.; Jordan, D. C.; Limperos, J. W. Making Sense of 3-D Printing: Creating a Map of Additive Manufacturing Products and Services. *Addit. Manuf.* **2014**, *1–4*, 64–76.
- (30) Jones, N. Science in Three Dimensions: The Print Revolution. *Nature* **2012**, *487*, 22–23.
- (31) Kruth, J.-P.; Leu, M. C.; Nakagawa, T. Progress in Additive Manufacturing and Rapid Prototyping. *CIRP Ann.* **1998**, *47*, 525–540.
- (32) Peterson, G. I.; Larsen, M. B.; Ganter, M. A.; Storti, D. W.; Boydston, A. J. 3D-printed Mechanochromic Materials. *ACS Appl. Mater. Interfaces* **2015**, *7*, 577–583.
- (33) Peterson, G. I.; Yurtoglu, M.; Larsen, M. B.; Craig, S. L.; Ganter, M. A.; Storti, D. W.; Boydston, A. J. Additive Manufacturing of Mechanochromic Polycaprolactone on Entry-Level Systems. *Rapid Prototyping* **2015**, *21*, 520–527.
- (34) Stefik, M.; Guldin, S.; Vignolini, S.; Wiesner, U.; Steiner, U. Block Copolymer Self-

- Assembly for Nanophotonics. *Chem. Soc. Rev.* **2015**, 44, 5076–5091.
- (35) Bates, F. S.; Hillmyer, M. A.; Lodge, T. P.; Bates, C. M.; Delaney, K. T.; Fredrickson, G. H. Multiblock Polymers: Panacea or Pandora's Box? *Science* **2012**, 336, 434–440.
- (36) Park, C.; Yoon, J.; Thomas, E. L. Enabling Nanotechnology with Self Assembled Block Copolymer Patterns. *Polymer* **2003**, 44, 6725– 6760.
- (37) Edrington, A. C.; Urbas, A. M.; DeRege, A. C.; Chen, C. X.; Swager, T. M.; Hadjichristidis, N.; Xenidou, M.; Fetters, L. J.; Joannopoulos, J. D.; Fink, Y.; Thomas, E. L. Polymer-Based Photonic Crystals. *Adv. Mater.* **2001**, 13, 421–425.
- (38) Fink, Y.; Urbas, A. M.; Bawendi, M. G.; Joannopoulos, J. D.; Thomas, E. L. Block Copolymers as Photonic Bandgap Materials. *J. Lightwave Technol.* **1999**, 17, 1963–1969.
- (39) Galisteo-López, J. F.; Ibisate, M.; Sapienza, R.; Froufe-Pérez, L. S.; Blanco, Á.; López, C. Self-Assembled Photonic Structures. *Adv. Mater.* **2011**, 23, 30–69.
- (40) Yoon, J.; Lee, W.; Thomas, E. L. Self-Assembly of Block Copolymers for Photonic-Bandgap Materials. *MRS Bull.* **2005**, 30, 721–726.
- (41) Rzayev, J. Molecular Bottlebrushes: New Opportunities in Nanomaterials Fabrication. *ACS Macro Lett.* **2012**, 1, 1146–1149.
- (42) Parnell, A. J.; Pryke, A.; Mykhaylyk, O. O.; Howse, J. R.; Adawi, A. M.; Terrill, N. J.; Fairclough, J. P. A. Continuously Tuneable Optical Filters from Self-Assembled Block Copolymer Blends. *Soft Matter* **2011**, 7, 3721–3725.
- (43) Hustad, P. D.; Marchand, G. R.; Garcia-Meitin, E. I.; Roberts, P. L.; Weinhold, J. D. Photonic Polyethylene from Self-assembled Mesophases of Polydisperse Olefin Block Copolymers. *Macromolecules* **2009**, 42, 3788–3794.
- (44) Kang, C.; Kim, E.; Baek, H.; Hwang, K.; Kwak, D.; Kang, Y.; Thomas, E. L. Full Color

- Stop Bands in Hybrid Organic/Inorganic Block Copolymer Photonic Gels by Swelling-Freezing. *J. Am. Chem. Soc.* **2009**, 131, 7538–7539.
- (45) Yoon, J.; Lee, W.; Thomas, E. L. Thermochromic Block Copolymer Photonic Gel. *Macromolecules* **2008**, 41, 4582–4584.
- (46) Kang, Y.; Walish, J. J.; Gorishnyy, T.; Thomas, E. L. Broad- Wavelength-Range Chemically Tunable Block-Copolymer Photonic Gels. *Nat. Mater.* **2007**, 6, 957–960.
- (47) Runge, M. B.; Bowden, N. B. Synthesis of High Molecular Weight Comb Block Copolymers and their Assembly into Ordered Morphologies in the Solid State. *J. Am. Chem. Soc.* **2007**, 129, 10551– 10560.
- (48) Yoon, J.; Mathers, R. T.; Coates, G. W.; Thomas, E. L. Optically Transparent and High Molecular Weight Polyolefin Block Copolymers Toward Self-Assembled Photonic Band Gap Materials. *Macromolecules* **2006**, 39, 1913–1919.
- (49) Urbas, A.; Sharp, R.; Fink, Y.; Thomas, E. L.; Xenidou, M. Fetters L. J. Tunable Block Copolymer/Homopolymer Photonic Crystals. *Adv. Mater.* **2000**, 12, 812–814.
- (50) Urbas, A.; Fink, Y.; Thomas, E. L. One-Dimensionally Periodic Dielectric Reflectors from Self-Assembled Block Copolymer-Homo- polymer Blends. *Macromolecules* **1999**, 32, 4748–4750.
- (51) Fredrickson, G. H.; Bates, F. S. Dynamics of Block Copolymers: Theory and Experiment. *Annu. Rev. Mater. Sci.* **1996**, 26, 501–550.
- (52) Bates, F. S.; Fredrickson, G. H. Block Copolymer Thermody- namics: Theory and Experiment. *Annu. Rev. Phys. Chem.* **1990**, 41, 525–557.
- (53) Macfarlane, R. J.; Kim, B.; Lee, B.; Weitekamp, R. A.; Bates, C. M.; Siu, F. L.; Chain, A. B.; Delaney, K. T.; Fredrickson, G. H.; Atwater, H. A.; Grubbs, R. H. Improving Brush

- Polymer Infrared One- Dimensional Photonic Crystals via Linear Polymer Additives. *J. Am. Chem. Soc.* **2014**, 136, 17374–17377.
- (54) Piunova, V. A.; Miyake, G. M.; Daeffler, C. S.; Weitekamp, R. A.; Grubbs, R. H. Highly Ordered Dielectric Mirrors via the Self-Assembly of Dendronized Block Copolymers. *J. Am. Chem. Soc.* **2013**, 135, 15609–15616.
- (55) Sveinbjörnsson, B. R.; Weitekamp, R. A.; Miyake, G. M.; Xia, Y.; Atwater, H. A.; Grubbs, R. H. Rapid Self-Assembly of Brush Block Copolymers to Photonic Crystals. *Proc. Natl. Acad. Sci. U. S. A.* **2012**, 109, 14332–14336.
- (56) Miyake, G. M.; Weitekamp, R. A.; Piunova, V. A.; Grubbs, R. H. Synthesis of Isocyanate-Based Brush Block Copolymers and Their Rapid Self-Assembly to Infrared-Reflecting Photonic Crystals. *J. Am. Chem. Soc.* **2012**, 134, 14249–14254.
- (57) Miyake, G. M.; Piunova, V. A.; Weitekamp, R. A.; Grubbs, R. H. Precisely Tunable Photonic Crystals from Rapidly Self-Assembling Brush Block Copolymer Blends. *Angew. Chem., Int. Ed.* **2012**, 51, 11246–11248.
- (58) Hu, M.; Xia, Y.; McKenna, G. B.; Kornfield, J. A.; Grubbs, R. H. Linear Rheological Response of a Series of Densely Branched Brush Polymers. *Macromolecules* **2011**, 44, 6935–6943.
- (59) Xia, Y.; Olsen, B. D.; Kornfield, J. A.; Grubbs, R. H. Efficient Synthesis of Narrowly Dispersed Brush Copolymers and Study of their Assemblies: The Importance of Side Chain Arrangement. *J. Am. Chem. Soc.* **2009**, 131, 18525–18532.
- (60) Xia, Y.; Kornfield, J. A.; Grubbs, R. H. Efficient Synthesis of Narrowly Dispersed Brush Polymers via Living Ring-Opening Metathesis Polymerization of Macromolecules *Macromolecules* **2009**, 42, 3761–3766.

- (61) Miyake, G. M.; Weitekamp, R. A.; Grubbs, R. H. *Handbook of Metathesis: Synthesis of Materials with Nanostructured Periodicity*, 2nd ed.; Wiley-VCH: Weinheim, Germany, **2015**.
- (62) Vougioukalakis, G. C.; Grubbs, R. H. Ruthenium-Based Heterocyclic Carbene-Coordinated Olefin Metathesis Catalysts. *Chem. Rev.* **2010**, 110, 1746–1787.
- (63) Leitgeb, A.; Wappel, J.; Slugovc, C. The ROMP Toolbox Upgraded. *Polymer* **2010**, 51, 2927–2946.
- (64) Bielawski, C. W.; Grubbs, R. H. *Controlled and Living Polymerizations*; Wiley-VCH: Weinheim, Germany, **2009**.
- (65) Bielawski, C. W.; Grubbs, R. H. Living Ring-Opening Metathesis Polymerization. *Prog. Polym. Sci.* **2007**, 32, 1–29.
- (66) Slugovc, C. The Ring Opening Metathesis Polymerisation Toolbox. *Macromol. Rapid Commun.* **2004**, 25, 1283–1297.
- (67) Hu, H.; Gopinadhan, M.; Osuji, C. O. Directed Self-Assembly of Block Copolymers: A Tutorial Review of Strategies for Enabling Nanotechnology with Soft Matter. *Soft Matter* **2014**, 10, 3867–3889.
- (68) Love, J. A.; Morgan, J. P.; Trnka, T. M.; Grubbs, R. H. A Practical and Highly Active Ruthenium-Based Catalyst that Effects the Cross Metathesis of Acrylonitrile. *Angew. Chem., Int. Ed.* **2002**, 41, 4035–4037.
- (69) Matson, J. B.; Grubbs, R. H. Synthesis of Fluorine-18 Functionalized Nanoparticles for use as in vivo Molecular Imaging Agents. *J. Am. Chem. Soc.* **2008**, 130, 6731–6733.
- (70) Xia Y.; Sveinbjornsson B. R.; Grubbs R. H.; Weitekamp R.; Miyake G. M.; Piunova V. A.; Daeffler C. S. *U.S. Patent 2,013,029,6491*, **2013**.

CHAPTER 3 – 3D PRINTING USING POWDER MELT EXTRUSION

Overview

Additive manufacturing (creating objects by adding material, also known as 3D printing) promises to revolutionize manufacturing industries. However, 3D printing of novel build materials is currently limited by constraints inherent to printer designs. In this work, a bench-top powder melt extrusion (PME) 3D printer head was designed and fabricated to print parts directly from powder-based materials rather than filament. The final design of the PME printer head evolved from the Rich Rap Universal Pellet Extruder (RRUPE) design and was realized through an iterative approach. The PME printer was made possible by modifications to the funnel shape, pressure applied to the extrudate by the auger, and hot end structure. Through comparison of parts printed with the PME printer with those from a commercially available fused filament fabrication (FFF) 3D printer using common thermoplastics poly(lactide) (PLA), high impact poly(styrene) (HIPS), and acrylonitrile butadiene styrene (ABS) powders (< 1 mm in diameter), evaluation of the printer performance was performed. For each build material, the PME printed objects show comparable viscoelastic properties by dynamic mechanical analysis (DMA) to those of the FFF objects. However, due to a significant difference in printer resolution between PME (X–Y resolution of 0.8 mm and a Z-layer height calibrated to 0.1 mm) and FFF (X–Y resolution of 0.4 mm and a Z-layer height of 0.18 mm), as well as, an inherently more inconsistent feed of build material for PME than FFF, the resulting print quality, determined by a dimensional analysis and surface roughness comparisons, of the PME printed objects was lower than that of the FFF printed parts based on the print layer uniformity and structure. Further, due to the poorer print resolution and inherent inconsistent build material feed of the PME, the bulk

tensile strength and Young's moduli of the objects printed by PME were lower and more inconsistent (49.2 ± 10.7 MPa and 1620 ± 375 MPa, respectively) than those of FFF printed objects (57.7 ± 2.31 MPa and 2160 ± 179 MPa, respectively). Nevertheless, PME print methods promise an opportunity to provide a platform on which it is possible to rapidly prototype a myriad of thermoplastic materials for 3D printing.

Introduction

Extrusion-based 3D printing is among the most widespread additive manufacturing techniques, with users spanning from hobbyists to industrial manufacturing companies [1–5]. The widespread adoption of extrusion-based 3D printing can be largely attributed to the low-cost and straightforward method of printing compared to other printing techniques (e.g. stereolithography, laser sintering, polymer jetting, etc.) [6–10]. Application of extrusion-based 3D printing techniques have enabled the rapid and customized production of 3D objects, ranging for example from art to coatings to force-sensing technologies [11–14]. A common extrusion-based additive manufacturing method is fused filament fabrication (FFF), in which a thermoplastic filament is heated and passed through a printer head to create a 3D printed object by layering the extrudate in specified shapes [15–18]. The materials compatible with FFF are mostly thermoplastics that are typically processed into filament and spooled for use in FFF. Unfortunately, evaluating the capability of a novel material to be printed by FFF can be challenging due to the difficulty of precision filament processing, even with specialized equipment. As such, the ability to extrude materials not in filament form could facilitate a more efficient method to screen novel materials for 3D printing and increase the build material landscape of 3D printing bypassing the filament-processing step of FFF.

The application of novel build materials for additive manufacturing [19–22] has the potential to transform the current landscape of 3D printing technology since the properties of the material inputs will dictate the optical, thermal, and mechanical properties of the final printed object. Recent developments in build materials have enabled the production of printed objects with tailored optical, thermal, electrical, mechanical, and chemical properties [23–27]. However, the adoption of these novel 3D printable materials has been slow due to the high cost and the requirement for pre-processing the raw materials into filament or pellets. To date, the two foremost examples of extrusion-based 3D printing from a pellet feedstock rather than a filament feedstock, have been demonstrated by big area additive manufacturing (BAAM) techniques [28–30] and Titan Robotics’ Atlas printer series [31]. Titan’s Atlas printer series can be modified to print production scale projects from thermoplastic pellets, and contains a build volume of 30” x 30” x 45”. However, the industrial scale of the BAAM techniques and the Atlas printers is not conducive to laboratory scale use. Thus, bench-top pellet extruders capable of printing less material have been fabricated such as, Direct3D [32] and the Rich Rap Universal Pellet Extruder (RRUPE) [33]. Although these two pellet extruders expand the variety of materials that can be printed [34] and are capable of printing smaller parts (on the order of 200 mm³ or less), they are not designed for 3D printing of material feedstock that is not pre-processed into the form of pellets. This limitation of pellet extruders further restricts which thermoplastic materials can be 3D printed and presents an obstacle to printing non-processed novel material feedstock. Rather than requiring new materials to be printed by the FFF or pellet extrusion techniques, the ability to print directly from powder granules makes the process of 3D printing novel materials more accessible by reducing the need for specialized equipment beyond a printer head.

Here, we report a bench-top PME printer that was fabricated through modification of the Rich Rap Universal Pellet Extruder (RRUPE) design [33] and tested with powders (particle size range of 0.038 mm–1 mm in diameter) of common 3D printing thermoplastics, including poly(lactide) (PLA), high impact poly(styrene) (HIPS), and acrylonitrile butadiene styrene (ABS) (Figure 3.18, 3.19, and 3.20). The sources of each of these thermoplastic powders were mechanically ground FFF printed parts. The parts being ground were often defective parts that would have been disposed of, normally. The resulting PME prints were compared to FFF prints based on print quality, print resolution, material viscoelasticity, and bulk material tensile properties to determine the initial viability of the PME 3D printing technique.

Printer Head Design and Modifications

Development of a 3D printer that can directly use a thermoplastic powder build material requires an understanding of the fundamental relationships between the printer head design and printer performance. Therefore, the design of the printer head is the major focus of the current study as it is critical to the success of printing 3D objects directly from powder. Analysis of current printer heads (e.g. RRUPE) designed to print pellets (particle sizes ~ 3–5 mm in diameter) inspired us to iteratively design and optimize a bench-top PME printer head. The resulting PME printer (Fig. 3.1) can successfully print 3D objects, which establishes a 3D printing platform that reduces the time needed for pre-processing build materials and allows researchers the potential to rapidly prototype novel build materials.

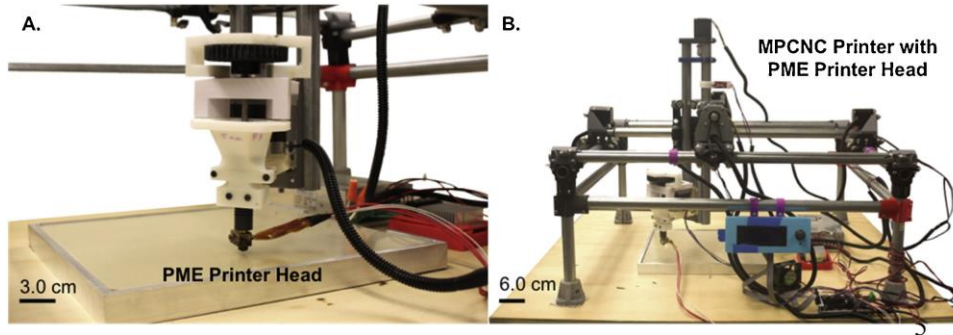


Fig. 3.1. Photographs of the final PME printer head (A.) and the PME printer head assembled on the open-source MPCNC printer (B.).

PME Printer Head Design

An open-source, customizable printer, the MPCNC [35], was obtained to provide the control and axes needed to move the printer head. The printer was controlled electronically and with software as shown in Figures 3.11 and 3.12. The ability of the RRUPE printer head design was then investigated for powder extrusion since most of the components can be 3D printed by FFF and readily retrofitted to the MPCNC printer, enabling design optimization (Fig. 3.2). Starting at the closest part to the build plate, the brass nozzle (nozzle diameter = 0.4 mm) is connected to a polyether ether ketone (PEEK) tube, which comprises the commercially available Reifsnyder Precision Works hot end (RPWHE) [36]. The printer-head funnel then supports the hot end and is responsible for directing the build material to the auger. Above the entrance to the funnel, the build material resides in the hopper before it is directed into the funnel. The auger passes through the funnel from the top of the hot end to a large gear. The large gear is spun in a counterclockwise rotation by the smaller gear attached to the NEMA 17 stepper motor (0.48 N-m) to feed material from the funnel into the hot end.

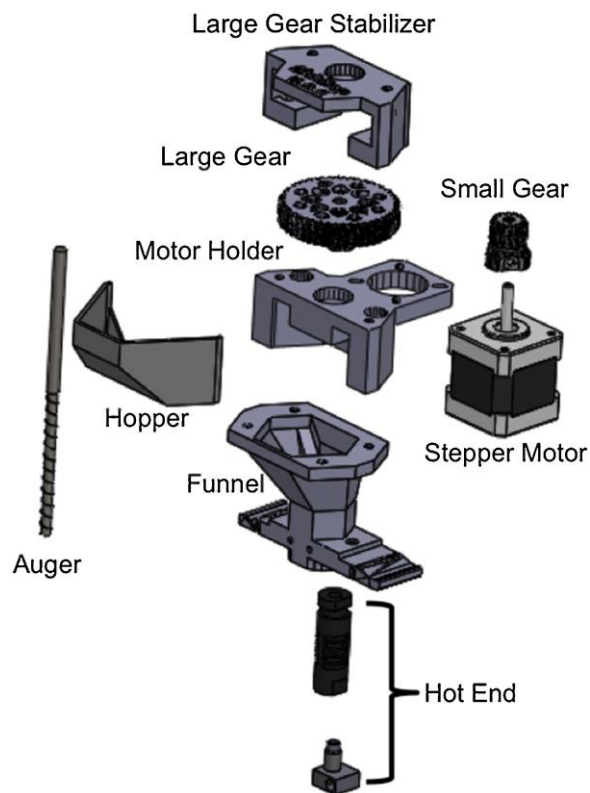


Fig. 3.2. Diagram of an exploded assembly model of the RRUPE design.

RRUPE Funnel Modifications for PME

Extrusion with the RRUPE design was evaluated using a powdered poly(lactide) (PLA) build material (< 1 mm in diameter, see Experimental Methods section and Figure 3.18 in Supporting Information for additional details), however, no extrusion of the PLA build material was observed. An analysis of the RRUPE printer head (Fig. 3.3) after a PLA powder extrusion attempt revealed that the funnel was not delivering powder to the hot end. To address this limitation, the funnel geometry was redesigned in 3-steps (Fig. 3.3): (1) the angle of the funnel was increased from 139° in the RichRap funnel (Fig. 3.3E) to 146° in the PME funnel (Fig. 3.3F) to better match the helix angle of the auger (typically 24° – 32°) with the supplementary angle of the funnel which would facilitate powder delivery to the auger without over-filling and clogging the auger; (2) the sharp angles in the interior of the funnel were replaced with fillets (top-down

view of the two funnels in Figs. 3.3G and 3.3H), which reduce the boundaries and points of friction that the powder experiences while traveling to the auger, and; (3) the two shelf cutouts (S1, S2) of RichRap’s design (Fig. 3.3E, 3.3G) were removed and replaced with a filleted, steep wall to reduce a non-productive build-up of powder build material within the funnel (Fig. 3.3F, 3.3 H). These three key modifications allowed powder build material to be efficiently directed into contact with the auger, allowing improved powder feed into the hot end.

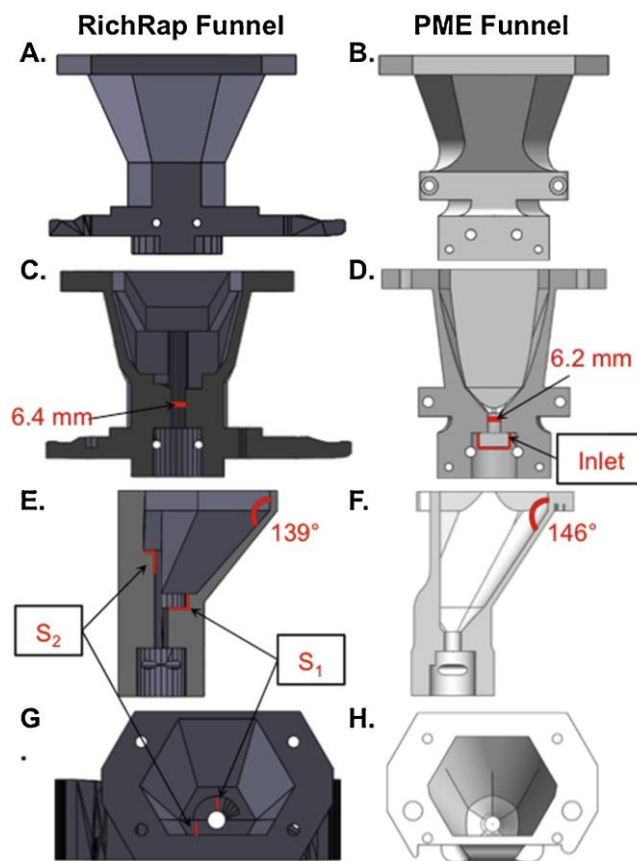


Fig. 3.3. The funnel design computer models of RichRap (A.) and PME (B.) with cross-sectional views from the front face (RichRap, C. and PME, D.) as well as the side profile cross-sectional views (RichRap, E. and PME, F.). The top-down view of the RichRap (G.) and PME (H.) funnels is shown.

Motor and Gearing System Modifications for PME

Although the redesigned funnel delivered powder build material into the hot end, the extrusion was limited to a globule of material around the nozzle. To overcome this deficiency, the torque on the auger was increased. The NEMA 17 motor was replaced with a larger stepper motor capable of producing 0.88 N-m of torque and the gearing ratio was adjusted to generate a 4X torque ratio instead of the original 2X torque ratio (see the Gearing Ratio Calculations section in the Experimental Methods for additional details). Combined with an increase in torque, increasing the diameter of the hot end nozzle to 0.8 mm from 0.4 mm allowed for consistent extrusion.

Addition and Modification of an Inlet

Despite constant extrusion, a buildup of powder material between the funnel and hot end was observed. This buildup of powder material exerted sufficient pressure to the top of the RPWHE and screws holding the hot end in place to split the funnel along the 3D printed layers adjacent to the screws. Although a funnel machined out of aluminum would help avoid this problem, the associated costs of machining this complex funnel part would create a large barrier to widespread adoption of powder melt extrusion. Therefore, to keep powder melt extrusion inexpensive and obtainable, the connection between the funnel and hot end was modified to consist of a short (5 mm) inlet from the funnel into the hot end (Fig. 3.3D) in order to reduce the observed pressure buildup.

The addition of the inlet extended successful extrusion to minutes from seconds, although the uniformity of the extruded material volume remained inconsistent. Therefore, it was hypothesized that the lack of consistency of the material feed into the hot end resulted in inconsistent extrusion. To facilitate a more consistent build material feed, the dimensions of the designed parts for the printer head and how they translated to the printed dimensions of the

printer head parts were examined. This comparison was done to determine how the exact dimensions of the printer head affected the feed of the powder into the hot end. The dimensions of the printed parts were found to be 0.2–1.0 % different than the design due to the extrudate contractions after printing [37]. Initially, it was assumed that these material contractions would not significantly affect the printer performance, especially as they would affect the funnel dimensions rather than the hot end. However, the contractions of the material comprising the funnel inlet that allowed the auger to transport material into the hot end were especially damaging to the extrusion performance by reducing the space between the auger and the sidewalls increasing the potential for the auger to rub against the sidewalls, as well as, reducing the amount of powder build material able to reach the hot end at one time. By accounting for the material contractions, the auger hole diameter was printed to the appropriate size that promotes minimal contact between the auger and the sidewalls and allows for a more consistent build material feed into the hot end, which leads to improved extrusion uniformity.

With a redesigned funnel, greater torque limit, and more accurate design tolerances, the fabricated printer head obtained constant powder melt extrusion (Fig. 3.4); however, during extrusion, a build material obstruction in the hot end formed approximately a few millimeters below the funnel inlet. This build material obstruction was a product of heat creep. Heat creep is the process of heat diffusion from the nozzle past the heat fins in the hot end, and as a result of the heat diffusion, the powder build material softens prematurely, and the increased viscosity of the coalescing powder granules clogs the hot end prohibiting any further extrusion or completion of 3D prints. Therefore, the most influential modification to the design of the printer head to enable PME printing was the design of the hot end to manage heat diffusion and minimize build material obstructions (Fig. 3.5).

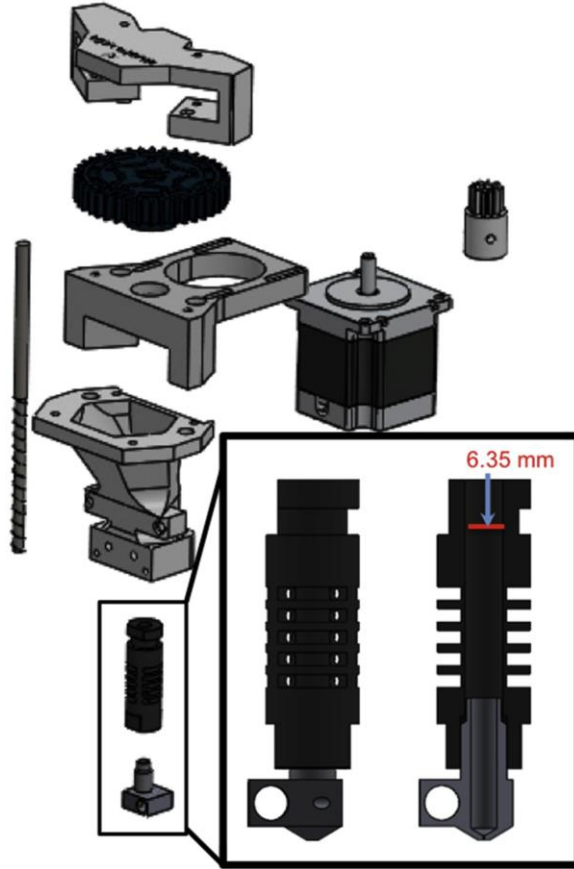


Fig. 3.4. A diagram of the exploded assembly computer model of the PME printer head with the RPWHE (inset shows a closer look at the RPWHE with a cross-sectional view).

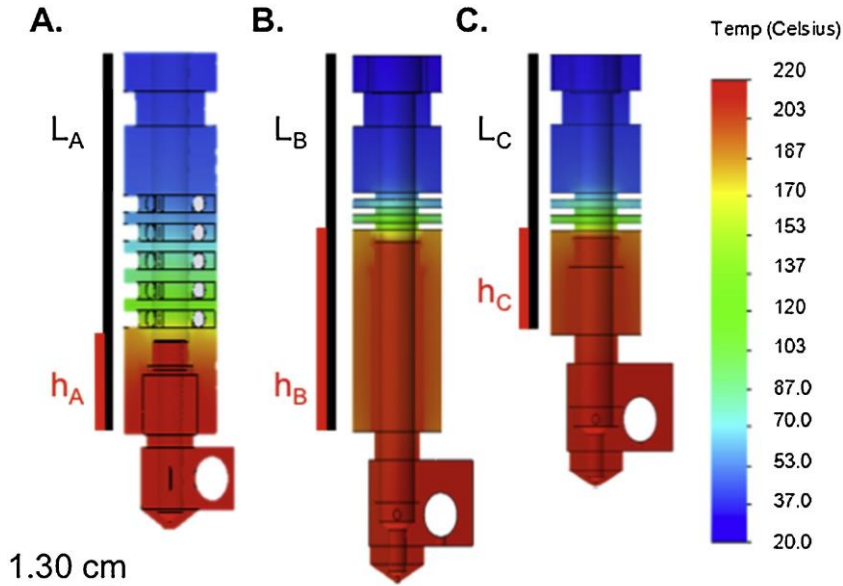


Fig. 3.5. Heat map portrayals of thermal simulations for the different hot ends surveyed for the PME printer. RPWHE length (L_A) = 5.08 cm, RPWHE metal insert length (h_A) = 1.30 cm, LTHE length (L_B) = 5.08 cm, LTHE metal insert length (h_B) = 2.56 cm, STHE length (L_C) = 3.69 cm, STHE metal insert length (h_C) = 1.30 cm.

Hot End Investigation and Optimization

To investigate the heat transfer within the hot end of the original RPWHE design, Solidworks Thermal Analysis software was used to simulate the thermal heat flow (Fig. 3.5A, heater cartridge reference temperature = 220 °C). This simulation revealed a large intermediate heat region (53°C–170°C) attributed to heat creep through the hot end. To limit the intermediate heat region within the hot end, two more hot ends were designed (Figs. 3.5B and 3.5C). The first design, a long travel hot end (LTHE), was the same length as the RPWHE (Fig. 3.5, $L_A = L_B$) but contained two annular heat fins to better confine heat flow and a longer metal insert into the hot end to bring higher temperatures farther into the hot end (Fig. 3.5, $h_A < h_B$). The LTHE design reduced the temperature of the medium heat region (50 °C – 170 °C) in comparison to the RPWHE. However, due to an increased amount of softened build material around the auger, using the LTHE resulted in increased lateral motion of the hot end during the print, reducing the

straightness of the printed lines and the overall print quality. To overcome this challenge of a long moment arm, a short travel hot end (STHE) (Fig. 3.5C) was designed (see Figure 3.16 and the Moment Arm Calculations section in the Experimental Methods). The STHE contains the same heat fin design as the LTHE, creating a sharp transition between cold powder and melted plastic; however, the STHE is shorter than both the RPWHE and the LTHE (Fig. 3.5) to minimize lateral motion of the hot end during the print as a result of a smaller moment arm. The reduction of the distance between the nozzle and the funnel in the STHE likely reduced the lateral movement experienced during printing leading to increased print quality as evidenced by more uniform print lines with minimal side to side travel observed qualitatively from a printed line (Figure 3.17). Overall, minimizing heat creep allowed for improved extrusion while the STHE increased the uniformity of the printed layers resulting in the best overall performance.

With an improved funnel and the STHE incorporated into the printer, the material capabilities of the PME printer head were evaluated (Fig. 3.6). The print temperature of PLA powder, high impact polystyrene (HIPS) powder, and acrylonitrile butadiene styrene (ABS) powder build material was optimized by systematically tuning the temperature of the hot end and observing extrusion consistency as well as the connectivity of printed lines at defined 5 °C temperature intervals starting at 100 °C + glass transition temperature or the melting point (see Table 3.4 for additional details). Operating at the optimized printing temperatures for each powder build material, the final version of the PME printer head was able to successfully complete 3D prints.

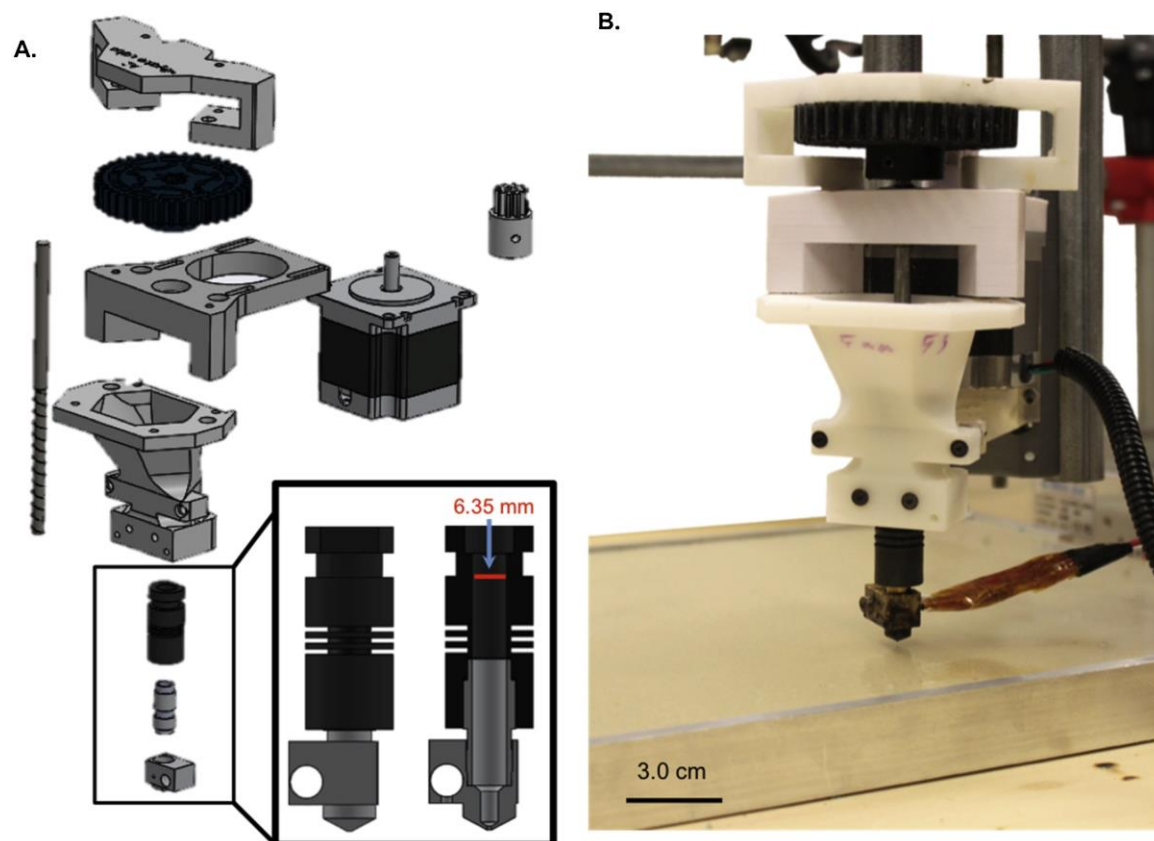


Fig. 3.6. A diagram of the exploded assembly computer model with an inset including a cross-sectional view of the STHE (A.) and a photograph of the assembled final version of the PME printer head (B).

Print Results and Discussion

The print performance of the final PME design (Fig. 3.6) was first compared by qualitatively observing the differences in print quality to that of a commercially available bench-top FFF printer, the FlashForge Creator Pro. The comparison in print quality between the two methods of printing demonstrates the promise of the PME technique (Fig. 3.7 and 3.41). A small cube (1 cm^3) was printed using both the PME (Fig. 3.7A, 3.7C, 3.7E) and the FFF printers. In addition, a 2D ladder object was printed to isolate the consistency and quality of the print layers (Fig. 3.7B, 3.7D, 3.7F). Although both techniques produced 3D objects, the FFF cube and ladder prints had higher print quality than the PME prints based on the layer uniformity with fewer print defects or lateral motion within layers (Fig. 3.7 and 3.41).

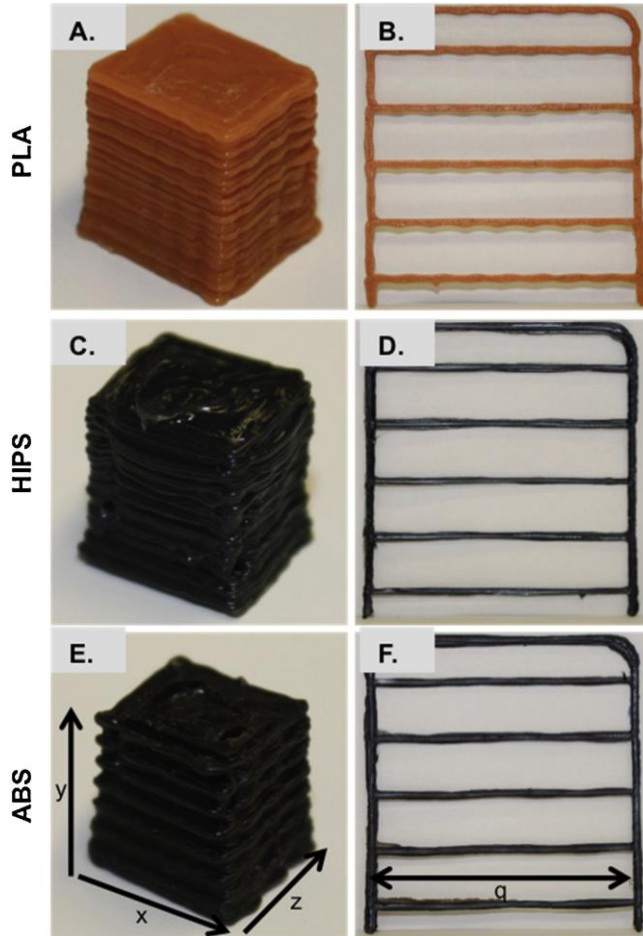


Fig. 3.7. Photographs of prints via Powder Melt Extrusion (PME) of all 3 materials (PLA cube (A.), PLA rail (B.), HIPS cube (C.), HIPS rail (D.), ABS cube (E.), ABS rail (F.)). X, Y, Z =1.0 cm: q =6.0 cm.

The lower print quality demonstrated here by the PME technique is due to inconsistent extrusion and lower print resolution. For PME, the extrusion method requires an auger to continually supply a steady stream of melted plastic to the nozzle to be extruded. However, due to a regular, drop-like appearance in the ladder prints (Fig. 3.7), it can be inferred that this characteristic is due to a less uniform feed of the build material to the nozzle compared to that of FFF printers. The print resolution of the PME technique is significantly lower than the print resolution of the FFF printer due to the differences in overall printer design and in nozzle diameter. In particular, the FlashForge Creator Pro has better X–Y resolution (0.4 mm) and Z-

layer height (0.18 mm) [38] than the PME (X–Y resolution =0.8mm, Z-layer height =0.1mm), leading to higher quality prints by the FlashForge Creator Pro.

Print dimensions

Table 3.1 provides quantitative measurements of the dimensions of each of the cubes printed in Fig. 3.7 and Figure 3.41. It is apparent that the dimensions of the PME printed cubes are consistently shorter than the target dimension of 1 cm. In the case of the PME printed ABS cube, the cube length falls short of 1 cm by 1.5 mm. The dimensions of the FFF printed cubes are also shorter than 1 cm, but not by more than 0.5 mm. These quantitative measurements further validate the qualitatively observed differences between the print qualities of the cubes discussed above.

Table 3.1. Measured dimensions and calculated densities for each one of the cubes printed by FFF and PME with percent error from the theoretical values included.

Build Material	Print Technique	Cube Length (cm) [% error]	Cube Width (cm) [% error]	Cube Height (cm) [% error]	Cube Volume (cm ³) [% error]	Cube Mass (g) [% error]	Density of Printed Cube (g/cm ³) [% error]	Density of Non-Printed Filament (g/cm ³)
PLA	FFF	0.969 [3.10]	0.960 [4.00]	1.03 [3.00]	0.962 [3.80]	0.683 [44.5]	0.710 [42.3]	1.23
	PME	0.939 [6.10]	1.02 [2.00]	0.939 [6.10]	0.900 [10.0]	0.971 [21.1]	1.08 [12.2]	
HIPS	FFF	0.986 [1.40]	0.976 [2.40]	1.01 [1.00]	0.967 [3.30]	0.529 [48.6]	0.547 [46.9]	1.03
	PME	0.885 [11.5]	1.00 [0.00]	0.882 [11.8]	0.782 [21.8]	0.647 [37.2]	0.827 [19.7]	
ABS	FFF	0.978 [2.20]	0.976 [2.40]	0.995 [0.50]	0.949 [5.10]	0.511 [54.8]	0.538 [52.4]	1.13
	PME	0.846 [15.4]	0.993 [0.70]	0.960 [4.00]	0.806 [19.4]	0.652 [42.3]	0.809 [28.4]	

Although the dimensions of the PME cubes are consistently shorter than those of the FFF cubes, the densities of the PME cubes are more similar to that of the density of a 100% infilled cube of the respective material than those of the FFF cubes. The density of a 100% infilled cube was estimated by calculating the density of the parent filament [39]. The FFF cubes are consistently close to half of the desired density, which demonstrates that although the print pattern follows the 100% infill pattern, there are separations between the layers and not much

layer overlap. In stark contrast, the PME cubes are closer to the desired 100% density, which demonstrates that the PME layers overlap more than that of the FFF layers to reduce the overall amount of void space within the print. The overlap of the PME layers compared to that of the FFF layers is another result of the inconsistent build material feed of the PME printing process.

Print surface roughness

To help quantify the print quality and the inconsistent layers produced with PME versus those produced with FFF beyond the dimensional analysis, surface roughness measurements (S_a) were taken using a profilometer. The three dimensional surface maps of one side of each cube are shown in Fig. 3.8. The PME cube surfaces are more heterogeneous compared to those of the FFF cube surfaces. Therefore, this surface variability is reflected in the S_a -values for each cube, which are 0.032 mm for the FFF printed PLA cube (Figure 3.8A), 0.057 mm for the PME printed PLA cube (Figure 3.8D), 0.016 mm for the FFF printed HIPS cube (Figure 3.8B), 0.062 mm for the PME printed HIPS cube (Figure 3.8E), 0.013 mm for the FFF printed ABS cube (Fig. 3.8C), and 0.058 mm for the PME printed ABS cube (Fig. 3.8F).

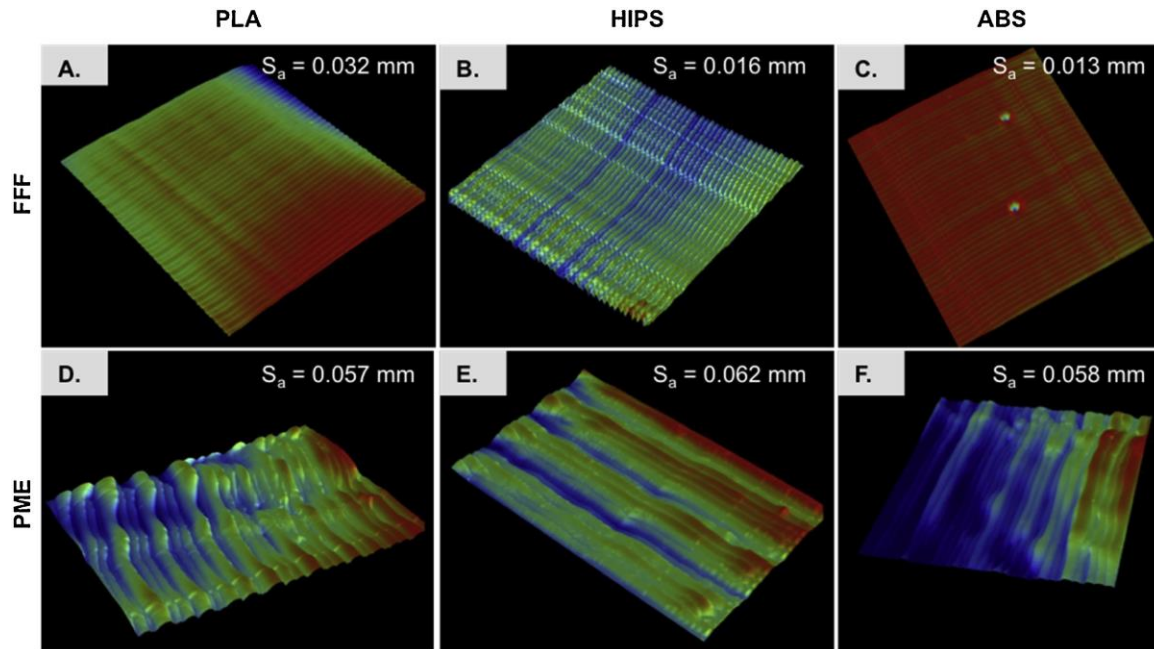


Fig. 3.8. Three-Dimensional renderings of profilometer generated surface maps for FFF printed parts out of PLA (A.), HIPS (B.), and ABS (C.), as well as, for PME printed parts out of PLA (D.), HIPS (E.), and ABS (F.) Red is indicative of a peak (+) above the designated 0 point (green) while blue is indicative of a valley (-) below the designated 0 point. The range of the measurement is ± 500 microns around the 0 point (For interpretation of the references to colour in this figure legend, the reader is referred to the web version of this article).

In every material printed, the surface roughness values of the PME printed cubes are more than those of the FFF printed cubes. This further verifies that the print quality of the PME printed parts is not as precise as the FFF printed parts due to printed layer inconsistencies produced by inconsistent build material extrusion in PME.

Print microstructures

To look closer at the difference in the layer consistency between the PME and FFF print methods, scanning electron microscopy (SEM) micrographs were taken of freeze-fractured tabs produced by each print method (Fig. 3.9). The PME printed layers were observed to either blend together or have gaps between adjacent layers due to uneven extrusion, whereas, the FFF printed layers are distinguishable from each other and contain minimal amounts of irregular gaps between adjacent layers. These visualized defects of the PME printed tabs provide insight into

the internal structures of the 3D printed objects and suggest that microscopic defects due to less uniform extrusion give rise to poorer macroscopic print resolution compared with the FFF prints.

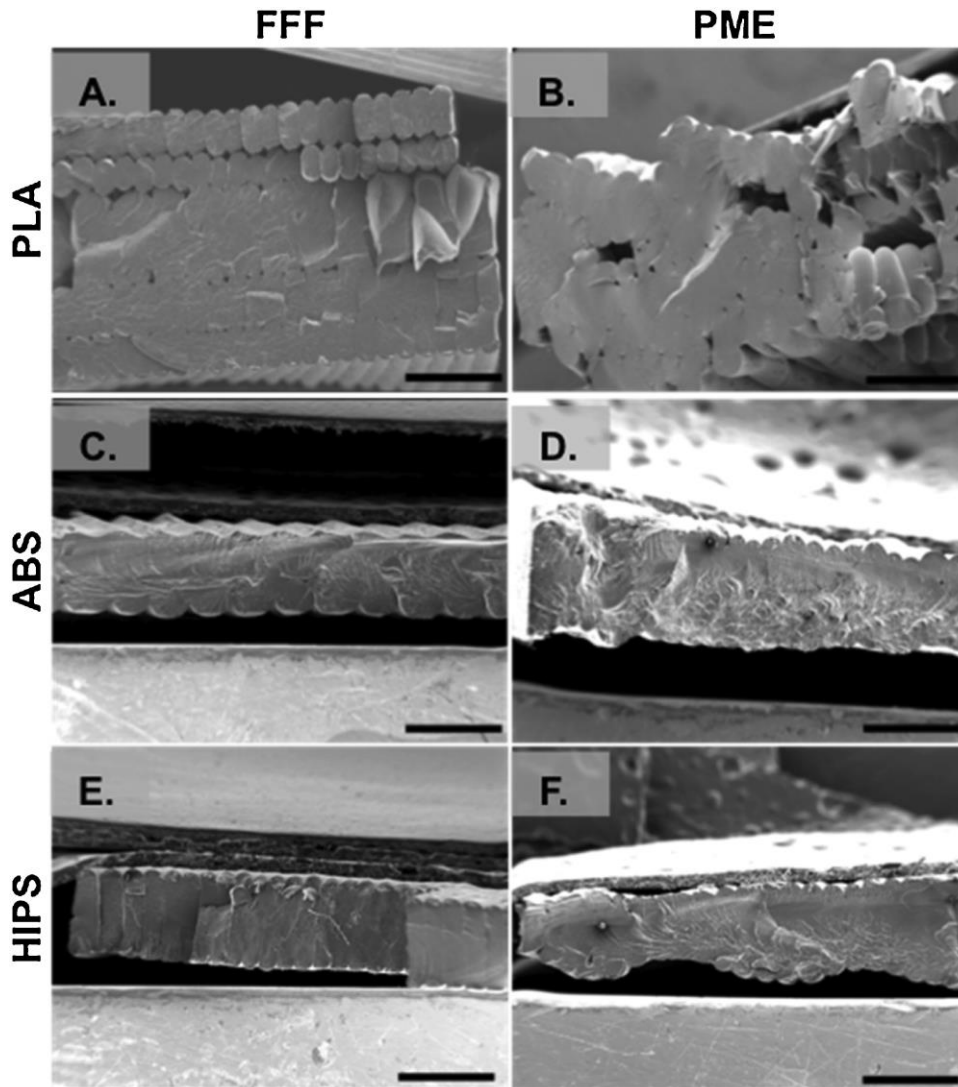


Fig. 3.9. SEM images of cross-sections of freeze-fractured 3D printed tabs from of PLA via the FFF printer (A.) and the PME printer (B.), of HIPS via the FFF printer (C.) and the PME printer (D.), of ABS via the FFF printer (E.) and the PME printer (F.). Scale bar =1.0 mm.

Bulk tensile properties of 3D printed objects

Before bulk tensile properties were analyzed, the integrity of the PME extrudate was verified to explore if degradation of the build material occurred during the powder preparation process. The powder preparation process involved taking FFF prints and mechanically grinding

them into a powder form (see Experimental Methods for additional details). Comparison of the viscoelastic properties of the rectangular tabs printed by PME (average width = 10.9 mm, average thickness = 1.66 mm) and FFF (average width = 12.9 mm, average thickness = 1.00 mm) in each material (PLA, HIPS, and ABS) on a dynamic mechanical analyzer (DMA) revealed that printing using the PME process did not affect the material performance of parts relative to those printed by FFF (Figure 3.36). Specifically, the average storage moduli (E') of tabs from each method directly are nearly identical under tension for each material. Further, as expected, the glass transition temperature marked by the alpha transition of the storage modulus trace is systematically greater than the temperature determined by DSC in every case (Figure 3.36 and Table 3.4).

To compare the mechanical properties of parts printed by the different methods, the bulk tensile properties of ASTM standard type 5 dog bones printed in PLA by both PME and FFF print methods were tested with the print layers oriented parallel to the direction of the tensile force (Fig. 3.10). The print temperatures of the ABS and HIPS materials were too high to complete full dog bone prints without destroying the inside of the PEEK tube of the STHE, and therefore, these objects could not be printed with the current set up. Testing the dog bones with the print layers oriented parallel to the direction of the tensile force reduced the amount of extraneous variables such as layer adhesion or number of layers present [39–41]. Although data beyond the initial failure is insignificant for the purpose of this study, the triangular shapes of the stress-strain traces can be explained by considering the print orientation of the dog bones. As tension is applied parallel to each printed strand, each strand breaks individually. Thus, when one strand in the print breaks, the bulk stress measured lessens, but the strain continues until every strand is broken.

Analysis of the stress-strain curves for dog bones prepared using each printing method revealed that the tensile properties of the tabs were affected depending on the print technique (Fig. 10). Less variation of the average tensile strength values between samples of the FFF printed tabs (57.7 ± 2.31 MPa) (Fig. 3.10A) than that of the PME printed tabs (49.2 ± 10.7 MPa) was observed (Fig. 10B). Furthermore, the average Young's Modulus values exhibited by the FFF printed tabs (2160 ± 179 MPa) were more consistent (Fig. 3.10A) than those exhibited by the PME printed tabs (1620 ± 375 MPa) (Fig. 3.10B). The minimal variation of the FFF prints' tensile properties is not surprising after observing the layer uniformity within the SEM micrographs (Fig. 3.9). Additionally, the inconsistency of the PME prints' tensile properties is not surprising considering the lack of uniformity between layers within the PME prints as observed in the SEM micrographs (Fig. 3.9). Therefore, PME shows promise to be used as a viable 3Dprinting technique, however, to realize PME as an industrially viable printing option comparable to the FFF technique, further optimization and analysis of the PME print parameters and design will be needed.

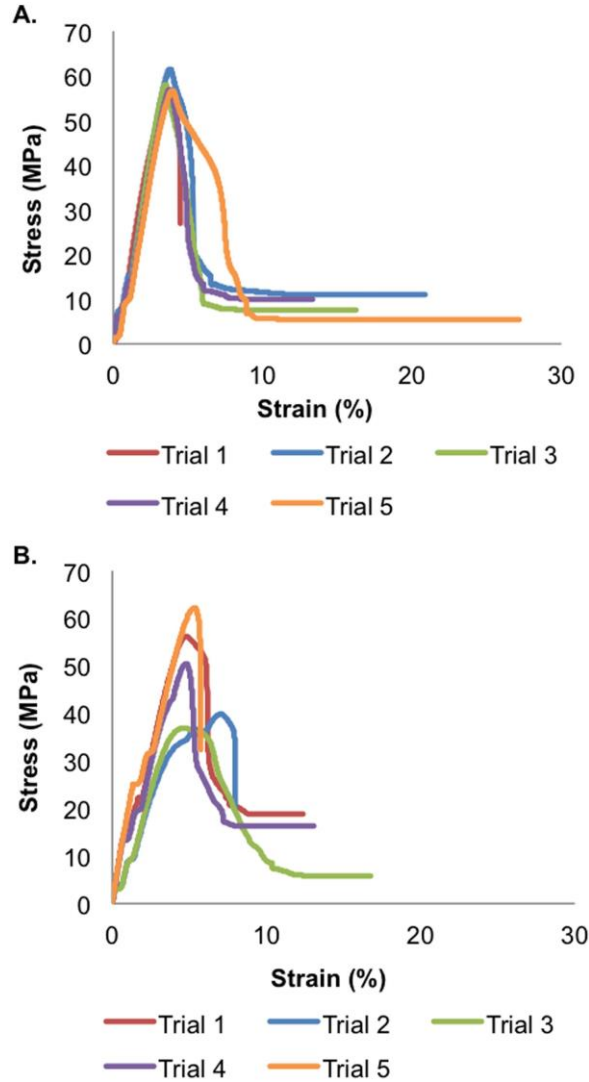


Fig. 3.10. Plots of the stress-strain relationship for the printed PLA dog-bones by FFF (A.) and PME (B.) under tension.

Conclusions

A bench-top PME printer head was developed and tested. Each part of the RRUPE printer head was systematically investigated and modified to gain a fundamental understanding of the principles needed to fabricate a PME printer head. The final version of the PME printer head is able to successfully 3D print from a variety of thermoplastic powder build materials (PLA, HIPS, ABS). Printing by PME was also shown to minimally affect the viscoelastic

properties of the material when compared to those of the FFF printed parts. However, the inconsistencies of the PME printed layers shown by dimensional analysis, surface roughness measurements, and SEM micrographs did present variable tensile properties in the printed parts when compared to the more consistent layers produced from the FFF print method. The layer inconsistencies of PME printed parts are likely a result of uneven powder melt extrusion which presents further challenges in achieving consistent material flow during extrusion, as well as being able to enhance PME print resolution. PME print methods have the potential to reduce the time needed for the processing of 3D printing build materials, presenting the opportunity to provide a platform on which it is possible to rapidly prototype a myriad of thermoplastic materials for 3D printing.

Experimental Method

All filaments were purchased from Gizmo Dorks and Hatchbox. PLA pellets were purchased from Filabot. The powder used was made by taking printed filament objects and grinding them up in a kitchen coffee bean grinder with dry ice to a size smaller than 1 mm determined by a kitchen sifter. NEMA 23 motor was purchased from StepperOnline on Amazon. The hot-ends were machined by and purchased from Reifsnyder Precision Works. The MPCNC 3D printer used was assembled as shown on <https://www.v1engineering.com/assembly/>. All other parts were purchased from local hardware stores. Colorado State University's Central Instrument Facility provided the Scanning Electron Microscopy images. All of the printed parts on the printer head were completed on a Flashforge Creator Pro 3D Printer using standard print parameters for the material that was to be printed. The 3D models were sliced by the software, Flashprint by Flashforge, in order for the Flashforge printer to produce a print. All of the PME prints were designed using Solidworks before being input into a slicer software program and then

Pronterface. The slic3r software was used to slice the models into G-code that would then be used by the software, PronterFace, to control the printing for the powder melt extrusion on the MPCNC. All prints analyzed in this study were printed at a targeted 100 % infill parameter. Profilometry was conducted at Colorado State University's Central Instrument Facility using a Bruker Dektak XT Stylus profilometer. Each map scan was completed with a 1 mm range with a stylus of radius 12.5 micrometers and force of 10 mg. The duration of each trace was 25 sec with a map resolution of 50 micrometers/trace. Differential Scanning Calorimetry (DSC) was conducted using a TA Instruments DSC Q20. To reset thermal history, an initial sweep ramped from 25 °C to 150 °C at a ramp rate of 10 °C/min. The temperature was held constant at 150 °C for 1 minute before it was cooled to 25 °C at a ramp rate of -10 °C/min where the temperature was held constant at 25°C for 1 minute. Thermal data was collected from the second sweep which consists of ramping the temperature from 25 °C up to 150 °C at a rate of 5 °C/min., isotherming at 150 °C again for 1 minutes before ramping back to 25 °C at a rate of -5 °C/minute. Thermal Gravimetric Analysis (TGA) was conducted using a TA Instruments TGA Q50. The thermal decomposition data was obtained under a nitrogen gas flow of 40 mL/min by ramping the temperature from 25 °C up to 700 °C at a ramp rate of about 10 °C/minute. The mechanical response of the polymers was characterized using a TA Instruments DMA Q800 V20.26 Build 45. The polymer sample's mechanical properties were evaluated in the DMA was under a constant nitrogen flow and a constant strain of 0.3% as the DMA ramped the temperature at 5 °C/min from -60 °C to 300 °C. An Instron 5966 with a 10 kN load cell was used to follow the ASTM D638-14 procedure pulling at a rate of 5 mm/min.

Design and Development of Printer Head

Electronic Component Assembly

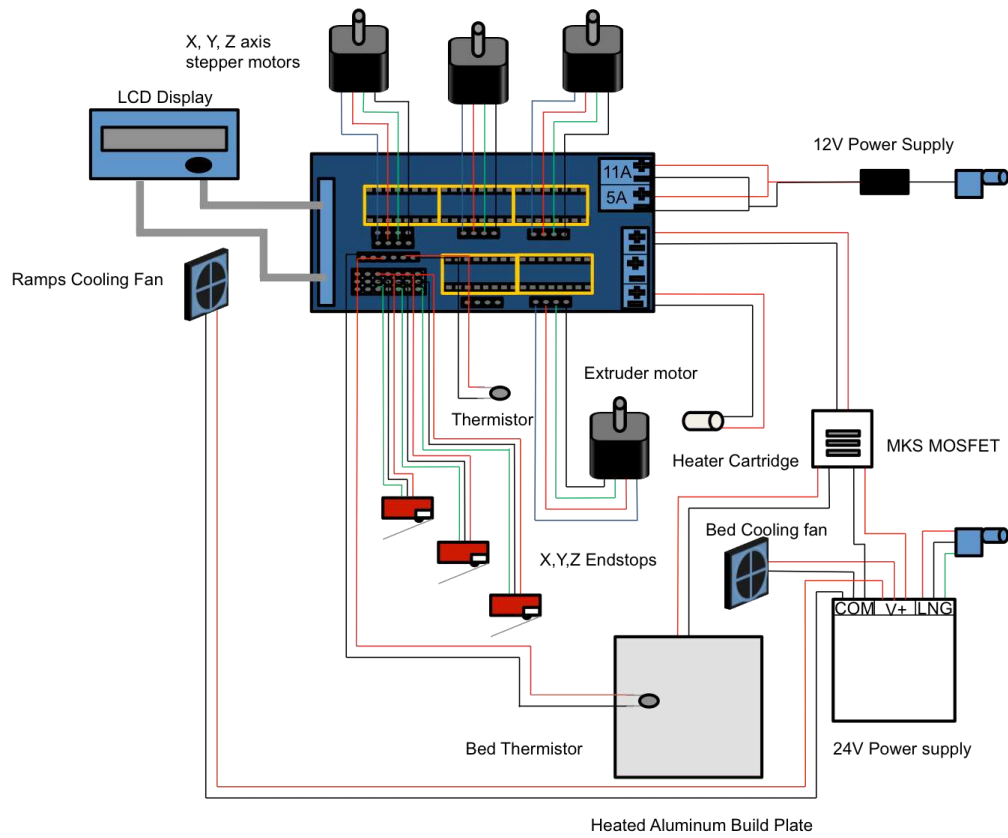


Figure 3.11. A schematic of the electronic set-up and design needed to run the PME MPCNC printer.

Control System Process

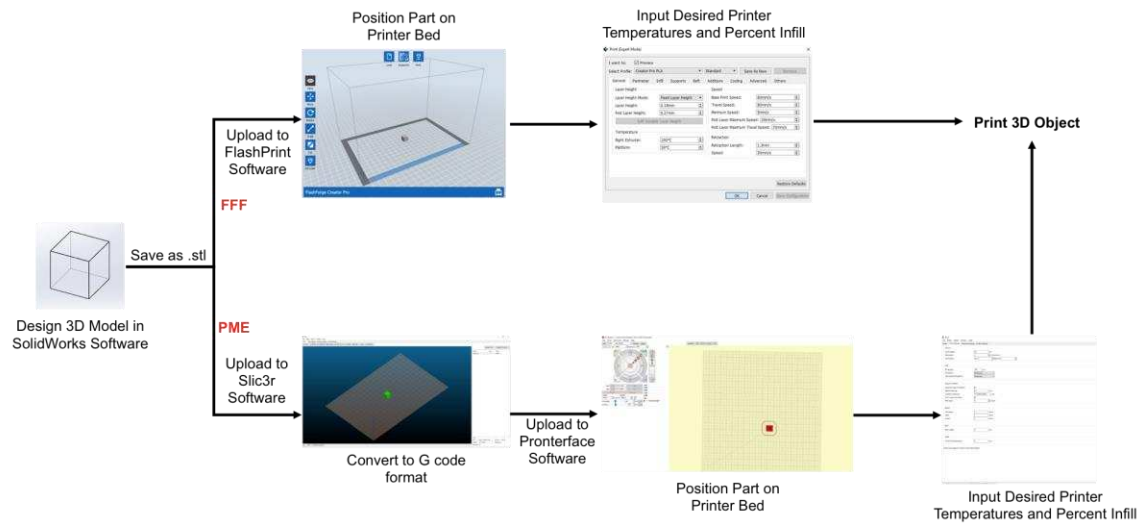


Figure 3.12. Flowchart depicting the design and control pathways for the FFF and the PME printing techniques.

Gearing Ratio Calculations

Legend:

D1: Small Gear Diameter

D2: Large Gear Diameter

ALW: Allowable Width

DP1: Large Gear Dedendum Circle

DP2: Small Gear Dedendum Circle

DW: Dedendum Width

ID: Inner Diameter

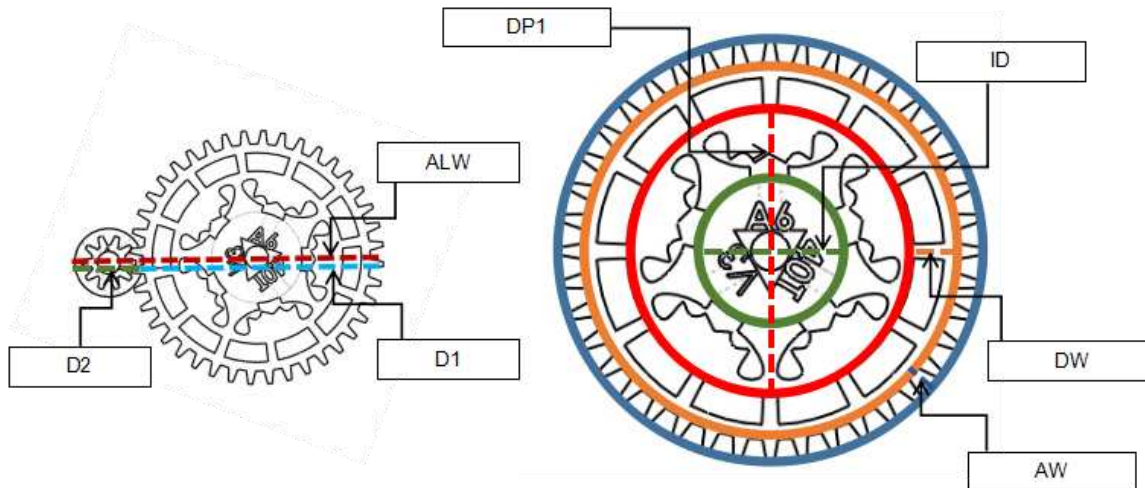
AW: Addendum Width

TM: Torque Multiplier

T1: Large Gear Number of Gear Teeth

T2: Small Gear Number of Gear Teeth

PD: Pitch Diameter



Choose torque multiplier value

$$\frac{D1}{D2} = \frac{DP1}{DP2} = \frac{Rpm2}{Rpm1} = \frac{1}{TM}$$

Choose allowable width (inches)

$$D1 + D2 = ALW$$

$$DP1 = ALW - DP2$$

$$\frac{DP1}{DP2} = \frac{1}{TM}$$

$$DP1 = \frac{DP2}{TM}$$

$$\therefore \frac{DP2}{TM} = ALW - DP2$$

$$DP2 = TM * ALW - TM * DP2$$

$$ALW * TM = DP2 + TM * DP2$$

Determine large and small gear dedendum circle widths

$$\frac{ALW * TM}{1 + TM} = DP2$$

$$ALW - DP2 = DP1$$

Assume number of teeth = T1

$$\frac{T1}{DP1} = \frac{T2}{DP2} = PD$$

Determine dedendum width

$$\frac{T1 * DP2}{DP1} = T2$$

$$\frac{1}{PD} = AW$$

$$1.2 * AW = DW$$

Hot End Design

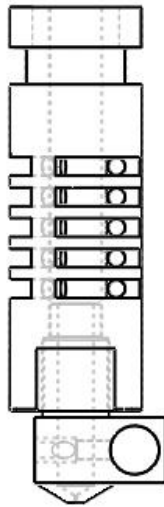


Figure 3.13: A drawing of the original Reifsnyder hot end design. [33]

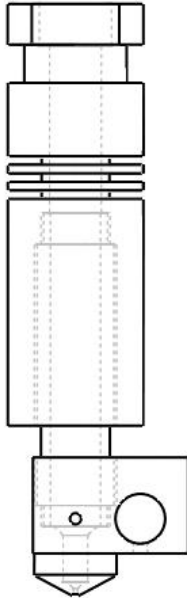


Figure 3.14: A drawing of the Long travel PEEK tube hot end design (LTHE).

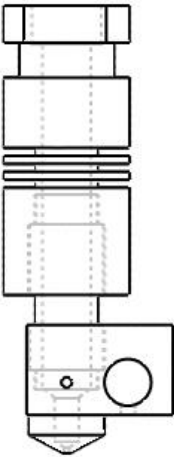


Figure 3.15: A drawing of the Short PEEK tube hot end design (STHE).

Moment Arm Calculations

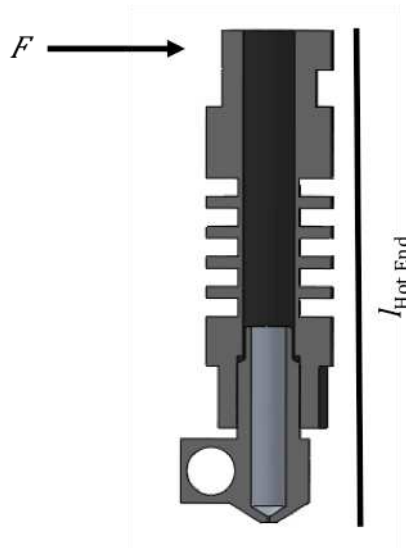


Figure 3.16. 3D model cross-section of a hot end.

First, to calculate the lateral force, we used the following equation:

$$Torque (\tau) = Force (F) \times radius (r)_{auger}$$

If the stepper motor delivers $\tau_{input} = 0.88 \text{ N}\cdot\text{m}$ to the gearing system, the τ_{output} can be calculated as such:

$$\frac{Diameter_{Gear\ 1}}{Diameter_{Gear\ 2}} = \frac{\tau_{output}}{\tau_{input}}$$

where $Diameter_{Gear\ 1} = 0.069 \text{ m}$ and $Diameter_{Gear\ 2} = 0.019 \text{ m}$. This results in a $\tau_{output} = 3.19 \text{ N}\cdot\text{m}$, and with the $r_{auger} = 0.003 \text{ m}$, then the resulting lateral force = 1063 N. Using this lateral force, it is possible to calculate the moment arm for each hot end as shown below:

$$Moment\ arm (M) = Length (l)_{Hot\ End} \times Force (F)$$

For the LTHE, the $l_{Hot\ End} = 0.0678 \text{ m}$, and when multiplied to the lateral force of 1063 N, the resulting $M = 72.1 \text{ N}\cdot\text{m}$.

For the STHE, the $l_{\text{Hot End}} = 0.0567$ m, and when multiplied to the lateral force of 1063 N, the resulting $M = 60.3$ N*m.

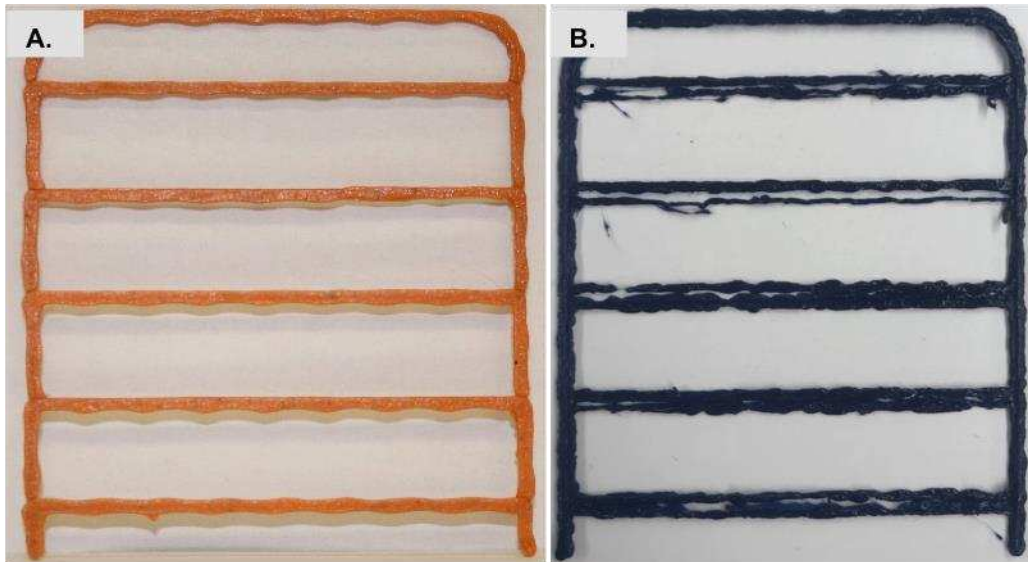


Figure 3.17. Photographs of the ladders printed using PLA with the STHE (A.) and the LTHE (B.).

Printing Parameters

Table 3.2. PME Print Parameters

Type of Print	Extruder Temperature (°C)	Hot Bed Temperature (°C)	Extrusion Multiplier	X,Y,Z Speed (mm/s)	Speed (1 st Layer) (mm/s)
ABS					
Cube	255	60	38	20,20,10	10
Rails	255	60	60	20,20,10	10
DMA Strips	250	60	60	20,20,10	10
HIPS					
Cube	245	60	38	20,20,10	10
Rails	240	60	38	20,20,10	10
DMA Strips	240	60	38	20,20,10	10
PLA					
Cube	225	60	250	20,20,10	10
Rails	225	60	250	20,20,10	10
DMA Strips	225	60	250	20,20,10	10

Table 3.3. FFF Print Parameters

Filament	Extruder Temperature (°C)	Hot Bed Temperature (°C)	Speed (mm/s)	Speed (1 st Layer) (mm/s)
ABS	220	105	60,80,20	20
HIPS	240	110	45,80,20	20
PLA	200	50	60,80,20	20

Material Properties

Build Material Particle Sizes

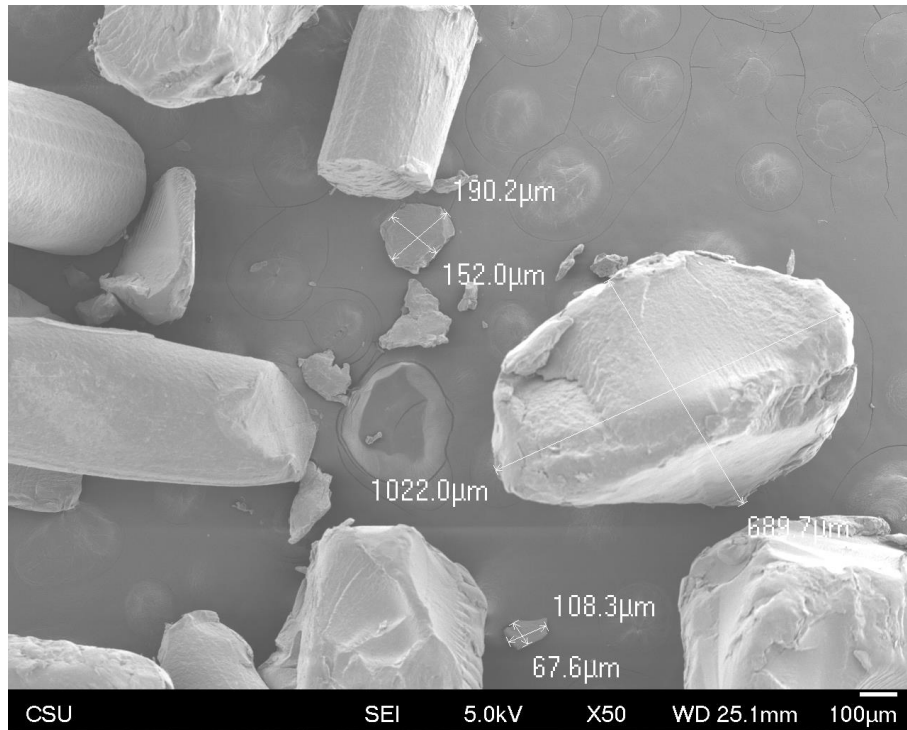


Figure 3.18. SEM micrograph at 50X magnification of PLA powder build material with particle size ranging from 67.6 micrometers to 1.02 mm

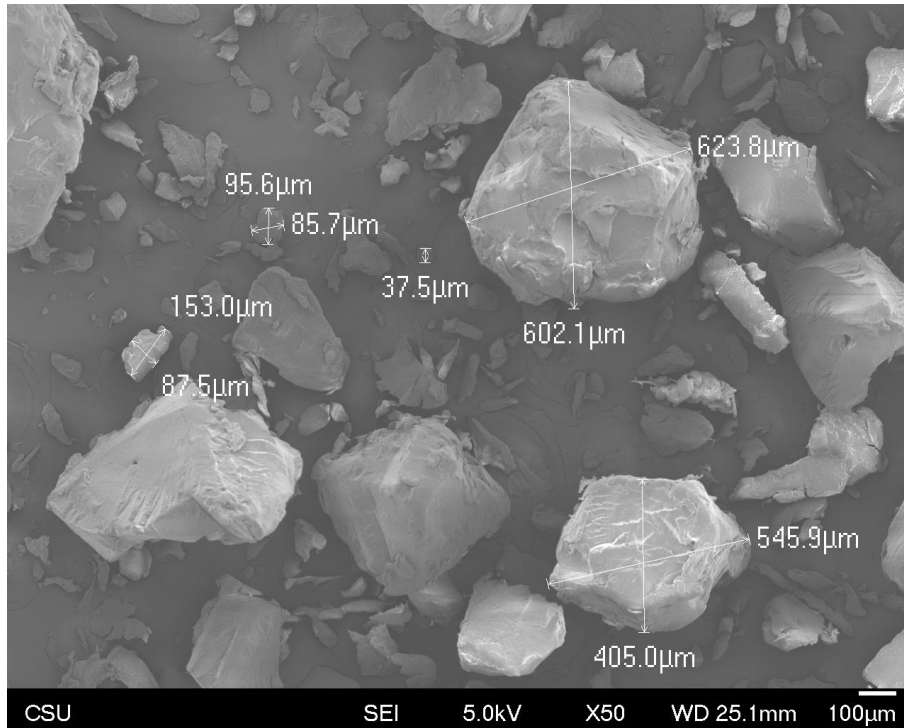


Figure 3.19. SEM micrograph at 50X magnification of ABS powder build material with particle size ranging from 37.5 micrometers to 623.8 micrometers.

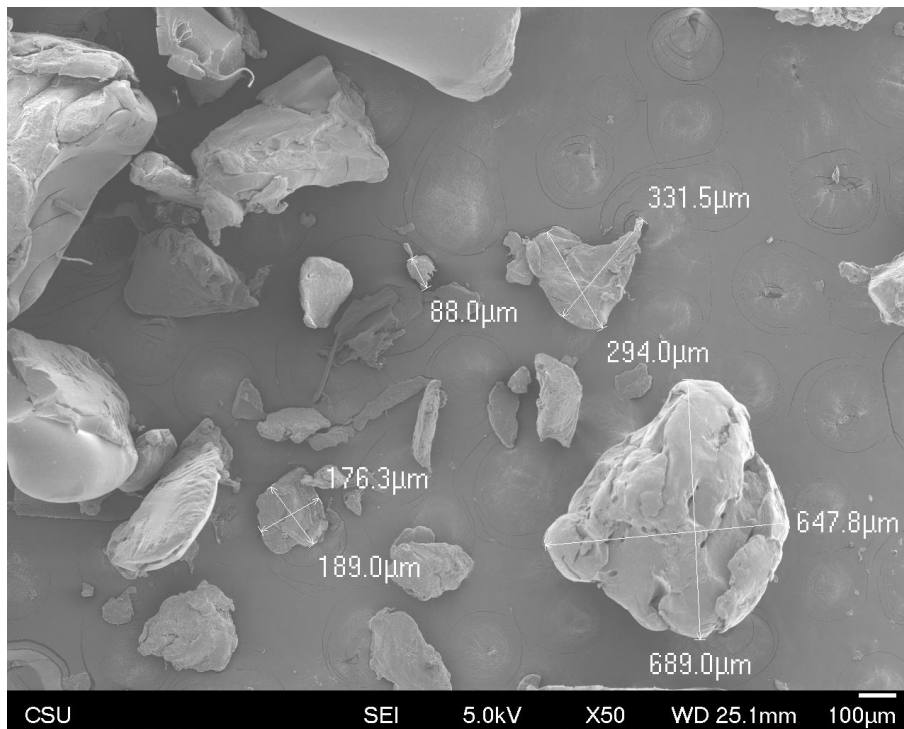


Figure 3.20. SEM micrograph at 50X magnification of HIPS powder build material with particle size ranging from 88 micrometers to 689 micrometers.

Print Temperature Optimization

Table 3.4. Thermal properties of commercial 3D printed filaments.

Powder Polymer Sample	T_g [°C]	T_c [°C]	T_m [°C]	T_d [°C]
PLA	62	97	169	326
ABS	103	-	-	366
HIPS	98	-	-	356

*Column titles are defined as such: Glass transition temperature (T_g), Crystallization temperature (T_c), Melt temperature (T_m), Decomposition temperature at 5% weight loss (T_d).

The best temperatures to print the materials via PME are as follows: PLA print temperature is 225 °C, HIPS print temperature is 240-245 °C, and ABS print temperature is 250 °C.

Thermal Gravimetric Analysis (TGA)

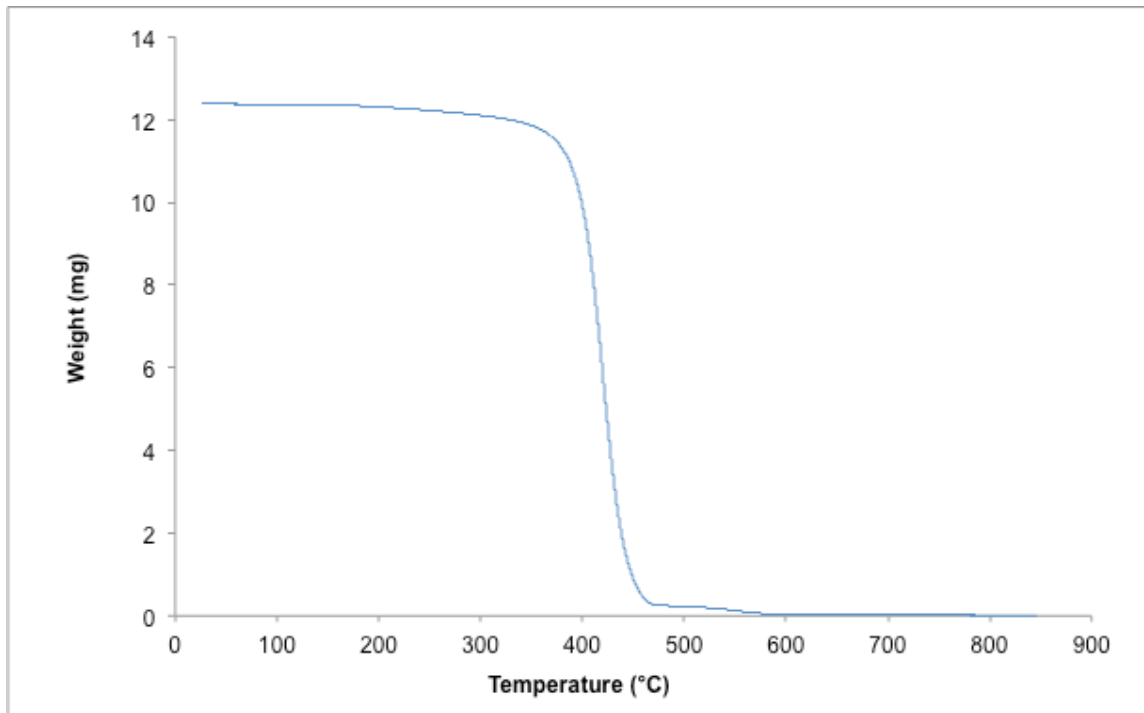


Figure 3.21. Plot of sample mass vs. temperature. TGA trace of ABS powder. Decomposition temperature at 5% weight loss is 359 °C.

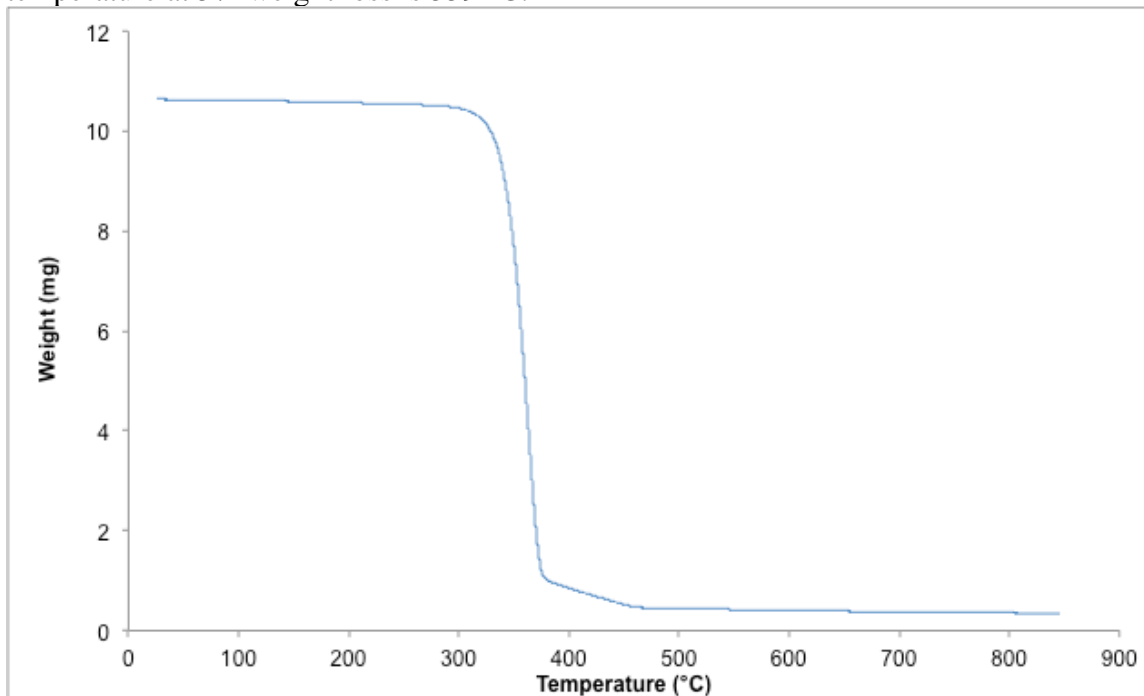


Figure 3.22. Plot of sample mass vs. temperature. TGA trace for PLA powder. Decomposition temperature at 5% wt. loss is 326 °C.

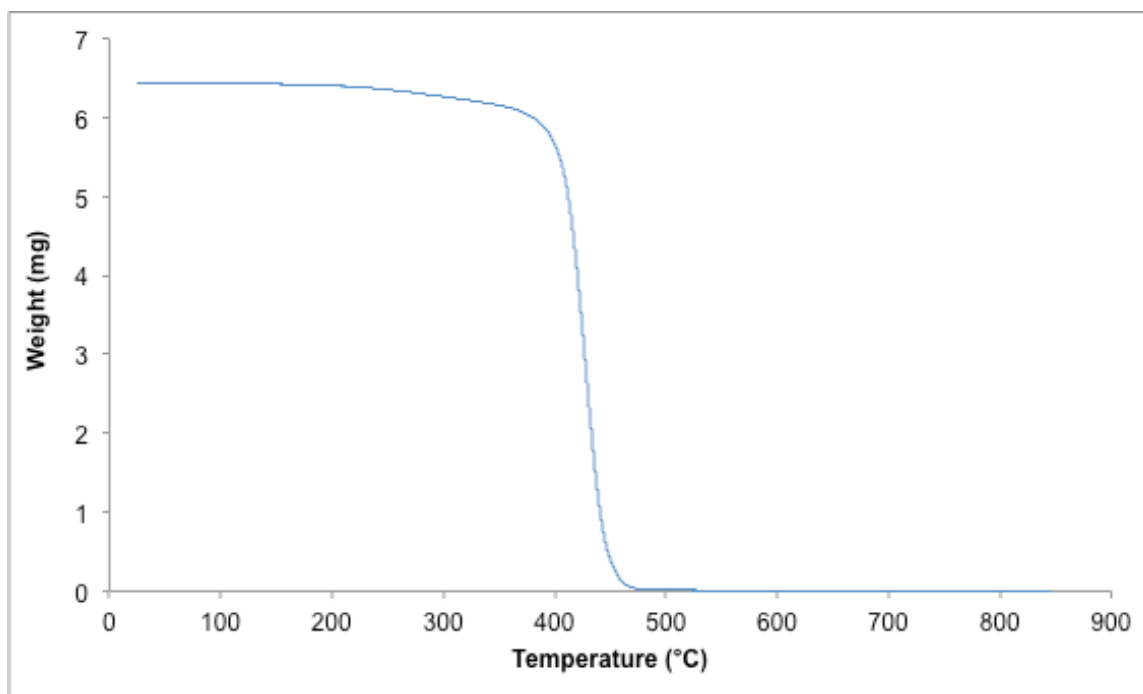


Figure 3.23. Plot of sample mass vs. temperature. TGA trace for HIPS powder. Decomposition temperature at 5% wt. loss is 363 °C.

Differential Scanning Calorimetry (DSC)

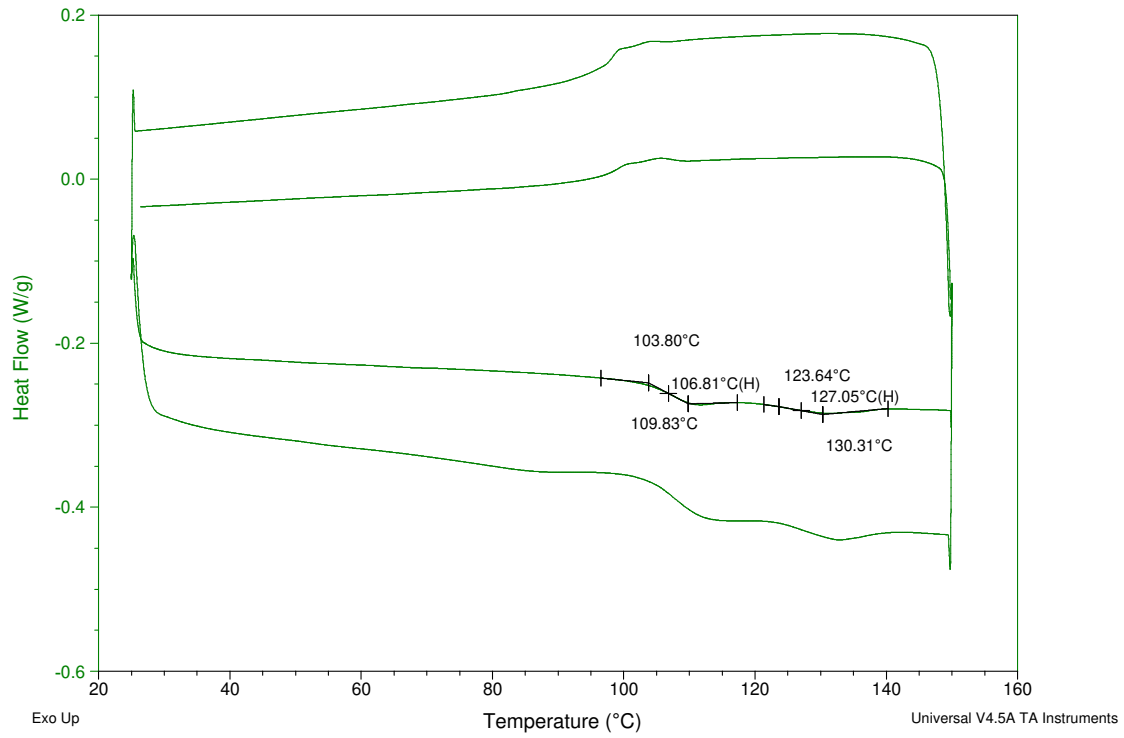


Figure 3.24. Full DSC trace for ABS filament after printer extrusion. Two T_g transitions are present at 107 °C and 127 °C.

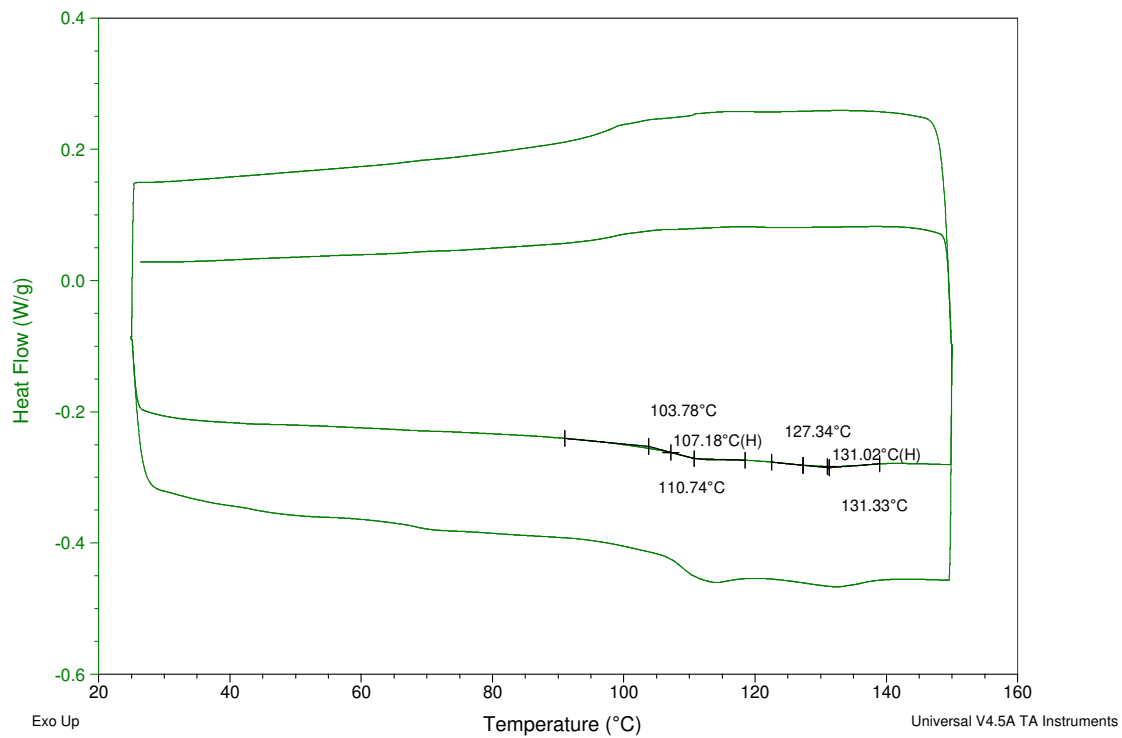


Figure 3.25. Full DSC trace for ABS powder. Two T_g transitions are present at 107 °C and 131 °C.

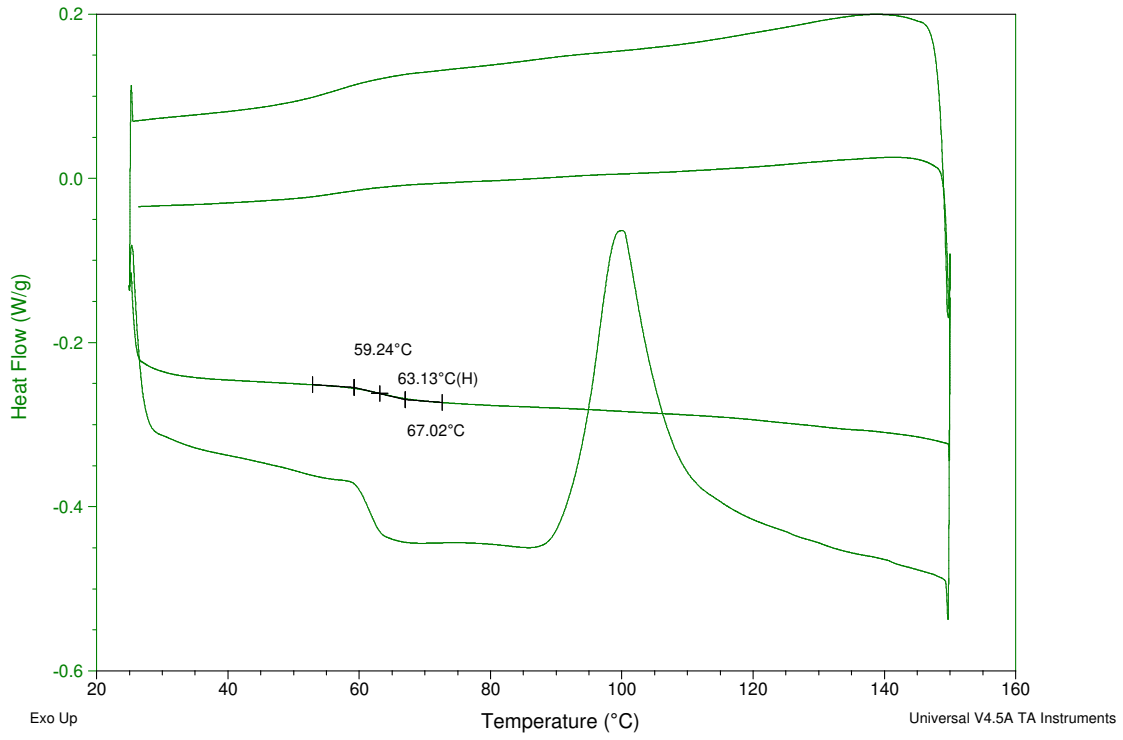


Figure 3.26. Full DSC trace for PLA filament after printer extrusion. One T_g is present at 63.1 °C.

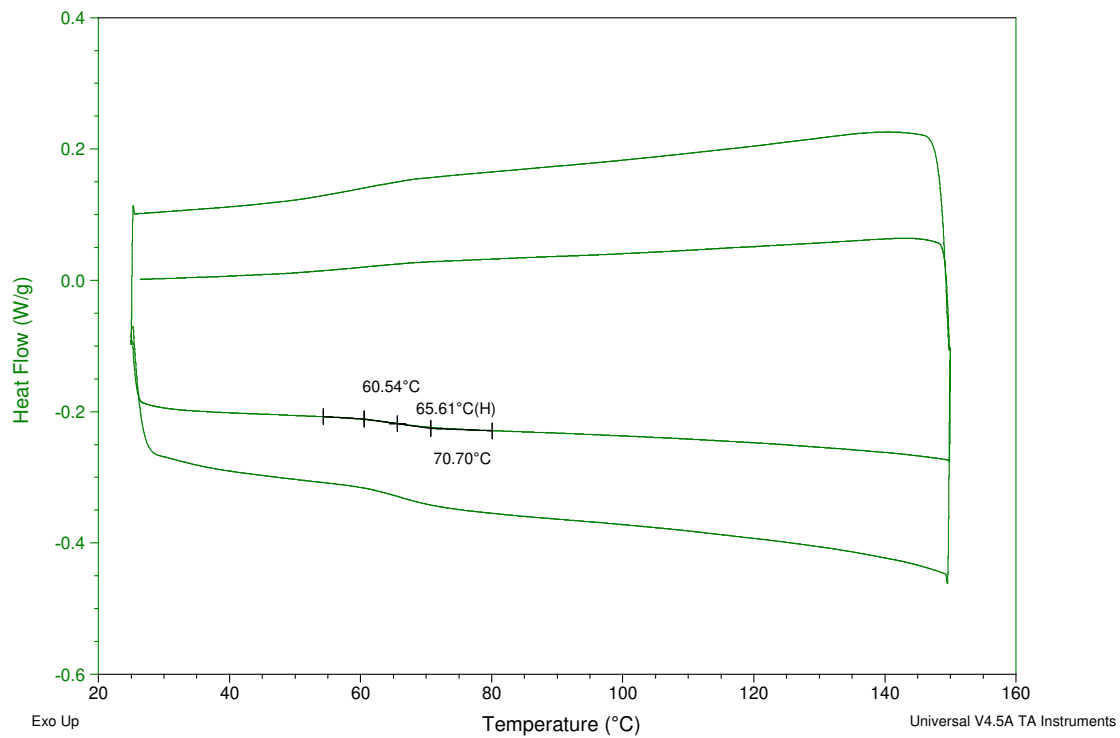


Figure 3.27. Full DSC trace for PLA powder. One T_g is present at 65.6 °C.

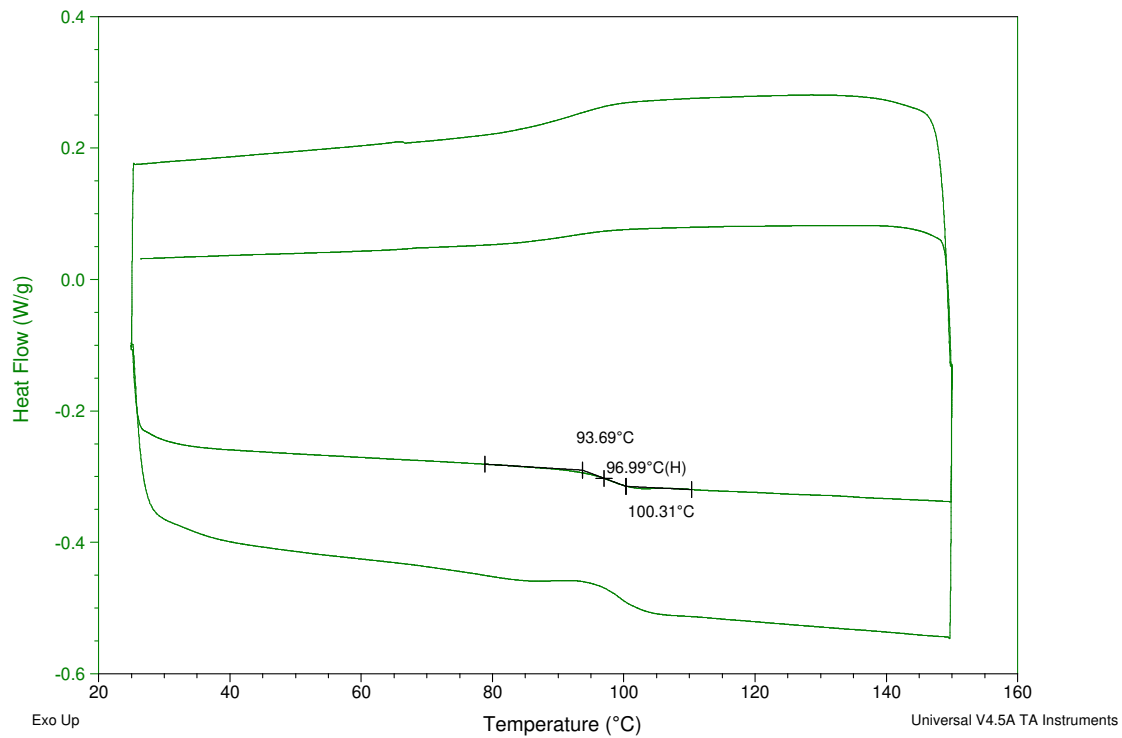


Figure 3.28. Full DSC trace of HIPS filament after printer extrusion. One T_g is present at 97.0 °C.

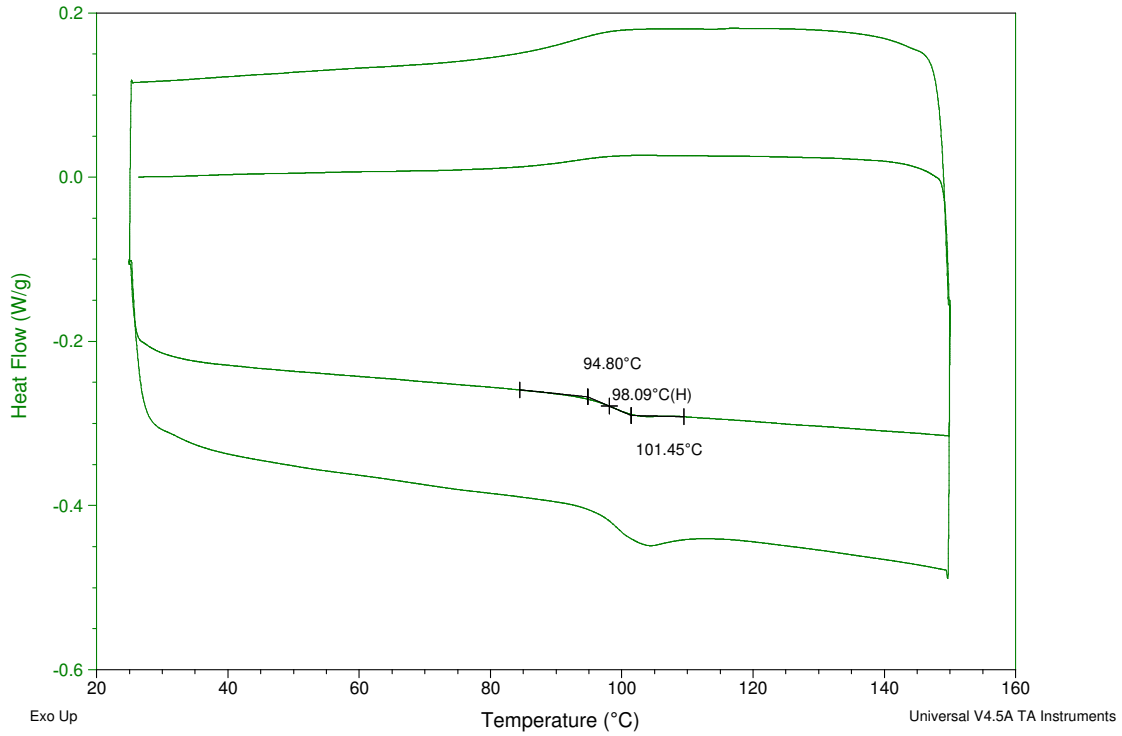


Figure 3.29. Full DSC trace for HIPS powder. One T_g is present at 98.1 °C.

Material Mechanical Properties

Dynamic Mechanical Analysis (DMA)

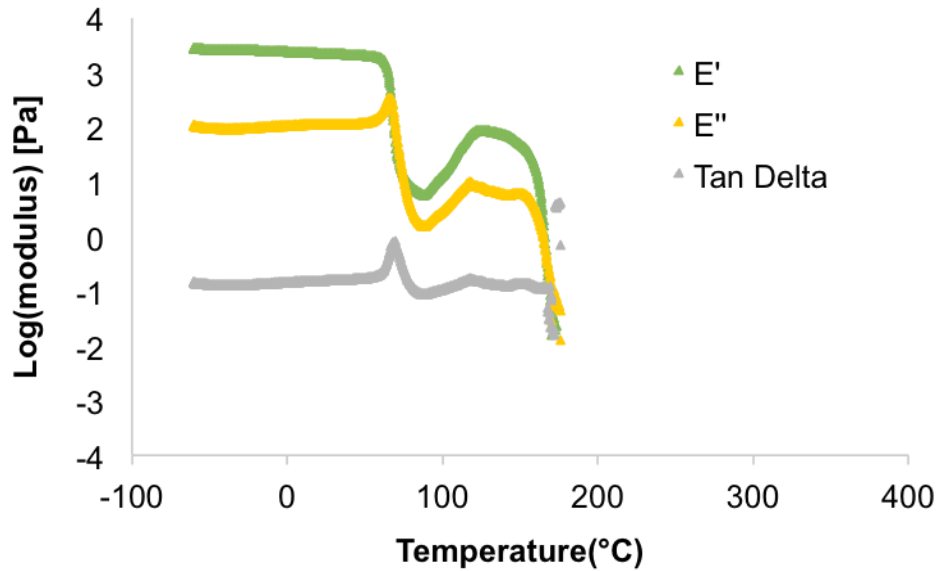


Figure 3.30. Dynamic Mechanical analysis of PLA tabs printed via FFF

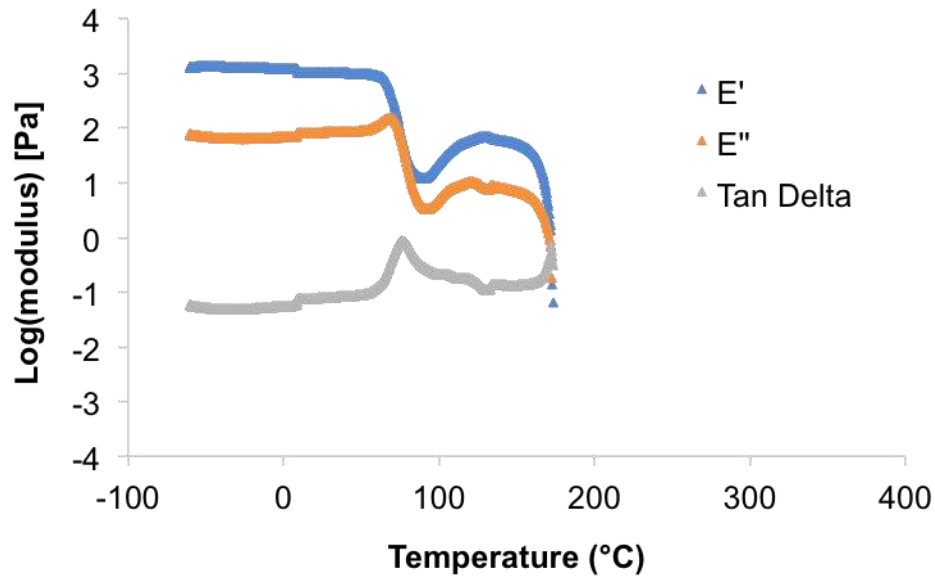


Figure 3.31. Dynamic mechanical analysis of PLA tabs printed via PME.

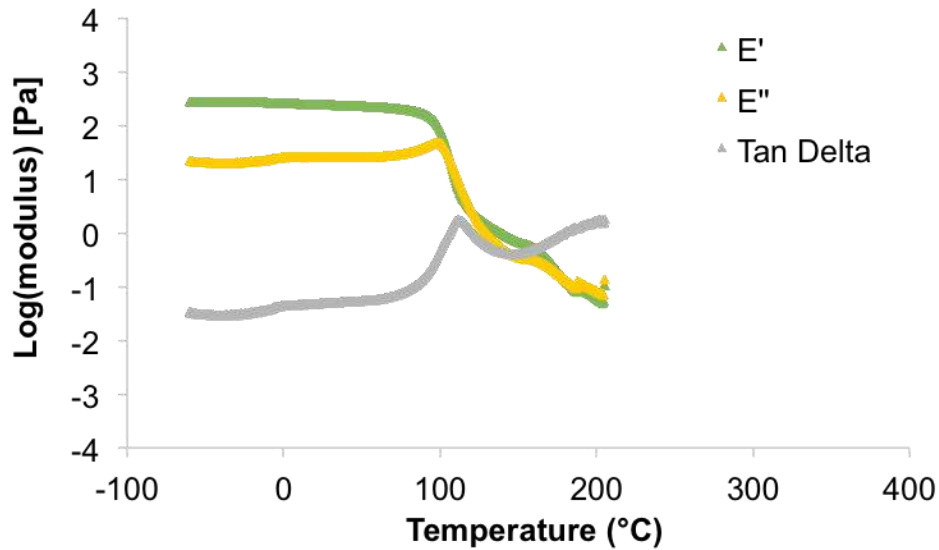


Figure 3.32. Dynamic mechanical analysis of ABS tabs printed via FFF.

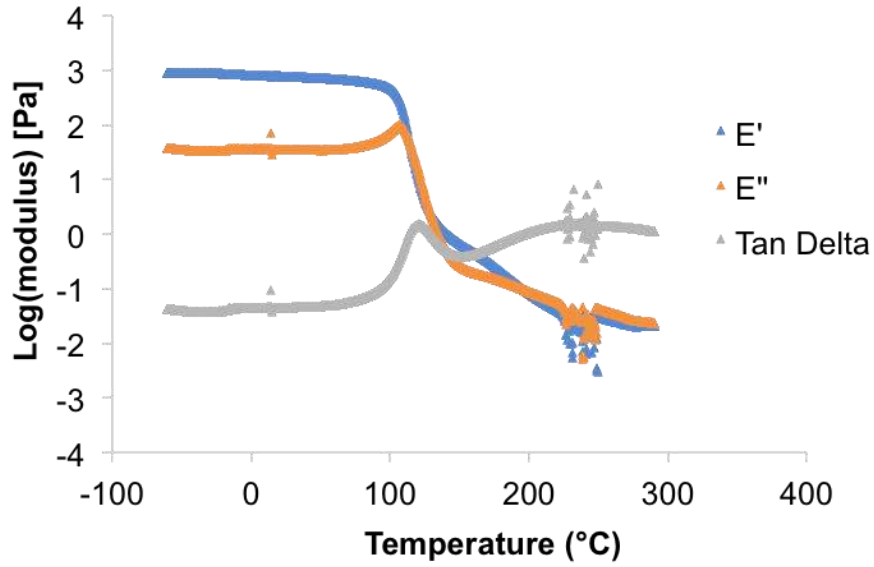


Figure 3.33. Dynamic mechanical analysis of ABS tabs printed via PME.

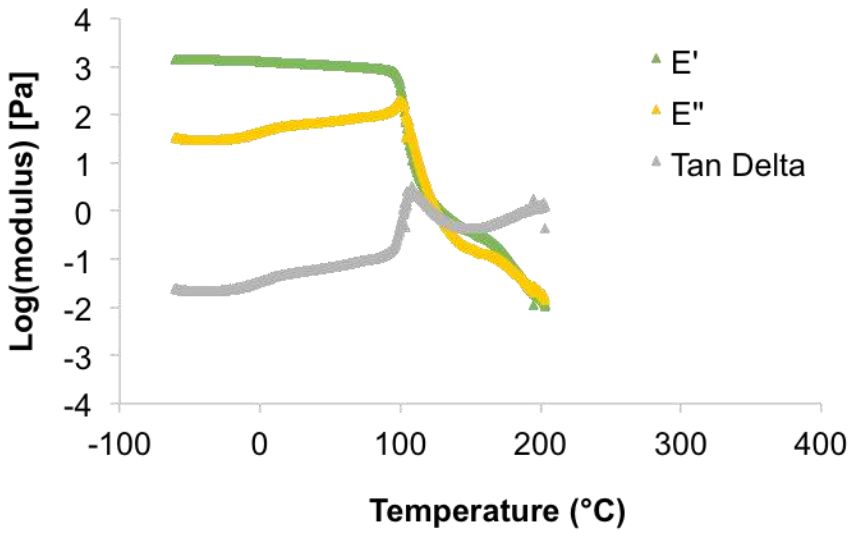


Figure 3.34. Dynamic mechanical analysis of HIPS tabs printed via FFF.

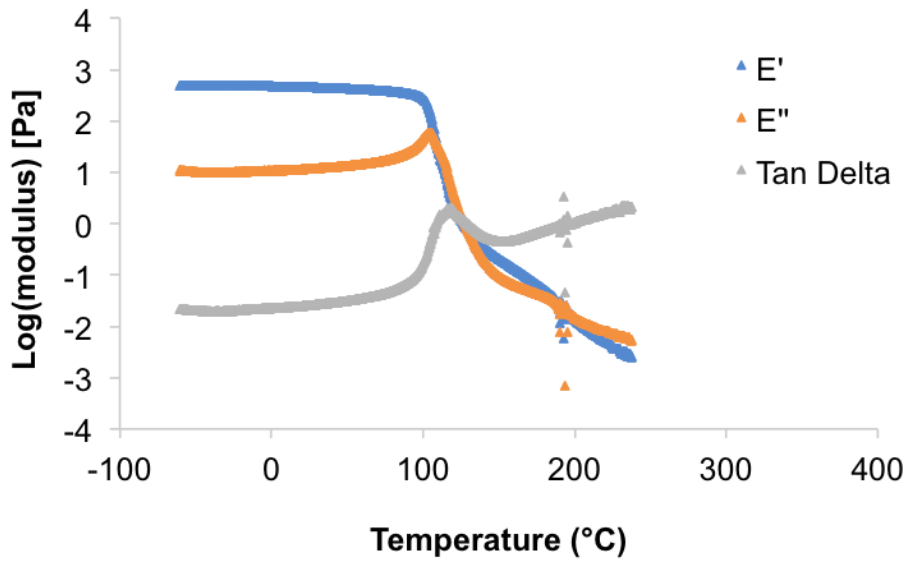


Figure 3.35. Dynamic mechanical analysis of HIPS tabs printed via PME.

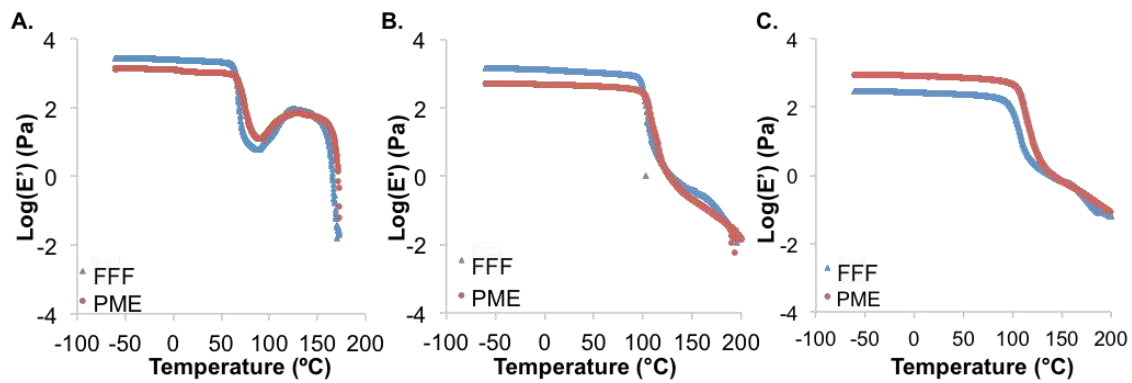


Figure 3.36. Plots of the storage modulus under tension (E') vs. temperature during a dynamic mechanical analysis for the tabs printed by FFF and PME for PLA (A.), HIPS (B.), and ABS(C.).

Tensile Testing

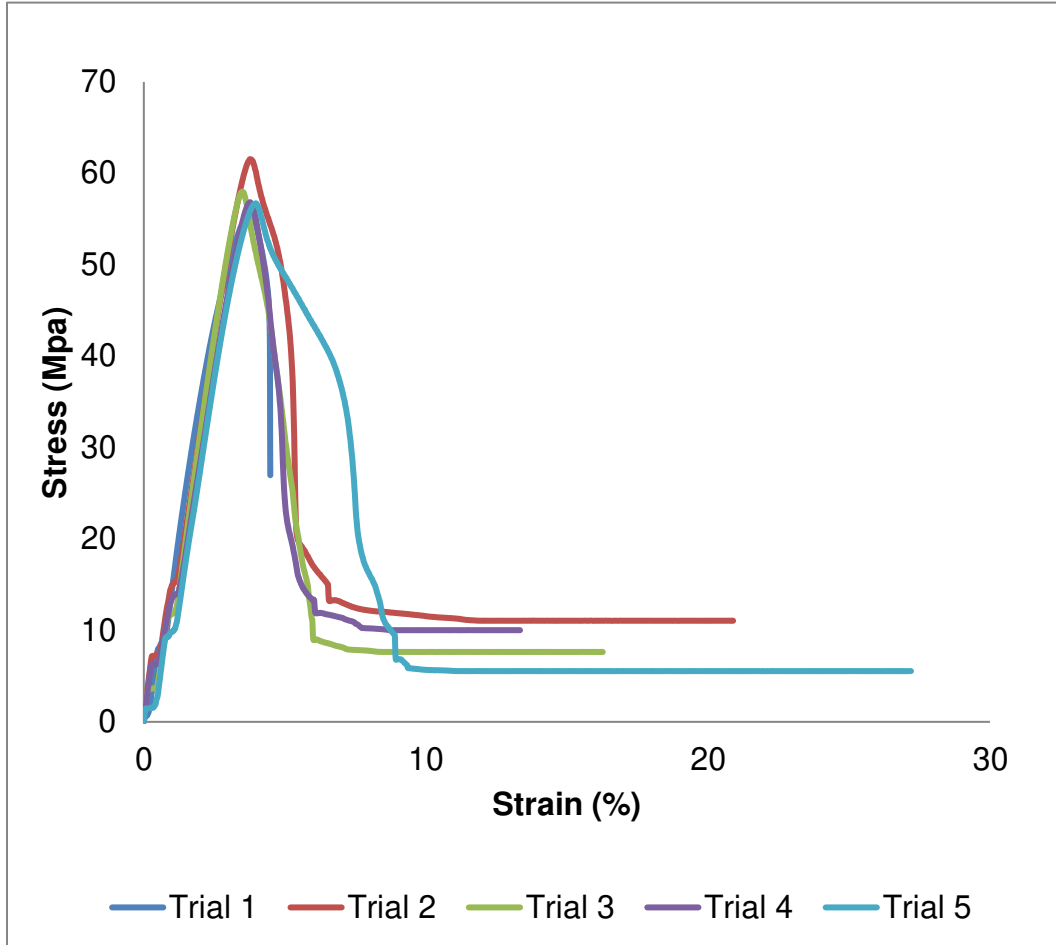


Figure 3.37. Plots of tensile stress vs. tensile strain for PLA ASTM Type V dog bones printed using FFF 3D printer.

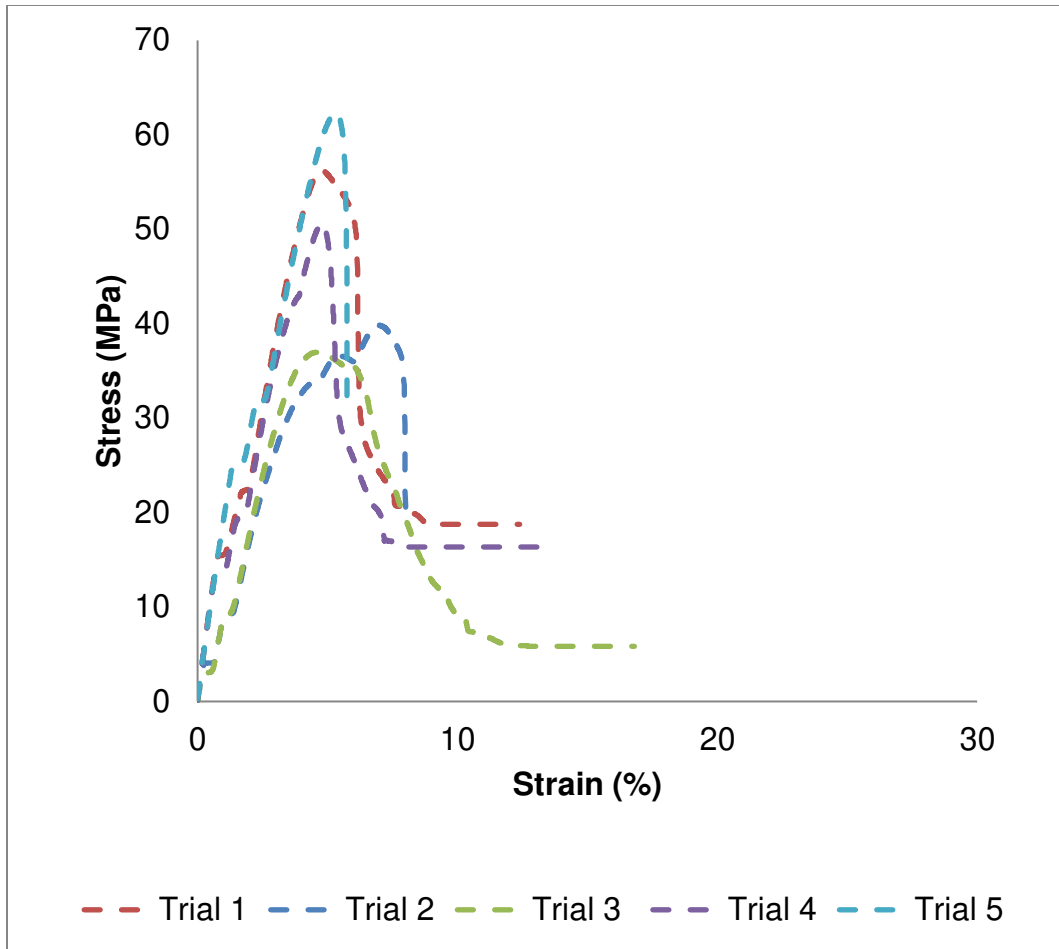


Figure 3.38. Plots of tensile stress vs. tensile strain for PLA ASTM Type V dogbones printed using PME 3D printer.

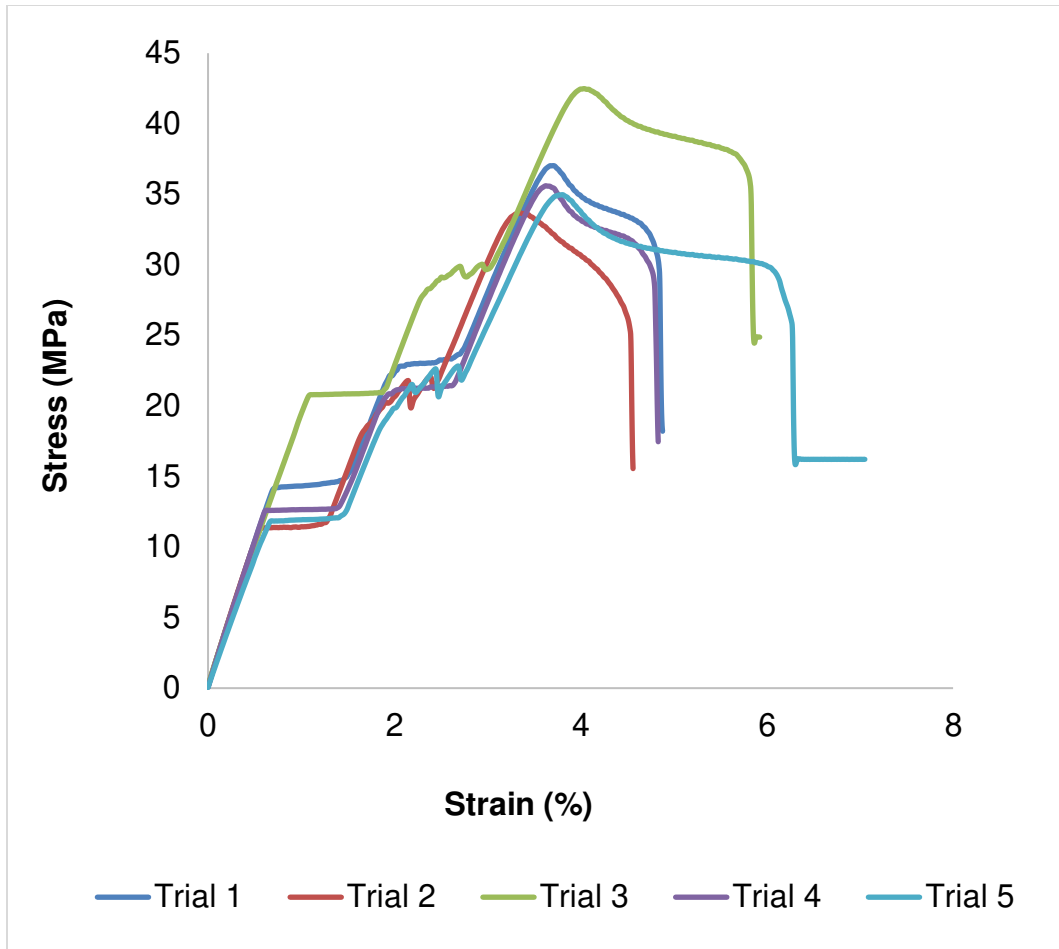


Figure 3.39. Plots of tensile stress vs. tensile strain for HIPS ASTM Type V dogbones printed using FFF 3D printer.

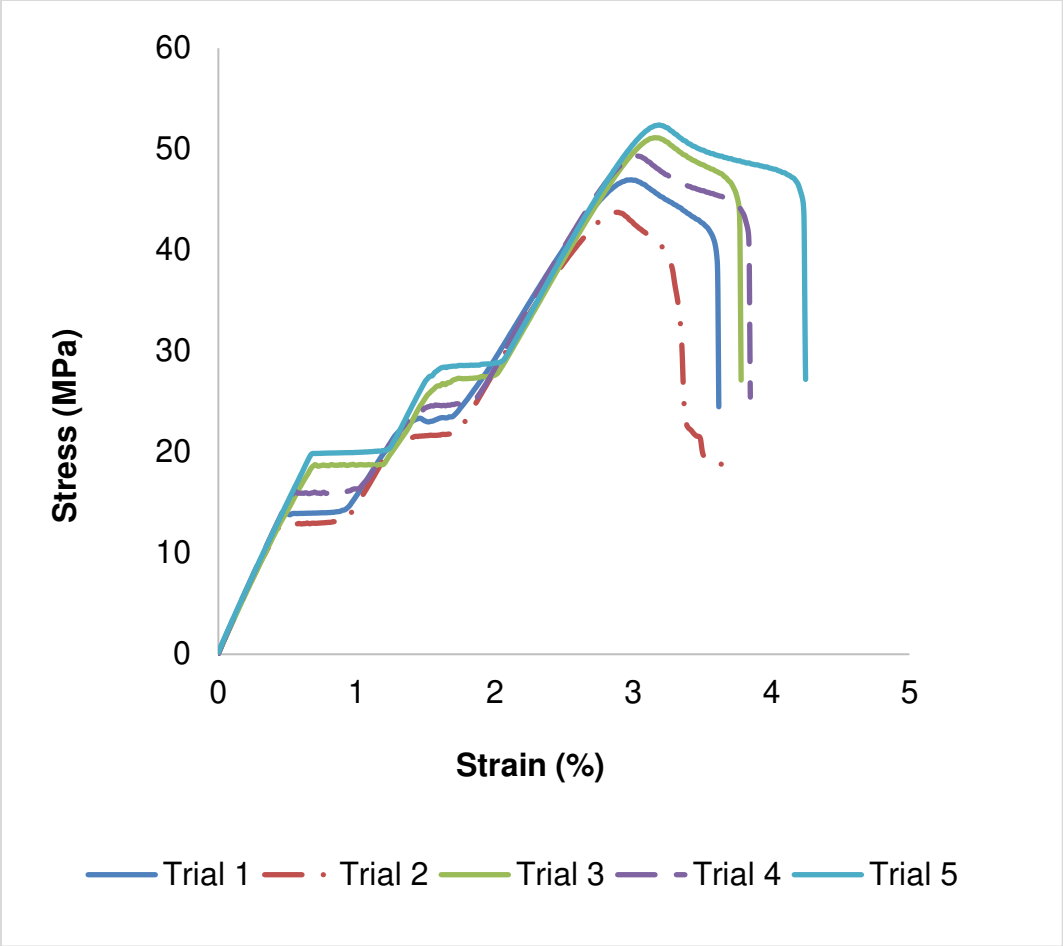


Figure 3.40. Plots of tensile stress vs. tensile strain for ABS ASTM Type V dogbones printed using FFF 3D printer.

Print Performance Compared

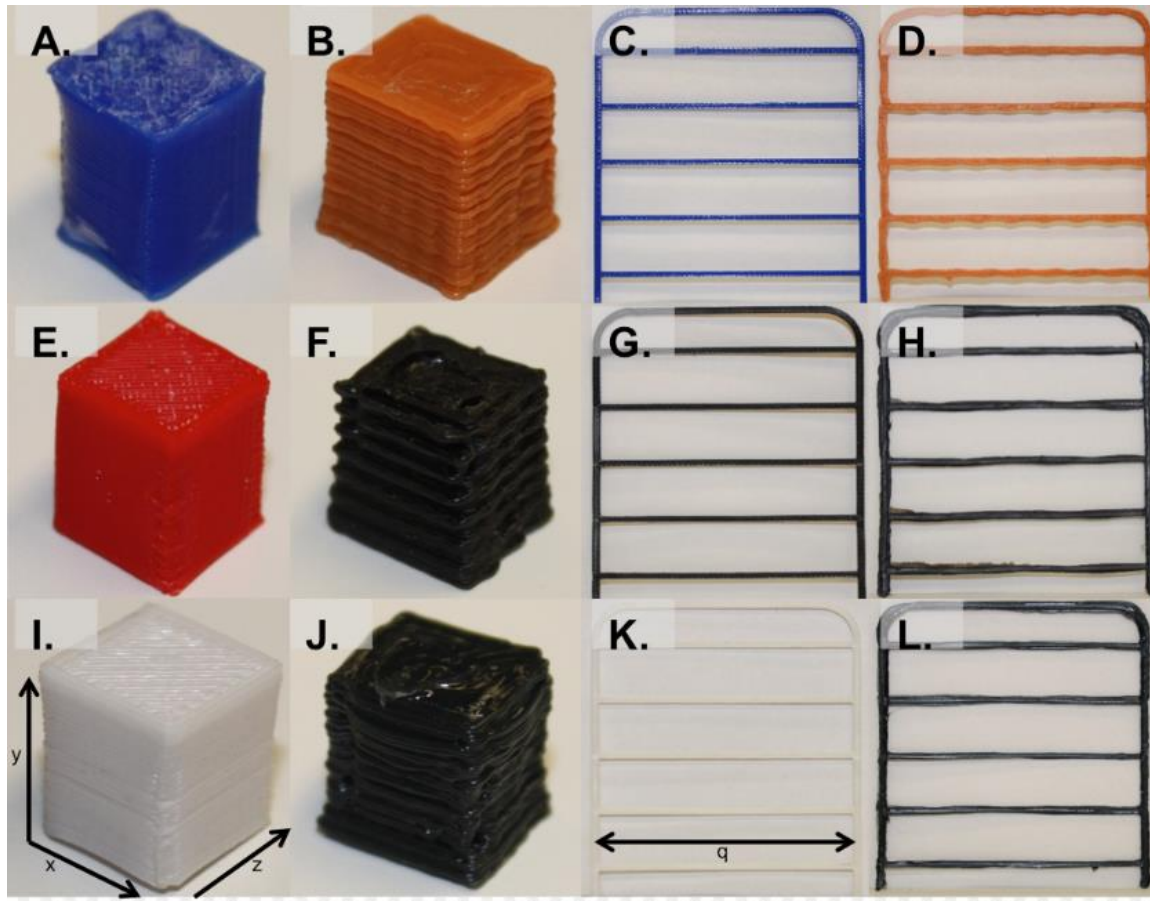


Figure 3.41. FFF prints of all 3 materials ((A) PLA cube, (E) ABS cube, (I) HIPS cube, (C) PLA rail, (G) ABS rail, (K) HIPS rail) are pictured alongside Powder Melt Extruder (PME) prints of all 3 materials ((B) PLA cube, (F) ABS cube, (J) HIPS cube, (D) PLA rail, (H) ABS rail, (L) HIPS rail. X,Y, and Z = 1 cm: q = 6 cm.

References

- [1] N. Jones, Science in three dimensions: the print revolution, *Nature* 487 (2012) 22–23.
- [2] J.-P. Kruth, M.C. Leu, T. Nakagawa, Progress in additive manufacturing and rapid prototyping, *CIRP Ann. Manuf. Technol.* 47 (1998) 525–540.
- [3] B.P. Connor, G.P. Manogharan, A.N. Martof, L.M. Rodomsky, C.M. Rodomsky, D.C. Jordan, J.W. Limperos, Making sense of 3-D printing: creating a map of additive manufacturing products and services, *Addit. Manuf.* 1–4 (2014) 64–76.
- [4] Y. Huang, M.C. Leu, J. Mazumder, A. Donmez, Additive manufacturing: current state, future potential, gaps and needs, and recommendations, *J. Manuf. Sci. Eng.* 137 (2015) 014001-1–014001-10.
- [5] I. Campbell, D. Bourell, I. Gibson, Additive manufacturing: rapid prototyping comes of age, *Rapid Prototyp. J.* 18/4 (2012) 255–258.
- [6] K.V. Wong, A. Hernandez, A review of additive manufacturing, *ISRN Mech. Eng.* 10 (2012) 208760.
- [7] J.R. Tumbleston, D. Shirvanyants, N. Ermoshkin, R. Januszewicz, A.R. Johnson, D. Kelly, K. Chen, R. Pinschmidt, J.P. Rolland, A. Ermoshkin, E.T. Samulski, J.M. DeSimone, Continuous liquid interface production of 3D objects, *Science* 347 (2015) 1349–1352.
- [8] H. Yin, Y. Ding, Y. Zhai, W. Tan, X. Yin, Orthogonal programming of heterogeneous micro-mechano-Environments and geometries in three-dimensional bio-stereo- lithography, *Nat. Comm.* 9 (2018) 4096.
- [9] J.-P. Kruth, P. Mercelis, J. Van Vaerenbergh, Binding mechanisms in selective laser sintering and selective laser melting, *Rapid Prototyp. J.* 11/1 (2005) 26–36.

- [10] N.D. Dolinski, Z.A. Page, E.B. Callaway, F. Eisenreich, R.V. Garcia, R. Chavez, D.P. Bothman, S. Hecht, F.W. Zok, C.J. Hawker, Solution mask liquid lithography (SMaLL) for one-step, multimaterial 3D printing, *Adv. Mater.* 30 (2018) 1800364.
- [11] S.S. Crump, Apparatus and Method for Creating Three-Dimensional Objects, US Patent 5121329, Priority Date October 30, 1989 (1992).
- [12] E. MacDonald, R. Wicker, Multiprocess 3D printing for increasing component functionality, *Science* 353 (2016) aaf2093.
- [13] G.I. Peterson, M.B. Larsen, M.A. Ganter, D.W. Storti, A.J. Boydston, 3D-printed mechanochromic materials, *ACS Appl. Mater. Interfaces* 7 (2015) 577–583.
- [14] O. Rios, W. Carter, B. Post, P. Lloyd, D. Fenn, C. Kutchko, R. Rock, K. Olson, B. Compton, 3D printing via ambient reactive extrusion, *Mater. Today Comm.* 15 (2018) 333–336.
- [15] ISO/ASTM 52900, Standard Terminology for Additive Manufacturing – General Principles – Terminology, (2015).
- [16] B.N. Turner, R. Strong, S.A. Gold, A review of melt extrusion additive manufacturing processes: I. Process design and modeling, *Rapid Prototyp. J.* 20/3 (2014) 192–204.
- [17] B.N. Turner, S.A. Gold, A review of melt extrusion additive manufacturing processes: II. materials, dimensional accuracy, and surface roughness, *Rapid Prototyp. J.* 21/3 (2015) 250–261.
- [18] T.A. Osswald, J. Puentes, J. Kattinger, Fused filament fabrication melting model, *Addit. Manuf.* 22 (2018) 51–59.
- [19] M. Hofmann, 3D printing gets a boost and opportunities with polymer materials, *ACS Macro Lett.* 3 (2014) 382–386.

- [20] J.W. Stansbury, M.J. Idacavage, 3D printing with polymers: challenges among expanding options and opportunities, *Dent. Mater.* 32 (2016) 54–64.
- [21] S.C. Ligon, R. Liska, J. Stampfl, M. Gurr, R. Mulhaupt, Polymers for 3D printing and customized additive manufacturing, *Chem. Rev.* 117/15 (2017) 10212–10290.
- [22] D. Robertson, C.M. Shemelya, E. MacDonald, R. Wicker, Expanding the applicability of FDM-type technologies through materials development, *Rapid Prototyp. J.* 21/2 (2015) 137–143.
- [23] B.M. Boyle, T.A. French, R.M. Pearson, B.G. McCarthy, G.M. Miyake, Structural color for additive manufacturing: 3D-Printed photonic crystals from block copolymers, *ACS Nano* 11 (2017) 3052–3058.
- [24] F. Ning, W. Cong, J. Qiu, J. Wei, S. Wang, Additive manufacturing of carbon Fiber reinforced thermoplastic composites using fused deposition modeling, *Compos. Part B Eng.* 80 (2015) 369–378.
- [25] D. Espalin, D.W. Muse, E. MacDonald, R.B. Wicker, 3D printing multifunctionality: structures with electronics, *Int J Adv Manuf Technol* 72 (2014) 963–978.
- [26] S.E. Bakarich, R. Gorkin III, M. Panhuis, G.M. Spinks, Three-dimensional printing Fiber reinforced hydrogel composites, *ACS Appl. Mater. Interfaces* 6 (2014) 15998–16006.
- [27] A.J. Boydston, B. Cao, A. Nelson, R.J. Ono, A. Saha, J.J. Schwartz, C.J. Thrashert, Additive manufacturing with stimuli-responsive materials, *J. Mater. Chem. A Mater. Energy Sustain.* 6 (2018) 20621.
- [28] N. Holshouser, L. Palas, L. Kunc, R. Lloyd, D. Blue, D. Peter, Out of bounds additive manufacturing, *Advanced Materials and Processes (AM&P)* 171 (3) (2013) 15–17.

- [29] C.E. Duty, V. Kunc, B. Compton, B. Post, D. Erdman, R. Smith, R. Lind, P. Lloyd, L. Love, Structure and mechanical behavior of big area additive manufacturing (BAAM) materials, *Rapid Prototyp. J.* 23/1 (2017) 181–189.
- [30] V. Kishore, C. Ajinjeru, A. Nycz, B. Post, J. Lindahl, V. Kunc, C. Duty, Infrared preheating to improve interlayer strength of big area additive manufacturing (BAAM) components, *Addit. Manuf.* 14 (2017) 7–12.
- [31] Titan 3D Robotics, *The Atlas: Purpose Built, Production Ready*, (2016) (Accessed 24 January, 2019), <http://www.titan3drobotics.com/atlas/>.
- [32] Direct3D, *Direct3D: Pellet Extrusion Made Possible* (Accessed 24 January, 2019), <https://www.direct3d.it/>.
- [33] Rich Rap Blogspot, *Reprap Development and Further Adventures in DIY 3D Printing: Quest for a Universal Pellet Extruder for 3D Printing*, (2014) <https://richrap.blogspot.com/2014/12/no-more-filament-quest-for-universal.html>.
- [34] N. Volpato, D. Kretschek, J.A. Foggatto, C.M. Gomez da Silva Cruz, Experimental analysis of an extrusion system for additive manufacturing based on polymer pellets, *Int. J. Adv. Manuf. Technol.* 81 (2015) 1519–1531.
- [35] V1 Engineering, *The MPCNC Assembly: Before You Begin*, (2018) (accessed 24 January, 2019), <https://www.v1engineering.com/assembly/>.
- [36] L.L.C. Hotends, *Hotends About Us*, (2011) (Accessed 24 January, 2019), <https://www.hotends.com/aboutus>.
- [37] 3D Hubs, *Basic Manufacturing Principles: Dimensional Accuracy of 3D Printed Parts*, (2019) (Accessed 24 January, 2019), <https://www.3dhubs.com/knowledge-base/dimensional-accuracy-3d-printed-parts#fdm>.

- [38] FlashForge 3D Printer, Creator Pro 3D Printer Overview. <http://www.flashforge.com/creator-pro-3d-printer/>, 2012-2018. (Accessed 24 January 2019).
- [39] C.M. Shemelya, A. Riviera, A.T. Perez, C. Rocha, M. Liang, X. Yu, C. Kief, D. Alexander, J. Stegeman, H. Xin, R.B. Wicker, E. Macdonald, D.A. Roberson, Mechanical, Electromagnetic, and X-ray Shielding Characterization of a 3D Printable Tungsten-Polycarbonate Polymer Matrix Composite for Space-Based Applications, *J. Korean Inst. Electr. Electron. Mater. Eng.* 44 (2015) 2598–2607.
- [40] A.R. Torrado Perez, D.A. Roberson, R.B. Wicker, J. Fail, *Anal. and Preven.* 14 (2014) 343–353.
- [41] C. Rocha, A. Torrado-Perez, D.A. Roberson, C. Shemelya, E. MacDonald, R. Wicker, *J. Mater. Res.* 29 (2014) 1859–1866.

CHAPTER 4 – IMPACT OF THE PENDANT GROUP ON THE CHAIN CONFORMATION AND BULK PROPERTIES OF NORBORNENE IMIDE-BASED POLYMERS

Overview

Three series of well-defined norbornene imide-based polymers with different pendant groups were synthesized to investigate the effect of the pendant group on the polymer conformation in solution and bulk melt properties. Each of these three series was examined by analyzing the polymers' bulk z-average radius of gyration via static light scattering and the polymers' melt viscoelastic properties via oscillatory measurements and differential scanning calorimetry. Sterically bulky pendant wedge groups modestly increase the rodlike conformation of the norbornene-imide polymer, however, the inherent rigidity of the polymer main-chain can still be observed with less bulky substituents. In stark contrast, the different side groups significantly impacted the bulk viscoelastic and thermal properties. By increasing the pendant group size, the chain diameter of the polymer increases and lowers the entanglement modulus. Finally, as the wedge pendant group size increases, the segmental relaxation time and the fragility index of these norbornene-based polymers are decreased.

Introduction

Bottlebrush polymers are molecules containing densely spaced polymeric side chains grafted onto a central backbone. These densely packed polymeric side chains give a cylindrical conformation to the bottlebrush molecule. It is this cylindrical conformation of bottlebrush polymers that imparts significant influences on the bulk materials properties.¹⁻⁴ An increase in grafting density and length of the side chains increases the cross-sectional diameter and

persistence length of the brush polymer chains, while also creating a secondary relaxation process and a reduction of the entanglement modulus.⁵⁻⁸ These unique properties of molecular brush polymers are due to the added degrees of freedom available to the longer side chains, which give rise to more entropically favored conformations compared to shorter side chains. Therefore, the brush backbone adopts a more rodlike shape when paired with longer side chains to help accommodate more favorable side chain conformations. A number of theoretical models have been developed to describe the origin of the differences in physical properties between linear polymers and brush polymers.^{9,10} Theories, including the packing model^{11,12} and reptation theory,^{1,13} have aided in conceptualizing many of the experimental results observed in brush polymers. Two of the most valuable interpretations of these models are in predicting brush polymer conformation and describing the two distinct rheological relaxations of brush polymers.

The polymer architecture described as dendronized polymers,¹⁴ however, has received less attention with respect to the theoretical understanding of their structure and dynamics. Dendronized polymers are polymers with side groups extending away from the backbone that contain one or more branch points in which another generation of branches begins. Often, these dendronized polymers can be directly polymerized from discrete monomers¹⁵⁻¹⁹ and contain unique chemical²⁰ and physical properties that have enabled many different, new applications such as gene delivery vectors,²¹ stimuli-responsive materials,²² catalytic frameworks,²³ or polymeric photonic crystals.^{8,24,25} Dendronized polymers also present the opportunity to expand polymer physics models to this intermediate regime of polymer architectures due to the facility with which polymer girth and functionality can be tuned.²⁶⁻³¹ Previously, the effects of a large-molecular-weight wedge pendant group on the linear rheological responses of a norbornene imide-based polymer were investigated.²⁷ Multiple molecular weights of polymers synthesized

from an alkyl wedge monomer with three n-dodecyl alkyl chains (DDW) were investigated. This series of wedge polymers exhibited a reduced degree of entanglement as given from a low rubbery plateau modulus value (order of 104 Pa) and a low glassy modulus (~ 108 Pa) observed by rheology. Typically, linear polymers exhibit a rubbery plateau modulus value around 105–106 Pa and a glassy modulus value around a value of 109–1010 Pa.³² The study also reported a dynamic fragility value of $m = 65$ for the DDW polymer, which is consistent with a flexible chain polymer rather than a stiff backbone polymer as might be expected from a norbornene backbone. The relative contributions of the pendant group size to the norbornene imide- based polymer properties, however, remain unclear. The work reported herein aims to investigate the effects on the polymer conformation, thermal, rheological, and mechanical properties of polymers possessing dendronized pendant groups of varying sizes at a norbornene imide backbone. The results reveal that the size of the side group appears to less significantly impact the fractal dimensions of the polymer chain but significantly impacts the thermomechanical and dynamic properties of these polymers.

Results and Discussion

To investigate the effects of the side group on norbornene- based polymers, three different norbornene-based monomers were polymerized using ruthenium-mediated ring-opening metathesis polymerization (ROMP)^{33–36} to produce a series of polymers possessing degrees of polymerization (DP) through the polymer backbone ranging from oligomeric DPs of 9 up to polymer DPs as high as 9905. The ROMP produced well-defined polymers within each polymer series, accessing a large range of backbone DPs with low dispersity (< 1.30) (Tables 4.2–4.4). Each of the three polymer series was chosen to systematically increase the sterics of the side group attached to the norbornene backbone: an n-hexyl side group [p(HNb)], a dendronized

group with three ethyl alkyl chains attached [p(EtW)], and a dendronized group with three n-dodecyl alkyl chains attached [p(DDW)] (Figure 4.1).

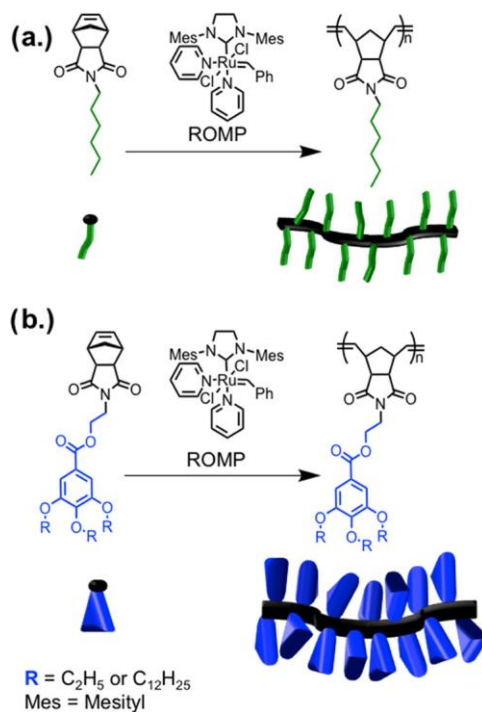


Figure 4.1. Synthetic Approach to the Linear HNb MW Series (a) and the Ethyl ($R = C_2H_5$) or the Dodecyl ($R = C_{12}H_{25}$) Alkyl Wedge MW Series (b).

Characteristics of the chain conformation including the scaling factor and fractal dimension can be obtained by comparing the z-average radii of gyration (R_z) of these polymers in solution to their number-average molecular weights (M_n) or their DPs.^{37–40} The R_z and M_n values of the polymers were determined in tetrahydrofuran using multiangle static light scattering coupled with gel permeation chromatography (GPC–MALS). The slope of the best-fit line of R_z versus DP corresponds to the scaling factor (f) of the polymer series (Figures 4.2 and 4.17). For the p(HNb) polymer series, a scaling factor of 0.62 ± 0.04 was determined, whereas for the wedge polymer series, scaling factors of 0.68 ± 0.05 for the p(EtW) series and 0.69 ± 0.03 for the p(DDW) series were determined (Figure 4.2). These scaling factors correspond to fractal

dimension values (f^{-1}) of 1.61 for the p(HNb) series, 1.47 for the p(EtW) series, and 1.45 for the p(DDW) series (see fractal dimension analysis in Experimental Methods for more details).

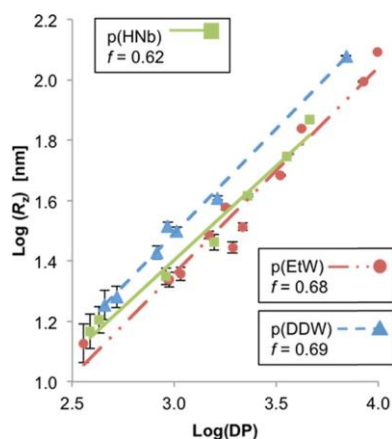


Figure 4.2. Double logarithmic plot of the radius of gyration (R_z) vs the degree of polymerization (DP) of the p(HNb) series (green squares), the p(EtW) series (red circles), and the p(DDW) series (blue triangles) with the relative uncertainty in R_z measurements shown with error bars.

The observations of these scaling factors and fractal dimensions are significant for two reasons. First, according to the scaling theory,⁴¹ in a good solvent a rigid-rod polymer theoretically exhibits a scaling factor of 1, whereas a random self-avoiding walk (RSAW) flexible polymer theoretically exhibits a scaling factor of 0.6.^{42,43} These scaling factors correspond to a fractal dimension value of 1 for rigid-rod polymers and a value of 1.67 for RSAW polymers. The fractal dimensions of the polymers studied herein are found to have values between the rigid-rod and RSAW polymers and are considered semiflexible. Second, when comparing the fractal dimension of p(HNb), 1.61, to the two wedge polymers' fractal dimensions (1.47 for p(EtW) and 1.45 for p(DDW)), the data suggests that the rigidity of the norbornene-based wedge polymers arises somewhat from the inherent rigidity of the polymer main chain and less than might be expected from the bulkiness of the wedgelike side groups. Further, the bulkiness of the wedge side groups that controls the conformation of the polymer stems from the planar ester and benzene motifs of the side chain rather than the alkyl substituents. This

observation is in agreement with the observations often made in brush polymer systems where the longer the side chain, or the greater the radius of gyration of the side chain, the more the rigid-rod character of the polymer conformation.^{10,44} This agreement with trends seen in brush polymer systems is further confirmed when comparing the polymer persistent lengths (l_p) estimated from the R_z values for each polymer (Tables 4.8–4.10). The expression used to estimate the l_p is shown below

$$R_z^2 = Ll_p - l_p^2 + \frac{2}{L}l_p^3 - \frac{2}{L^2}(1 - e^{-\frac{L}{l_p}})l_p^4 \quad (1)$$

where L is the contour length estimated by the product of the degree of polymerization and the backbone monomer size.³⁰ The p(HNb) with a DP = 912 (pHNb)-DP912 has an estimated l_p of 1.1 ± 0.1 nm, which is similar to the estimated l_p of the p(EtW)-DP943 at 1.0 ± 0.1 nm. However, as the side group increases in size to that of the p(DDW) series, so does the l_p as shown by the estimated l_p of p(DDW)-DP930 at 2.3 ± 0.1 nm. The l_p for the p(DDW) is about double the size of the p(HNb) and p(EtW) l_p .

To examine the bulk thermal, mechanical, and rheological properties of these three polymers, we carried out differential scanning calorimetry (DSC), dynamic mechanical analysis (DMA), and rheological measurements. Figure 4.3a plots the glass transition temperature (T_g) values, determined by DSC, as a function of DP for the three polymer series studied. All three polymers showed an increase of T_g with DP at low molecular weights (4–21 kg/mol) and approached their respective asymptotic values. This trend is similar to that of conventional linear polymers and can be rationalized by either conformational entropy theory or chain-end free volume arguments.⁴⁵ Among the three series, p(HNb) exhibited the most dramatic decrease in T_g with the reduction in DP at low- molecular-weight regimes. For p(HNb) and p(EtW), the asymptotic T_g values were 84 and 89 °C, respectively. Clearly, the replacement of hexyl side

group with ethyl wedge did not significantly affect the segmental relaxation process. In contrast, the asymptotic T_g value of p(DDW) was 38 °C, nearly 50 °C below that of the other two polymers. The significant reduction of T_g in p(DDW) can be attributed to the internal plasticization effect caused by the flexible n-dodecyl side groups, as commonly observed for other polymers, such as poly(n-alkyl methacrylates).^{46,47} As such, the C₁₂ alkyl groups on the wedge side group significantly enhanced the segmental relaxation, in contrast to their negligible impact on the chain dimensionality.

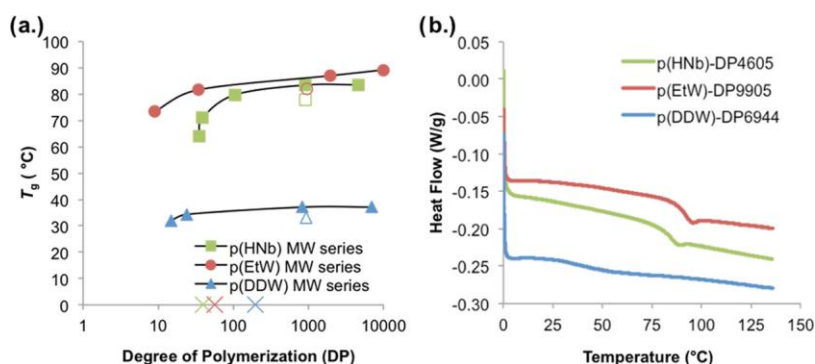


Figure 4.3. Plot of the T_g as a function of DP for p(HNb) (green squares), p(EtW) (red circles), and p(DDW) (blue triangles) (a). The DMA T_g value is shown with unfilled symbols of the respective polymer series (square for p(HNb), circle for p(EtW), and triangle for p(DDW)). The masses of entanglement of each of the series are marked as an “x” in each series’ respective color (green for p(HNb), red for p(EtW), and blue for p(DDW)). The lines are used to guide the eyes. The second heating DSC traces (ramp rate of 5 °C/min) for the high-MW polymers in each series are plotted (b).

Additionally, the DP corresponding to the entanglement molecular weight (M_e), obtained from the rheological characterization below, is also marked in Figure 4.3a. The leveling-off of the T_g values may only be related to the onset of entanglement in the p(HNb) series but not as apparent in the dendronized polymers. This is in contrast to most linear polymers⁴⁸ and warrants further investigation.

To investigate the mechanical properties of these polymers, DMA with a temperature ramp rate of 3 °C/min and a constant strain of 0.3% was performed on p(HNb)-DP912, p(EtW)-DP943, and p(DDW)-DP930, three representative polymers with similar DPs. Figure 4.4 shows

the storage modulus ($E'(\omega)$), loss modulus ($E''(\omega)$), and $\tan(\delta)$, as a function of temperature from DMA measurements under dynamic tensile loading. Similarly to the DSC measurements, the T_g value estimated by DMA, marked by the abrupt drop in $E'(\omega)$, for p(DDW)-DP930 (~ 36 °C) was much lower than p(EtW)-DP943 or p(HNb)-DP912 (~ 80 °C). Note that these values appeared systematically lower than the values obtained from DSC, most likely due to the slower ramp rate of the DMA than that of the DSC. Further, these values were plotted in Figure 4.3a as a comparison of the T_g values obtained for well-entangled polymer samples by both DSC and DMA techniques.

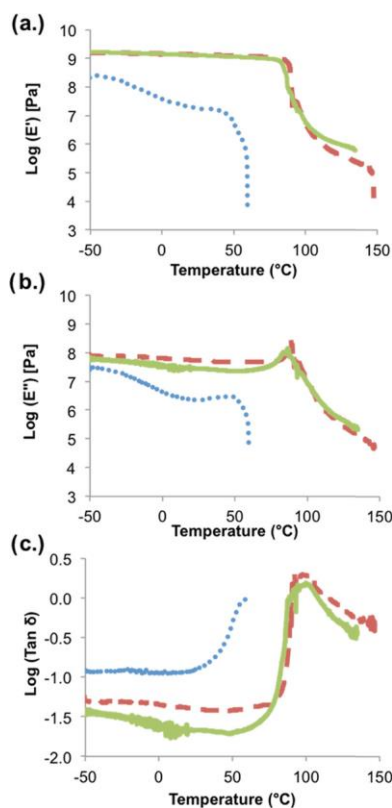


Figure 4.4. Dynamic mechanical responses of the p(HNb)-DP912 (green solid line), p(EtW)-DP943 (red dashed line), and the p(DDW)-DP930 (blue dotted line) are plotted as the storage modulus (a), the loss modulus (b), and the $\tan\delta$ (c) versus temperature.

Figure 4.4 also shows that p(HNb)-DP912 and p(EtW)-DP943 had very similar glassy modulus values of ~ 1.5 GPa at -50 °C, which is within the typical range of glassy polymers.

However, the glassy modulus of p(DDW)-DP930 at $-50\text{ }^{\circ}\text{C}$ was 0.2 GPa, which was nearly 1 order of magnitude lower than those of p(HNb)-DP912 and p(EtW)-DP943. Such an uncommonly low value of glassy modulus for p(DDW) is consistent with the previous report.²⁷ Moreover, p(DDW)-DP930 showed over a 1 order of magnitude reduction in modulus from 0.2 GPa at $-50\text{ }^{\circ}\text{C}$ to 0.014 GPa at $36\text{ }^{\circ}\text{C}$ within the glassy state. Since this behavior was not observed in p(EtW)-DP943, this relaxation process and the corresponding low value of modulus can be attributed to the presence of n-dodecyl wedge side groups. Further, such a low glassy modulus is not associated with the presence of a secondary relaxation as the glassy modulus at $-110\text{ }^{\circ}\text{C}$ (0.3 GPa) is similar to that of the glassy modulus at $-50\text{ }^{\circ}\text{C}$ (0.2 GPa). Instead, the similarity in glassy modulus values at these two temperatures suggests a relatively low degree of packing, potentially in combination with low cohesive forces, of the p(DDW) sample.^{8,49,50} At temperatures above the T_g , both p(HNb)-DP912 and p(EtW)-DP943 showed the presence of the rubbery plateau with modulus $\sim 0.1\text{ MPa}$, indicating that both polymers were well-entangled. In contrast, the rubbery plateau for p(DDW)-DP930, if present, was challenging to detect under tensile loading.

To investigate the melt dynamics of these polymers, rheological measurements were carried out for the three polymers. Figure 4.5a shows the dynamic shear storage modulus $G'(\omega)$ as a function of frequency at the same reference temperature ($T_{\text{ref}} = 120\text{ }^{\circ}\text{C}$), for p(HNb)-DP912, p(EtW)-DP943, and p(DDW)-DP930 (see Figure 4.37 for the approximately isofrictional master curves). These master curves, covering a window of 8 to 10 orders of magnitude in frequency, were constructed via standard time and temperature superposition (TTS) processes at a reference temperature $T_{\text{ref}} = 120\text{ }^{\circ}\text{C}$. All three polymers displayed characteristic regions similar to those of conventional linear polymers: a glass-to-rubber transition region at high frequency, a rubbery

plateau, and a terminal flow region at low frequency. Despite the similar shape, the master curve of p(DDW)-DP930 shifted to the high-frequency side by nearly 3 orders of magnitude in frequency. This enhanced relaxation rate, especially the segmental relaxation process associated with the glass-to-rubber transition region, was caused by the much lower T_g value compared to that of the other two polymers (Figure 4.3). Furthermore, the rubbery modulus, G_N^0 , for p(DDW)-DP930 was significantly lower than that of the other polymers (vide infra). The chain relaxation time (τ_1) marking the onset of the terminal flow regime for the three polymers can be estimated at the crossover frequency ($G'(\omega) = G''(\omega)$) (Figure 4.5a).⁵¹ Specifically, τ_1 was estimated to be 2450, 384, and 0.37 s for p(HNb)-DP912, p(EtW)-DP943, and p(DDW)-DP930 at 120 °C, respectively. The much faster τ_1 for p(DDW)-DP930 is mostly attributed to the much faster segmental relaxation process, which sets the monomer friction coefficient that governs the chain relaxation process.

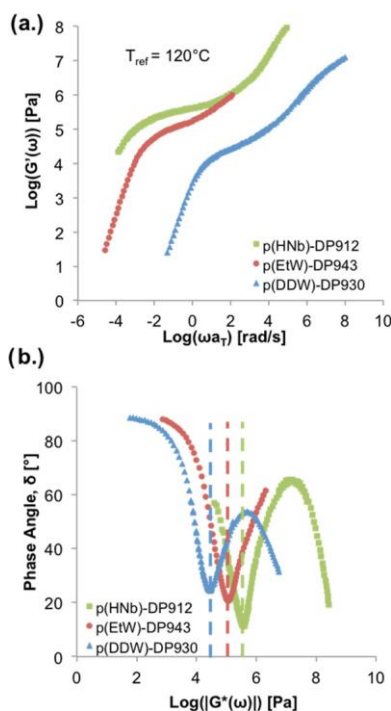


Figure 4.5. Dynamic storage modulus master curves vs frequency (a) and the van Gorp–Palmen (VGP) traces of phase angle vs complex modulus (b) for the p(HNb)-DP912 (green squares),

p(EtW)- DP943 (red circles), and the p(DDW)-DP930 (blue triangles). The dash lines in (b) mark the position of the local minimums.

To validate the TTS practice, van Gorp–Palmen (VGP) plots (Figure 4.5b) were constructed for all three polymers.^{52,53} The VGP plot, or phase angle (δ) as a function of complex modulus ($G^*(\omega)$), is temperature-invariant (i.e., for each sample, the data was taken at varying temperatures and plotted without any shifts). All three polymers displayed smooth, continuous VGP curves (Figure 4.5b), which validated the TTS used to construct the master curves in Figure 4.5a. In addition, the VGP traces of the three polymers show a similar shape: with decreasing $G^*(\omega)$, the phase angle first increased to a local maximum, decreased to a local minimum, and finally increased to a plateau of 90° , characteristic of pure viscous behavior. Such an evolution agrees well with the three regions of relaxation behaviors seen in Figure 4.5a. The overall shape of the curves matched well with those of conventional monodisperse, linear polymers, but differed from the H- shaped and star-shaped polymers with long side chains.⁵⁴

The local minimum in the VGP plots, marked by the dashed lines in Figure 4.5b, provided a reliable estimation of the plateau modulus, G_N^0 ,⁴⁹

$$G_N^0 = \lim_{\delta \rightarrow 0} |G^*(\delta)| \quad (2)$$

Accordingly, G_N^0 values were determined to be 3.79×10^5 , 1.06×10^5 , and 2.57×10^4 Pa for p(HNb)-DP912, p(EtW)-DP943, and p(DDW)-DP930, respectively. In addition, the phase angle at the minimum increased as p(HNb)-DP-912 < p(EtW)- DP943 < p(DDW)-DP930. The values of both the phase angle and complex modulus at the minimum indicating the degree of entanglement and the rubbery elasticity, increased in the order of p(HNb)-DP-912 > p(EtW)-DP943 > p(DDW)-DP930.

To fully understand the influence of the side groups on the melt dynamics, rheological measurements of the three polymer series with varying molecular weights were carried out.

Figure 4.6 shows the dynamic master curves obtained from TTS with $T_{\text{ref}} = 120 \text{ }^\circ\text{C}$ for p(HNb) and p(EtW) and $T_{\text{ref}} = 80 \text{ }^\circ\text{C}$ for p(DDW).⁵⁵ An analysis of the horizontal shift factors (a_T) used to complete these dynamic master curves will be completed following the detailed discussion of the melt dynamics. Note that the lower reference temperature for p(DDW) polymers was adopted to allow comparison with the other two polymer series within the same frequency window, as the T_g values for the p(DDW) series are much lower than those for the other two polymer series (Figure 4.3).

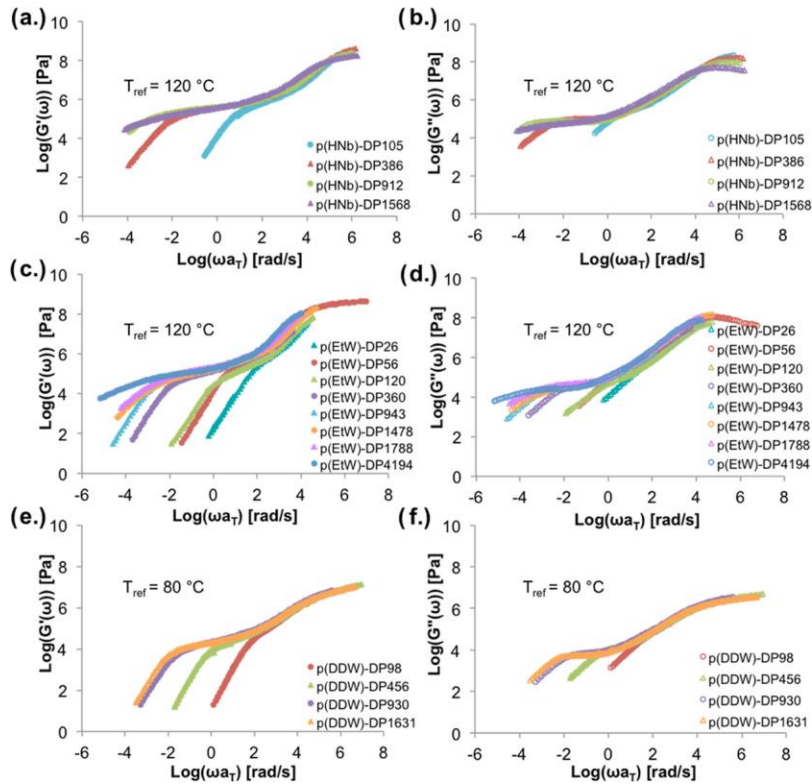


Figure 4.6. Dynamic master curves for all three polymers that exhibit the storage modulus (a) and loss modulus (b) of the p(HNb) series ($T_{\text{ref}} = 120 \text{ }^\circ\text{C}$), the storage modulus (c) and the loss modulus (d) of the p(EtW) series ($T_{\text{ref}} = 120 \text{ }^\circ\text{C}$), and the storage modulus (e) and the loss modulus (f) of the p(DDW) series ($T_{\text{ref}} = 80 \text{ }^\circ\text{C}$).

From Figure 4.6, polymers with low DPs, e.g., p(EtW)-DP26 and p(DDW)-DP98, showed typical rheological responses of unentangled chains with an absence of a rubbery plateau. With an increase in DP, the rubbery plateaus become more extended and more evident, indicating the formation of entangled, transient polymer networks.^{56,57} Figure 4.7 shows the VGP plots for all of the polymers, again confirming the validity of TTS used in constructing all of the master curves in Figure 4.6. VGP plots also showed that the local minimum converged at similar $G^*(\omega)$ values (marked by the dashed line) with an increase of DP for all three polymer series.

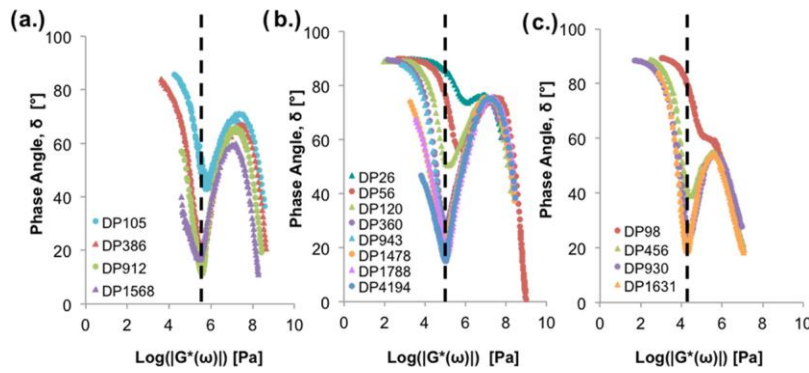


Figure 4.7. VGP plots of the phase angle versus the magnitude of the complex modulus for the p(HNb) series (a), the p(EtW) series (b), and the p(DDW) series (c). The dashed lines mark the position of the local minima.

As mentioned earlier, G_N^0 can be obtained from the local minimum, which can then be used to estimate the average M_e for each polymer

$$M_e = \frac{\rho RT}{G_N^0} \quad (3)$$

where ρ is the polymer melt density at T (e.g., T_{ref} in this case).^{27,40} Using the data for the highest DP of each polymer series as they were well entangled, G_N^0 and M_e values were estimated. Specifically, G_N^0 values for p(HNb)-DP1568, p(EtW)-DP4194, and p(DDW)-DP1631 were determined to be 2.81×10^5 , 1.03×10^5 , and 1.87×10^4 Pa, respectively. Subsequently, M_e values for p(HNb)-DP1568 ($T_{\text{ref}} = 120$ °C), p(EtW)-DP4194 ($T_{\text{ref}} = 120$ °C), and p(DDW)-

DP1631 ($T_{\text{ref}} = 80 \text{ }^\circ\text{C}$) were estimated to be 9.89×10^3 , 2.53×10^4 , and $1.71 \times 10^5 \text{ g/mol}$, respectively. The M_e value of p(DDW)-DP1631, consistent with the value reported in ref 27, is among the lowest value observed for synthetic polymers.⁵⁸ The comparison clearly shows that the increase in the size of the side groups dramatically increases the value of M_e . Normalized by the molecular weight of the corresponding repeating units (M_0), the average number of repeating units between entanglements ($N_e = M_e/M_0$) for p(HNb)-DP1568, p(EtW)- DP4194, and p(DDW)-DP1631 were 30, 60, and 198, respectively. Clearly, the dramatic increase in N_e occurred when n-dodecyl wedge side groups replaced the ethyl wedge side groups (Figure 4.1).

Figure 4.8 plots the phase angle at the local minimum (δ_m) as a function of molecular weight, normalized by the value of M_e . Interestingly, the three different polymer series collapsed into a similar dependency in the double logarithmic plot (inset of Figure 4.8), showing a decrease of δ_m with an increase of molecular weight. This dependency can be empirically fitted as $\log(\delta) = 1.74 \cdot \log(M_n/M_e) - 0.34$ and suggests that the terminal relaxation is separated from the fast local relaxation with a narrow mode distribution as M_n/M_e increases. Moreover, Figure 4.8 suggests that all three types of polymers attained well-entangled behavior (i.e., $\delta_m < 20^\circ$) when the molecular weights reached above 10 times the value of M_e , which is similar to conventional linear polymers.^{53,54} Figure 4.8 also shows that p(EtW)-DP26 (and DP-56) and p(DDW)- DP98, all of which were below $2M_e$, were all unentangled as their $\delta_m > 45 \text{ }^\circ\text{C}$ (loss component dominant). This observation was consistent with the absence of rubbery plateaus in their mechanical spectra (Figure 4.6). It is worth noting that these unentangled chains also displayed a local minimum in the VGP plots, which is most likely attributed to the entropic elasticity of these shorter chains (i.e., the Rouse modes). Such a trend is consistent with the predictions of the packing model: with an increase of chain cross-section, the M_e value increases. This trend is also

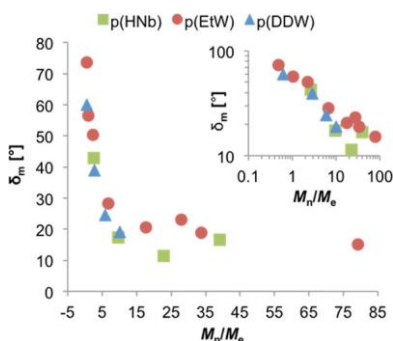
consistent with the trends seen in bottlebrush polymers and further supports the arguments of the packing model, which states that as the ratio between backbone lengths per unit volume gets smaller, the entanglement decreases. In other words, as the diameter of the polymer chain increases, the entanglement decreases.¹¹

Figure 4.8. Phase angle at the local minimum (δ_m) of the VGP traces (data shown in Figure 4.7) as a function of molecular weight (normalized by M_e values estimated using the largest DP for each polymer series) for the three series of polymers. The inset shows the same data as that plotted in the double logarithmic plot.

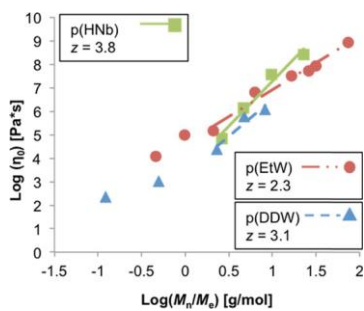
For each of the polymer series, at close to isofrictional conditions, Figure 4.9 shows plots of the zero-shear viscosity (η_0) data against the reduced molecular weight (M_n/M_e) together with the results of power-law fitting of those data, $\eta_0 \sim (M_n/M_e)^z$ when $M_n/M_e > 2$ with the exponent z as indicated in the legend. The η_0 value is estimated from the dynamic modulus master curves using the following equation:²⁶

$$\eta_0 = \lim_{\omega \rightarrow 0} \frac{G''(\omega)}{\omega} \quad (4)$$

The p(HNb) series has z value of 3.8, which resembles the value of 3.4 of an ordinary, linear polymer, but for the p(EtW) and p(DDW) series, the z values were reduced to 2.3 and 3.1,



respectively. This drop in z value indicates that the dendronized polymers are less entangled than the standard, linear polymer. It is important to note that the apparent difference between the z



values of the p(EtW) and p(DDW) series is most likely due to the shorter M_n/M_e range of polymers tested for the p(DDW) series. Further, the p(EtW) and p(DDW) series do not reach the z value of 1 that completely unentangled systems such as polymer brushes or second generation wedges do.²⁶ Therefore, the z value for the dendronized polymer series plotted in Figure 4.9 demonstrates further support for the arguments proposing that as the polymer chain diameter is increased, the entanglement decreases.

Figure 4.9. Double logarithmic plots of the zero shear-rate viscosity (η_0) as a function of molecular weight, normalized by the value of M_e for the p(HNb) series (green squares), the p(EtW) series (red circles) series, and the p(DDW) series (blue triangles) series at a reference temperature close to isofrictional conditions ($T_{ref} = T_g + X$, where $X = 36$ °C for p(HNb), 31 °C for p(EtW), and 42 °C for p(DDW)).

Figure 4.10 shows the temperature dependence of a_T used to construct the master curves shown in Figure 5, which were described by the Williams–Landel–Ferry (WLF) equation⁵⁹

$$\log a_T = - \frac{C_1(T - T_{ref})}{C_2 + T - T_{ref}} \quad (5)$$

with $T_{ref} = T_g + X$ °C to attain close to isofrictional conditions for all three polymer series, where $X = 36$ °C for p(HNb), $X = 31$ °C p(EtW), and $X = 42$ °C for p(DDW). Accordingly, the WLF constants for polymers with M_n -independent T_g values, C_1 and C_2 , are listed in Table 4.1. To further evaluate the temperature dependence of the a_T near the T_g for all three polymer series, the $C_{1,g}$ and $C_{2,g}$ values were calculated with $T_{ref} = T_g$ for all three polymers (Table 4.1).⁶⁰ Specifically, T_g values used were 84 °C for p(HNb), 89 °C for p(EtW), and 38 °C for p(DDW), based on the asymptotic T_g value from Figure 4.3, and the corresponding WLF parameters are listed in Table 4.1.

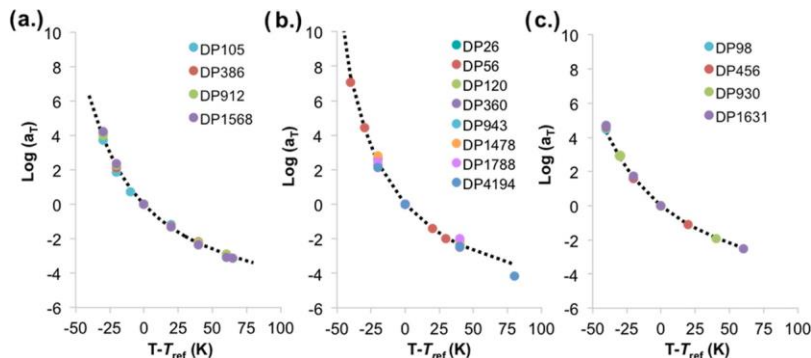


Figure 4.10. TTS shift factors (a_T) used to construct the master curves versus temperature for the p(HNb) MW series (a), the p(EtW) MW series (b), and the p(DDW) MW series (c). The black dashed lines represent WLF fits at a reference temperature close to isofrictional conditions for all three samples ($T_{ref} = T_g + X$, where $X = 36$ °C for p(HNb), $X = 31$ °C p(EtW), and $X = 42$ °C for p(DDW)).

Table 4.1. WLF constants obtained using close to isofrictional conditions and when $T_{ref} = T_g$

WLF constants	p(HNb)		p(EtW)		p(DDW)	
T_{ref}	120 °C	84 °C	120 °C	89 °C	80 °C	38 °C
C_1	6.94	12.17	6.82	11.5	6.70	11.4
C_2	83.8	47.8	76.7	45.7	102	59.8

Often, the temperature dependence of the relaxation processes of polymers near T_g is quantified by the fragility index (m).⁶¹⁻⁶³ Here, m values of the three series of polymers can be estimated using the WLF parameters, $C_{1,g}$, $C_{2,g}$, with $T_{ref} = T_g$ (Table 4.1)²⁷

$$m = T_g \left. \frac{C_{1,g}}{C_{2,g}} \right|_{T_{ref}=T_g} \quad (6)$$

Using eq 6, the values of m for p(HNb), p(EtW), and p(DDW) were estimated to be 91.1, 90.7, and 59.1, correspondingly. In comparison with p(HNb), both wedgelike polymers showed lower m values. However, a further increase of the alkyl side chain length on the wedge from ethyl to n-dodecyl significantly reduced the fragility of the wedgelike polymers.^{61,62,64} This trend is consistent with that observed in polymers with flexible backbones: attachment of aromatic side groups raises the fragility of the polymer, whereas an increase of the length of alkyl side chain length reduces the fragility index.⁶¹ For example, within the p(alkyl methacrylate) family, the

fragility index decreases from a value greater than 80 to less than 40 when the alkyl chain length increases from C₂ to C₁₀.⁶¹ Note that the p(DDW) displayed a value of $m = 59$, which is within the range of a typical “strong” polymer such as polyisobutylene.^{63,65}

Conclusions

Three series of well-defined polymers with varying degrees of polymerization of norbornene backbones and varying pendant wedge groups were synthesized. Each of the three polymer series systematically increased the size of the pendant group to determine the effect that the pendant group size had on both solution conformation and bulk melt properties of the polymers. Comparisons of these polymer series lead to three significant observations of the dynamics of these norbornene imide-based polymers. First, regardless of the pendant group, these norbornene imide-based polymers exhibit a more rodlike conformation in the solution phase than RSAW polymers. Interestingly, the pendant wedge groups increase the rodlike conformation of the polymer main chain in comparison to the hexyl side group, but the longer, n-dodecyl alkyl chain did not have as great of an effect on the conformation compared to the ethyl alkyl chain. Although, it is important to note that the persistence lengths for the p(DDW) and p(EtW) series reported here are fairly short compared to those reported for similar dendronized polymers.¹⁶ This observation can potentially be attributed to the structure of the dendron pendant group as well as the proximity of the branching point to the polymer backbone. However, further experimentation would help elucidate the underlying reasons for this observed difference. Second, the increased size of the pendant wedge groups increases the polymer chain diameter that leads to a dramatic increase in the molecular weight between entanglements, which can be qualitatively rationalized by the packing model. Third, the side groups had a tremendous impact on the fragility of the norbornene-imide backbone polymers. Replacing the n-hexyl group with

ethyl-wedge side groups slightly lowered the fragility of the polymer, whereas a further increase in the alkyl side group length on the wedgelike polymer significantly reduces the fragility of the polymer. The fundamental understanding on the effects of side groups on the norbornene-based polymers will allow for molecular design of polymers with desired combinations of properties that are critical for both applications and manufacturing.

Experimental Methods

$(\text{H}_2\text{IMes})(\text{PPh}_3)(\text{Cl})_2\text{RuCHPh}$ was received as a research gift from Materia Inc. and was converted to $(\text{H}_2\text{IMes})(\text{py})_2(\text{Cl})_2\text{RuCHPh}$ via literature procedure.⁶⁶ All other chemicals were purchased from Sigma-Aldrich or VWR. All polymerizations were performed in a nitrogen-filled glovebox. Columns were run using a Combiflash Rf+ autocolumn from Teledyne ISCO. NMR spectra were recorded on a Bruker Ultrashield 400 MHz spectrometer. Chemical shifts were referenced using internal solvent resonance, ^1H : 7.26 ppm and ^{13}C : 77.16 ppm for CDCl_3 . The chemical shifts are reported as parts per million relative to tetramethylsilane. Deuterated chloroform was purchased from Cambridge Isotope Laboratories. Mass spectra were provided by Colorado State University's Central Instrument Facility using LC-TOF dual ESI source, positive mode with dichloromethane (DCM) as the solvent.

Analysis of isolated and vacuum-dried polymer molecular weight and dispersity was performed using gel permeation chromatography (GPC) coupled with multi-angle light scattering (MALS), using an Agilent HPLC fitted with one guard column and three Plgel 5 μM MIXED-C gel permeation columns in series. The detectors used were a Wyatt Technology TrEX differential refractometer and a Wyatt Technology miniDAWN TREOS light scattering detector, which allows the direct measurement of absolute molecular weight. Absolute molecular weights were determined using dn/dc values calculated by assuming 100% mass recovery of the polymer

sample injection into the GPC. The solvent used was tetrahydrofuran (THF) with a flow rate of 1.0 mL per minute. The R_z value of each polymer was calculated using the multi angle light scattering detector in the miniDAWN TREOS.

Thermal Gravimetric Analysis (TGA) was conducted using a TA Instruments TGA Q50 or TGA Q500. The thermal decomposition data was obtained under a nitrogen gas flow of 40 mL/min by ramping the temperature from 25 °C up to 850 °C at a ramp rate of about 10 °C/minute.

Differential Scanning Calorimetry (DSC) was conducted using a TA Instruments DSC 2500. To erase thermal history, an initial sweep ramped from 0 °C to 150 °C at a ramp rate of 10 °C/min. The temperature was held constant at 150 °C for 3 minutes before it was cooled to 0 °C at a ramp rate of -10 °C/min where the temperature was held constant at 0°C for 3 minutes. Thermal data was collected from the second sweep which consists of ramping the temperature from 0 °C up to 150 °C at a rate of 5 °C/min., isotherming at 150 °C again for 3 minutes before ramping back to 0 °C at a rate of -5 °C/minute.

The mechanical response of the polymers was characterized using a TA Instruments DMA Q800 V20.26 Build 45. The polymer sample's mechanical properties were evaluated in the DMA under a constant nitrogen flow and a constant strain of 0.3% as the DMA ramped the temperature at 3 °C/min. from -50 °C to 300 °C.

The rheological experiments were performed using an AR-G2 and DHR-2 rheometers (TA Instruments) with 8 mm parallel plate geometry under nitrogen purge. The sample was loaded onto the 8 mm plate at experimental conditions until melting and then slowly pressed until the gap was approximately 1 mm using axial stress. Before testing, the samples were kept for 30 minutes – 2 hours until the axial stress was 0.0 ± 0.2 N. First, strain sweep experiments

were performed to determine the linear viscoelastic region of the materials. Oscillatory frequency sweep was carried out from 0.01 to 100 rad/s with a strain in the linear strain regime. The temperature regime for the reference temperature of the time-temperature superposition (TTS) was determined based on the T_g of the polymer series. The TTS was completed with a vertical and lateral shift within the TA Trios Software. Van Gorp-Palmen plots were used to establish the validity of the time-temperature superposition of the polymer series.

Monomer Synthesis

N-(hydroxyethyl)-cis-5-norbornene-exo-2,3-dicarboximide was prepared according to literature procedure.⁶⁷ The Benzoic acid, 3,4,5-tris(dodecyloxy)-, 2-[(3aR,4R,7S,7aS)-1,3,3a,4,7,7a-hexahydro-1,3-dioxo-4,7-methano-2H-isoindol-2-yl]ethyl ester (dodecyl wedge, DDW) monomer, the Benzoic acid, 3,4,5-tris(ethyloxy)-, 2-[(3aR,4R,7S,7aS)-1,3,3a,4,7,7a-hexahydro-1,3-dioxo-4,7-methano-2H-isoindol-2-yl]ethyl ester (ethyl wedge, EtW) monomer, and monomer precursors were prepared according to a previously reported literature procedure.⁶⁸ N-Hexyl-exo-norbornene-dicarboximide monomer was prepared according to a previously reported literature procedure.⁶⁹ The procedural details are detailed below. The NMR spectra resembled those reported in the literature for these compounds.

N-Hexyl-exo-Norbornene-5,6-dicarboximide Monomer (HNb)

A 500 mL round bottom flask was charged with toluene (200 mL) and a stir bar. The flask was then charged with cis-5-norbornene-exo-2,3-dicarboxylic anhydride (10.0 g, 61.0 mmol, 1.00 equiv.) and triethylamine (0.726 g, 7.00 mmol, 0.120 equiv.). While stirring and starting to heat, hexylamine (15.3 g, 151 mmol, 2.50 equiv.) was added to the mixture slowly. A reflux condenser was attached to the flask and the mixture was heated at 110 °C for 12 hours. The reaction mixture was then allowed to cool to room temperature before washing the solution

with 0.1 M HCl (100 mL). Following the acid wash, the organic phase was further washed twice with a brine solution (200 mL) and once with DI H₂O (200 mL). The toluene was then removed in vacuo to reveal yellow oil. The wet product was then dissolved in methylene chloride and dried over anhydrous magnesium sulfate. The solution was then filtered, concentrated, and put on the Combiflash autocolumn to run a silica column using methylene chloride until the first compound eluted as shown by the return to baseline of the Combiflash trace. The product was collected and concentrated in vacuo. The product as a clear oil was then sparged with nitrogen overnight to obtain a > 99 percent yield. ¹H NMR (400 MHz, CDCl₃) δ 6.21 (s, 2H), 3.37 (t, 2H), 3.19 (s, 2H), 2.6 (s, 2H), 1.45 (m, 3.15), 1.20 (m, 7.24), 0.79 (m, 3H). ¹³C NMR (101 MHz, CDCl₃) δ 177.53, 137.41, 47.69, 44.79, 42.24, 38.61, 30.97, 27.93, 26.26, 22.11, 13.61. LC-TOF (ESI): Calculated for M+H C₁₅H₂₁N₁O₂, 248.1645: Observed 248.1667.

Methyl 3,4,5-tris(ethoxy)benzoate

A 200 mL schlenk was charged with DMF (130 mL) and a stir bar. The solution was sparged with nitrogen for 30 minutes. Once sufficiently deoxygenated, the flask was charged with potassium carbonate (30.91 g, 0.224 mol, 6 eq.) and methyl gallate (6.86 g, 0.037 mol, 1 eq.) under positive nitrogen. While stirring, 1-bromoethane (24.37 g, 0.224 mol, 6 eq.) was added to the mixture slowly. A reflux condenser was attached to the flask and the mixture was heated at 80 °C for 12 hours. The reaction mixture was then allowed to cool to room temperature and then poured into 2 L of stirring DI water. The white precipitate was then filtered out and dissolved in diethyl ether and dried over MgSO₄. The solution was then filtered and the solvent was removed in vacuo to yield the product as a white solid (8.383g, 0.031 mol, 83.8%). ¹H NMR (400 MHz, CDCl₃) δ 7.27 (s, 2H), 4.12 (m, 7H), 3.89 (s, 3H), 1.44 (t, 7H), 1.36 (t, 3H) [Water singlet from CDCl₃ at 1.55 ppm]. ¹³C NMR (101 MHz, CDCl₃) δ 167.09, 152.67, 142.27,

125.15, 108.25, 69.22, 65.04, 52.31, 15.99, 15.02. LC-TOF (ESI): Calculated for M+ C₁₄H₂₀O₅H, 269.31; Observed 269.1391.

Methyl 3,4,5-tris(ethoxy)benzoic acid

A 500 mL round-bottom flask was charge with methyl 3,4,5-tris(ethoxy)benzoate (8.38 g, 0.031 mol, 1 eq.), potassium hydroxide (14.02 g, 0.250 mol, 8 eq), 100% ethanol (300 mL) and a stir bar. A water-cooled reflux condenser was attached to the flask and the mixture was refluxed at 90 °C for 2 hours. The reaction mixture was allowed to cool to room temperature. The mixture was then acidified to a pH of 1 with 6M HCl (55mL). The acidified solution was then added to 2L of stirring DI water. The white precipitate was then filtered and dissolved in diethyl ether and dried over anhydrous MgSO₄. The solvent was then removed in vacuo to yield Methyl 3,4,5-tris(ethoxy)benzoic acid (6.53 g, 0.026 mol, 77.9%) as a white solid. ¹H NMR (400 MHz, CDCl₃) δ 11.74 (bs, 1H), 7.34 (s, 2H), 4.15 (m, 6H), 1.45 (t, 6H), 1.37 (t, 3H) [Water singlet from CDCl₃ at 1.55 ppm]. ¹³C NMR (101 MHz, CDCl₃) δ 171.35, 152.80, 143.10, 123.69, 108.73, 69.22, 65.04, 16.20, 15.02. LC-TOF (ESI): Calculated for M+ C₁₃H₁₈O₅H, 255.28; Observed 255.1228.

Ethyl Wedge Monomer (EtW)

A 200 mL Schlenk flask with a stir bar was flame-dried under vacuum three times. Once cool, the flask was backfilled with nitrogen then charged with 4-dimethylaminopyridine (0.314 g, 0.00257 mol, 0.1 eq.), N-(hydroxyethyl)-cis-5-norbornene-exo-2,3-dicarboximide (5.85g, 0.0282 mol, 1.1 eq.), Methyl 3,4,5-tris(ethoxy)benzoic acid (6.53g, 0.026 mol, 1 eq.), and methylene chloride (70 mL) under positive nitrogen. The solids were allowed to dissolve. The solution was then cooled in an ice bath and charged with dicyclohexylcarbodiimide (5.827g,

0.0282 mol, 1.1 eq) under positive nitrogen and stirred at 0 °C and allowed to warm to room temperature while stirring over 18 hours. The solution was then filtered and the solid was washed with methylene chloride. The methylene chloride was then removed in vacuo to yield a white solid. This solid was then dissolved in ether and the product was recrystallized out of ether twice to yield white crystals as the pure EtW product (~4.8g, 0.011 mol, 73.5%). ¹H NMR (400 MHz, CDCl₃) δ 7.22 (s, 2H), 6.27 (t, 2H), 4.40 (t, 2H), 4.12 (m, 6H), 3.9 (t, 2H), 3.23 (s, 2H), 2.70 (s, 2H), 1.45 (t, 7H), 1.35 (t, 3H), 1.25 (d, 1H) [Water singlet from CDCl₃ at 1.55 ppm]. ¹³C NMR (101 MHz, CDCl₃) δ 177.75, 166.11, 152.82, 142.30, 137.99, 124.18, 108.45, 69.01, 65.04, 61.84, 48.13, 45.42, 42.99, 37.84, 15.99, 15.02. LC-TOF (ESI): Calculated for M+Na C₂₄H₂₉NO₇Na, 466.50; Observed 466.1831.

Methyl 3,4,5-tris(dodecyloxy)benzoate

A 200 mL schlenk was charged with DMF (100 mL) and a stir bar. The solution was sparged with nitrogen for 30 minutes. Once sufficiently deoxygenated, the flask was charge with potassium carbonate (12.03 g, 0.087 mol, 6 eq.) and methyl gallate (2.67 g, 0.015 mol, 1 eq.) under positive nitrogen. While stirring, 1-bromododecane (21.70 g, 0.087 mol, 6 eq.) was added to the mixture slowly. A reflux condenser was attached to the flask and the mixture was heated at 80 °C for 12 hours. The reaction mixture was allowed to cool to room temperature and diluted with DI water. The solution was then washed with diethyl ether twice. Then, the organic phase was washed with DI water and a small amount of brine solution. The organic phase was then run through an alumina plug and dried over anhydrous MgSO₄. The solution was then filtered and the solvent was removed in vacuo. The white solid was kept under vacuum overnight in an attempt to fully dry the product (13.98 g, 0.020 mol). The product yielded was not completely

pure (see DDW synthesis) but brought forward regardless. ^1H NMR (400 MHz, CDCl_3) δ 7.24 (s, 2H), 4.01 (m, 6H), 3.89 (s, 3H), 1.78 (m, 7H), 1.47 (m, 7H), 1.27 (s, 54H), 0.88 (t, 9H) [Water singlet from CDCl_3 at 1.55 ppm]. ^{13}C NMR (101 MHz, CDCl_3) δ 166.91, 152.88, 142.55, 124.95, 107.97, 73.76, 69.50, 52.31, 32.31, 30.50, 29.8 (m), 29.56 (m), 26.23, 22.87, 14.29. LC-TOF (ESI): Calculated for $\text{M}+\text{Na}$ $\text{C}_{44}\text{H}_{80}\text{O}_5\text{Na}$, 689.12; Observed 711.5911.

Methyl 3,4,5-tris(dodecyloxy)benzoic acid

A 500 mL round-bottom flask was charged with Methyl 3,4,5-tris(dodecyloxy)benzoate (13.9818 g, 0.020 mol, 1 eq.), potassium hydroxide (9.11 g, 0.162 mol, 8 eq.), 100% ethanol (200 mL) and a stir bar. A water-cooled reflux condenser was attached to the flask and the mixture was refluxed at 90 °C for 2 hours. The reaction mixture was allowed to cool to room temperature. The mixture was then acidified to a pH of 1 with 6M HCl (50mL). The acidified solution was then added to 2L of stirring DI water. The white precipitate was then filtered and dissolved in diethyl ether and dried over anhydrous MgSO_4 . The solvent was then removed in vacuo and the solid was kept under vacuum overnight to yield Methyl 3,4,5-tris(dodecyloxy)benzoic acid (12.21 g, 0.018 mol, 87.3%) as a white solid. ^1H NMR (400 MHz, CDCl_3) δ 7.31 (s, 2H), 4.12 (m, 1H), 4.03 (m, 6H), 1.78 (m, 7H), 1.47 (m, 7H), 1.27 (s, 56H), 0.88 (t, 10H) [Water singlet from CDCl_3 around 2.0 ppm]. ^{13}C NMR (101 MHz, CDCl_3) δ 152.94, 108.76, 73.90, 69.52, 32.22, 30.76, 29.80 (m), 29.50 (m), 26.23 (m), 22.85, 14.23. LC-TOF (ESI): Calculated for $\text{M}+\text{NH}_4$ $\text{C}_{43}\text{H}_{78}\text{O}_5\text{NH}_4$, 693.129; Observed 692.6204.

Dodecyl Wedge Monomer (DDW)

A 200 mL Schlenk flask with a stir bar was flame-dried under vacuum three times. Once cool, the flask was backfilled with nitrogen then charged with 4-dimethylaminopyridine (0.221

g, 0.0018 mol, 0.1 eq.), N-(hydroxyethyl)-cis-5-norbornene-exo-2,3-dicarboximide (4.123g, 0.0199 mol, 1.1 eq.), methyl 3,4,5-tris(dodecyloxy)benzoic acid (12.21g, 0.0181 mol, 1 eq.), and methylene chloride (90 mL) under positive nitrogen. The solids were allowed to dissolve. The solution was then cooled in an ice bath and charged with dicyclohexylcarbodiimide (4.105g, 0.0199 mol, 1.1 eq) under positive nitrogen and stirred at 0 °C and allowed to warm to room temperature while stirring over 18 hours. The solution was then filtered and the solid was washed with methylene chloride. The methylene chloride was then removed in vacuo to yield a white solid. This solid was then run on a silica column using a 9 Hexanes: 1 Ethyl Acetate mixture. The first analyte to elute is an ester impurity and the second analyte to elute is the pure monomer. The monomer in solution was then dried in vacuo to yield a white solid (~5g, 0.00578 mol, 41.0%). ¹H NMR (400 MHz, CDCl₃) δ 7.20 (s, 2H), 6.26 (s, 2H), 4.40 (t, 2H), 4.01 (t, 6H), 3.91 (t, 2H), 3.23 (s, 2H), 2.70 (s, 2H), 1.79 (m, 6H), 1.48 (m, 8H) 1.27 (s, 51H), 0.88 (t, 9H) [Water singlet from CDCl₃ at 1.55 ppm]. ¹³C NMR (101 MHz, CDCl₃) δ 177.85, 166.12, 153.08, 142.46, 137.97, 124.18, 108.02, 73.73, 69.09, 61.80, 48.01, 45.42, 42.99, 37.60, 32.00, 30.50, 29.82(m), 29.45(m), 26.26, 22.85, 14.31. LC-TOF (ESI): Calculated for M+NH₄ C₅₄H₈₉NO₇NH₄, 882.349; Observed 881.7011.

Polymer Synthesis

Poly(HNb) Molecular Weight Series

In a nitrogen-filled glovebox, a 20 mL vial was charged with a stir bar, 0.5 g (0.002 mol) of HNb monomer and 5 mL of THF. With rapid stirring, the appropriate amount of G3 catalyst completely dissolved in THF was quickly added via syringe. After one hour, the polymerization was quenched by the addition of 1 mL of ethyl vinyl ether. The polymer was precipitated out into 15 mL of methanol and allowed to stir overnight, after which the polymer was isolated, washed

with excess methanol, and dried under reduced pressure at 50 °C to a constant weight. Yield was near quantitative by mass.

Isolated and representative poly(HNb) ^1H NMR (400 MHz, CDCl_3): δ 5.75 (bs), 5.5 (m), 3.42 (bs), 3.25 (bs), 3.01 (m), 2.69 (bd), 2.13 (m), 1.55 (s), 1.27 (s), 0.87 (s) [Water singlet from CDCl_3 at 1.55 ppm].

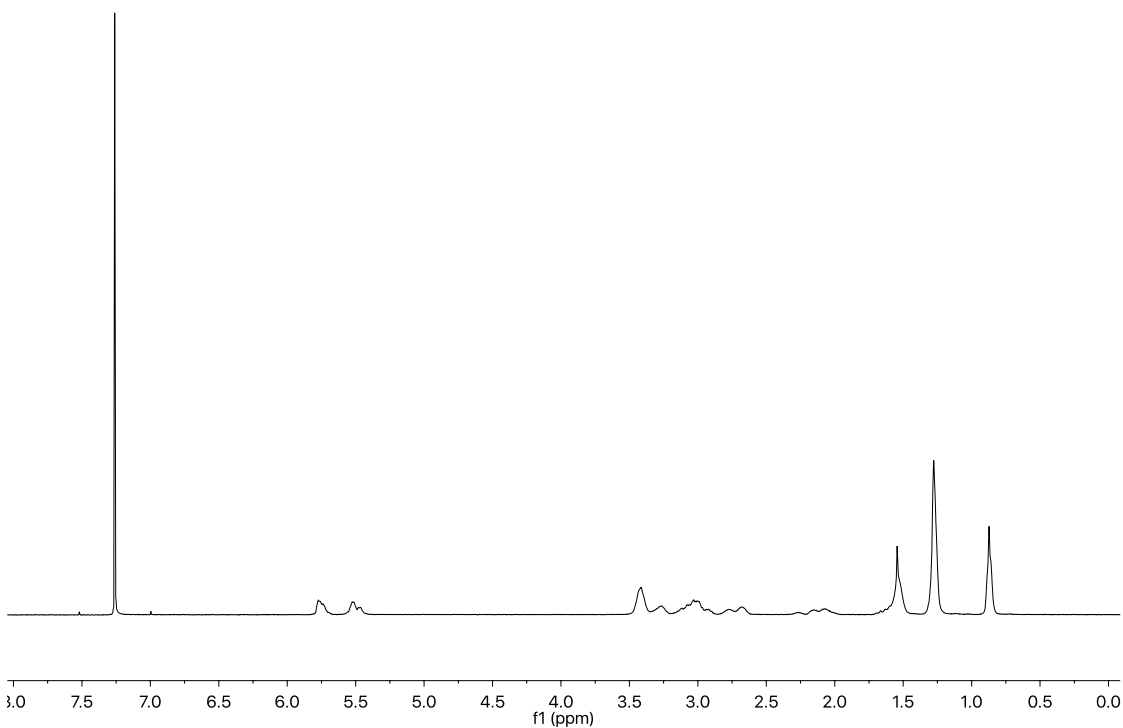


Figure 4.11. ^1H NMR spectra of p(HNb)-DP386 in CDCl_3 .

Poly(EtW) Molecular Weight Series

In a nitrogen-filled glovebox, a 20 mL vial was charged with a stir bar, 0.5 g (0.002 mol) of EtW monomer and 5 mL of THF. With rapid stirring, the appropriate amount of G3 catalyst completely dissolved in THF was quickly added via syringe. After one hour, the polymerization

was quenched by the addition of 1 mL of ethyl vinyl ether. The polymer was precipitated out into 15 mL of methanol and allowed to stir overnight, after which the polymer was isolated, washed with excess methanol, and dried under reduced pressure at 50 °C to a constant weight. Yield was near quantitative by mass.

Isolated and representative poly(EtW) ^1H NMR (400 MHz, CDCl_3): δ 7.22 (d), 5.50 (m), 5.06 (m), 4.4 (bs), 4.1 (d), 3.85 (bs), 2.95 (bs), 2.59 (bs), 2.0 (bs), 1.41 (bt), 1.33 (t), 1.25 (s) [Water singlet from CDCl_3 at 1.55 ppm].

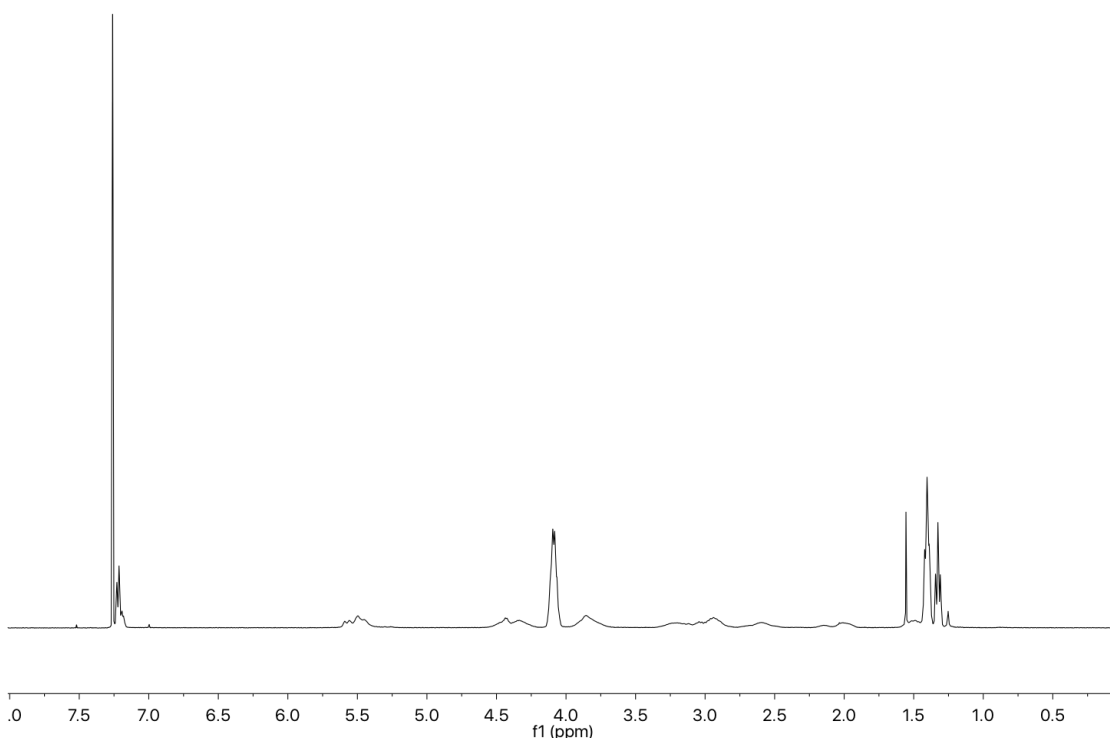


Figure 4.12. ^1H NMR of p(EtW)-DP360 in CDCl_3 .

Poly(DDW) Molecular Weight Series

In a nitrogen-filled glovebox, a 20 mL vial was charged with a stir bar, 0.5 g (0.0006 mol) of DDW monomer and 5 mL of THF. With rapid stirring, the appropriate amount of G3 catalyst completely dissolved in THF was quickly added via syringe. After one hour, the

polymerization was quenched by the addition of 1 mL of ethyl vinyl ether and diluted with DCM. The solution was then run through an alumina plug and concentrated in vacuo. The polymer was then precipitated out into 15 mL of methanol and allowed to stir overnight, after which the polymer was isolated, washed with excess methanol, and dried under reduced pressure at 50 °C to a constant weight. Yield was near quantitative by mass, some loss occurred in transfer.

Isolated and representative poly(DDW) NMR ^1H NMR (400 MHz, CDCl_3): δ 7.21(d), 5.5(bs), 4.37(bs), 3.98 (bt), 3.84 (bs), 3.00 (bs), 1.78 (m), 1.45 (bs), 1.29 (s), 0.88 (t) [Water singlet from CDCl_3 at 1.55 ppm].

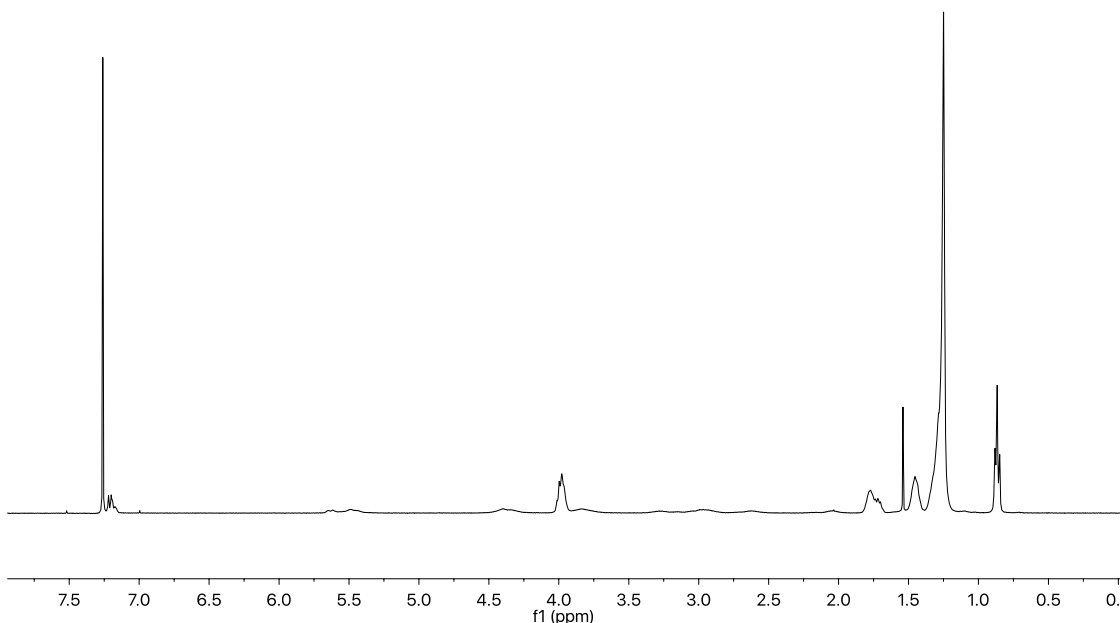


Figure 4.13. ^1H NMR spectra of p(DDW)-DP456 in CDCl_3 .

*Polymer Characterization via Gel Permeation Chromatography – Multi Angle Light Scattering
Traces (GPC-MALS)*

Table 4.2. GPC analysis data of poly(HNb) MW series.

Polymer Sample	GPC M_w (kg/mol)	GPC M_n (kg/mol)	Degree of Polymerization from M_n	Dispersity (M_w/M_n)
p(HNb)-DP35	8.64	8.56	35	1.01
p(HNb)-DP39	9.70	9.65	39	1.01
p(HNb)-DP105	26.1	25.9	105	1.01
p(HNb)-DP187	46.7	46.2	187	1.01
p(HNb)-DP386	97.0	95.5	386	1.02
p(HNb)-DP429	1.20×10^2	1.06×10^2	429	1.13
p(HNb)-DP912	2.31×10^2	2.26×10^2	912	1.02
p(HNb)-DP1568	3.96×10^2	3.88×10^2	1568	1.02
p(HNb)-DP2296	5.86×10^2	5.68×10^2	2296	1.03
p(HNb)-DP3556	9.22×10^2	8.80×10^2	3556	1.05
p(HNb)-DP4605	1.25×10^3	1.14×10^3	4605	1.09

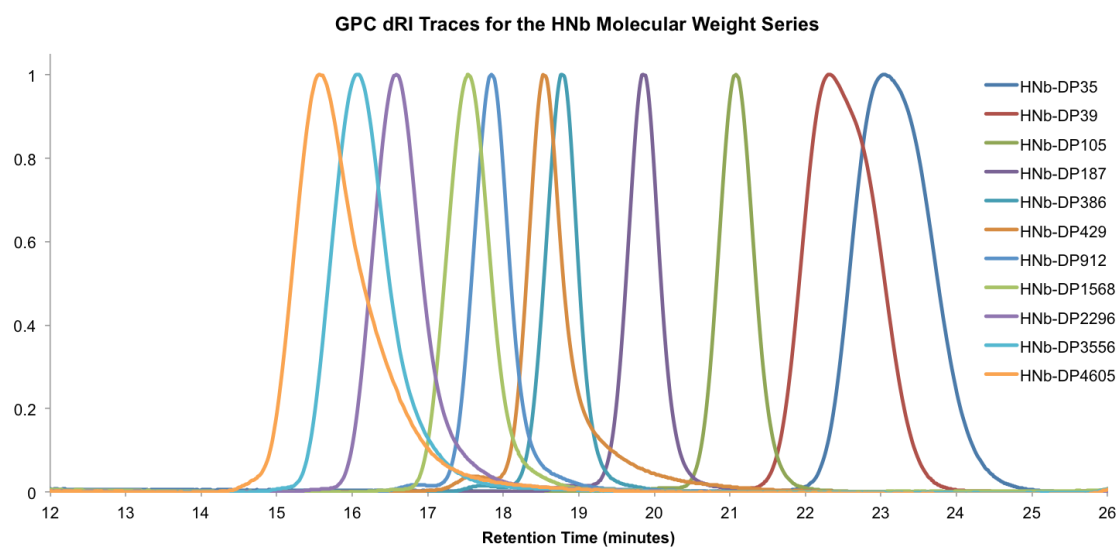


Figure 4.14. Normalized Scaling of GPC RI detector traces for p(HNb) MW series.

Table 4.3. GPC analysis data of poly(EtW) MW series.

Polymer Sample	GPC M_w (kg/mol)	GPC M_n (kg/mol)	Degree of Polymerization from M_n	Dispersity (M_w/M_n)
p(EtW)-DP9	4.29	4.10	9	1.05
p(EtW)-DP26	11.8	11.7	26	1.01
p(EtW)-DP34	15.3	14.8	34	1.03
p(EtW)-DP56	24.9	24.9	56	1.01
p(EtW)-DP84	37.4	37.3	84	1.01
p(EtW)-DP120	53.7	53.3	120	1.01
p(EtW)-DP360	1.63×10^2	1.60×10^2	360	1.02
p(EtW)-DP943	4.22×10^2	4.18×10^2	943	1.01
p(EtW)-DP1076	4.91×10^2	4.77×10^2	1,076	1.03
p(EtW)-DP1478	6.89×10^2	6.56×10^2	1,478	1.05
p(EtW)-DP1788	8.61×10^2	7.93×10^2	1,788	1.09
p(EtW)-DP1929	8.66×10^2	8.56×10^2	1,929	1.01
p(EtW)-DP2160	9.74×10^2	9.58×10^2	2,160	1.02
p(EtW)-DP3321	1.52×10^3	1.47×10^3	3,321	1.03
p(EtW)-DP4194	2.37×10^3	1.86×10^3	4,194	1.27
p(EtW)-DP8435	4.08×10^3	3.74×10^3	8,435	1.11
p(EtW)-DP9905	5.27×10^3	4.39×10^3	9,905	1.20

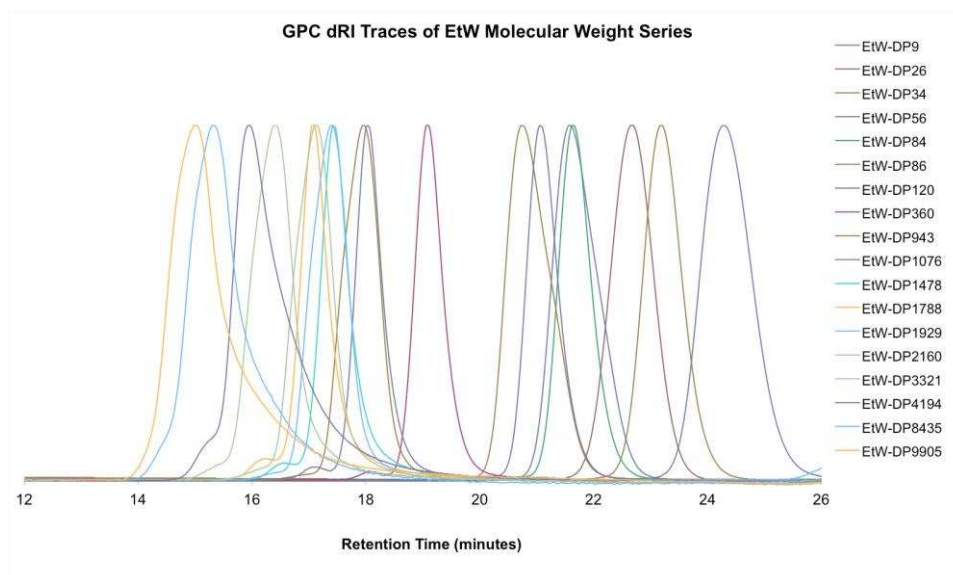


Figure 4.15. Normalized Scaling of GPC RI detector traces for p(EtW) MW series.

Table 4.4. GPC analysis data of poly(DDW) MW series.

Polymer Sample	GPC M_w (kg/mol)	GPC M_n (kg/mol)	Degree of Polymerization from M_n	Dispersity (M_w/M_n)
p(DDW)-DP15	13.2	12.9	15	1.02
p(DDW)-DP24	21.4	21.0	24	1.02
p(DDW)-DP55	47.9	47.5	55	1.01
p(DDW)-DP98	84.8	84.6	98	1.01
p(DDW)-DP456	3.99×10^2	3.94×10^2	456	1.01
p(DDW)-DP521	4.65×10^2	4.50×10^2	521	1.03
p(DDW)-DP822	7.13×10^2	7.10×10^2	822	1.01
p(DDW)-DP930	8.58×10^2	8.03×10^2	930	1.07
p(DDW)-DP1030	9.29×10^2	8.90×10^2	1,030	1.04
p(DDW)-DP1631	1.42×10^3	1.41×10^3	1,631	1.01

p(DDW)-DP6944	6.42×10^3	6.00×10^3	6,944	1.07
---------------	--------------------	--------------------	-------	------

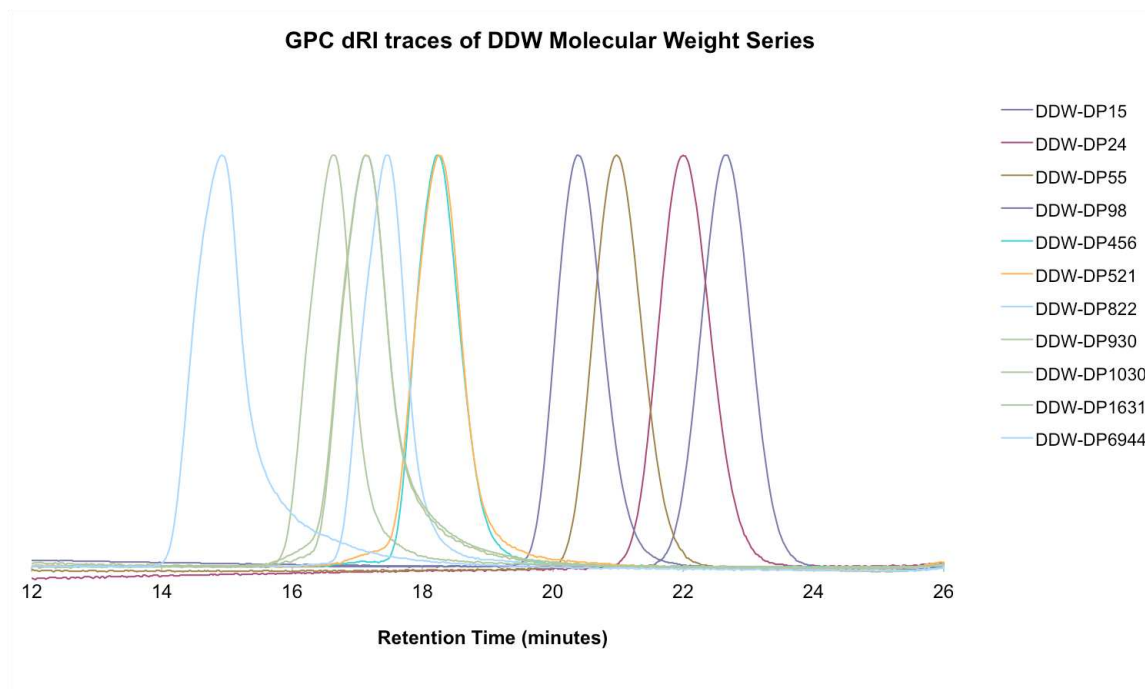


Figure 4.16. Normalized Scaling of GPC RI detector traces for p(DDW) MW series.

Characterization of Molecular Conformation from GPC-MALS

Table 4.5. Poly(HNb) MW series data obtained from GPC-MALS for the M_n and the radius of gyration measured with static light scattering (R_z) as long as the polymer was larger than 10 nm in diameter in THF.

Polymer Sample	GPC M_n (kg/mol)	$\log M_n$	R_z from GPC-MALS (nm)	Log R_z
p(HNb)-DP386	95.5	4.98	15	1.2
p(HNb)-DP429	1.06×10^2	5.03	16	1.2
p(HNb)-DP912	2.26×10^2	5.35	22	1.3
p(HNb)-DP1568	3.88×10^2	5.59	29	1.5
p(HNb)-DP2296	5.68×10^2	5.75	41	1.6
p(HNb)-DP3556	8.80×10^2	5.94	56	1.7
p(HNb)-DP4605	1.14×10^3	6.06	74	1.9

Table 4.6. Poly(EtW) MW series data obtained from GPC-MALS for the M_n and the Radius of gyration measured with static light scattering (R_z) as long as the polymer was larger than 10 nm in diameter in THF.

Polymer Sample	GPC M_n (kg/mol)	log M_n	R_z from GPC MALS (nm)	Log R_z
p(EtW)-DP360	1.60×10^2	5.20	13	1.1
p(EtW)-DP943	4.18×10^2	5.62	22	1.3
p(EtW)-DP1076	4.77×10^2	5.68	23	1.4
p(EtW)-DP1478	6.56×10^2	5.82	31	1.5
p(EtW)-DP1788	7.93×10^2	5.90	38	1.6
p(EtW)-DP1929	8.56×10^2	5.93	28	1.4
p(EtW)-DP2160	9.58×10^2	5.98	33	1.5
p(EtW)-DP3321	1.47×10^3	6.17	48	1.7
p(EtW)-DP4194	1.86×10^3	6.27	69	1.8
p(EtW)-DP8435	3.74×10^3	6.57	98	2.0
p(EtW)-DP9905	4.39×10^3	6.64	120	2.1

Table 4.7. Poly(DDW) MW Series data obtained from GPC-MALS for the M_n and R_z values as long as the diameter was larger than 10 nm in THF.

Polymer Sample	GPC M_n (g/mol)	log M_n	R_z from GPC MALS (nm)	Log R_z
p(DDW)-DP456	3.94×10^2	5.60	18	1.3
p(DDW)-DP521	4.50×10^2	5.65	19	1.3
p(DDW)-DP822	7.10×10^2	5.85	27	1.4
p(DDW)-DP930	8.03×10^2	5.91	33	1.5
p(DDW)-DP1030	8.90×10^2	5.95	32	1.5
p(DDW)-DP1631	1.41×10^3	6.15	41	1.6
p(DDW)-DP6944	6.00×10^3	6.78	120	2.1

Fractal Dimension Analysis

Working from Flory's universal power law,

$$R \sim N^{\nu}$$

where R = polymer size, N = number of monomers, ν = the scaling exponent, and the fact that the fractal dimension, D' , is equal to the inverse of the scaling exponent we were able to determine the wedge-type polymer scaling exponent as well as the fractal dimension of the wedge-type polymers shown.

From Tables S3 and S4 of polymer R_z vs. polymer M_n , we get the relation of

$$R_z \sim M_n^{\nu}$$
$$M_n = \text{Monomer MW} * N$$

So, by substituting equations, the resulting relation follows

$$R_z \sim (\text{Monomer MW} * N)^{\nu} \sim (\text{Monomer MW})^{\nu} (N)^{\nu}$$

Therefore, the prefactor term that includes the monomer MW can be disregarded and we are left with our scaling factor of 0.62 for the p(HNb) MW series, 0.68 for the p(EtW) MW series, and 0.69 for the p(DDW) MW series in the solvent, THF. This also means that the fractal dimension, D' , for the p(HNb), p(EtW), and the p(DDW) respectively are 1.61, 1.47, and 1.45 which are in between a rigid rod D' of 1 than a random self-avoiding walk polymer D' of 1.67.

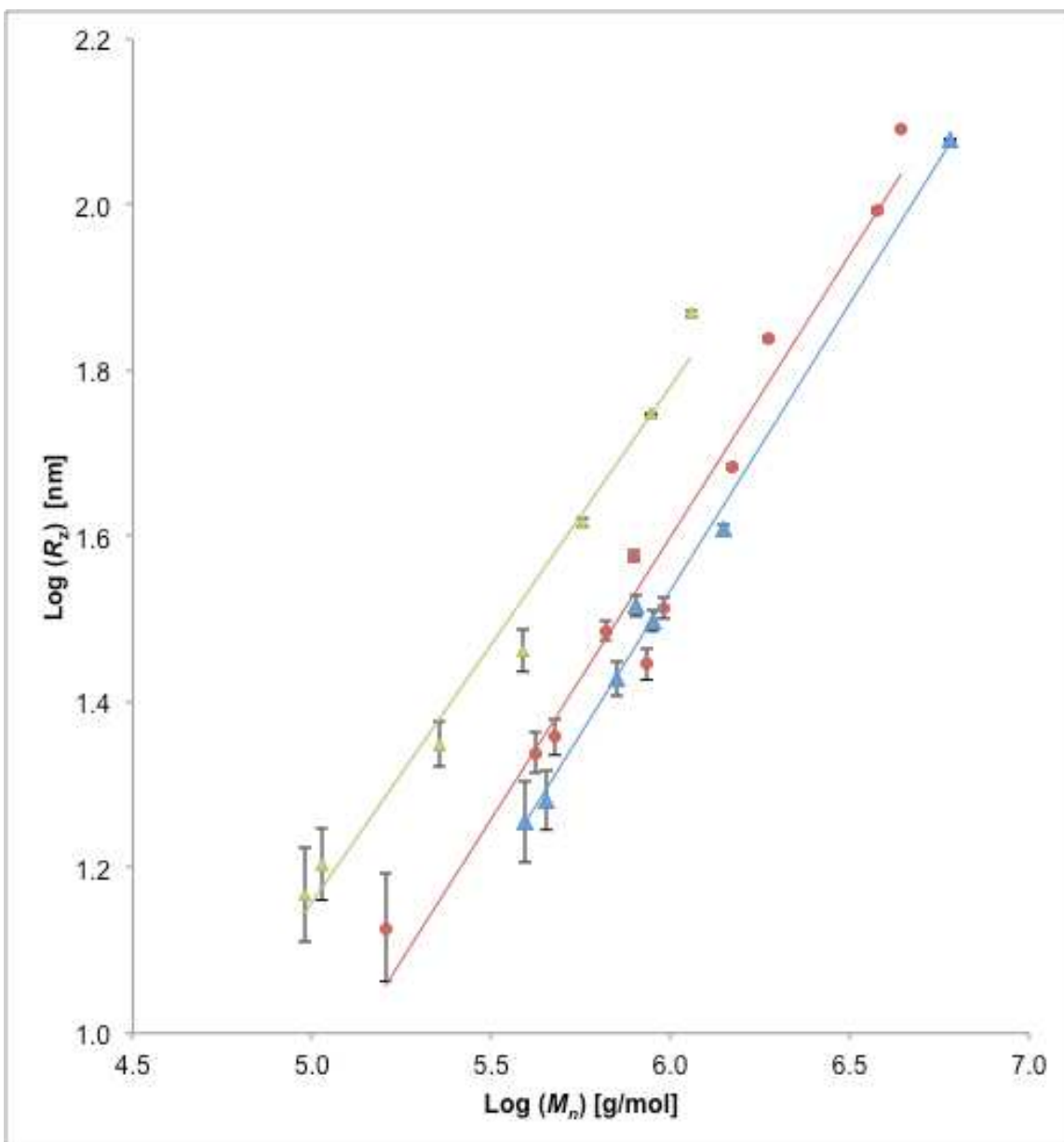


Figure 4.17. Double logarithmic plot of the radius of gyration (R_z) vs. the number-average molecular weight (M_n) of the p(HNb) series (green squares), the p(EtW) series (red circles), and the p(DDW) series (blue triangles).

Table 4.8. Contour and Persistence lengths estimated from the R_z measurements for the p(HNb) MW series. Monomer size (b_0) was estimated to be 0.485 nm assuming an equal amount of cis-/trans- norbornene units. Monomer molecular weight (M_0) is 247.34 g/mol.

Polymer Sample	M_w [kg/mol]	Contour Length (L_w) [nm]	R_z [nm]	Persistence Length (l_p) [nm]	l_p Error [\pm nm]
p(HNb)-DP386	97.0	190	14.7	1.14	0.300
p(HNb)-DP429	1.20×10^2	236	16.0	1.09	0.218
p(HNb)-DP912	2.31×10^2	452	22.3	1.10	0.137
p(HNb)-DP1568	3.96×10^2	776	29.0	1.09	0.130
p(HNb)-DP2296	5.86×10^2	1.15×10^3	41.4	1.50	0.033
p(HNb)-DP3556	9.22×10^2	1.81×10^3	55.9	1.73	0.007
p(HNb)-DP4605	1.25×10^3	2.44×10^3	73.9	2.24	0.031

Table 4.9. Contour and Persistence lengths estimated from the R_z measurements for the p(EtW) MW series. Monomer size (b_0) was estimated to be 0.485 nm assuming an equal amount of cis-/trans- norbornene units. Monomer molecular weight (M_0) is 443.5 g/mol.)

Polymer Sample	M_w [kg/mol]	Contour Length (L_w) [nm]	R_z [nm]	Persistence Length (l_p) [nm]	l_p Error [\pm nm]
p(EtW)-DP360	1.63×10^2	178	13.4	1.01	0.302
p(EtW)-DP943	4.22×10^2	461	21.8	1.03	0.116
p(EtW)-DP1076	4.91×10^2	537	22.8	0.970	0.099
p(EtW)-DP1478	6.89×10^2	753	30.6	1.25	0.070
p(EtW)-DP1788	8.61×10^2	941	37.7	1.51	0.045
p(EtW)-DP1929	8.66×10^2	947	27.9	0.823	0.072
p(EtW)-DP2160	9.74×10^2	107×10^3	32.6	0.999	0.058
p(EtW)-DP3321	1.52×10^3	1.66×10^3	48.3	1.41	0.020
p(EtW)-DP4194	2.37×10^3	2.59×10^3	69.0	1.84	0.029
p(EtW)-DP8435	4.08×10^3	4.46×10^3	98.4	2.17	0.026
p(EtW)-DP9905	5.27×10^3	5.77×10^3	123	2.64	0.011

Table 4.10. Contour and Persistence lengths estimated from the R_z measurements for the p(DDW) MW series. Monomer size (b_0) was estimated to be 0.485 nm assuming an equal amount of cis-/trans- norbornene units. Monomer molecular weight (M_0) is 864.34 g/mol.

Polymer Sample	M_w [kg/mol]	Contour Length (L_w) [nm]	R_z [nm]	Persistence Length (l_p) [nm]	l_p Error [\pm nm]
p(DDW)-DP456	3.99×10^2	224	18.0	1.46	0.329
p(DDW)-DP521	4.65×10^2	261	19.1	1.41	0.231
p(DDW)-DP822	7.13×10^2	400	26.8	1.80	0.177
p(DDW)-DP930	8.58×10^2	481	32.8	2.25	0.130
p(DDW)-DP1030	9.29×10^2	521	31.5	1.91	0.115
p(DDW)-DP1631	1.42×10^3	797	40.6	2.07	0.058
p(DDW)-DP6944	6.42×10^3	3.60×10^3	120	4.00	0.008

Thermal Properties

Thermal Gravimetric Analysis (TGA)

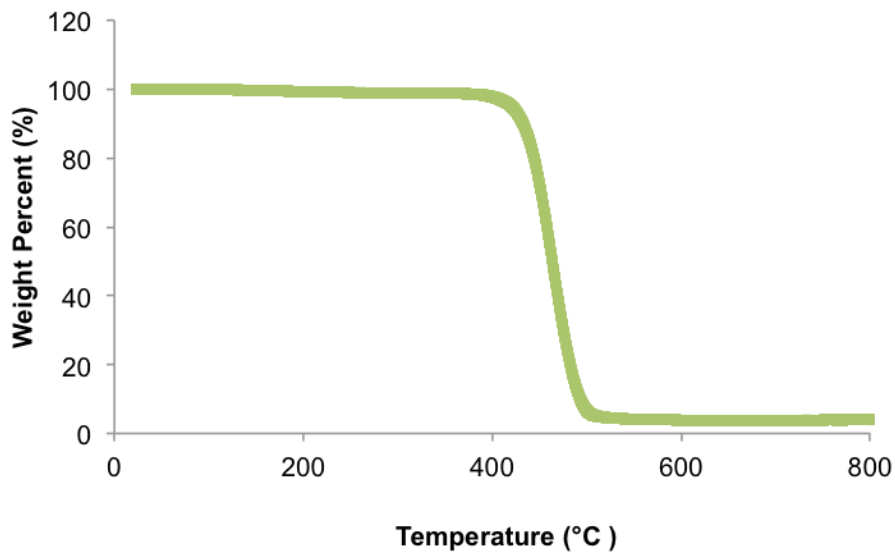


Figure 4.18. TGA plot of p(HNb)-DP4605. Decomposition temperature at 5% weight loss is 420 °C.

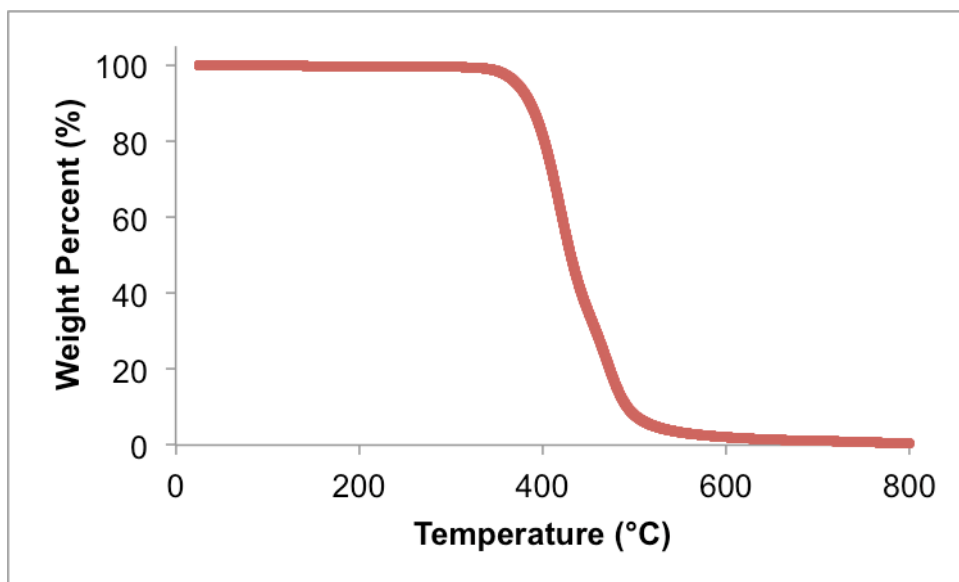


Figure 4.19. TGA plot of p(EtW)-DP9905. Decomposition temperature at 5% weight loss is 373 °C.

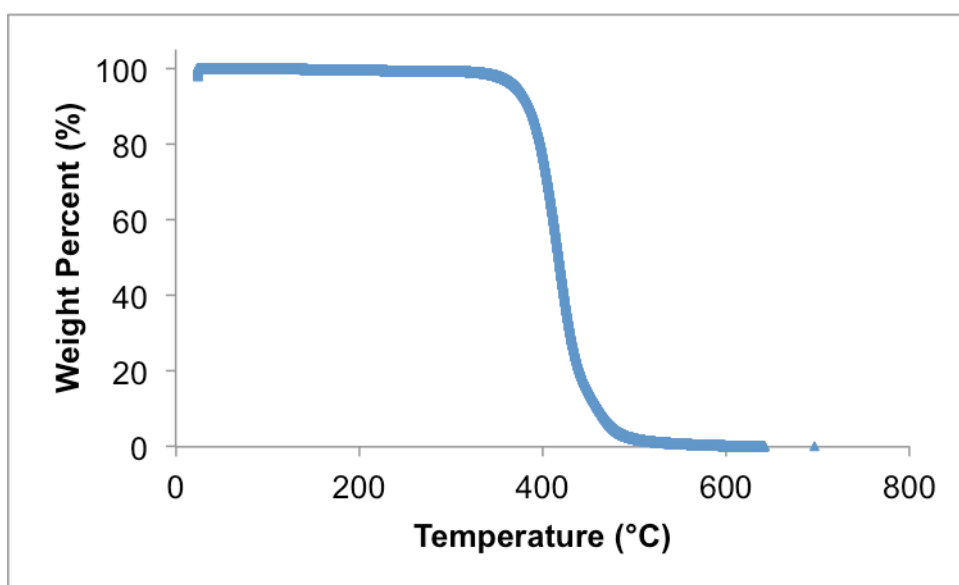


Figure 4.20. TGA plot of p(DDW)-DP6944. Decomposition temperature at 5% weight loss is 372 °C.

Differential Scanning Calorimetry (DSC)

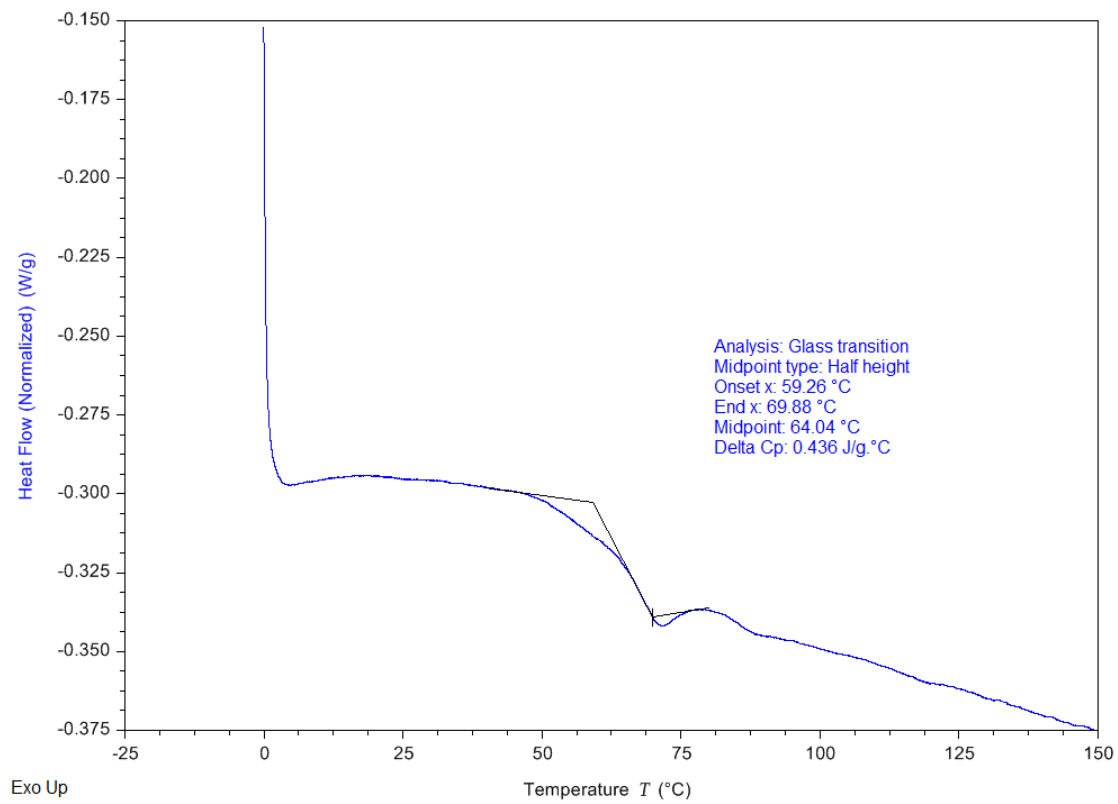


Figure 4.21. Isolated DSC 2nd heat trace for p(HNb)-DP35.

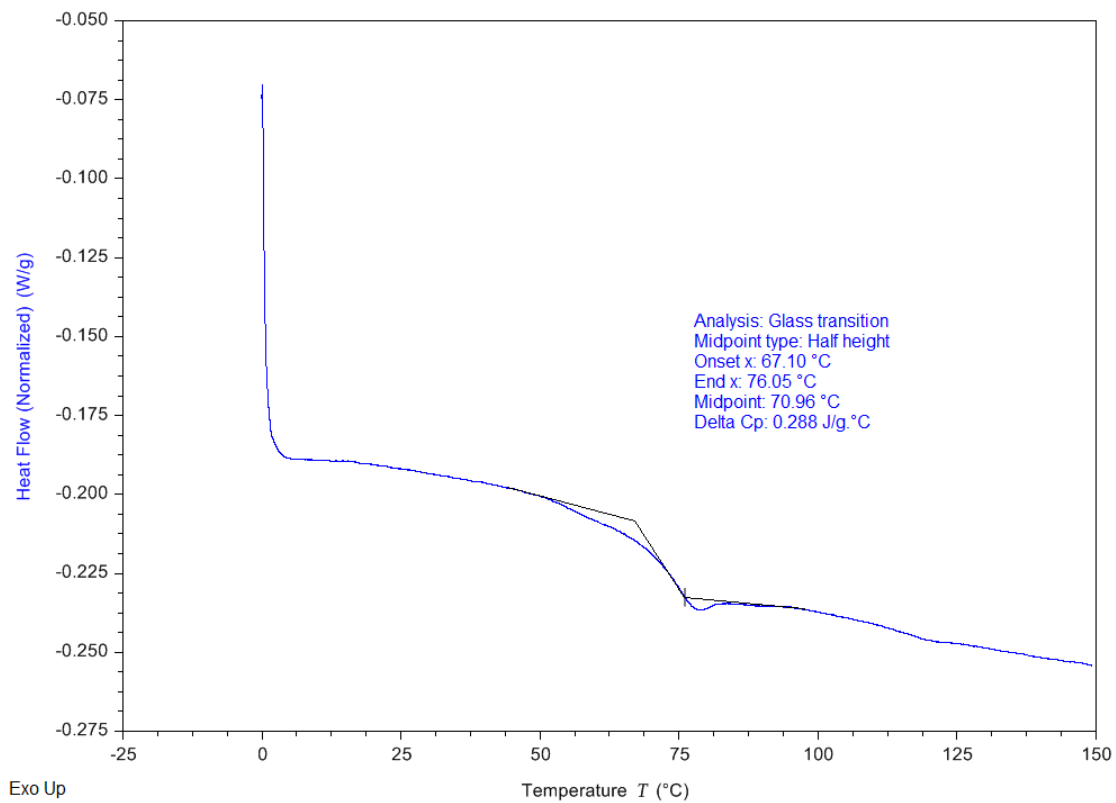


Figure 4.22. Isolated DSC 2nd heat trace for p(HNb)-DP39.

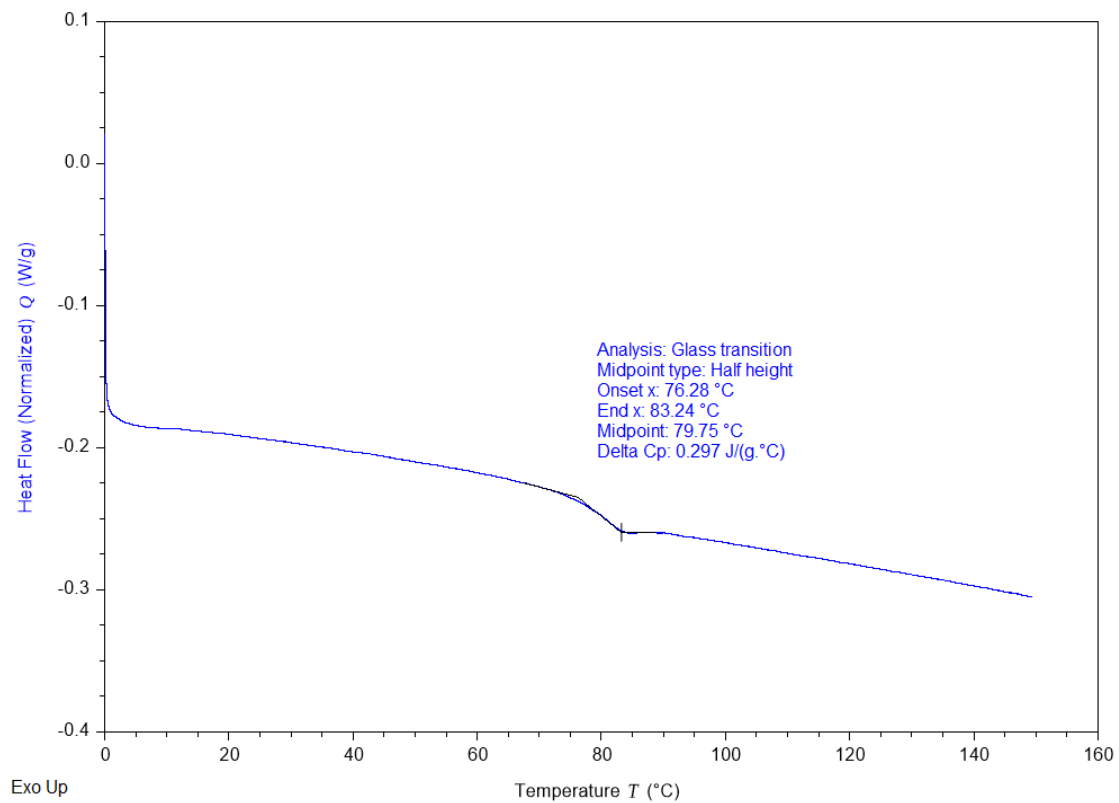


Figure 4.23. Isolated DSC 2nd heat trace for p(HNb)-DP105.

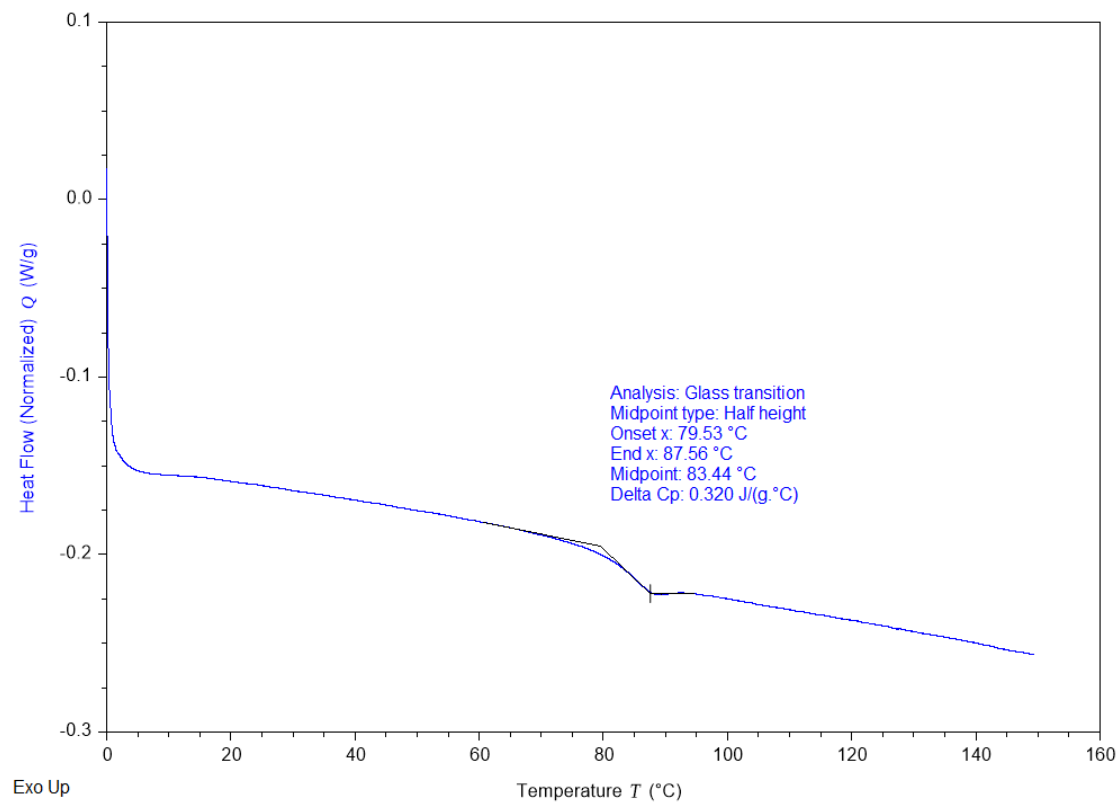


Figure 4.24. Isolated DSC 2nd heat trace for p(HNb)-DP912.

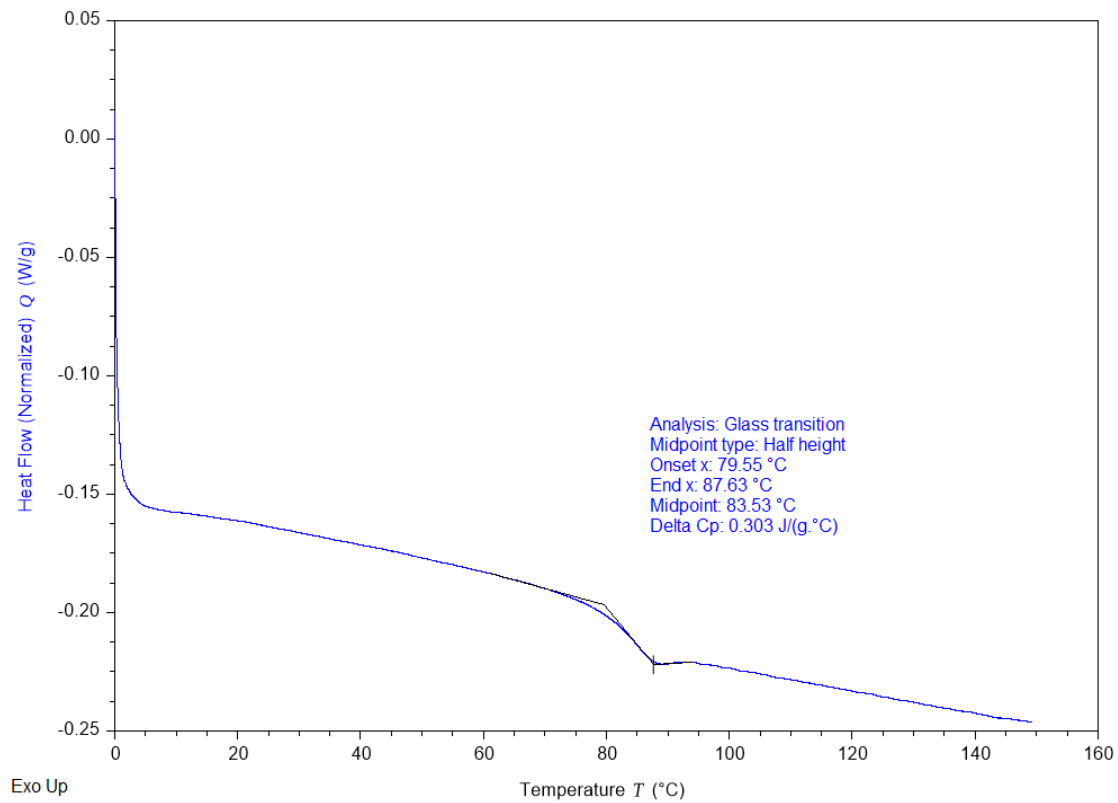


Figure 4.25. Isolated DSC 2nd heat trace for p(HNb)-DP4605.

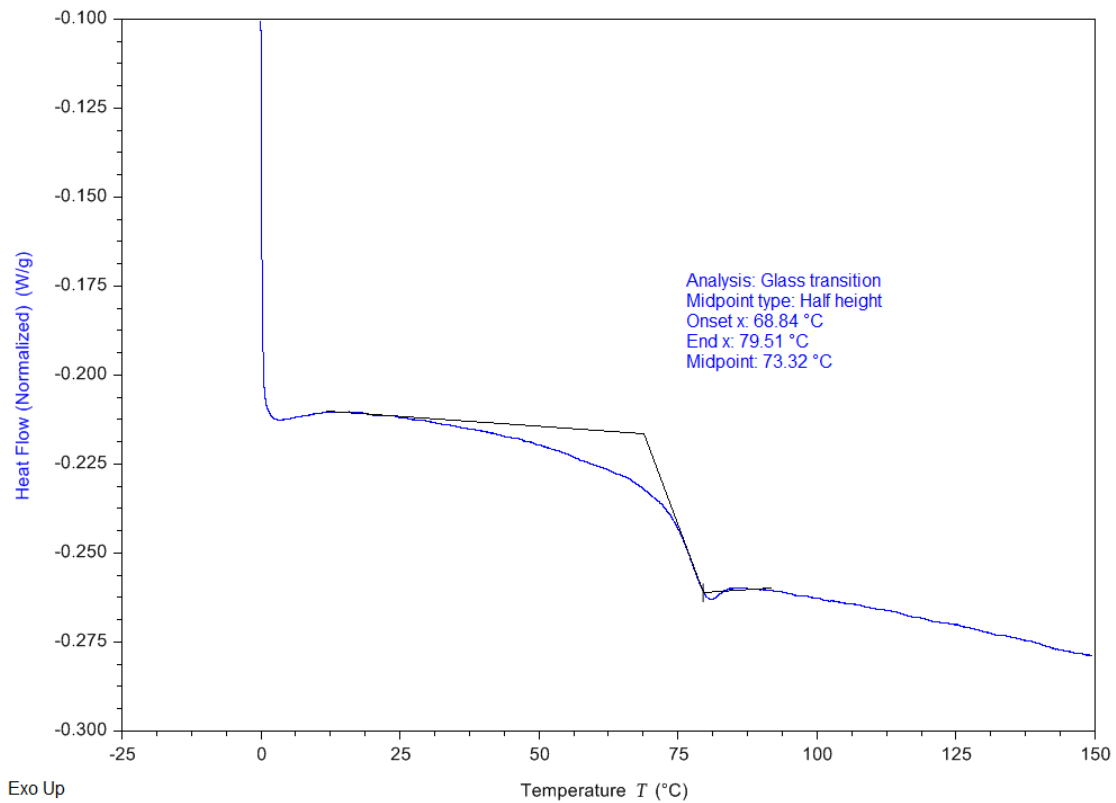


Figure 4.26. Isolated DSC 2nd heat trace for p(EtW)-DP9.

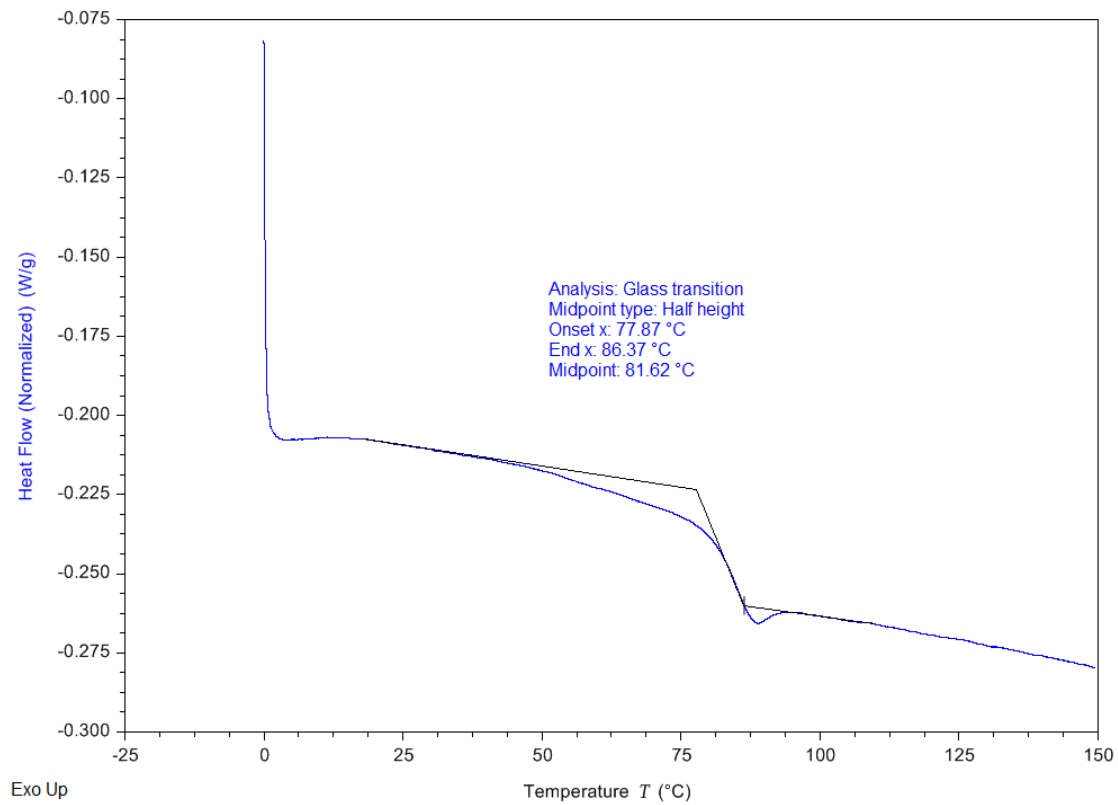


Figure 4.27. Isolated DSC trace of 2nd heat for p(EtW)-DP34

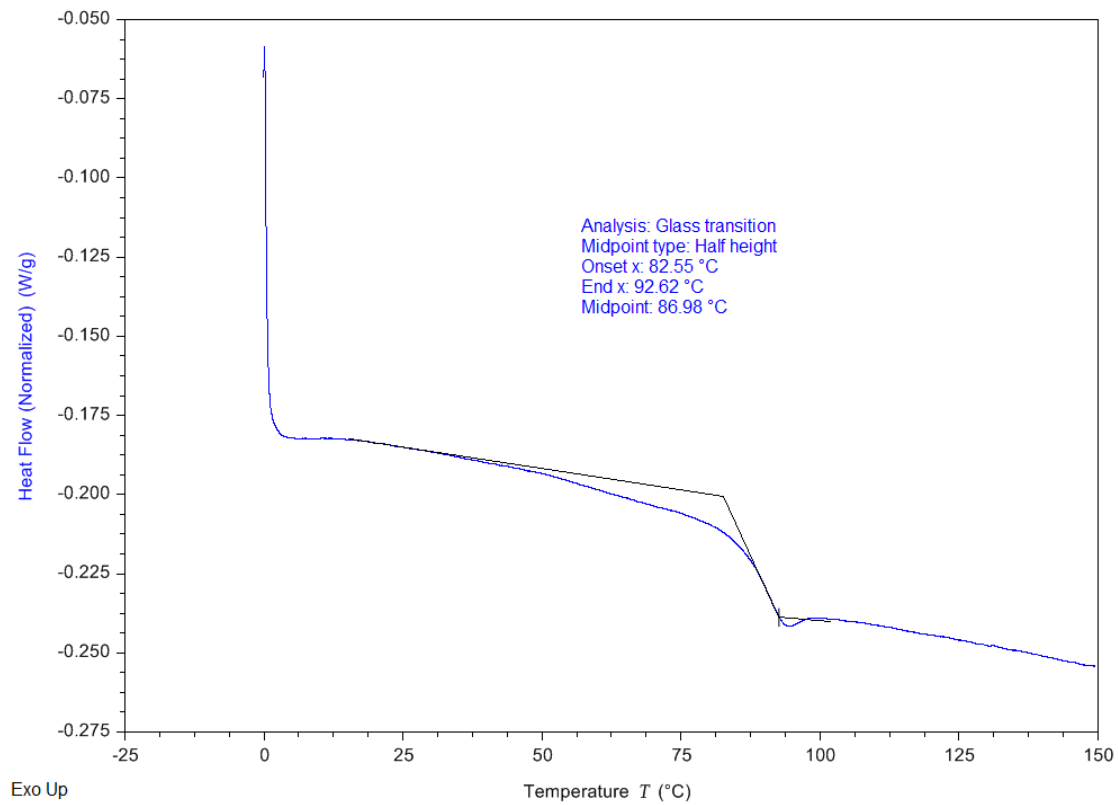


Figure 4.28. Isolated DSC trace of 2nd heat for p(EtW)-DP1929.

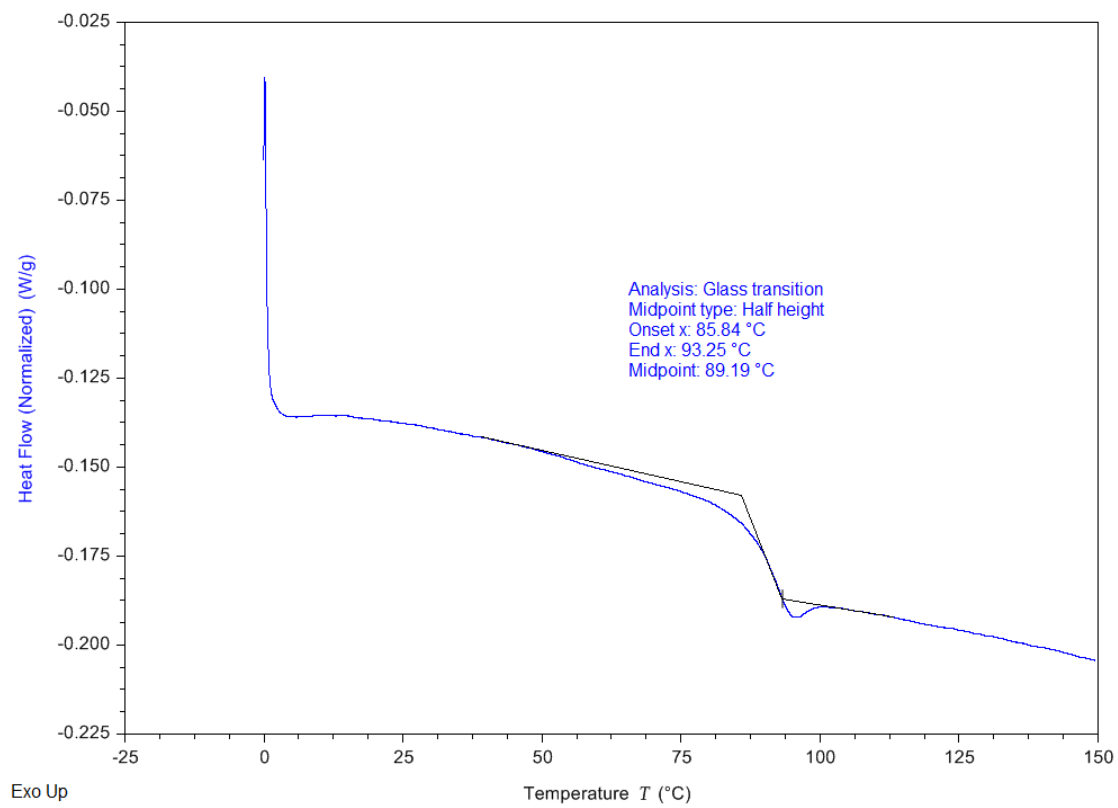


Figure 4.29. DSC trace of 2nd heat for p(EtW)-DP9905.

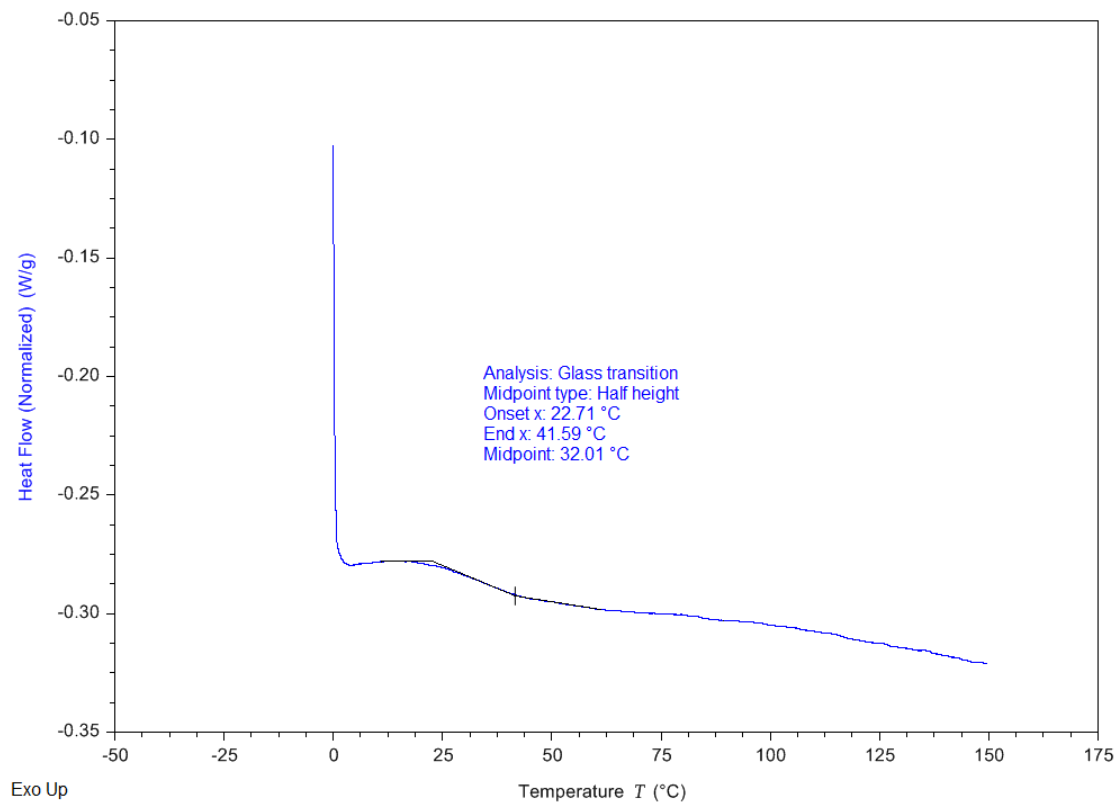


Figure 4.30. Isolated DSC trace of 2nd heat for p(DDW)-DP15.

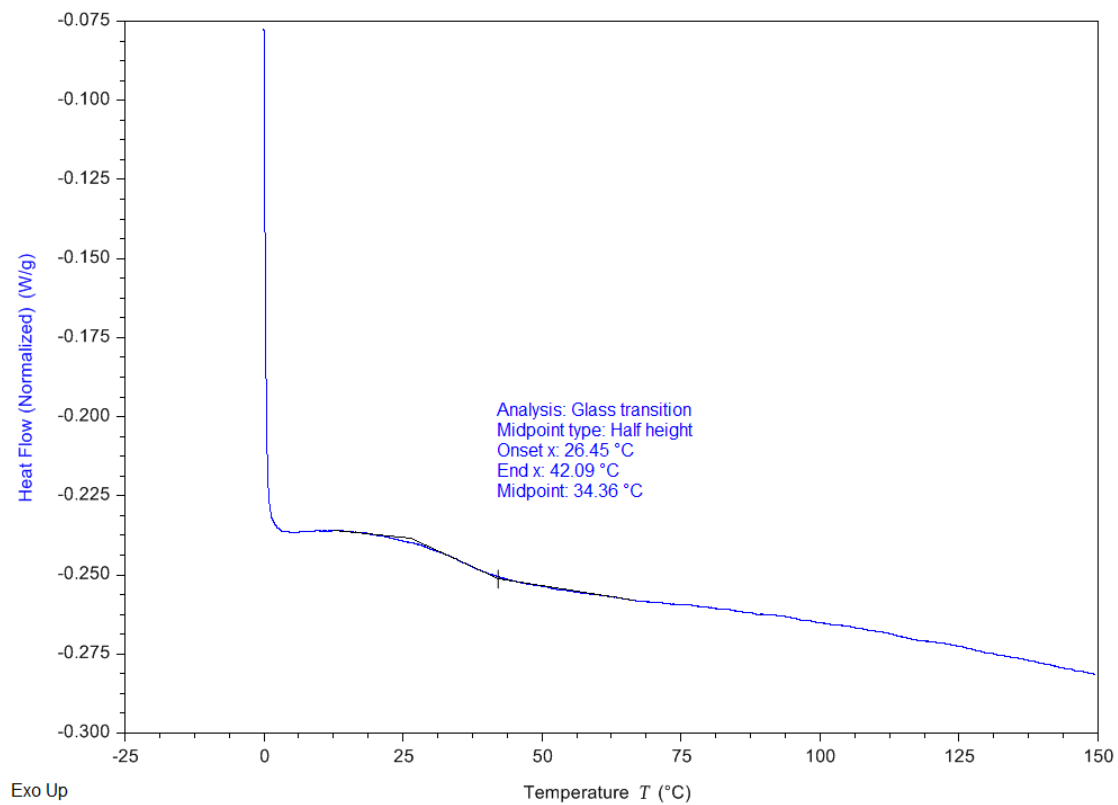


Figure 4.31. Isolated DSC trace of 2nd heat for p(DDW)-DP24.

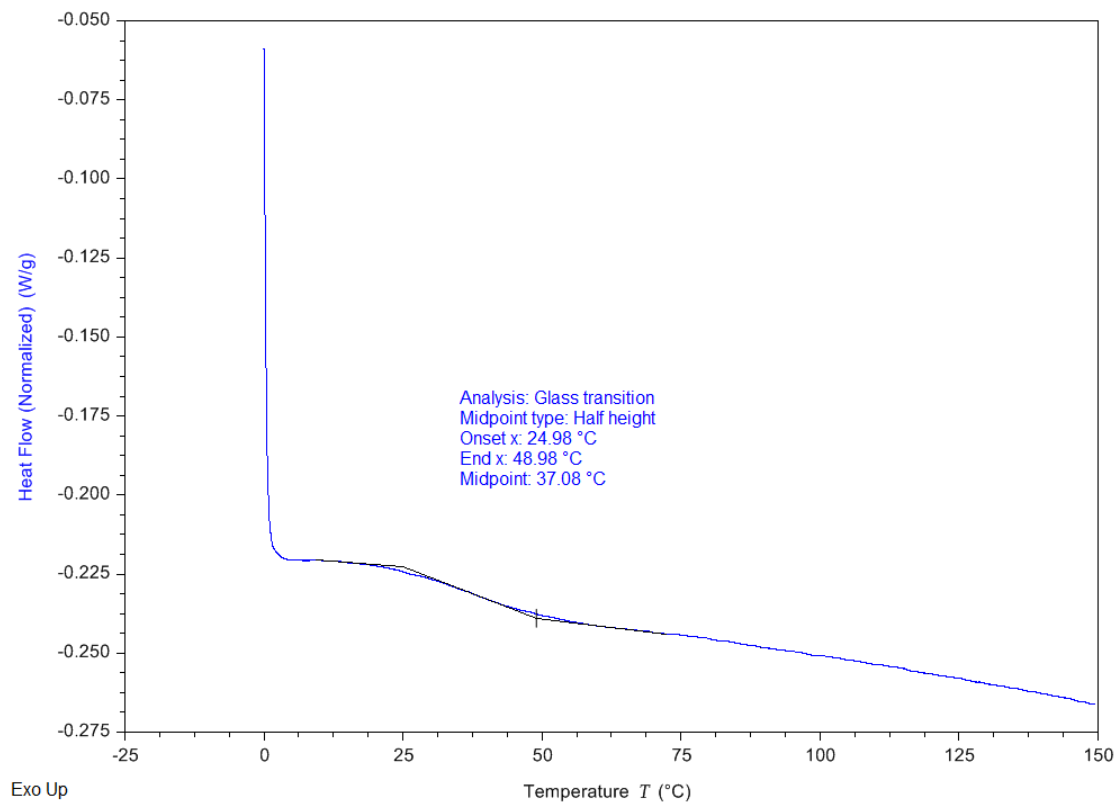


Figure 4.32. Isolated DSC trace of 2nd heat for p(DDW)-DP822.

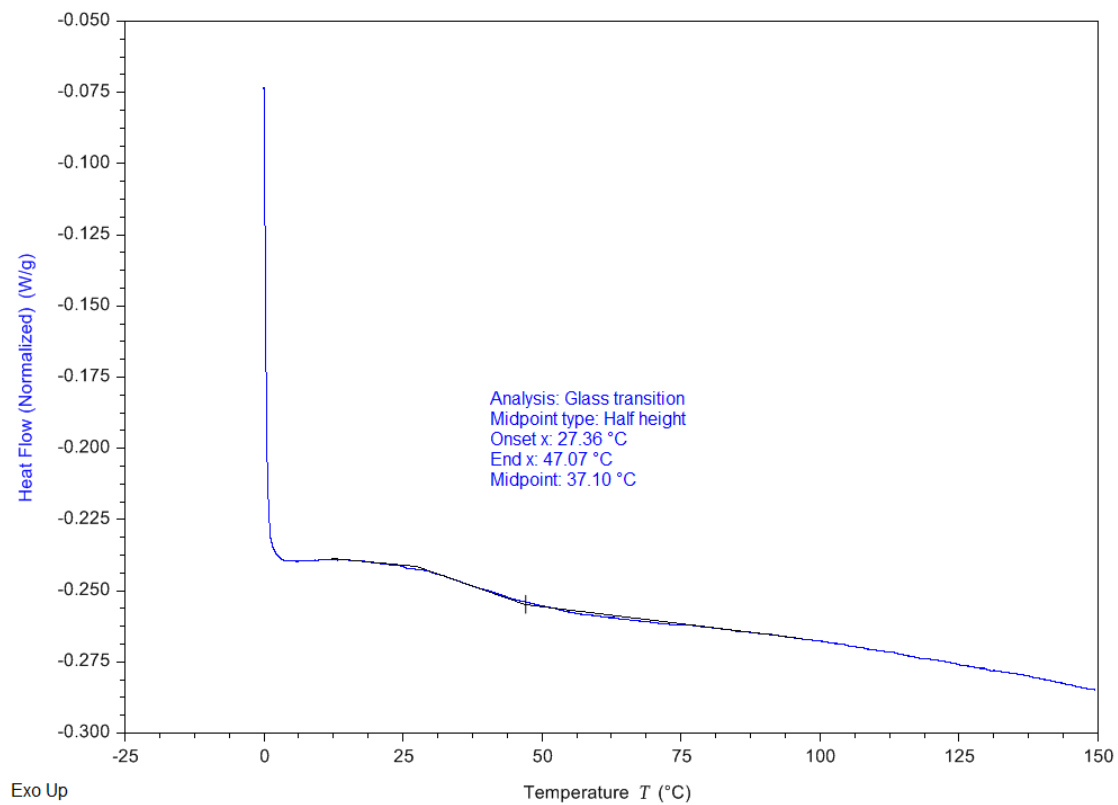


Figure 4.33. Isolated DSC trace of 2nd heat for p(DDW)-DP6944

Mechanical Properties

Dynamic Mechanical Analysis (DMA)

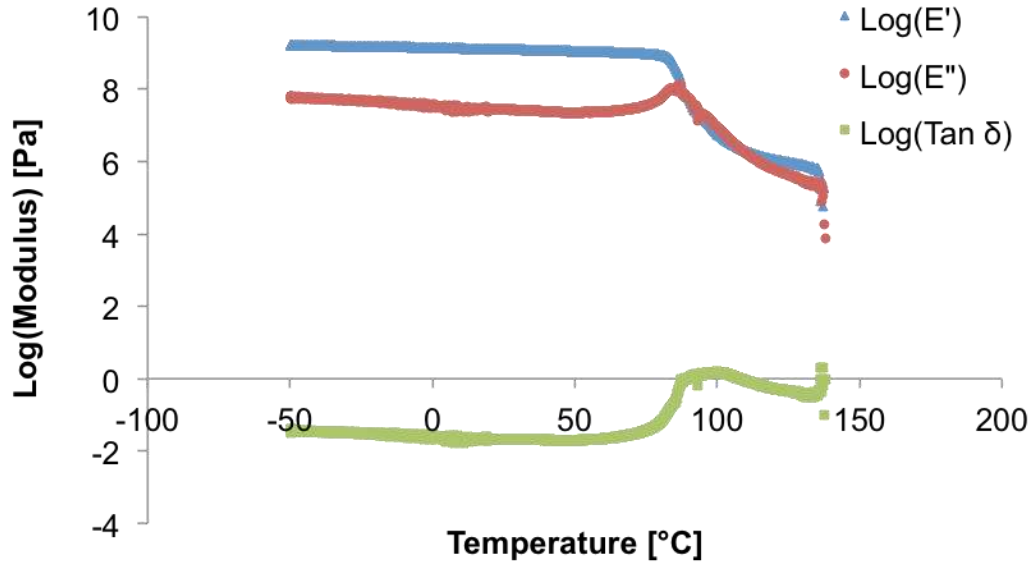


Figure 4.34. Poly(HNb)-DP912 DMA trace.

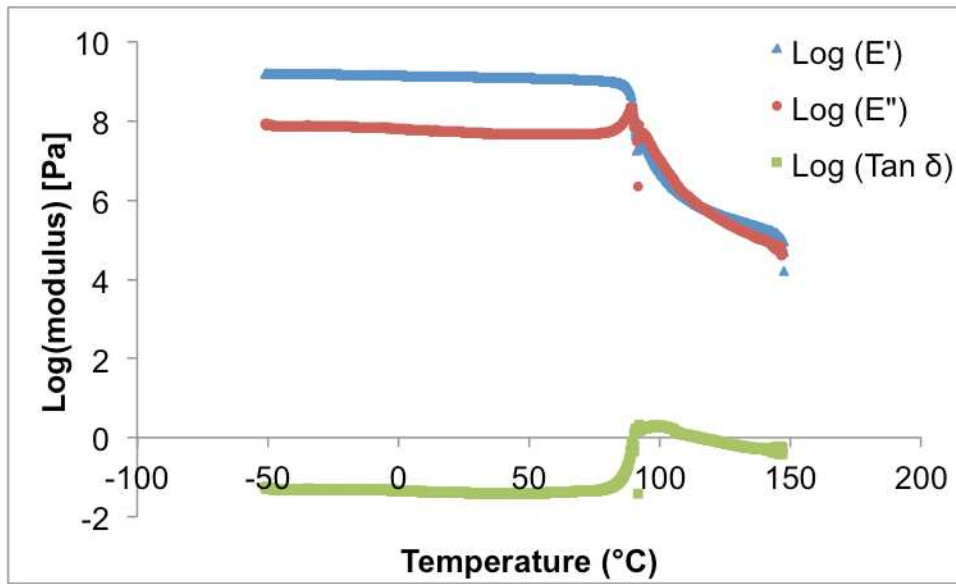


Figure 4.35. Poly(EtW)-DP943 DMA trace.

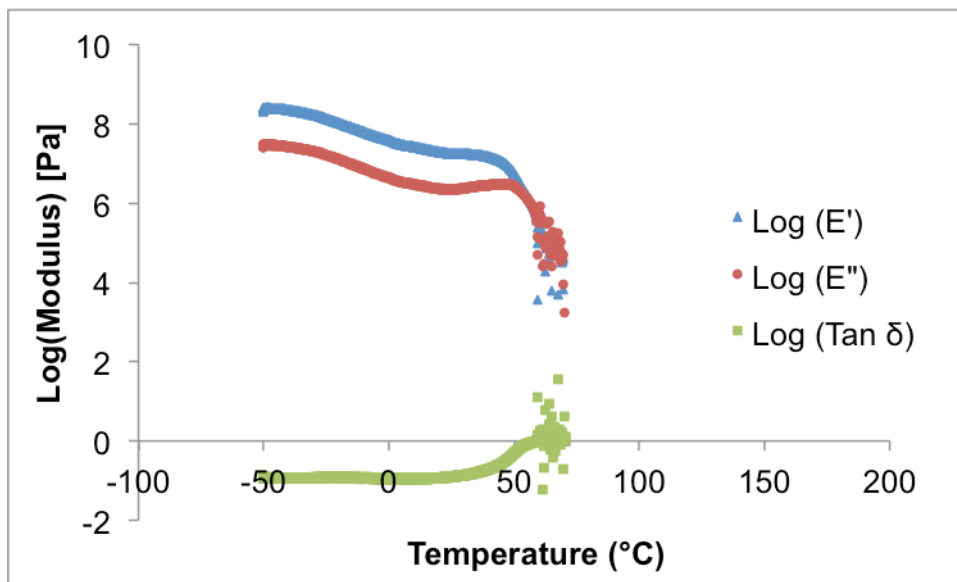


Figure 4.36. Poly(DDW)-DP930 DMA trace.

Rheological Properties

Method for Density Estimation

The polymer density was estimated using a pellet at the glass transition temperature on the rheometer. The pellet was first heated and liberated of all air bubbles and was then cooled to the glass transition temperature, where the gap size at 0 N was recorded. Then, in order to determine the volume of the polymer, the gap size was used as the height of the cylinder and the plate diameter was used as the diameter of the cylinder. This pellet was then weighed to get a mass. In order to calculate the density, the mass was divided by the calculated volume.

Isofrictional Measurements

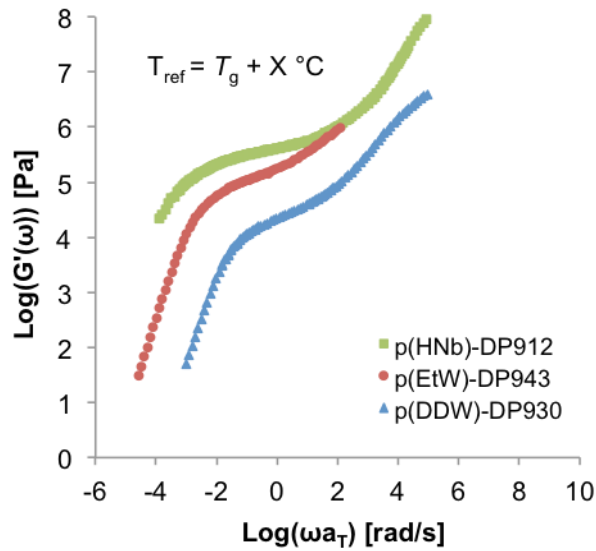


Figure 4.37. The isofrictional dynamic storage modulus master curves vs. frequency for the p(HNb)-DP912 (green squares), p(EtW)-DP943 (red circles), and the p(DDW)-DP930 (blue triangles). The temperature for each sample is close to isofrictional conditions with $X = 36 \text{ } ^\circ\text{C}$ for p(HNb)-DP912, $X=31 \text{ } ^\circ\text{C}$ for p(EtW)-DP943, and $X=42 \text{ } ^\circ\text{C}$ for p(DDW)-DP930.

p(HNb) Series Individual Mastercurves

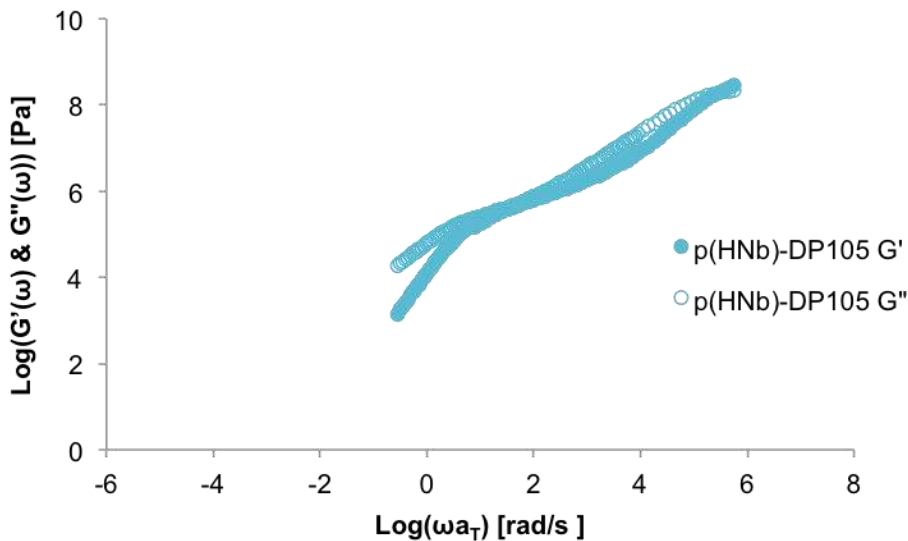


Figure 4.38. The dynamic mastercurve for p(HNb)-DP105 referenced to $120 \text{ } ^\circ\text{C}$.

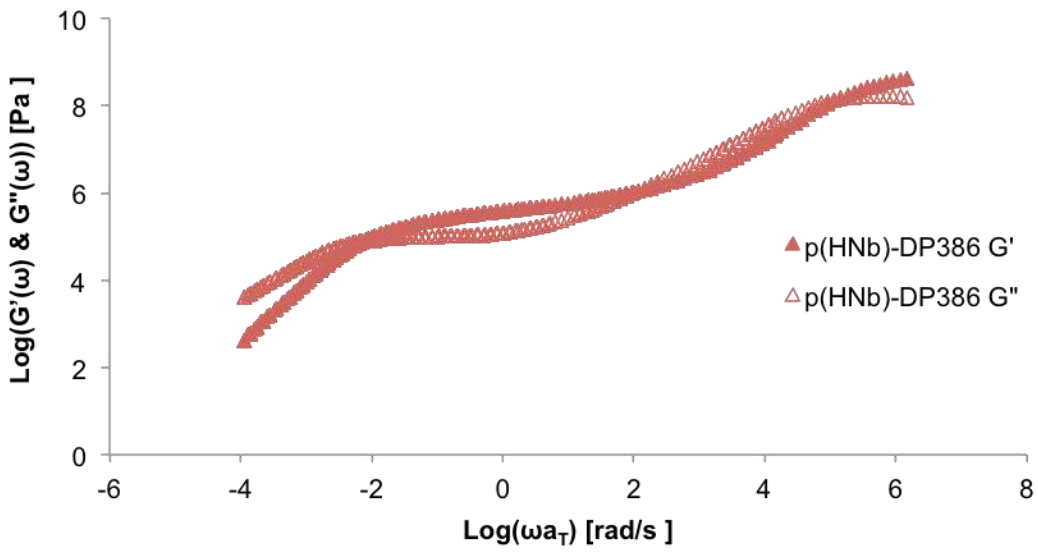


Figure 4.39. The dynamic mastercurve for p(HNb)-DP386 referenced to 120 °C.

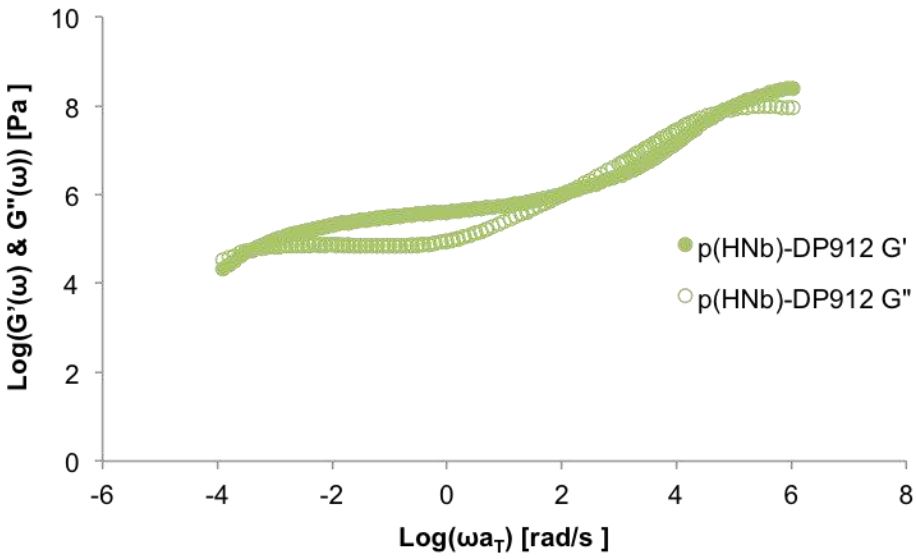


Figure 4.40. The dynamic mastercurve for p(HNb)-DP912 referenced to 120 °C.

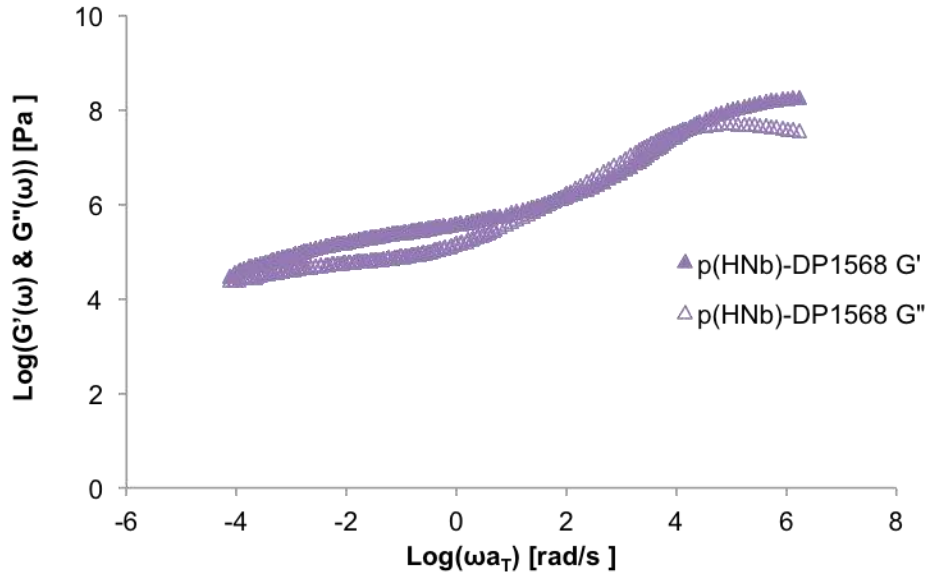


Figure 4.41. The dynamic mastercurve for p(HNb)-DP1568 referenced to 120 °C.

p(EtW) Series Individual Mastercurves

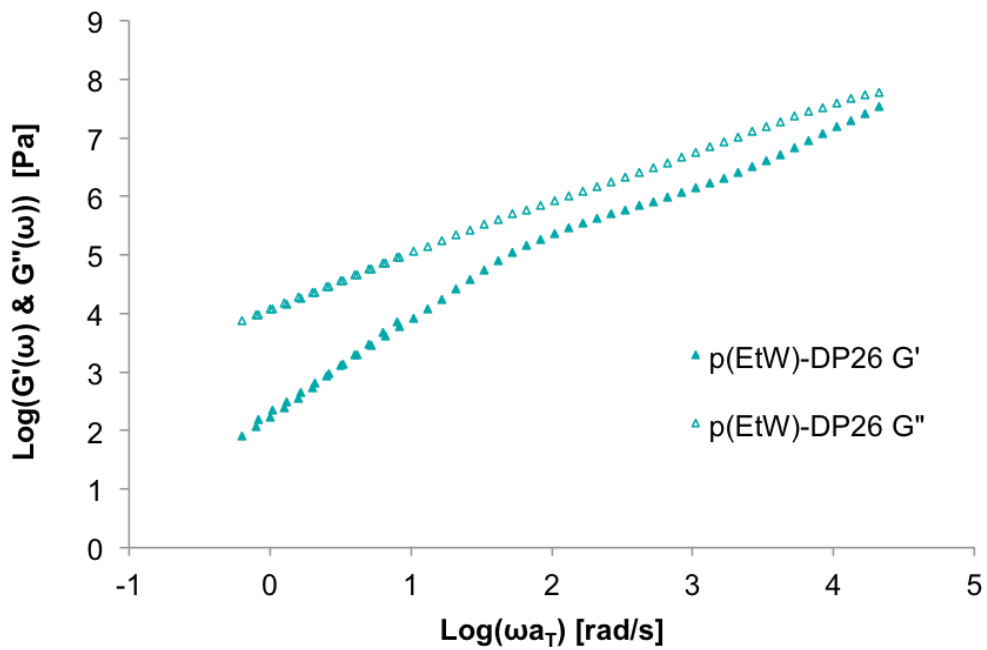


Figure 4.42. The dynamic mastercurve of p(EtW)-DP26 referenced to 120 °C.

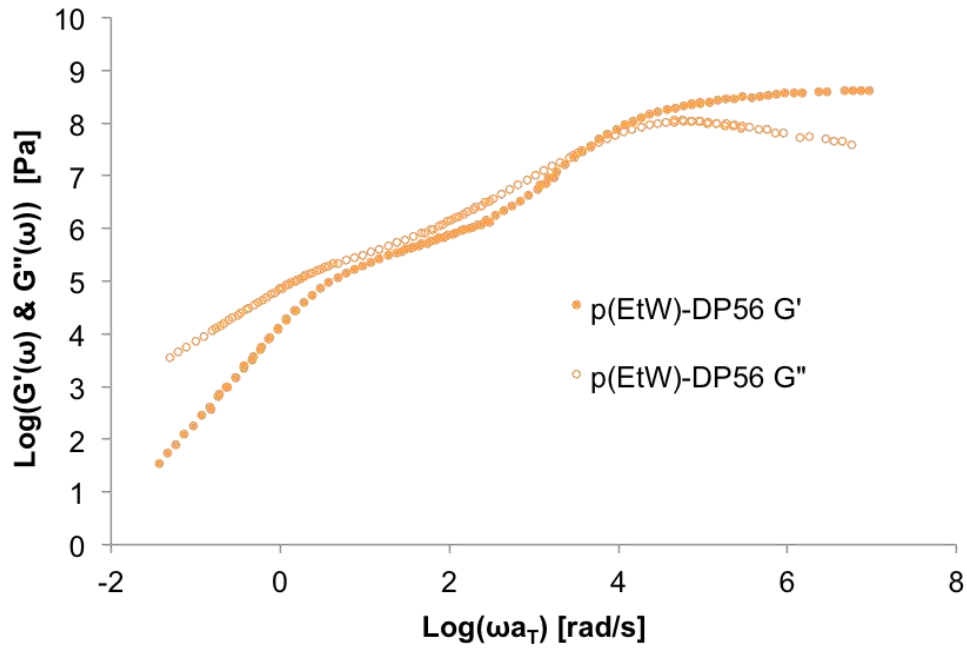


Figure 4.43. The dynamic mastercurve for p(EtW)-DP56 referenced to 120 °C.

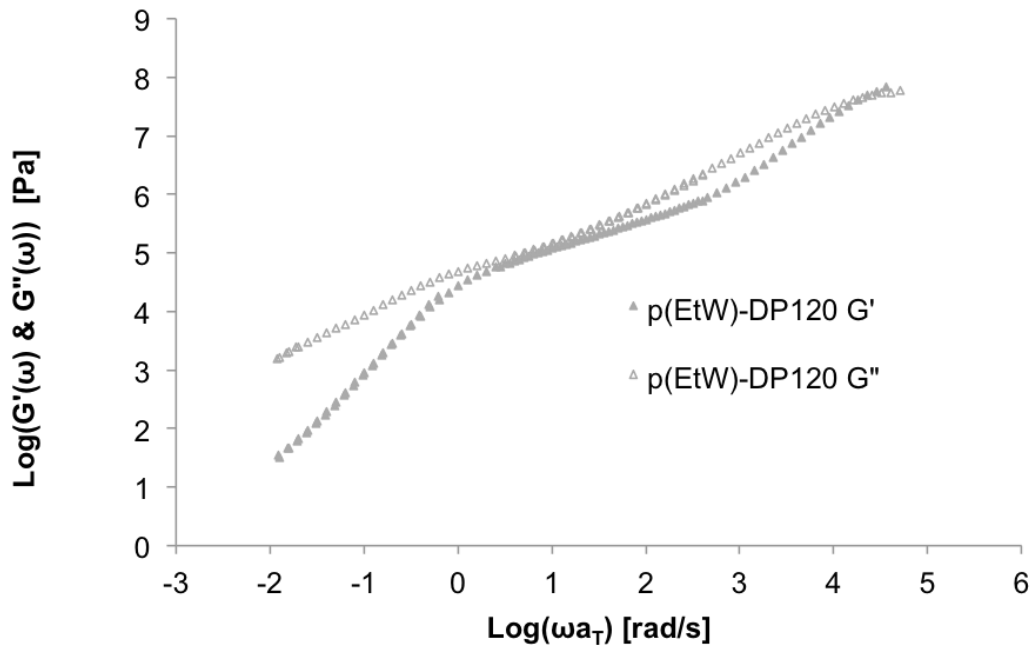


Figure 4.44. The dynamic mastercurve for p(EtW)-DP120 referenced to 120 °C.

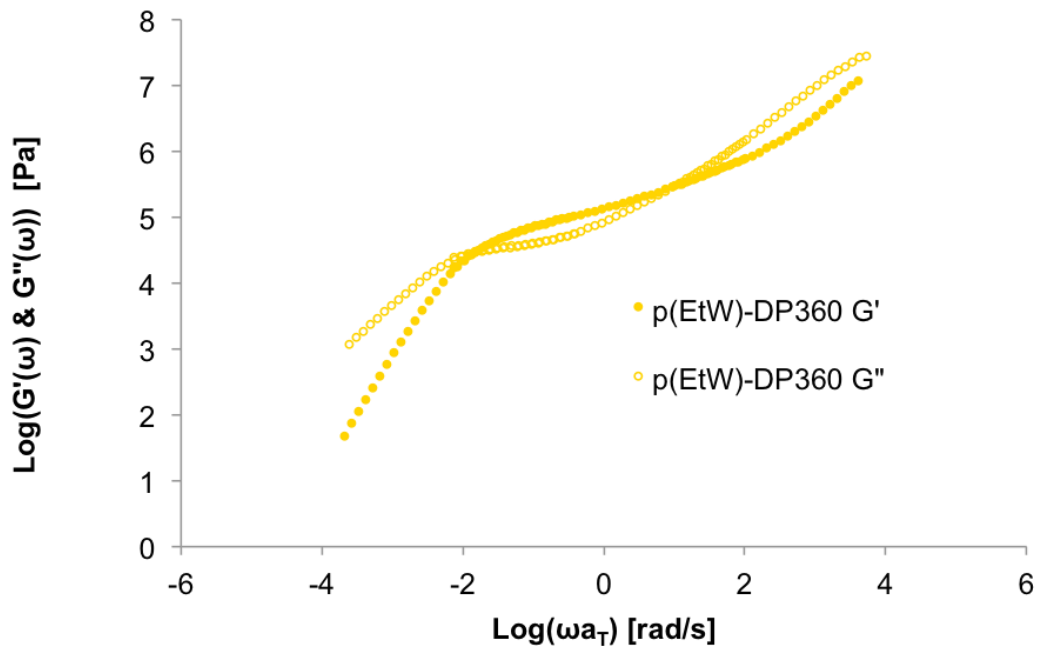


Figure 4.45. The dynamic mastercurve for p(EtW)-DP360 referenced to 120 °C.

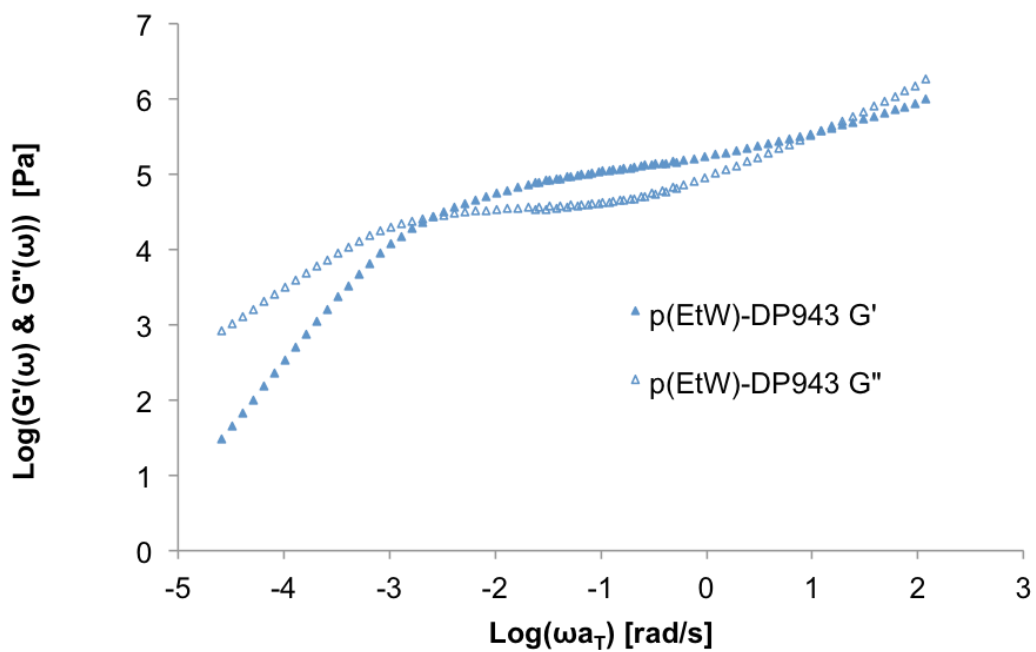


Figure 4.46. The dynamic mastercurve for p(EtW)-DP943 referenced to 120 °C.

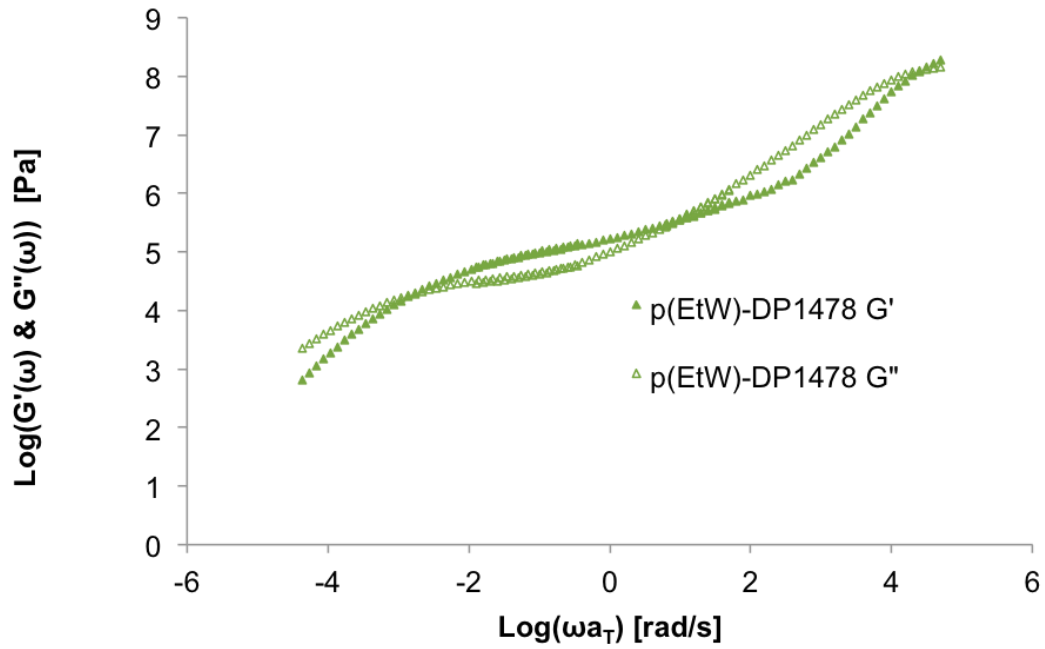


Figure 4.47. The dynamic mastercurve for p(EtW)-DP1478 referenced to 120 °C.

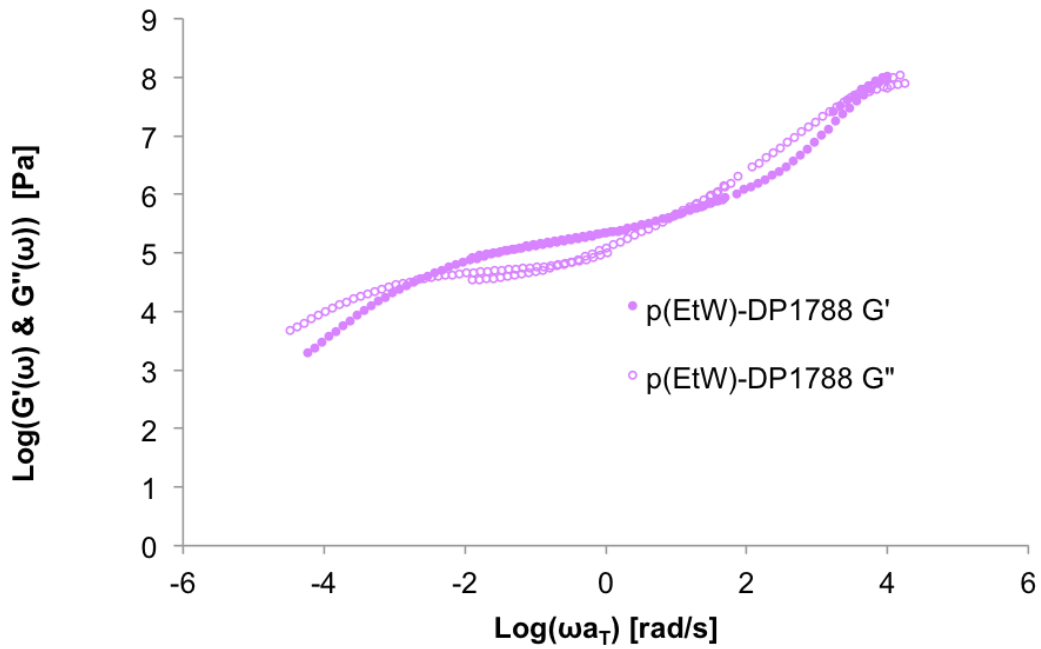


Figure 4.48. The dynamic mastercurve for p(EtW)-DP1788 referenced to 120 °C.

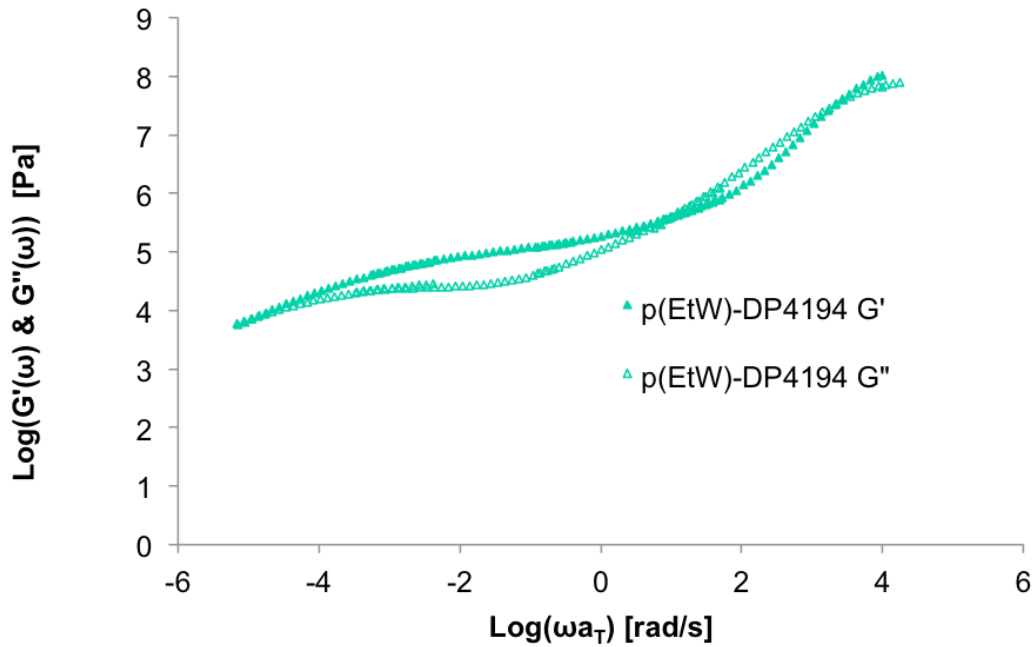


Figure 4.49. The dynamic mastercurve for p(EtW)-DP4194 referenced to 120 °C.

p(DDW) Series Individual Mastercurves

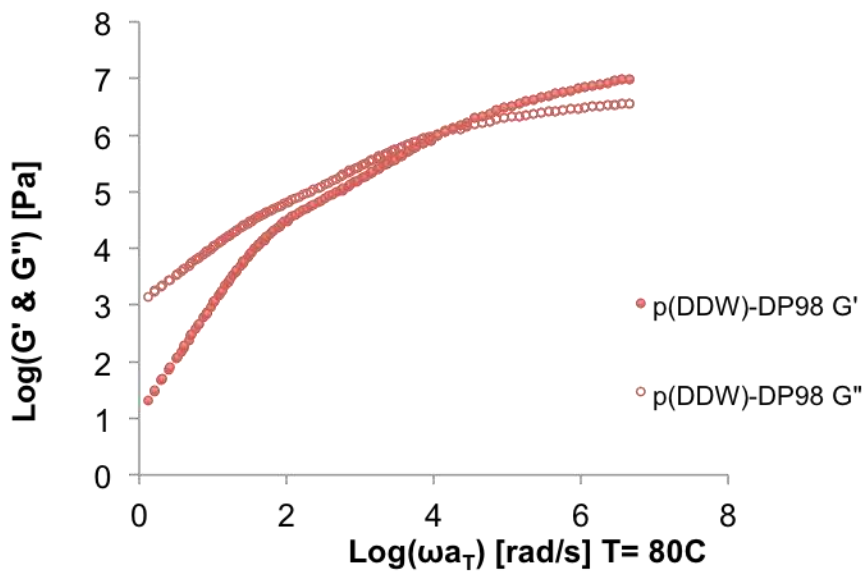


Figure 4.50. The dynamic mastercurve for p(DDW)-DP98 referenced to 80 °C.

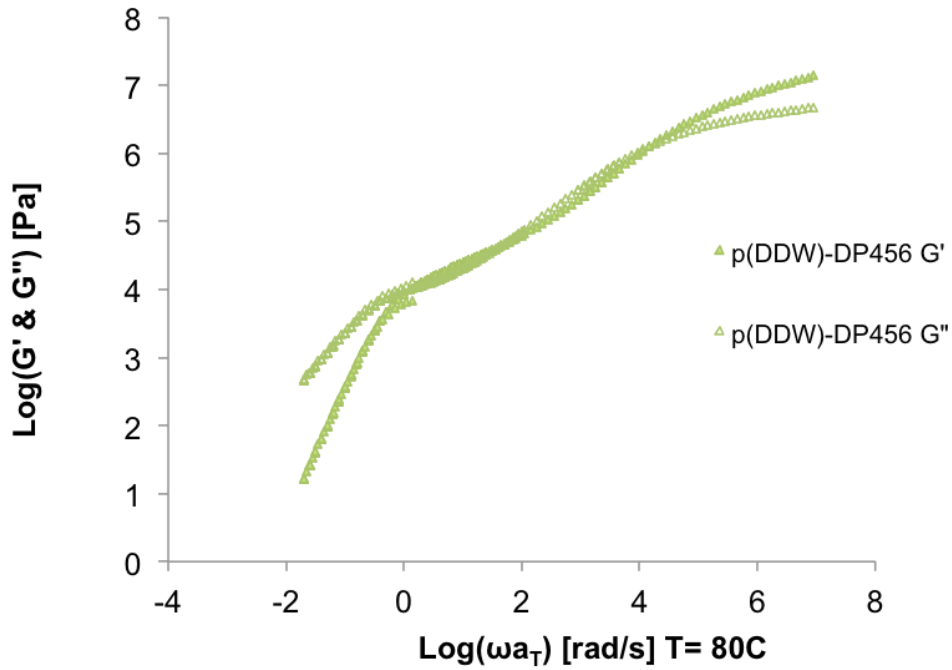


Figure 4.51. The dynamic mastercurve for p(DDW)-DP456 referenced to 80 °C.

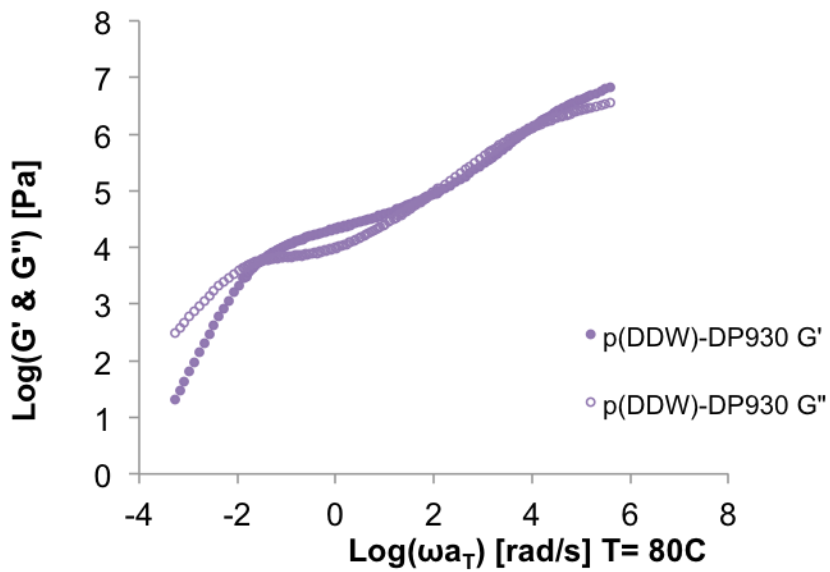


Figure 4.52. The dynamic mastercurve for p(DDW)-DP930 referenced to 80 °C.

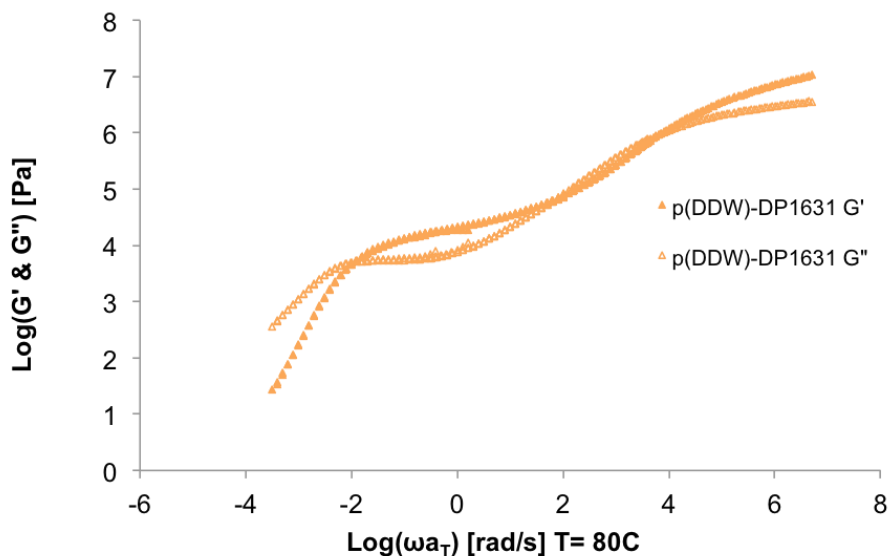


Figure 4.53. The dynamic mastercurve for p(DDW)-DP1631 referenced to 80 °C.

References

- (1) Daniel, W. F. M.; Burdynska, J.; Vatankhah-Varnoosfaderani, M.; Matyjaszewski, K.; Paturej, J.; Rubinstein, M.; Dobrynin, A. V.; Sheiko, S. S. Solvent-free, supersoft and superelastic bottlebrush melts and networks. *Nat. Mater.* **2016**, 15, 183–190.
- (2) Verduzco, R.; Li, X.; Pesek, S. L.; Stein, G. E. Structure, function, self-assembly, and applications of bottlebrush copolymers. *Chem. Soc. Rev.* **2015**, 44, 2405.
- (3) Dalsin, S. J.; Rions-Maehren, T. G.; Beam, M. D.; Bates, F. S.; Hillmyer, M. A.; Matsen, M. W. Bottlebrush Block Polymers: Quantitative Theory and Experiments. *ACS Nano* **2015**, 9, 12233– 12245.
- (4) Rzayev, J. Molecular Bottlebrushes: New Opportunities in Nanomaterials Fabrication. *ACS Macro Lett.* **2012**, 1, 1146–1149.

- (5) Haugan, I. N.; Maher, M. J.; Chang, A. B.; Lin, T.-P.; Grubbs, R. H.; Hillmyer, H. A.; Bates, F. S. Consequences of Grafting Density on the Linear Viscoelastic Behavior of Graft Polymers. *ACS Macro Lett.* **2018**, *7*, 525–530.
- (6) Dalsin, S. J.; Hillmyer, M. A.; Bates, F. S. Linear Rheology of Polyolefin-Based Bottlebrush Polymers. *Macromolecules* **2015**, *48*, 4680–4691.
- (7) Hu, M.; Xia, Y.; McKenna, G. B.; Kornfield, J. A.; Grubbs, R. H. Linear Rheological Response of a Series of Densely Branched Brush Polymers. *Macromolecules* **2011**, *44*, 6935–6943.
- (8) Aluculesei, A.; Pipertzis, A.; Piunova, V. A.; Miyake, G. M.; Floudas, G.; Fytas, G.; Grubbs, R. H. Thermomechanical Behavior and Local Dynamics of Dendronized Block Copolymers and Constituent Homopolymers. *Macromolecules* **2015**, *48*, 4142–4150.
- (9) Hsu, H.-P.; Paul, W.; Binder, K. One- and Two-Component Bottle-brush Polymers: Simulations Compared to Theoretical Predictions. *Macromol. Theory Simul.* **2007**, *16*, 660–689.
- (10) Paturej, J.; Sheiko, S. S.; Panyukov, S.; Rubinstein, M. Molecular Structure of Bottlebrush Polymers in Melts. *Sci. Adv.* **2016**, *2*, No. e1601478.
- (11) Kavassalis, T. A.; Noolandi, J. Entanglement Scaling in Polymer Melts and Solutions. *Macromolecules* **1989**, *22*, 2709–2720.
- (12) Cao, Z.; Carrillo, J.-M. Y.; Sheiko, S. S.; Dobrynin, A. V. Computer Simulations of Bottle Brushes: From Melts to Soft Networks. *Macromolecules* **2015**, *48*, 5006–5015.

- (13) Fetters, L. J.; Lohse, D. J.; Milner, S. T.; Graessley, W. W. Packing Length Influence in Linear Polymer Melts on Entanglement, Critical, and Reptation Molecular Weights. *Macromolecules* **1999**, *32*, 6847–6851.
- (14) Hawker, C. J.; Frechet, J. M. J. Preparation of Polymers with Controlled Molecular Architecture. A New Convergent Approach to Dendritic Macromolecules. *J. Am. Chem. Soc.* **1990**, *112*, 7638–7647.
- (15) Percec, V.; Ahn, C.-H.; Bera, T. K.; Ungar, G.; Yeardley, D. J. P. Coassembly of a Hexagonal Columnar Liquid Crystalline Superlattice from Polymer(s) Coated with a Three-Cylindrical Bundle Supra- molecular Dendrimer. *Chem. - Eur. J.* **1999**, *5*, 1070–1083.
- (16) Zhang, B.; Wepf, R.; Fischer, K.; Schmidt, M.; Besse, S.; Lindner, P.; King, B. T.; Sigel, R.; Schurtenberger, P.; Talmon, Y.; Ding, Y.; Kroger, M.; Halperin, A.; Schluter, A. D. The Largest Synthetic Structure with Molecular Precision: Towards a Molecular Object. *Angew. Chem., Int. Ed.* **2011**, *50*, 737–740.
- (17) Karakaya, B.; Claussen, W.; Gessler, K.; Saenger, W.; Schluter, A.-D. Toward Dendrimers with Cylindrical Shape in Solution. *J. Am. Chem. Soc.* **1997**, *119*, 3296–3301.
- (18) Helms, B.; Mynar, J. L.; Hawker, C. J.; Frechet, J. M. J. Dendronized Linear Polymers via “Click Chemistry”. *J. Am. Chem. Soc.* **2004**, *126*, 15020–15021.
- (19) Boydston, A. J.; Holcombe, T. W.; Unruh, D. A.; Frechet, J. M. J.; Grubbs, R. H. A Direct Route to Cyclic Organic Nanostructures via Ring-Expansion Metathesis Polymerization of a Dendronized Macro- monomer. *J. Am. Chem. Soc.* **2009**, *131*, 5388–5389.

- (20) Ter Huurne, G. M.; Vantomme, G.; van den Bersselaar, B. W. L.; Thota, B. N. S.; Voets, I. K.; Palmans, A. R. A.; Meijer, E. W. The Effect of Dendritic Pendants on the Folding of Amphiphilic Copolymers via Supramolecular Interactions. *J. Polym. Sci., Part A: Polym. Chem.* **2019**, 411–421.
- (21) Deng, J.; Zhou, Y.; Xu, B.; Mai, K.; Deng, Y.; Zhang, L.-M. Dendronized Chitosan Derivative as a Biocompatible Gene Delivery Carrier. *Biomacromolecules* **2011**, 12, 642–649.
- (22) Li, W.; Wu, D.; Schluter, A. D.; Zhang, A. Synthesis of an Oligo(ethylene glycol)-Based Third-Generation Thermoresponsive Dendronized Polymer. *J. Polym. Sci., Part A: Polym. Chem.* **2009**, 47, 6630–6640.
- (23) Knapen, J. W. J.; van der Made, A. W.; de Wilde, J. C.; van Leeuwen, P. W. N. M.; Wijkens, P.; Grove, D. M.; van Koten, G. Homogeneous catalysts based on silane dendrimers functionalized with arylnickel(II) complexes. *Nature* **1994**, 372, 659–663.
- (24) Piunova, V. A.; Miyake, G. M.; Daeffler, C. S.; Weitekamp, R. A.; Grubbs, R. H. Highly Ordered Dielectric Mirrors via the Self- Assembly of Dendronized Block Copolymers. *J. Am. Chem. Soc.* **2013**, 135, 15609–15616.
- (25) Boyle, B. M.; French, T. A.; Pearson, R. M.; McCarthy, B. G.; Miyake, G. M. Structural Color for Additive Manufacturing: 3D- Printed Photonic Crystals from Block Copolymers. *ACS Nano* **2017**, 11, 3052–3058.
- (26) Qian, Z.; Koh, Y. P.; Pallaka, M. R.; Chang, A. B.; Lin, T.-P.; Guzman, P. E.; Grubbs, R. H.; Simon, S. L.; McKenna, G. B. Linear Rheology of a Series of Second-Generation

- Dendronized Wedge Polymers. *Macromolecules* **2019**, 2063–2074.
- (27) Hu, M.; Xia, Y.; Daeffler, C. S.; Wang, J.; McKenna, G. B.; Kornfield, J. A.; Grubbs, R. H. The Linear Rheological Responses of Wedge-Type Polymers. *J. Polym. Sci., Part B: Polym. Phys.* **2015**, 53, 899–906.
- (28) Pasquino, R.; Zhang, B.; Sigel, R.; Yu, H.; Ottiger, M.; Bertran, O.; Aleman, C.; Schluter, A. D.; Vlassopoulos, D. Linear Viscoelastic Response of Dendronized Polymers. *Macromolecules* **2012**, 45, 8813– 8823.
- (29) Costanzo, S.; Scherz, L. F.; Schweizer, T.; Kroger, M.; Floudas, G.; Schluter, A. D.; Vlassopoulos, D. Rheology and Packing of Dendronized Polymers. *Macromolecules* **2016**, 49, 7054–7068.
- (30) Dutertre, F.; Bang, K.-T.; Loppinet, B.; Choi, I.; Choi, T.-L.; Fytas, G. Structure and Dynamics of Dendronized Polymer Solutions: Gaussian Coil or Macromolecular Rod? *Macromolecules* **2016**, 49, 2731–2740.
- (31) Ouali, N.; Mery, S.; Skoulios, A.; Noirez, L. Backbone Stretching of Wormlike Carbosilane Dendrimers. *Macromolecules* **2000**, 33, 6185–6193.
- (32) Graessley, W. W. *The Entanglement Concept in Polymer Rheology*; Springer: Berlin, **1974**.
- (33) Miyake, G. M.; Weitekamp, R. A.; Grubbs, R. H. *Handbook of Metathesis: Synthesis of Materials with Nanostructured Periodicity*, 2nd ed.; Wiley-VCH: Weinheim, Germany, **2015**.
- (34) Vougioukalakis, G. C.; Grubbs, R. H. Ruthenium-Based Heterocyclic Carbene-Coordinated Olefin Metathesis Catalysts. *Chem. Rev.* **2010**, 110, 1746–1787.

- (35) Bielawski, C. W.; Grubbs, R. H. Living Ring-Opening Metathesis Polymerization. *Prog. Polym. Sci.* **2007**, *32*, 1–29.
- (36) Leitgeb, A.; Wappel, J.; Slugovc, C. The ROMP Toolbox Upgraded. *Polymer* **2010**, *51*, 2927–2946.
- (37) Flory, P. J.; Fisk, S. Effect of Volume Exclusion on the Dimensions of Polymer Chains. *J. Chem. Phys.* **1966**, *44*, 2243.
- (38) Fixman, M. Radius of Gyration of Polymer Chains. *J. Chem. Phys.* **1962**, *36*, 306.
- (39) Dünweg, B.; Kremer, K. Molecular Dynamics Simulation of a Polymer Chain in Solution. *J. Chem. Phys.* **1993**, *99*, 6983.
- (40) Fetters, L. J.; Lohse, D. J.; Richter, D.; Witten, T. A.; Zirkel, A. Connection between Polymer Molecular Weight, Density, Chain Dimensions, and Melt Viscoelastic Properties. *Macromolecules* **1994**, *27*, 4639–4647.
- (41) De Gennes, P. G. *Scaling Concepts in Polymer Physics*; Cornell University Press: London, U.K., **1979**.
- (42) Benoit, H.; Doty, P. Light Scattering from Non-Gaussian Chains. *J. Phys. Chem.* **1953**, *57*, 958–963.
- (43) Marsh, D. Scaling and Mean-Field Theories Applied to Polymer Brushes. *Biophys. J.* **2004**, *86*, 2630–2633.
- (44) Hsu, H.-P.; Paul, W.; Rathgeber, S.; Binder, K. Characteristic Length Scales and Radial Monomer Density Profiles of Molecular Bottle-Brushes: Simulation and Experiment.

- Macromolecules* **2010**, 43, 1592–1601.
- (45) Ding, Y.; Kisliuk, A.; Sokolov, A. P. When Does a Molecule Become a Polymer? *Macromolecules* **2004**, 37, 161–166.
- (46) Floudas, G.; Stepanek, P. Structure and Dynamics of Poly(n- decyl methacrylate) below and Above the Glass Transition. *Macromolecules* **1998**, 31, 6951–6957.
- (47) Beiner, M.; Korus, J.; Donth, E. Dynamic Glass Transition above the Cooperativity Onset in Poly(n-octyl methacrylate). *Macromolecules* **1997**, 30, 8420–8424.
- (48) Rong, W.; Fan, Z.; Yu, Y.; Bu, H.; Wang, M. Influence of entanglements on glass transition of atactic polystyrene. *J. Polym. Sci., Part B: Polym. Phys.* **2005**, 43, 2243.
- (49) Ngai, K. L.; Paluch, M. Classification of Secondary Relaxation in Glass-Formers based on Dynamic Properties. *J. Chem. Phys.* **2004**, 120, 857.
- (50) Mirigian, S.; Schweizer, K. S. Elastically Cooperative Activated Barrier Hopping Theory of Relaxation in Viscous Fluids. II. Thermal Liquids. *J. Chem. Phys.* **2014**, 140, No. 194507.
- (51) Sunthar, P. In *Rheology of Complex Fluids*; Deshpande, A. P.; Krishnan, J. M.; Kumar, S., Eds.; Springer: New York, **2010**.
- (52) van Gorp, M.; Palmen, J. Time-Temperature Superposition for Polymeric Blends. *Rheol. Bull.* **1998**, 67, 5–8.
- (53) Trinkle, S.; Friedrich, C. Van Gorp-Palmen-Plot: a way to characterize polydispersity of linear polymers. *Rheol. Acta* **2001**, 40, 322–328.

- (54) Trinkle, S.; Walter, P.; Friedrich, C. Van Gorp-Palmen Plot II – classification of long chain branched polymers by their topology. *Rheol. Acta* **2002**, 41, 103–113.
- (55) Dealy, J.; Plazek, D. Time-Temperature Superposition – A User’s Guide. *Rheol. Bull.* **2009**, 78, 16–31.
- (56) Fetters, L. J.; Lohse, D. J.; Graessley, W. W. Chain Dimensions and Entanglement Spacings in Dense Macromolecular Systems. *J. Polym. Sci., Part B: Polym. Phys.* **1999**, 37, 1023–1033.
- (57) Patel, S. K.; Malone, S.; Cohen, C.; Gillmor, J. R.; Colby, R. H. Elastic Modulus and Equilibrium Swelling of Poly(dimethylsiloxane) Networks. *Macromolecules* **1992**, 25, 5241–5251.
- (58) Fetters, L. J.; Lohse, D. J.; Richter, D.; Witten, T. A.; Zirkel, A. Connection between Polymer Molecular Weight, Density, Chain Dimensions, and Melt Viscoelastic Properties. *Macromolecules* **1994**, 27, 4639–4647.
- (59) Williams, M. L.; Landel, R. F.; Ferry, J. D. The Temperature Dependence of Relaxation Mechanisms in Amorphous Polymers and Other Glass-Forming Liquids. *J. Am. Chem. Soc.* **1955**, 77, 3701–3707.
- (60) Ferry, J. D. In *Visoelastic Properties of Polymers*, 3rd ed.; Ferry, J. D., Ed.; John Wiley & Sons: New York, **1980**; p 304.
- (61) Kunal, K.; Robertson, C. G.; Pawlus, S.; Hahn, S. F.; Sokolov, A. P. Role of Chemical Structure in Fragility of Polymers: A Qualitative Picture. *Macromolecules* **2008**, 41,

7232–7238.

- (62) Ding, Y.; Sokolov, A. P. Breakdown of Time-Temperature Superposition Principle and Universality of Chain Dynamics in Polymers. *Macromolecules* **2006**, *39*, 3322–3326.
- (63) Ngai, K. L.; Roland, C. M. Chemical Structure and Intermolecular Cooperativity: Dielectric Relaxation Results. *Macromolecules* **1993**, *26*, 6824–6830.
- (64) He, X.; Wu, J.; Huang, G.; Wang, X. Effect of Alkyl Side Chain Length on Relaxation Behaviors in Poly(n-alkyl Acrylates) and Poly(n-alkyl Methacrylates). *J. Macromol. Sci., Part B* **2010**, *50*, 188–200.
- (65) Angell, C. A. Relaxation in liquids, polymers and plastic crystals – strong/fragile patterns and problems. *J. Non-Cryst. Solids* **1991**, 131–133, 13–31.
- (66) Love J. A.; Morgan J. P.; Trnka T. M.; Grubbs R. H. A Practical and Highly Active Ruthenium-Based Catalyst that Effects the Cross Metathesis of Acrylonitrile. *Angew. Chem., Int. Ed.* **2002**, *41*, 4035-4037.
- (67) Matson J. B.; Grubbs R. H. Synthesis of Fluorine-18 Functionalized Nanoparticles for use as *in vivo* Molecular Imaging Agents. *J. Am. Chem. Soc.* **2008**, *130*, 6731-6733.
- (68) Xia Y.; Sveinbjornsson B. R.; Grubbs R. H.; Weitekamp R.; Miyake G. M.; Piunova V. A.; Daeffler C. S. Periodic Nanostructures from Self Assembled Wedge-Type Block Copolymers. *U.S. Patent 2,013,029,6491*, **2013**.
- (69) Cole, J. P.; Lessard, J. J.; Lyon, C. K.; Tuten, B. T.; Berda, E. B Intra-chain radical chemistry as a route to poly-(norbornene imide) single-chain nanoparticles: structural considerations and the role of adventitious oxygen. *Polym. Chem.* **2015**, *6*, 5555.

CHAPTER 5 – IMPACT OF BACKBONE STRUCTURE ON POLYMER DYNAMICS AND BRUSH BLOCK COPOLYMER SELF-ASSEMBLY

Overview

Four series of brush block copolymers (BBCP) with near identical side chain compositions but varying backbone structures were synthesized to investigate the effect of backbone structure on the process of thermal BBCP self-assembly to photonic crystals (PCs). Each of the self-assembled PC films were examined by reflection measurements and scanning electron microscopy to compare the resulting properties of the polymeric photonic crystal and the nanostructured morphology impacted by the backbone structure. It was found that the composition of the backbone within a BBCP has a dramatic effect on the ability of the BBCP to self-assemble into ordered nanostructures and on the local ordering of the nanostructure morphology in higher molecular weight (MW) BBCPs ($> 1,500$ kg/mol). BBCPs with a norbornene imide-based backbone were able to self-assemble to longer wavelength reflecting PCs and had greater local ordered nanostructures with higher MW polymers. Lastly, by analyzing the melt rheological responses of the backbone compositions, both as linear polymers and homobrush polymers, it was observed that the inherent stiffness of the backbone promotes enhanced local ordering in the nanostructure morphology and larger domain sizes.

Introduction

Photonic crystals (PC) are periodic dielectric materials possessing a photonic band gap that inhibits the propagation of specific frequencies of light.^{1,2} The wavelength of reflected light by the material is derived from the interaction of light with the nanostructure morphology and

enables applications as light guides, optical filters, and reflective coatings.^{3,4,5} There are many routes to synthetic PCs, but one of the most economical and scalable methods to PCs is through the self-assembly of block copolymers (BCP) to nanostructured materials.^{6,7,8,9,10} These block copolymers can employ polymer architectures such as linear,¹¹ dendritic,^{6,12} and bottlebrush copolymers.^{13,14} The self-assembly of linear BCPs (LBCP) is largely governed by the interaction parameter of the two blocks, the volume fraction of each block, and the degree of polymerization of each block.^{15,16} However, the inherent chain entanglement in linear polymers challenges the ability of LBCPs to self-assemble to domain sizes large enough to reflect wavelengths of light longer than green.¹⁷ Therefore, by exploiting more rigid polymer architectures, polymeric PC materials can be enabled to reflect wavelengths of light across the visible spectrum and into the near-IR, in part due to a reduction in the amount of polymer chain entanglement.^{6,12,18,19,20} In particular, bottlebrush BCPs (BBCP) significantly reduce chain entanglement and have been shown to rapidly self-assemble to domains large enough to reflect wavelengths of light across the visible spectrum and into the near-IR.^{21,22,23,24,25,26,27}

The bottlebrush polymer architecture consists of densely spaced polymeric side chains grafted onto a central polymer backbone.²⁸ The polymeric side chains promote the cylindrical conformation of bottlebrush macromolecules due to the steric repulsion between neighboring side chains. This cylindrical conformation significantly influences bulk materials properties, such as extending the persistence length, reducing the entanglement modulus, and creating a secondary relaxation.^{29,30,31,32,33,34} The bottlebrush backbone composition plays an essential role in the global conformation of the homobrush polymers, both due to the phenomena of excluded volume between the side chains and the chain stiffness parameter of the polymer.^{35,36,37,38}

Synthetic advancements allow alteration of the side chains or the main chain backbone to modulate the properties of the brush polymer and the resulting brush polymer bulk material.³⁹

Currently, however, there is a gap in knowledge on how the dynamics of a homobrush polymer translate to a BBCP's dynamics. Among the various synthetic schemes, there are no established benefits of one synthetic route to a bottlebrush polymer over another in terms of synthesizing a BBCP that can efficiently self-assemble to a PC capable of efficiently reflecting wavelengths of light across the visible spectrum.^{40,41} Watkins and co-workers have started to address this question with insightful observations into how the backbone length, side chain length, molecular asymmetry, and volume fraction of BBCPs affect the nanostructure phase map and the relaxation modes of BBCPs.^{42,43} Unfortunately, there is no clear predictor of how modifying the backbone structure of the BBCP influences the process of self-assembly and the resulting PC properties. The impact of the backbone on self-assembly and the resulting PC properties is of high importance, especially when considering the myriad of synthetic routes available to BBCPs. The composition of the backbone and influences on the BBCP could inform whether a certain synthetic route would be preferable for a specific application.

Herein, we report the effect of varying backbone structure on BBCP self-assembly and the resulting properties of the BBCP PC. We couple our observations of the BBCP self-assembly and PC film properties with an investigation into the polymer dynamics of linear and brush homopolymers containing identical backbone compositions to those of the BBCPs. The results reveal that the backbone composition of a BBCP has a significant influence on the reflection and nanostructure morphology of the resulting PC material. Overall, it is observed that more inherently rigid polymer backbones result in more efficient domain interface relaxation and

manifest into encouraging higher MW BBCPs to self-assemble to longer wavelength reflecting PCs.

Results and Discussion

To investigate the effect of backbone composition on the self-assembly of BBCPs to visible light reflecting, polymeric PCs, four different series of varying molecular weight (MW) BBCPs were synthesized using ruthenium-mediated ring opening metathesis polymerization (ROMP) (Figure 5.1). The macromonomers used in this study consisted of two different poly(lactide) (PLA) macromonomers, containing either a norbornene (NB-PLA, $M_n = 3,251$ g/mol) or a norbornene imide (NBI-PLA, $M_n = 3,428$ g/mol) chain end, as well as two poly(styrene) (PS) macromonomers, possessing either a norbornene (NB-PS, $M_n = 3,649$ g/mol) or a norbornene imide (NBI-PS, $M_n = 4,422$ g/mol) chain end. The resulting BBCP series, denoted by *p*(NBI-PLA)-*b*-*p*(NBI-PS), *p*(NB-PLA)-*b*-*p*(NBI-PS), *p*(NBI-PLA)-*b*-*p*(NB-PS), or *p*(NB-PLA)-*b*-*p*(NB-PS), were isolated as colorless materials before being self-assembled by thermal annealing for 16 hours under vacuum at a temperature of 140 °C. This annealing temperature was chosen because it is at least 40 °C above the glass transition temperature (T_g) of any of the brush block's T_g values (Figures 5.95-5.101), which enables self-assembly. Equal molarity of the macromonomers was polymerized to target a lamellar nanostructured morphology due to the ease of observing a change in the wavelength of reflection due to a change in the domain size with increasing BBCP MW using a modified form of Bragg's Law (Figure 5.1).

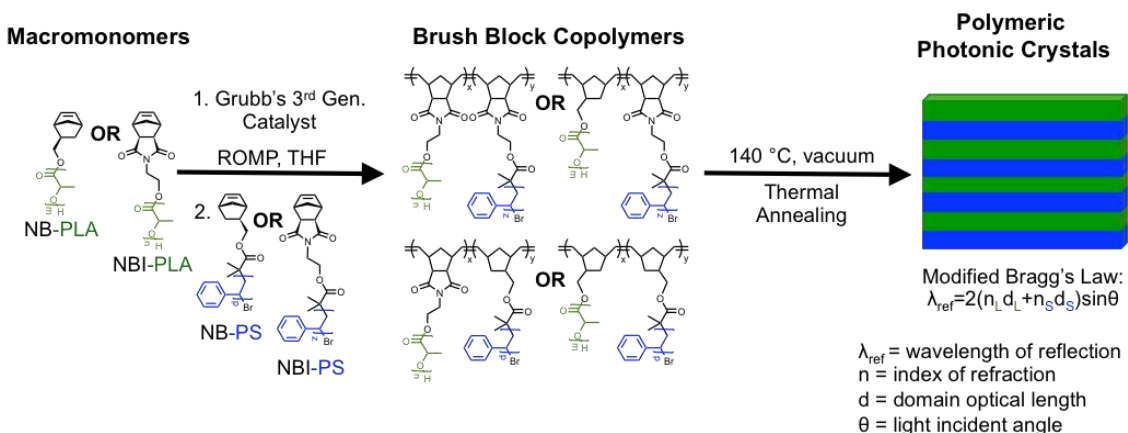


Figure 5.1. Synthetic approach to the four distinct BCCPs and their self-assembly to polymeric photonic crystals.

After thermal annealing, the films reflected wavelengths of light in the ultraviolet or visible spectrum due to the periodicity of the assembled nanostructure. The reflection profile of each of the four series of self-assembled BCCP films was characterized directly by measuring the percent of incident wavelengths of light across the ultraviolet and visible spectrum reflected by the assembled film (Figure 5.2A-D). These measurements were performed using a UV-Vis spectrophotometer outfitted with a diffuse reflectance accessory (DRA).

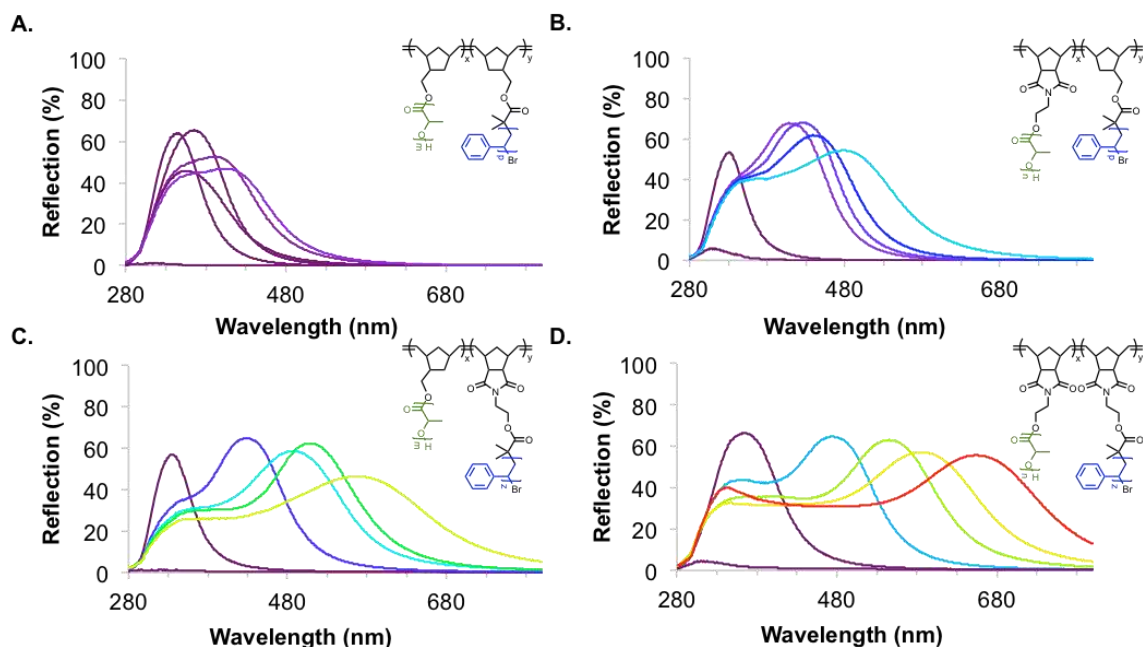


Figure 5.2. DRA traces of reflection (%) vs. wavelength (nm) for each of the four BCCP MW series assembled films (*p*(NB-PLA)-*b*-*p*(NB-PS) (A), *p*(NBI-PLA)-*b*-*p*(NB-PS) (B), *p*(NB-PLA)-*b*-*p*(NBI-PS) (C), and *p*(NBI-PLA)-*b*-*p*(NBI-PS) (D)).

Interestingly, investigating similar MW ranges of polymers, each of the series of BCCP annealed films reflection profiles span different ranges of wavelengths. The majority of the weight fraction of each of these BCCP compositions is almost indistinguishable, with the polymeric side chains being extremely similar, if not identical. The only significant compositional difference between each of these four BCCP series is the identity of the backbone. Even with higher MW BCCPs, the annealed films from the *p*(NB-PLA)-*b*-*p*(NB-PS) series did not reflect wavelengths of light longer than violet (406 nm), while the films fabricated from *p*(NBI-PLA)-*b*-*p*(NBI-PS) reflect wavelengths of light across the UV-visible spectrum ranging from ultraviolet (300 nm) to red-orange (655 nm).

Figure 5.3 plots the maximum wavelength of reflection with respect to each polymer's number-average MW (M_n) to highlight the impact that the different backbone compositions have

on the reflection of each of the BCCP series. The slope (m) of each of the best-fit lines in Figure 5.3 provides a means to quantify how increasing MW, or a higher degree of polymerization (DP), will affect the maximum wavelength of reflection of the thermally annealed films for each series. The $p(\text{NBI-PLA})-b-p(\text{NBI-PS})$ film series has an $m = 0.31$ which means that the backbone composition allows for a 0.31 nm increase in wavelength of reflection for every kilogram per mole of BCCP that is added to the polymeric PC film. In contrast, the m of the $p(\text{NB-PLA})-b-p(\text{NB-PS})$ is 0.04, which implies that an approximately eightfold increase in BCCP MW of this composition is needed to have domain sizes large enough to reflect similar wavelengths as the $p(\text{NBI-PLA})-b-p(\text{NBI-PS})$ film composition does. Comparatively, by replacing the NB-PS block with a NBI-PS block in the $p(\text{NB-PLA})-b-p(\text{NB-PS})$ composition, the m value increases to 0.16, rather than only increasing to 0.08, as replacing the NB-PLA block with a NBI-PLA block in the $p(\text{NB-PLA})-b-p(\text{NB-PS})$ composition does.

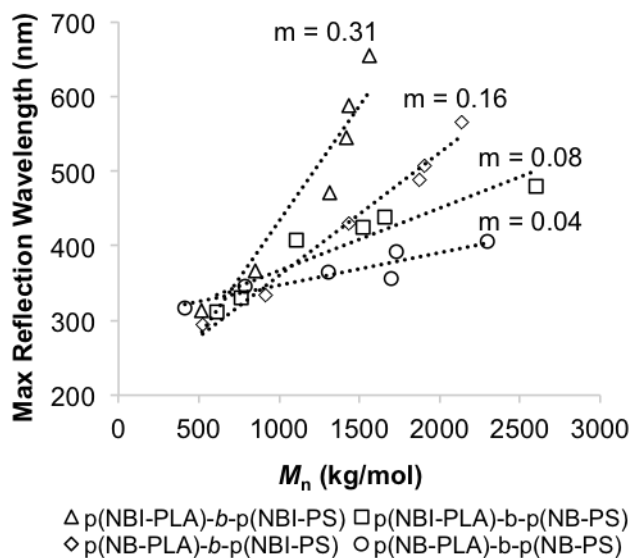


Figure 5.3. A plot of the max wavelength of reflection for each assembled film within each of the four BCCP series vs. the M_n of each polymer ($m =$ slope of best fit line).

Although the $p(\text{NBI-PLA})-b-p(\text{NBI-PS})$ films are able to reflect wavelengths of light across the visible spectrum and have the greatest m value, the bandwidths of the PCs are large and broaden with increasing maximum wavelengths of reflection. The bandwidth of a PC determines which range of wavelengths of light are reflected, and the ability to modulate the PC bandwidth allows for engineering PCs for specific applications.¹² A broad bandwidth (several hundred nanometers) can be targeted for IR reflecting windows, while a filter or waveguide application would target a narrow bandwidth (< 10 nm). To measure the bandwidth of a PC, the full-width-half-max (FWHM) value of the reflection trace is used. The measured FWHM value of 428 nm for the film assembled from the $p(\text{NBI-PLA})-b-p(\text{NBI-PS})$ BBCP (1.56×10^3 kg/mol) implies that the global ordering of the lamellar nanostructure is significantly more uniform for the film assembled from the $p(\text{NB-PLA})-b-p(\text{NB-PS})$ BBCP (2.30×10^3 kg/mol) with a FWHM of only 153 nm (Table 5.1). In fact, the longer the maximum wavelength of reflection for each BBCP composition, or the greater the m value for each series, the less global ordering is present in the nanostructure. The backbone composition significantly affects the global ordering of the nanostructure of a BBCP PC film in addition to the maximum wavelength of reflection.

Table 5.1. FWHM values calculated for each of the BBCP PC films from the DRA reflection traces in Figure 1.

$p(\text{NB-PLA})-b-p(\text{NB-PS})$		$p(\text{NBI-PLA})-b-p(\text{NB-PS})$		$p(\text{NB-PLA})-b-p(\text{NBI-PS})$		$p(\text{NBI-PLA})-b-p(\text{NBI-PS})$	
M_n (kg/mol)	FWHM (nm)	M_n (kg/mol)	FWHM (nm)	M_n (kg/mol)	FWHM (nm)	M_n (kg/mol)	FWHM (nm)
4.14×10^2	63	6.13×10^2	50	5.24×10^2	91	5.20×10^2	62
7.87×10^2	65	7.66×10^2	48	9.18×10^2	55	8.50×10^2	91
1.31×10^3	89	1.11×10^3	135	1.44×10^3	143	1.31×10^3	210
1.73×10^3	134	1.52×10^3	149	1.88×10^3	214	1.42×10^3	280
1.70×10^3	101	1.66×10^3	174	1.90×10^3	138	1.43×10^3	344
2.30×10^3	153	2.60×10^3	235	2.13×10^3	334	1.56×10^3	428

To visualize the nanostructure morphology, SEM micrographs were collected for each of the thermally annealed films (Figures 5.4 and 5.63-5.87). For the $p(\text{NB-PLA})-b-p(\text{NB-PS})$ composition, as the BCCP MW increases, the local ordering of the lamellar nanostructure quickly deteriorates (Figure 5.4A, 5.4E, and 5.4I). For the $p(\text{NBI-PLA})-b-p(\text{NB-PS})$ composition (Figure 5.4B, 5.4F, and 5.4J), the local ordering of the nanostructure loses its fidelity with increasing MW. However, the $p(\text{NBI-PLA})-b-p(\text{NB-PS})$ composition (1.11×10^3 kg/mol) does retain the ordering of its nanostructure morphology more effectively than that of the $p(\text{NB-PLA})-b-p(\text{NB-PS})$ composition at intermediate MW (1.31×10^3 kg/mol). The more efficient assembly can be quantitatively demonstrated by a greater wavelength of reflection of 408 nm for the $p(\text{NBI-PLA})-b-p(\text{NB-PS})$ composition (1.11×10^3 kg/mol) versus that of 365 nm for the $p(\text{NB-PLA})-b-p(\text{NB-PS})$ composition (1.31×10^3 kg/mol). A similar trend exists moving from the $p(\text{NBI-PLA})-b-p(\text{NB-PS})$ composition to the $p(\text{NB-PLA})-b-p(\text{NBI-PS})$ composition (Figure 5.4C, 5.4G, and 5.4K). The highest MW sample of the $p(\text{NB-PLA})-b-p(\text{NBI-PS})$ is more well-defined and ordered than that shown in the SEM micrograph of the highest MW of the $p(\text{NBI-PLA})-b-p(\text{NB-PS})$ and reflects a longer wavelength of light. Lastly, the $p(\text{NBI-PLA})-b-p(\text{NBI-PS})$ composition (Figure 5.4D, 5.4H, and 5.4L) maintains its nanostructure's local ordering throughout the entire MW series tested as seen by the reflecting the longest wavelength of reflection (Figures 5.2 and 5.3). Hence, the backbone composition of the BCCPs significantly impacts the local ordering of the thermally annealed film's nanostructure morphology.

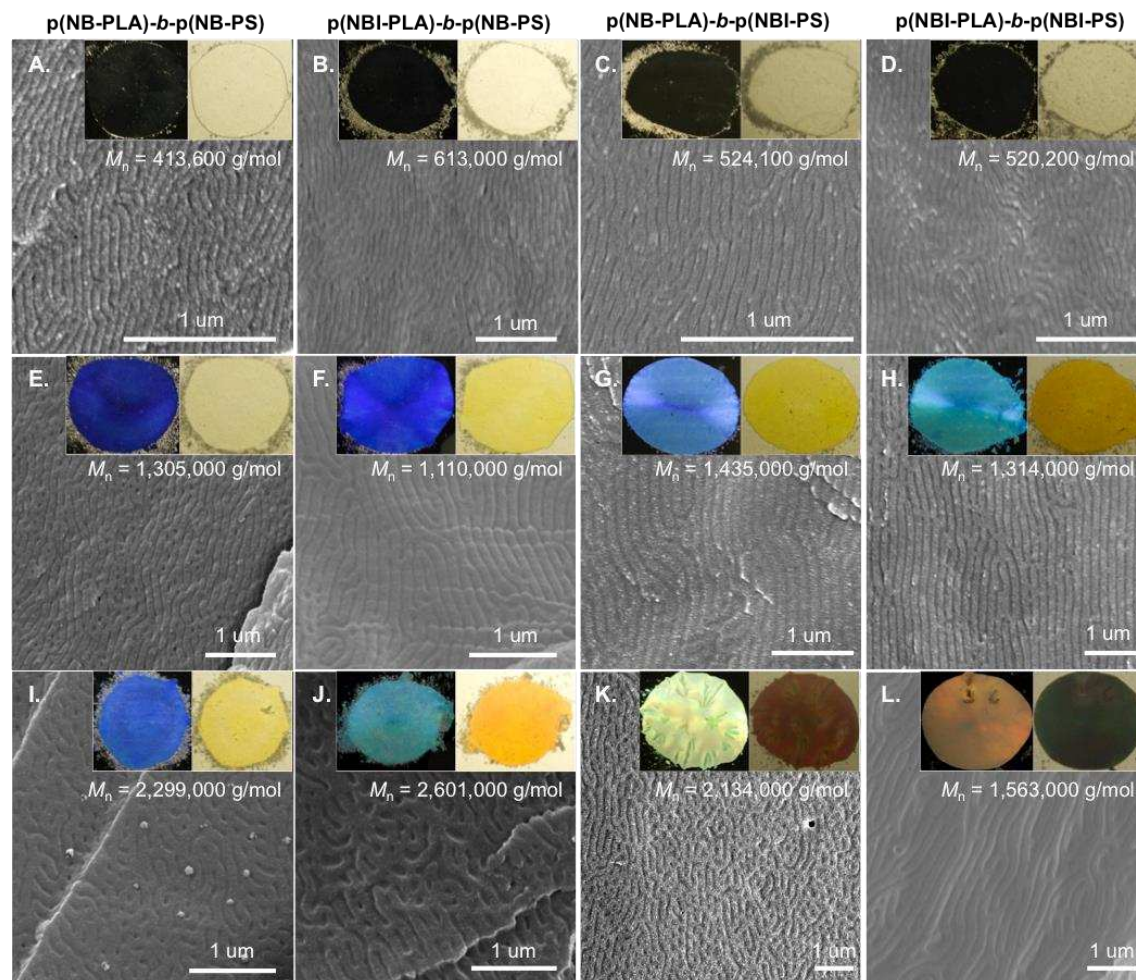


Figure 5.4. SEM micrographs of cross-sections of three films from each of the thermally annealed BCBP films of comparable MW (*p*(NB-PLA)-*b-p*(NB-PS) films shown in A, E, I; *p*(NBI-PLA)-*b-p*(NB-PS) films shown in B, F, J; *p*(NB-PLA)-*b-p*(NBI-PS) films shown in C, G, K; *p*(NBI-PLA)-*b-p*(NBI-PS) films shown in D, H, L) with photographs of the annealed film's reflection (left inset picture) and transmission (right inset picture).

To gain insight into why the backbone composition affects the self-assembly processes of the BCBPs, MW series of linear and brush homopolymers were synthesized using ruthenium-mediated ROMP in an attempt to mimic the backbone composition and isolate the effect of each backbone component on each block of the BCBPs (Figure 5.5). The polymer dynamics of these homopolymer series were characterized using rheological measurements.

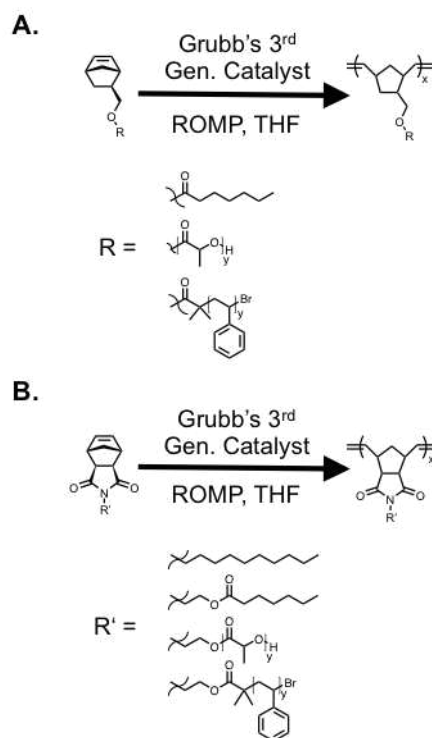


Figure 5.5. Synthetic strategy to homopolymers (linear and brush) with a norbornene backbone composition (A, Top to bottom: NB-Hep, NB-PLA, and NB-PS) and a norbornene imide backbone composition (B, Top to bottom: NBI-Dec, NBI-Hep, NBI-PLA, and NBI-PS).

The three linear polymers were synthesized from monomers composed of a norbornene group functionalized with heptanoic acid (NB-Hep, Figure 5.5A) or a norbornene imide group functionalized with either heptanoic acid (NBI-Hep, Figure 5.5B) or decane (NBI-Dec, Figure 5.5B). The $p(\text{NB-Hep})$ and $p(\text{NBI-Hep})$ polymer series are similar in chemical composition to each of the two different BBCP backbones, allowing comparison into the BBCP backbone dynamics without the polymeric side-chains. Additionally, the $p(\text{NBI-Dec})$ series is similar to the $p(\text{NBI-Hep})$ series and the omission of the carbonyl group on the $p(\text{NBI-Dec})$ series can isolate the impact of the carbonyl group versus the impact from the norbornene imide group.

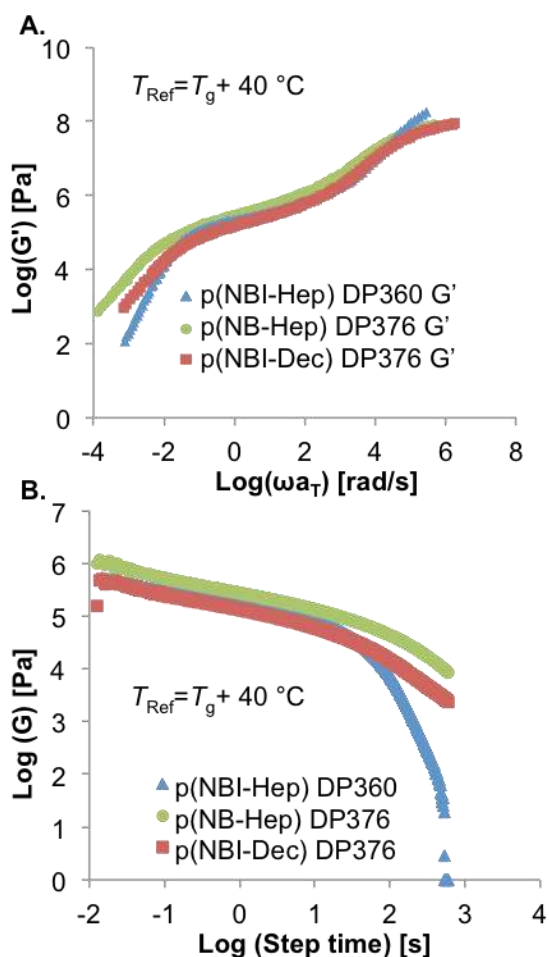


Figure 5.6. Storage modulus mastercurves of each of the three linear homopolymers at comparable DP (A) and 5% step-strain stress relaxation tests of each of the linear homopolymers (B) at a $T_{Ref} = T_g + 40 \text{ }^\circ\text{C}$.

The storage modulus mastercurves, covering a range of 8 to 10 orders of magnitude in frequency, constructed via standard time and temperature superposition (TTS) processes at a reference temperature $T_{Ref} = T_g + 40 \text{ }^\circ\text{C}$ for each of the three linear polymers at similar DP is shown in Figure 5.6A. All three polymers displayed characteristic regions similar to those of conventional linear polymers: a glass-to-rubber transition region at high frequency, a rubbery plateau, and a terminal flow region at low frequency. These mastercurves highlight the

differences in the polymer dynamics that can be attributed to the backbone. The most significant difference between each of the polymers can be seen in the chain relaxation time (τ_1). The chain relaxation time marks the onset of the terminal flow regime and can be estimated at the crossover frequency ($G'(\omega) = G''(\omega)$).⁴⁴ Specifically, the τ_1 was estimated to be 116 s for $p(\text{NB-Hep})$ DP376, 26 s for $p(\text{NBI-Hep})$ DP360, and 41 s for $p(\text{NBI-Dec})$ DP376. The faster τ_1 of $p(\text{NBI-Hep})$ compared to the τ_1 of $p(\text{NBI-Dec})$ can be attributed to a much faster segmental relaxation process, which sets the monomer friction coefficient that governs the chain relaxation process.⁴⁵ However, the drastic reduction of τ_1 from $p(\text{NB-Hep})$ to $p(\text{NBI-Hep})$ at isofrictional conditions can be related to the degree of chain entanglement and the rubbery elasticity, which can be estimated by a comparison of the values of both phase angle minimums shown in the van Gurp-Palmen (VGP) plots shown in Figure 5.109-5.115 and the magnitude of the plateau modulus (G_N^0) in the mastercurve for $p(\text{NB-Hep})$ and $p(\text{NBI-Hep})$ (Figure 5.6A).^{46,47} The magnitude of G_N^0 can be reliably estimated from the local minimum in the VGP plots shown in Figure 5.109-5.115.⁴⁸ Accordingly, the minimum phase angle and G_N^0 value for the $p(\text{NB-Hep})$ DP376 were determined to be 26° and 2.40×10^3 Pa, respectively. The minimum phase angle and G_N^0 value for the $p(\text{NBI-Hep})$ DP360 were determined to be 26° and 1.89×10^3 Pa, respectively. The rubbery elasticity of the $p(\text{NB-Hep})$ DP376 sample is higher in magnitude than that of the $p(\text{NBI-Hep})$ DP360 sample, which follows the fact that the less elastic material has a reduced τ_1 . To confirm the trend seen in the estimated τ_1 values from the mastercurves, a 5% step-strain stress relaxation experiment was conducted on each polymer sample at $T_{\text{Ref}} = T_g + 40$ °C. Indeed, the same trend appears over a time-span of 10 minutes (Figure 5.6B). The $p(\text{NBI-Hep})$ DP360 sample relaxes back to 0 Pa within the time frame, while the $p(\text{NBI-Dec})$ DP376 relaxes to approximately 2,405 Pa and the $p(\text{NB-Hep})$ DP376 sample relaxes to approximately 8,557 Pa.

Additionally, by analyzing the temperature dependence of the shift factors (a_T) used in the TTS of the mastercurves for each of the linear polymers as described by the Williams-Landel-Ferry (WLF) equation, it is possible to obtain a fragility index value (m_f) for each of the three polymer series (Figure 5.116).^{49,50} The m_f value describes the temperature dependence of the relaxation processes of the polymer near its T_g value.^{51,52,53} The higher the m_f value, the more drastic the temperature dependence and the more fragile the polymer. The m_f values of the $p(\text{NB-Hep})$ series, the $p(\text{NBI-Hep})$ series, and the $p(\text{NBI-Dec})$ series are 42.6, 77.8, and 64.5, correspondingly. The significant difference between the $p(\text{NB-Hep})$ series and the $p(\text{NBI-Hep})$ series demonstrates the difference in temperature dependence of the polymer relaxation close to the T_g as a result of the backbone composition. Also, the fact that the $p(\text{NBI-Hep})$ series has a higher m_f value implies that it is composed of a stiffer backbone than that of the $p(\text{NB-Hep})$ series which likely contributes to the lower magnitude of rubbery elasticity observed in the G_N^0 values (Figure 5.6A). Furthermore, the carbonyl group on the $p(\text{NBI-Hep})$ series significantly increases the fragility of the polymer compared to that of the $p(\text{NBI-Dec})$ series. Furthermore, the more rod-like character of the the $p(\text{NBI-Hep})$ series compared to the $p(\text{NB-Hep})$ series can also be seen in solution when comparing the z-average radius of gyration to the M_n of each series in tetrahydrofuran (THF) (Figure 5.28).

Conversely, the polymer dynamics at isofrictional conditions and similar DP of the four homobrush polymers ($p(\text{NB-PLA})$, $p(\text{NBI-PLA})$, $p(\text{NB-PS})$, and $p(\text{NBI-PS})$) exhibit a faster τ_1 with backbones composed of the norbornene group and a slower τ_1 with backbones composed of the norbornene imide group within polymers containing the same side-chain composition (Figure 5.7A and 5.7B). Again, these storage modulus mastercurves, covering a window of 8 to 10 orders of magnitude in frequency, were constructed via standard TTS processes at a reference

temperature $T_{\text{Ref}} = T_g + 30 \text{ }^\circ\text{C}$ for each of the four homobrush polymers. The estimated τ_1 for $p(\text{NB-PLA})$ DP159, $p(\text{NBI-PLA})$ DP189, $p(\text{NB-PS})$ DP172, and $p(\text{NBI-PS})$ DP140 is 4 s, 12 s, 43 s and 67 s, respectively. This trend can once again be confirmed by the results of the 5 % step-strain stress relaxation test where $p(\text{NB-PLA})$ DP159 relaxes to 0 Pa while $p(\text{NBI-PLA})$ DP189 relaxes to 10 Pa and $p(\text{NB-PS})$ DP172 relaxes to 272 Pa while $p(\text{NBI-PS})$ DP140 relaxes to 895 Pa (Figure 5.7C and 5.7D).

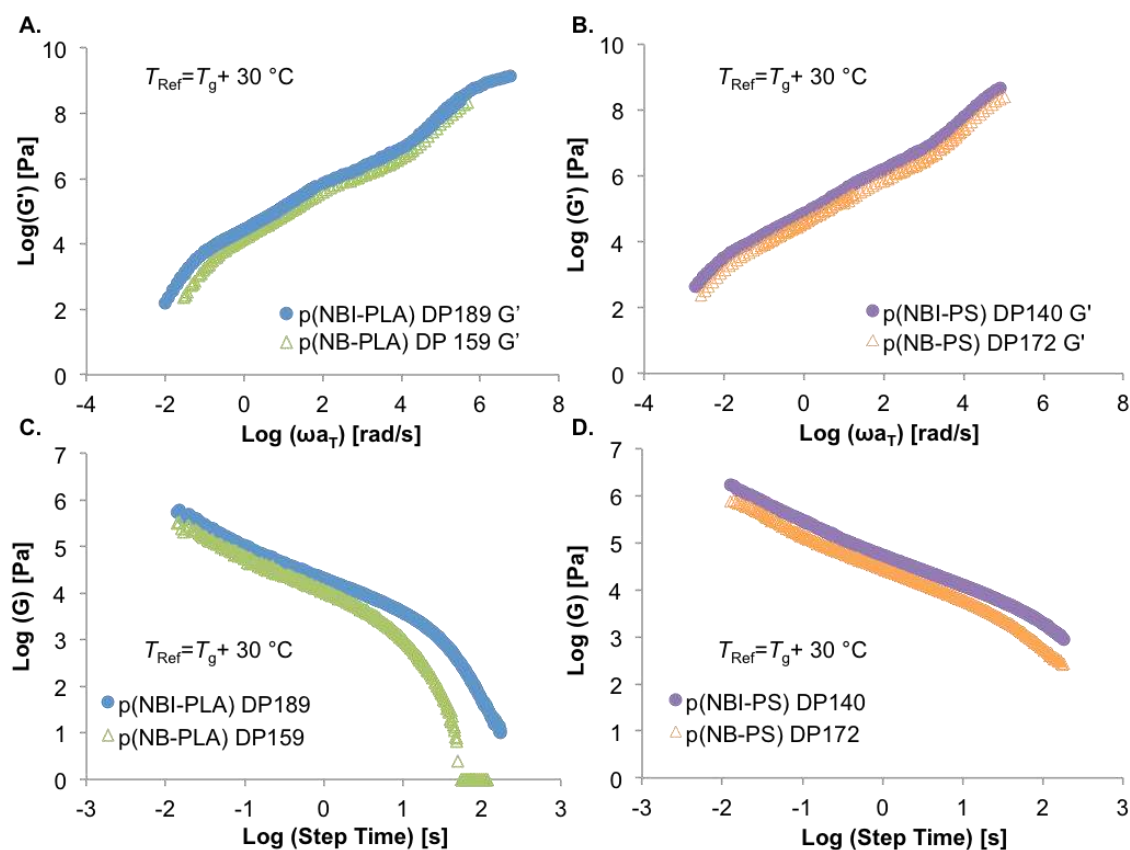


Figure 5.7. Storage modulus mastercurves of $p(\text{NB-PLA})$ and $p(\text{NBI-PLA})$ homobrush polymers (A) and of $p(\text{NB-PS})$ and $p(\text{NBI-PS})$ homobrush polymers (B) at a $T_{\text{Ref}} = T_g + 30 \text{ }^\circ\text{C}$. 5% step-strain stress relaxation tests of each of the 2 PLA homobrush polymers (C) and each of the 2 PS homobrush polymers (D) at a $T_{\text{Ref}} = T_g + 30 \text{ }^\circ\text{C}$.

Although it may seem that this observed trend for brush homopolymer τ_1 values is in direct contrast with what was observed in the linear homopolymer case (Figure 5.6), the slower τ_1 for the NBI backbone once it is incorporated into a brush polymer architecture confirms the

findings that the polymers constructed from NBI monomers yields an inherently stiffer backbone than the polymer constructed from NB monomers. This observation may be attributed to the concept of excluded volume and its effect on brush polymers.³⁵ The $p(\text{NB-PLA})$ or the $p(\text{NB-PS})$ brushes have a greater amount of excluded volume based on the degrees of freedom that the backbone composition affords the side chains closer to the backbone compared to that afforded to the side chains by the $p(\text{NBI-PLA})$ or the $p(\text{NBI-PS})$ brushes. This additional excluded volume translates into a more rigid brush macromolecule, which would manifest into a faster τ_1 for the homobrush in the same way that a more rigid linear polymer would relax faster than a more flexible linear polymer.

Once again, however, this insight into the relaxation of the homobrush polymers in the present study appears to contradict the differences observed in the abilities of the $p(\text{NB-PLA})$ - b - $p(\text{NB-PS})$ BBCP versus the $p(\text{NBI-PLA})$ - b - $p(\text{NBI-PS})$ BBCP to self-assemble to photonic crystals capable of reflecting longer wavelengths of light as seen in Figures 5.2 and 5.3. To resolve this apparent contradiction, it is important to consider the two distinct relaxation processes associated with lamellae forming BBCP that are not present in the relaxation of homobrush polymers.⁴² At shorter time scales, the relaxation of BBCPs with unentangled and densely grafted side chains is attributed to the cooperative mobility of internal slip layers within microphase-separated domains. This slipping is due to a high concentration of free chain ends in the middle of each domain. However, it is observed that the microphase separation dominates the longer time scale relaxation. The nanostructure morphology and the interface between the two microphase-separated domains are relatively soft, and therefore, require longer times to relax stress. Consequently, by applying this dual mode relaxation concept to the present study, it can be suggested that the inherently stiffer backbone composition of the norbornene imide group and

inherently less amount of excluded volume of the side-chains attached to the norbornene imide backbone both combine to produce a more efficient interfacial relaxation process and a more locally ordered morphology for the $p(\text{NBI-PLA})-b-p(\text{NBI-PS})$ BBCP as compared to the $p(\text{NB-PLA})-b-p(\text{NB-PS})$ BBCP. With more efficient interfacial relaxation, the regions of local ordering will be more prevalent and less energy input will be required for the domains to fully microphase segregate. Additionally, the inherently stiffer backbone allows for higher DP to increase the domain size in a more direct manner.

Conclusions

Four MW series of well-defined brush block copolymers with near identical side chain compositions but varying backbone compositions were synthesized using ruthenium-mediated ROMP. These BBCP materials were then thermally annealed to promote self-assembly into a periodic dielectric nanostructure able to interact with and reflect wavelengths of light throughout the UV and visible spectrum. Comparisons between the resulting reflections and nanostructure morphology of the polymeric photonic crystals with different backbone compositions lead to some significant observations and suggestions. The backbone composition dramatically affects the ability of the BBCP material to self-assemble into a nanostructure with regions of locally ordered domains large enough to reflect light across the visible spectrum from blue to red.

To gain further insight into the differences in the ability of brushes with different backbone compositions to self-assemble in the melt state, a series of linear and brush homopolymers were synthesized using ruthenium-mediated ROMP. These homopolymers mimicked the backbone composition of the BBCP materials and allowed for isolating and examining the polymer dynamics of the backbone without side-chains attached through a rheological study. By analyzing the observed τ_1 values, G_N^0 values, and fragility values of the

linear polymers, the norbornene imide backbone composition was determined to be inherently less elastic and stiffer than the norbornene backbone composition. Furthermore, rheological analysis of the homobrush polymers of each of the block and backbone compositions present in the BBCP materials, it is clear that the backbone composition significantly affected the dynamics of each homobrush in a similar way. The nature of the backbone's effect stems from the concept of excluded volume,³⁵ which allows the norbornene backbone composition to result in a stiffer brush macromolecule. However, when considering the present observations in the self-assembly of BBCPs with different backbone compositions and the observation of dual power law relaxations for lamellae forming BBCPs,⁴² it can be suggested that an inherently stiffer backbone is necessary in part to reduce the interfacial relaxation process to promote large regions of local ordering within the photonic crystal film, as well as be able to reflect beyond blue wavelengths of light by increasing the DP of each block.

Experimental Methods

(H₂IMes)(PPh₃)(Cl)₂RuCHPh was purchased from Umicore and was converted to (H₂IMes)(py)₂(Cl)₂RuCHPh via literature procedure.⁵⁴ All other chemicals were purchased from Sigma-Aldrich or VWR. All polymerizations were performed in a nitrogen-filled glovebox unless stated otherwise. Column chromatography was performed using a Combiflash Rf+ autocolumn from Teledyne ISCO. NMR spectra were recorded on a Bruker Ultrashield 400 MHz spectrometer. Chemical shifts were referenced using internal solvent resonance, ¹H: 7.26 ppm and ¹³C: 77.16 ppm for CDCl₃. The chemical shifts are reported as parts per million relative to tetramethylsilane. Deuterated chloroform was purchased from Cambridge Isotope Laboratories.

Analysis of isolated and vacuum-dried polymer MW and dispersity was performed using gel permeation chromatography (GPC) coupled with multi-angle light scattering (MALS), using

an Agilent HPLC fitted with one guard column and three Plgel 5 μ M MIXED-C gel permeation columns in series. The detectors used were a Wyatt Technology TrEX differential refractometer and a Wyatt Technology miniDAWN TREOS light scattering detector, which allows the direct measurement of absolute MW. Absolute MWs were determined using dn/dc values calculated by assuming 100% mass recovery of the polymer sample injection into the GPC. The solvent used was tetrahydrofuran (THF) with a flow rate of 1.0 mL per minute. The R_z value of each polymer was calculated using the multi angle light scattering detector in the miniDAWN TREOS.

Thermal Gravimetric Analysis (TGA) was conducted using a TA Instruments TGA Q50 or TGA Q500. The thermal decomposition data was obtained under a nitrogen gas flow of 40 mL/min by ramping the temperature from 25 °C up to 850 °C at a ramp rate of 10 °C/minute.

Differential Scanning Calorimetry (DSC) was conducted using a TA Instruments DSC 2500. To erase thermal history, an initial sweep ramped from 0 °C to 200 °C at a ramp rate of 10 °C/min. The temperature was held constant at 200 °C for 3 minutes before it was cooled to 0 °C at a ramp rate of -10 °C/min where the temperature was held constant at 0°C for 3 minutes. Thermal data was collected from the second sweep which consists of ramping the temperature from 0 °C up to 200 °C at a rate of 5 °C/min. However, for the NB-Hep polymer, the range of the test was -90 °C to 150 °C, but the rates of heating and cooling were the same as the rates used to test the rest of the polymers. This analysis was performed to measure the low glass transition temperature of that particular polymer.

The rheological experiments were performed using a DHR-2 rheometer (TA Instruments) with 8 mm parallel plate geometry under nitrogen purge. The sample was loaded onto the 8 mm plate at experimental conditions until melting and then slowly pressed until the gap was approximately 1 mm using axial stress. Before testing, the samples were kept for 30 minutes – 2

hours until the axial stress was 0.0 ± 0.2 N. First, strain sweep experiments were performed to determine the linear viscoelastic region of the materials. Oscillatory frequency sweep was carried out from 0.01 to 100 rad/s with a strain in the linear strain regime. The temperature regime for the reference temperature of the time-temperature superposition (TTS) was determined based on the T_g of the polymer series. The TTS was completed with a vertical and lateral shift within the TA Trios Software. Van Gorp-Palmen plots were used to establish the validity of the time-temperature superposition of the polymer series.

Reflection measurements were performed using a Cary 5000 UV/vis/NIR spectrophotometer, equipped with an integrating sphere diffuse reflectance accessory (DRA) (Internal DRA-2500) using the standard wide-open aperture. The samples were scanned at a rate of 600 nm/s from 800 to 280 nm.

Scanning electron microscopy images were taken on a JEOL JSM-6500F field emission scanning electron microscope after freeze fracturing the films and then staining the fractured films with RuO_4 . The samples were coated with a 10 nm thick layer of gold before imaging.

Monomer Synthesis

Exo-5-Norbornene-2-methanol

Preparation of exo-5-norbornene-2-methanol was prepared *via* slight modification to a previously reported procedure.⁵⁵ 12.4 g (3.0 eq, 326 mmol) of lithium aluminum hydride (LAH) was suspended in anhydrous THF (300 mL) under nitrogen atmosphere at 0°C. 15.0 g of exo-5-norbornene-2-carboxylic acid was added to the suspension as a solution in dry THF (15.0 g/20 mL). The 1000 mL flask was placed in an oil bath, and the reaction mixture refluxed for 16 h. Next, the reaction mixture was cooled in an ice bath, and Feiser workup procedure followed: dilute with ether at 0 °C, slowly add 0.5 mL water, add 0.5 mL 15% aqueous sodium hydroxide,

add 1.3 mL water, warm to room temperature and stir for 20 minutes, add magnesium sulfate, stir for 20 minutes, filter to remove salts. Next, the solution was concentrated under reduced pressure to yield a slightly yellow oil. The product was purified *via* distillation, yielding a colorless oil. Yield = 12.9 g, 95.5 %. ^1H NMR (400 MHz, CDCl_3) δ 6.05 (m, 2H), 3.67 (m, 1H), 3.50 (m, 1H), 2.99 (s, 0.15H), 2.91 (s, 0.15H), 2.79 (s, 1H), 2.73 (s, 1H), 2.10 (s, 1H), 1.83 (m, 0.1H), 1.59 (m, 1H), 1.27 (m, 3H), 1.08 (m, 1H).

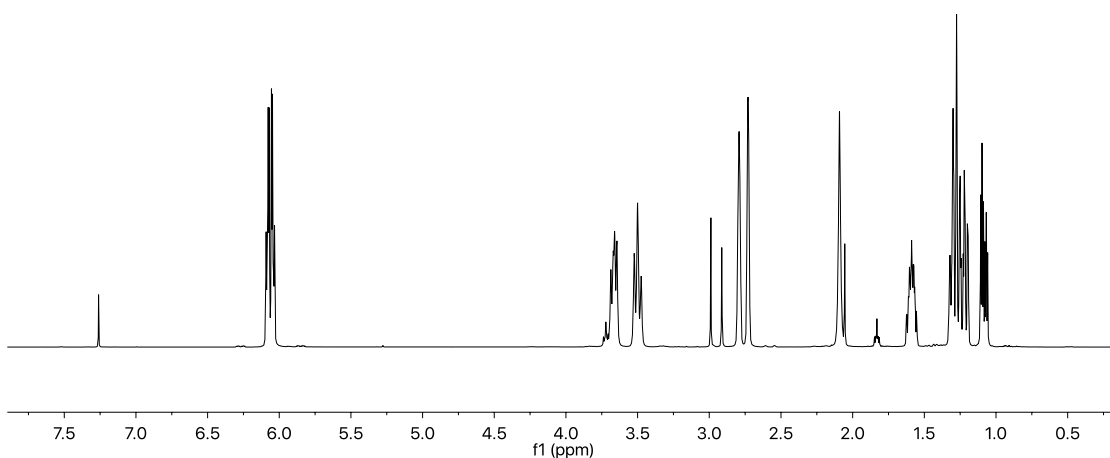


Figure 5.8. ^1H NMR spectra of *exo*-5-norbornene-2-methanol in CDCl_3 .

Exo-5-Norbornene-2-methyl heptanoate Monomer (*NB-Hep*)

A 100 mL Schlenk flask was charged with a stir bar and flame-dried. Once the flask was backfilled with nitrogen, 1.0 g (1.1 eq, 8.1 mmol) of *exo*-5-norbornene-2-methanol, 0.95 g (1.0 eq, 7.3 mmol) of *n*-heptanoic acid, and 0.089 g (0.1 eq, 0.73 mmol) of 4-Dimethylaminopyridine was added to the Schlenk flask under positive nitrogen. These solids were then dissolved in 50 mL of anhydrous dichloromethane. The solution was then cooled to 0 °C while stirring before 1.5 g (1.5 eq., 9.5 mmol) of 1-Ethyl-3-(3-dimethylaminopropyl)carbodiimide was added slowly

under positive nitrogen. The reaction solution was then allowed to stir and warm to room temperature for 16 hours. Next, the solution was washed with 0.1 M HCl twice and the organic layer was then dried over MgSO₄. The MgSO₄ was then filtered out before the solution was concentrated to an oily substance. Then, the crude product was dissolved in hexanes and run through a silica plug with 100 % Hexanes. The 1st peak was collected and concentrated in vacuo to yield the product as a clear oil. Yield = 0.77 g, 81 %. ¹H NMR (400 MHz, CDCl₃) δ 6.06 (m, 2H), 4.10 (m, 1H), 3.92 (m, 1H), 2.79 (s, 1H), 2.65 (s, 1H), 2.27 (t, 2H), 1.67 (m, 1H) 1.60 (m, 2H), 1.27 (m, 10H), 1.10 (m, 1H), 0.85 (m, 3H); ¹³C NMR (101 MHz, CDCl₃) δ 173.79, 136.89, 136.26, 68.25, 44.95, 43.64, 41.59, 37.97, 34.47, 31.46, 29.64, 28.80, 24.94, 22.52, 14.07.

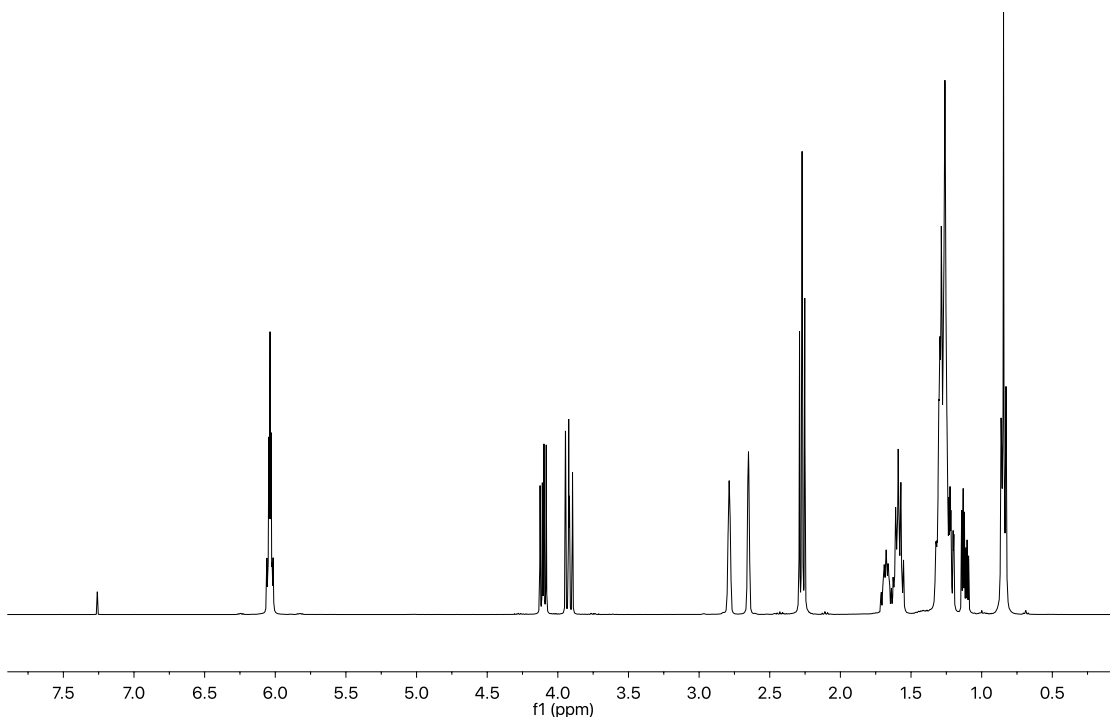


Figure 5.9. ¹H NMR spectra of NB-Hep monomer in CDCl₃.

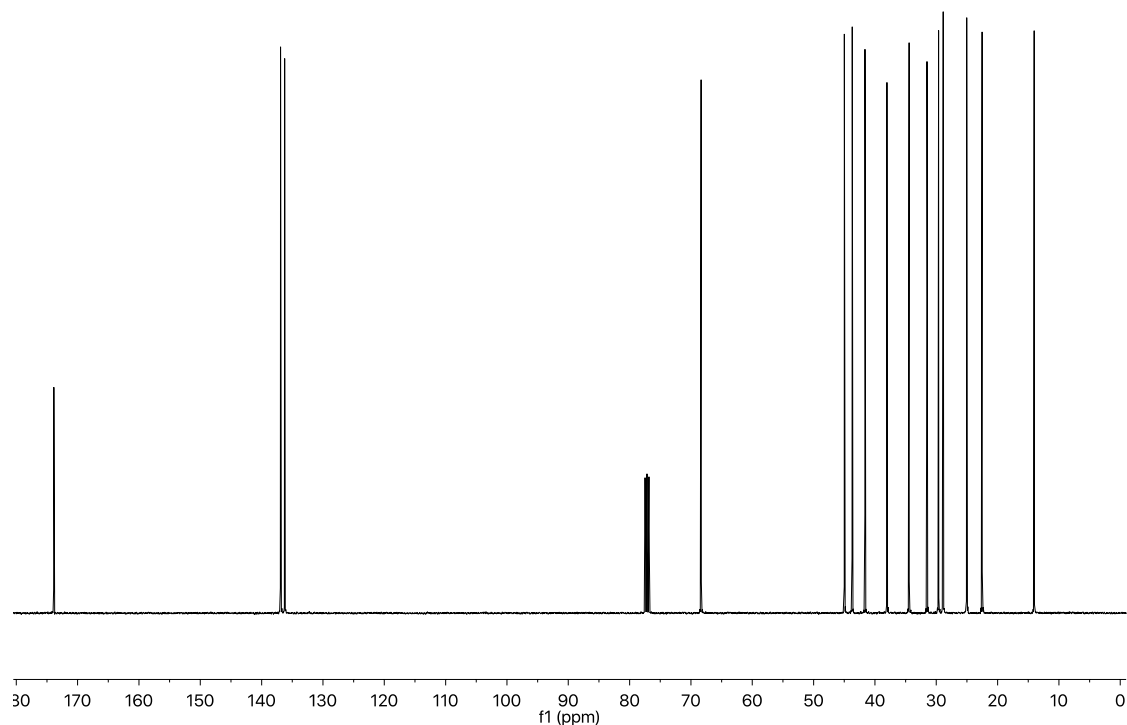


Figure 5.10. ^{13}C NMR spectra of NB-Hep monomer in CDCl_3 .

N-Methyl heptanoate-exo-norbornene-5,6-dicarboximide Monomer (NBI-Hep)

N-(hydroxyethyl)-cis-5-norbornene-exo-2,3-dicarboximide was prepared according to literature procedure.⁵⁶ A 100 mL Schlenk flask was charged with a stir bar and flame-dried. Once the flask was backfilled with nitrogen, 2.0 g (1.1 eq, 9.7 mmol) of N-(hydroxyethyl)-cis-5-norbornene-exo-2,3-dicarboximide, 1.1 g (1.0 eq, 8.8 mmol) of *n*-heptanoic acid, and 0.32 g (0.1 eq, 2.6 mmol) of 4-Dimethylaminopyridine was added to the Schlenk flask under positive nitrogen. These solids were then dissolved in 30 mL of anhydrous dichloromethane. The solution was then cooled to 0 °C while stirring before 2.3 g (1.5 eq., 13 mmol) of 1-Ethyl-3-(3-dimethylaminopropyl)carbodiimide was added slowly under positive nitrogen. The reaction solution was then allowed to stir and warm to room temperature for 16 hours. Next, the solution was washed with 0.1 M HCl twice and the organic layer was then dried over MgSO_4 . The MgSO_4 was then filtered out before the solution was concentrated to an oily substance. Then, the

crude product was dissolved in a 2 hexanes : 1 ethyl acetate mixture and run through a silica column. The product peak was collected and concentrated in vacuo to yield the product as a clear oil. Yield = 1.6 g, 80 %. ^1H NMR (400 MHz, CDCl_3) δ 6.28 (s, 2H), 4.23 (t, 2H), 3.74 (t, 2H), 3.27 (t, 2H), 2.69 (s, 2H), 2.25 (t, 2H), 1.55 (m, 3H), 1.28 (m, 7H), 0.85 (m, 3H); ^{13}C NMR (101 MHz, CDCl_3) δ 178.20, 173.06, 138.01, 60.55, 47.95, 45.37, 42.81, 37.72, 34.24, 31.57, 28.90, 24.78, 22.60, 14.14.

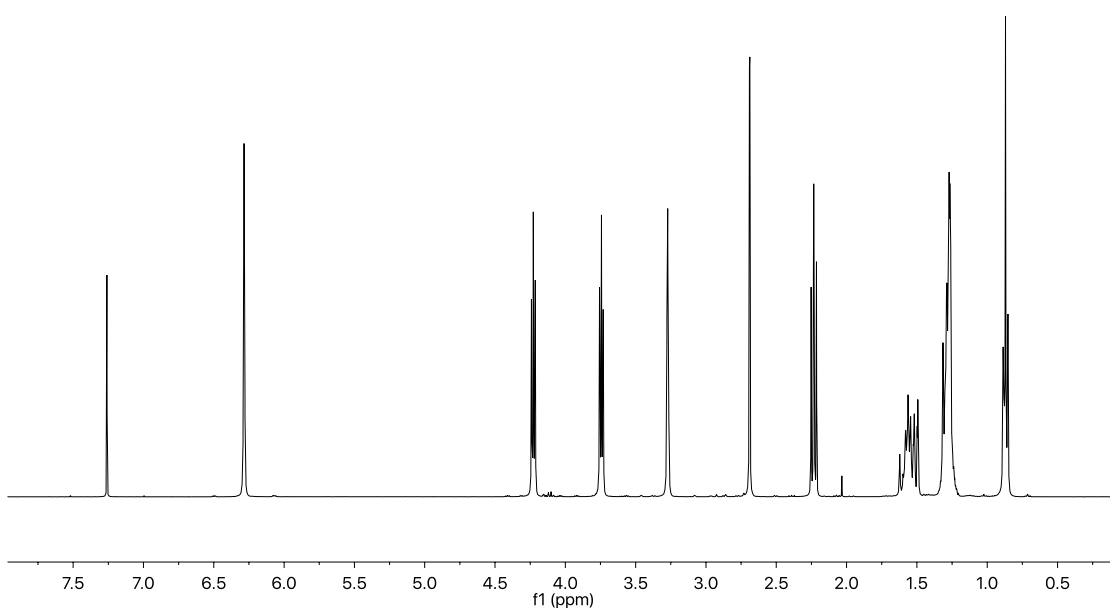


Figure 5.11. ^1H NMR spectra of NBI-Hep monomer in CDCl_3 .

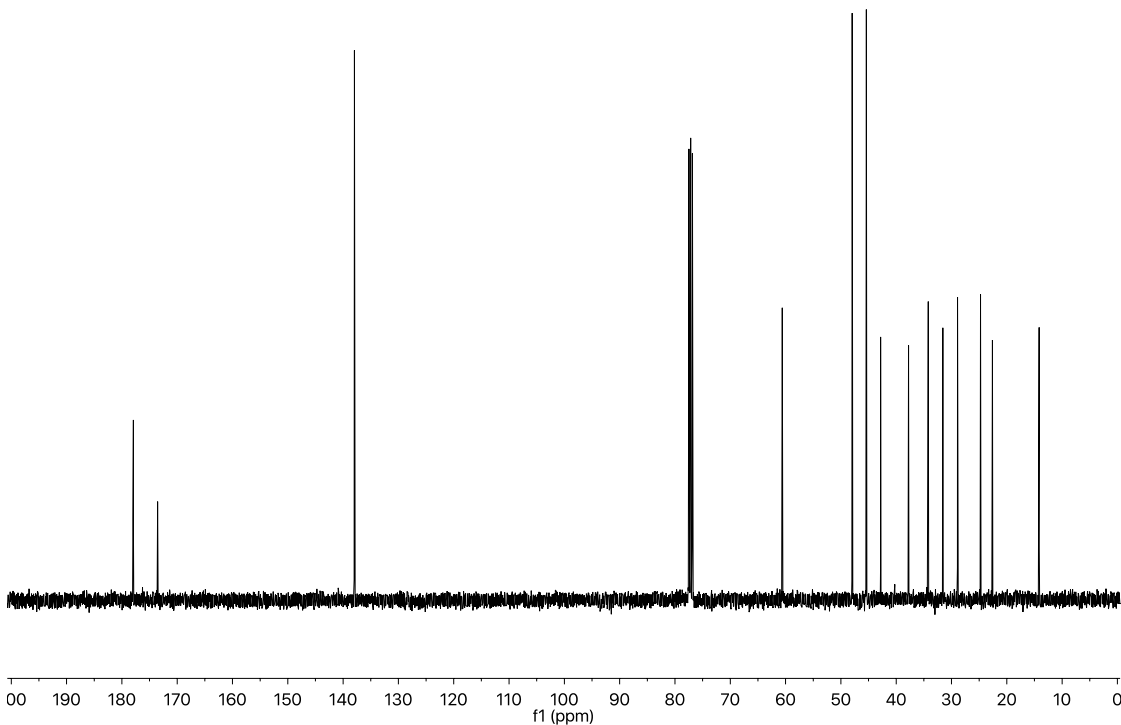


Figure 5.12. ^{13}C NMR spectra of NBI-Hep monomer in CDCl_3 .

N-Decyl-exo-Norbornene-5,6-dicarboximide Monomer (DecNBI)

N-Decyl-exo-Norbornene-5,6-dicarboximide was prepared according to literature procedure.¹⁸ There was one adjustment made to the reported synthetic procedure, which was to use *n*-decylamine instead of *n*-hexylamine. ^1H NMR (400 MHz, CDCl_3) δ 6.25 (s, 2H), 3.41 (t, 2H), 3.25 (s, 2H), 2.64 (s, 2H), 1.50 (m, 3H), 1.25 (m, 16H), 0.85 (t, 3H).

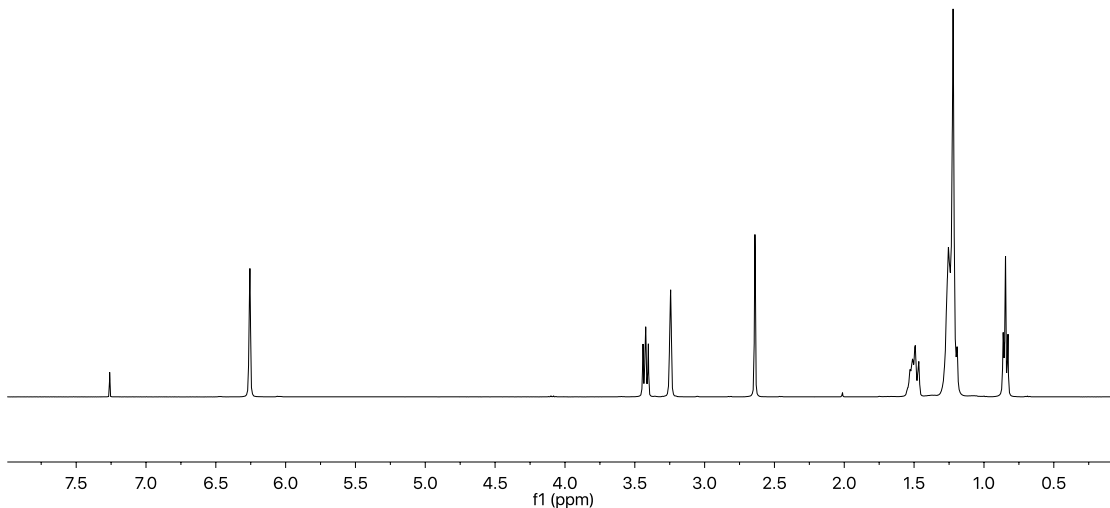


Figure 5.13. ^1H NMR spectra of NBI-Decyl monomer in CDCl_3 .

Macromonomer Synthesis

Norbornene capped Poly(lactide) Macromonomer (NB-PLA MM)

To a degassed, backfilled with nitrogen, and three times flame dried 500mL Schlenk flask equipped with a stir bar was added freshly sublimed and stored under nitrogen racemic lactide monomer (20.0 g, 0.14 mol, 22 eq.), $\text{Sn}(\text{Oct})_2$ [purity 92.5-100% purchased from Sigma and used as is] (4.2 μL , 0.4% wt. relative to alcohol initiator), and exo-5-norbornene-2-methanol (1.3 g, 11 mmol, 1.0 eq.). Once combined, the reaction mixture was placed in an oil bath preheated to 130 $^\circ\text{C}$. During the reaction, the lactide sublimes on the sidewalls of the flask: to mitigate this issue, a Bunsen burner was used to heat the sidewalls every 15 minutes to melt lactide monomer back into solution. This heating of the sidewalls was done to ensure consumption of monomer. The reaction was complete in 4 hours, which was qualitatively tracked by the rate of sublimation of lactide onto the sidewalls. After monomer consumption was

determined to be complete, the NB-PLA was allowed to cool and dissolved in anhydrous DCM and diluted to a concentration of 1g NB-PLA / 15 mL. The DCM solution was filtered through ~100 g of celite to remove tin catalyst. Once the solution was completely filtered an additional 200 mL of DCM was washed through the celite pad to recover any remaining polymer. Solvent was removed under reduced pressure. The NB-PLA was then dried in a vacuum overnight at 60 - 70 °C to remove remaining solvent, giving a near quantitative yield (<95%). For the BBCP MM, the GPC results show a MM with $M_n = 3,251$ g/mol PDI = 1.07. For the homobrush MM, the GPC results show a MM with $M_n = 3,065$ g/mol PDI = 1.21.

Norbornene-imide capped Poly(lactide) Macromonomer (NBI-PLA MM)

The procedure for the synthesis of NB-PLA was used to make NBI-PLA, however, N-(hydroxyethyl)-cis-5-norbornene-exo-2,3-dicarboximide was used in place of exo-5-norbornene-2-methanol as the initiator. For the BBCP MM, the GPC results show a MM with $M_n = 3,428$ g/mol PDI = 1.06. For the homobrush MM, the GPC results show a MM with $M_n = 3,150$ g/mol PDI = 1.13.

Norbornene capped Poly(styrene) Macromonomer (NB-PS MM)

This macromonomer was made following the universal thermally-driven ATRP conditions for styrene with slight modifications.⁵⁷ The ATRP initiator, N - ((2 - Bromo - 2 - methylpropanoyl) ethyl) - cis - 5 - norbornene - *exo* -2 - methanol, was prepared as previously reported.⁵⁸

To a degassed, backfilled with nitrogen, and three times flame dried 200 mL Schlenk flask equipped with a stir bar was added freshly distilled styrene monomer (23 g, 0.23 mol, 58 eq.), N - ((2 - Bromo - 2 - methylpropanoyl) ethyl) - cis - 5 - norbornene - *exo* -2 - methanol

(1.1 g, 3.9 mmol, 1.0 eq.), pre-activated copper wire (5 cm), copper bromide (0.043 g, 0.19 mmol, 0.05 eq), and 2-propanol (26 mL). To pre-activate the copper wire, it was soaked in concentrated hydrochloric acid for 15 minutes, and rinsed in DI water and dried. This mixture was then sparged with nitrogen for 15 minutes. Once the solution had been sparged, N-pentamethyldiethylenetriamine (0.24 g, 1.4 mmol, 0.36 eq) was added to the mixture and heated to 60 °C while stirring. The reaction was monitored via NMR and was cooled down to room temperature at 50 % conversion of monomer to polymer.

Once cooled, the reaction mixture was dissolved in DCM and filtered through a large, neutral alumina column to remove the copper salts. The resulting solution was then concentrated in vacuo before using column chromatography to purify the product. Three 80 gram silica columns were loaded with the crude polymer product and a gradient column was run starting with 35 % DCM and 65 % Hexanes ramping up to 100 % DCM. The purified product peak was then isolated and concentrated in vacuo. This product was then dissolved in DCM and precipitated into room temperature methanol. The precipitate was then filtered and dried in a vacuum oven overnight at 70 °C. Yield = 16 %, M_n = 3,649 g/mol, PDI = 1.05

Norbornene-imide capped Poly(styrene) Macromonomer (NBI-PS MM)

The same procedure for the synthesis of NB-PS was used to make NBI-PS, however, the ATRP initiator, N - ((2 - Bromo - 2 - methylpropanoyl) ethyl) - cis - 5 - norbornene - *exo* -2,3-dicarboximide (3.5 g, 9.9 mmol, 1.0 eq.), was used in place of the previous initiator, N - ((2 - Bromo - 2 - methylpropanoyl) ethyl) - cis - 5 - norbornene - *exo* -2 - methanol. This procedure was completed as previously reported.¹³ Yield = 10 %, M_n = 4,422 g/mol, PDI = 1.01.

General Homopolymer Synthesis

In a nitrogen-filled glovebox, a 20 mL vial was charged with a stir bar, 0.1 g of monomer or macromonomer and diluted to 0.05 M with anhydrous THF. With rapid stirring, the appropriate amount of G3 catalyst completely dissolved in THF was quickly added via syringe. At full conversion determined by GPC, the polymerization was quenched by the addition of 0.5 mL of ethyl vinyl ether. The polymer was precipitated out into 20 mL of methanol at room temperature (except for the PLA homobrushes and NB-Hep polymers which were precipitated into methanol at -78 °C), after which the polymer was isolated, washed with excess methanol, and dried under reduced pressure at 50 °C to a constant weight. Yield was near quantitative by mass.

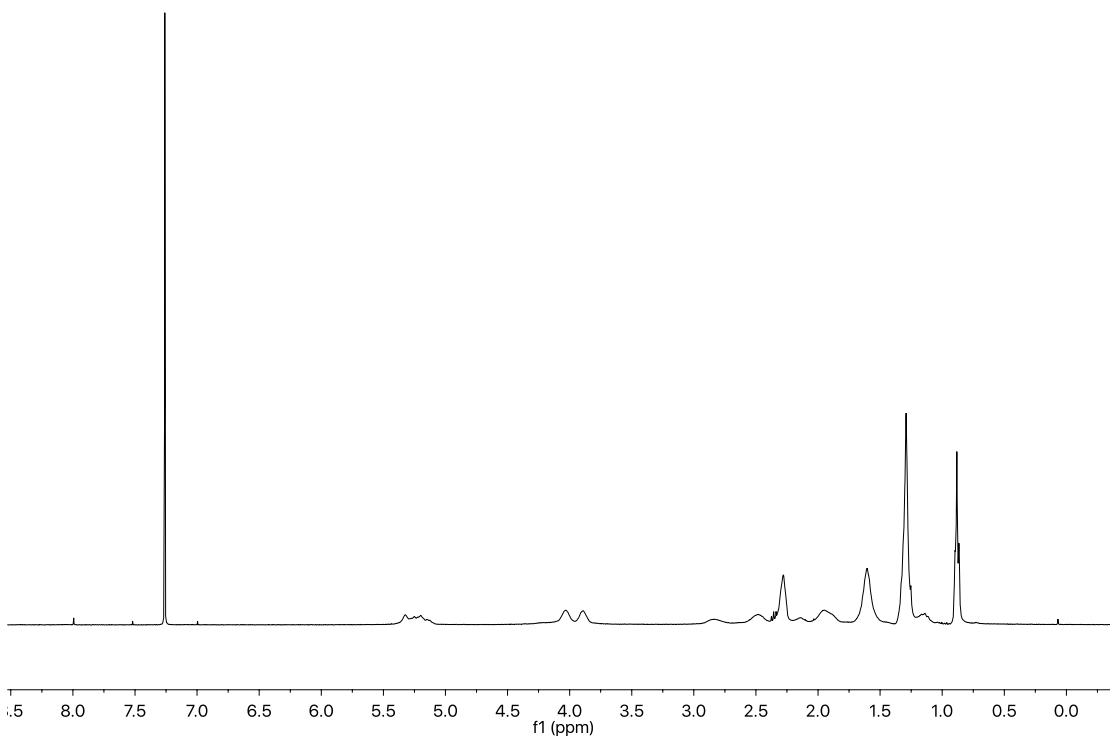


Figure 5.14. Isolated and representative poly(NB-Hep) (polymer shown $M_n = 2.55 \times 10^2$ kg/mol) ^1H NMR (400 MHz, CDCl_3): δ 5.27 (m), 3.97 (d), 2.86 (bs), 2.5 (bs), 2.29 (m), 2.15 (bs), 1.97 (bs), 1.61 (bs), 1.24 (m), 0.90 (s) [Water singlet from CDCl_3 at 1.55 ppm].

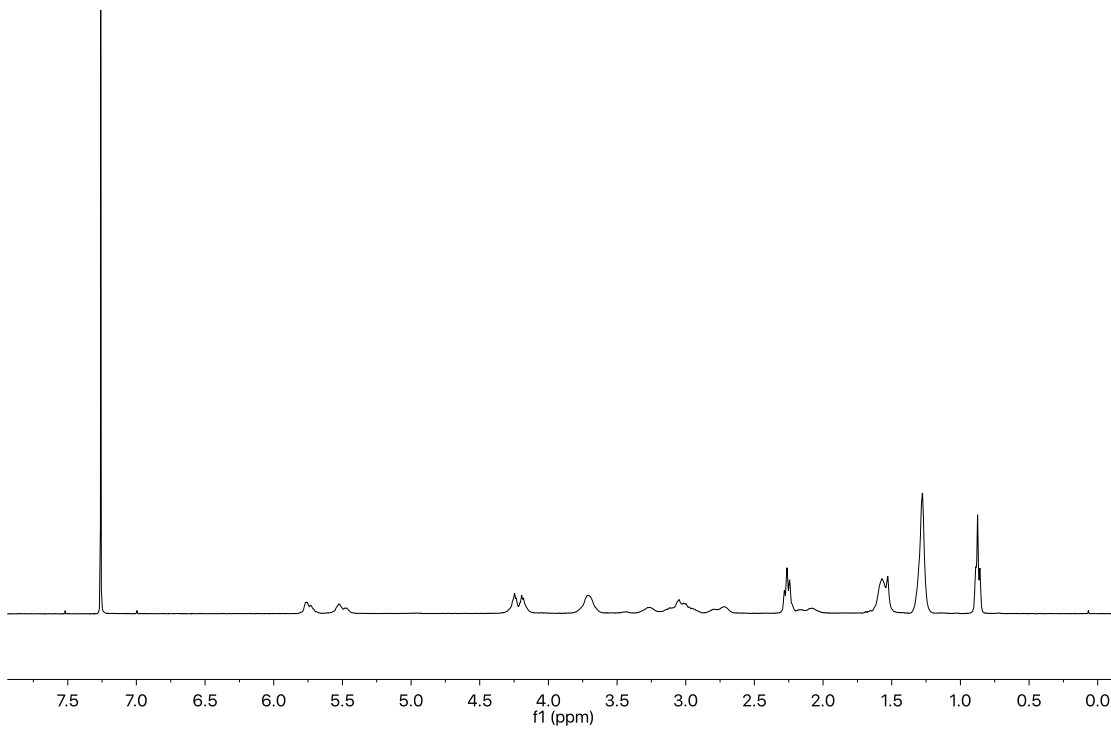


Figure 5.15. Isolated and representative poly(NBI-Hep) (polymer shown $M_n = 3.74 \times 10^2$ kg/mol) ^1H NMR (400 MHz, CDCl_3): δ 5.75 (d), 5.50 (d), 4.23 (d), 3.71 (bs), 3.02 (m), 2.25 (m), 1.57 (bs), 1.28 (bs), 0.88 (m) [Water singlet from CDCl_3 at 1.55 ppm].

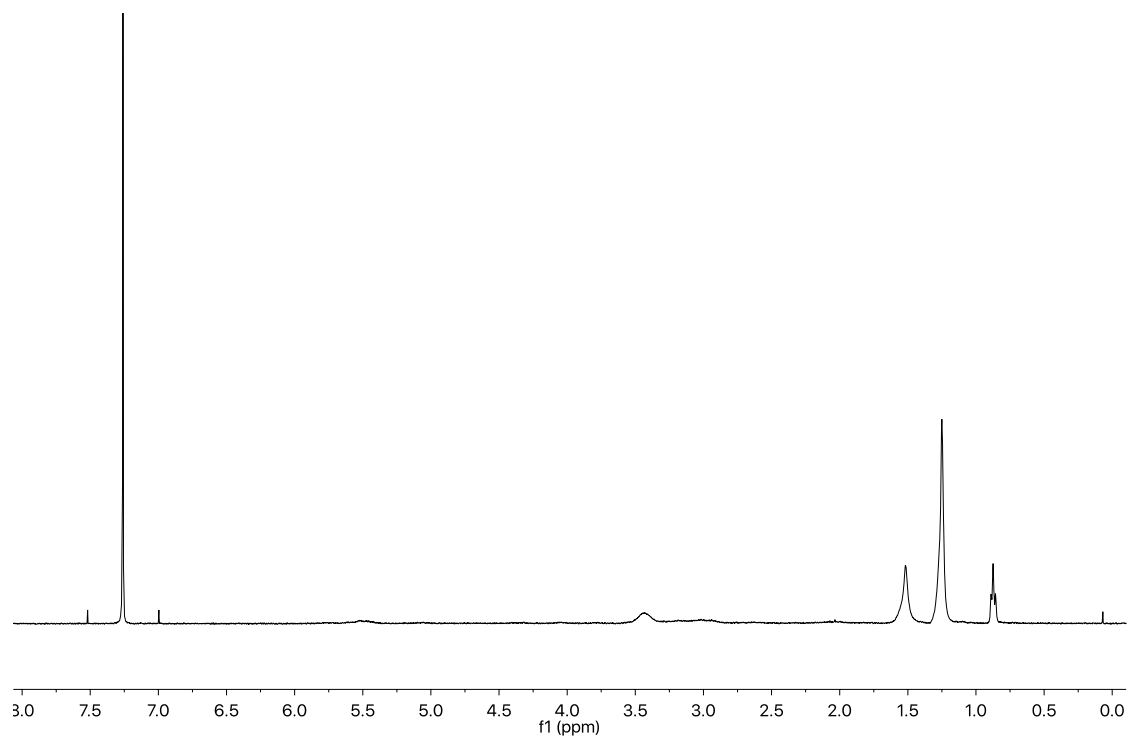


Figure 5.16. Isolated and representative poly(NBI-Dec) (polymer shown $M_n = 7.80 \times 10^2$ kg/mol) ¹H NMR (400 MHz, CDCl₃): δ 5.50 (bs), 3.43 (bs), 1.51 (bs), 1.24 (s), 0.88 (t) [Water singlet from CDCl₃ at 1.55 ppm].

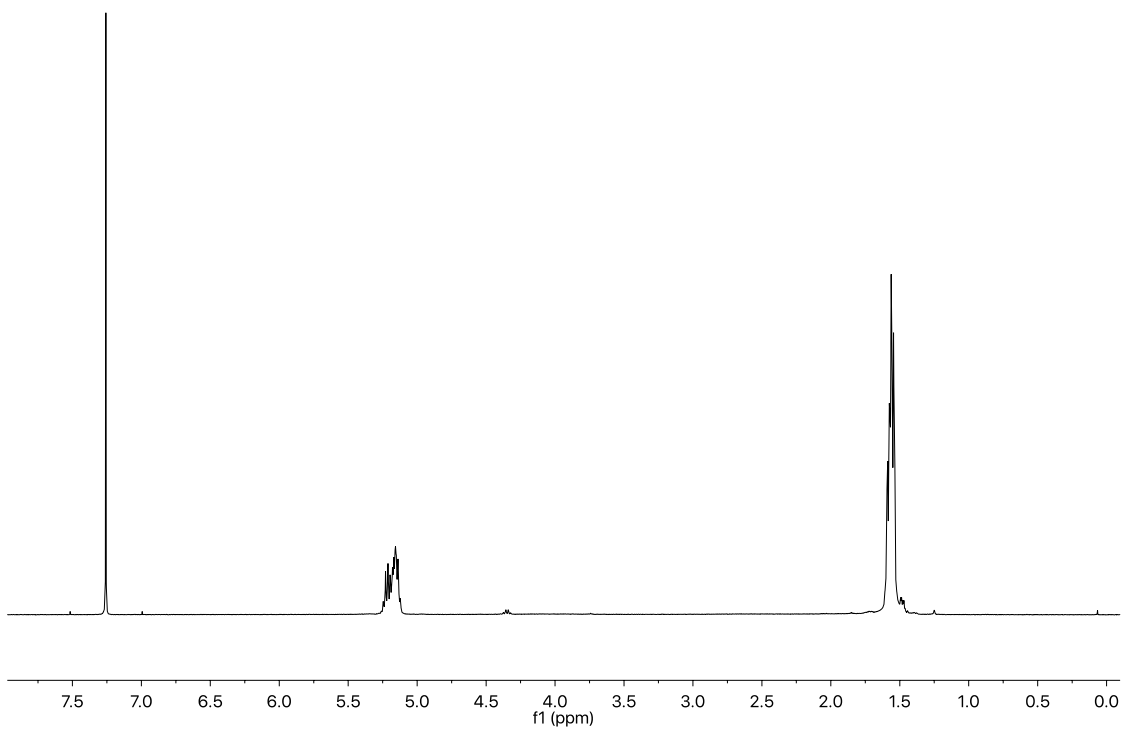


Figure 5.17. Isolated and representative poly(NB-PLA) (polymer shown $M_n = 1.56 \times 10^3$ kg/mol) ¹H NMR (400 MHz, CDCl₃): δ 5.18 (m), 4.35 (q), 1.56 (m), 1.26 (s) [Water singlet from CDCl₃ at 1.55 ppm].

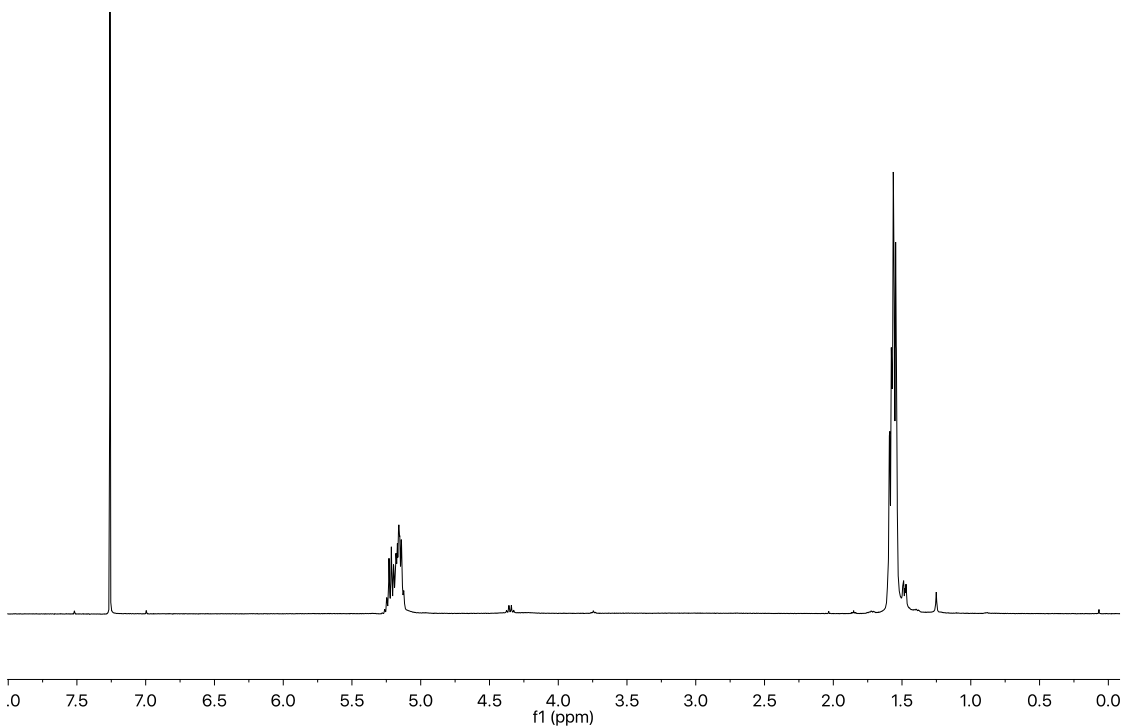


Figure 5.18. Isolated and representative poly(NBI-PLA) (polymer shown $M_n = 3.58 \times 10^3$ kg/mol) ¹H NMR (400 MHz, CDCl₃): δ 5.18 (m), 4.35 (q), 3.75 (m), 1.56 (m), 1.26 (s) [Water singlet from CDCl₃ at 1.55 ppm].

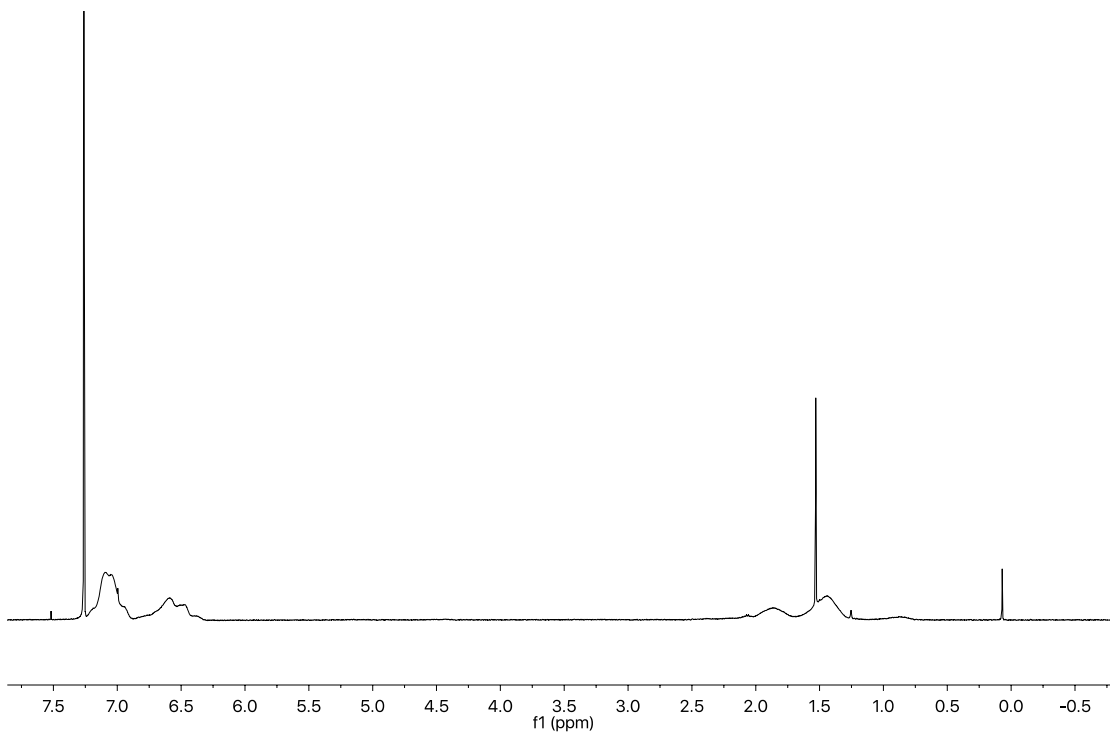


Figure 5.19. Isolated and representative poly(NB-PS) (polymer shown $M_n = 1.24 \times 10^3$ kg/mol) ¹H NMR (400 MHz, CDCl₃): δ 7.08 (m), 6.62 (m), 1.86 (bs), 1.46 (bs), 0.87 (bs), [Water singlet from CDCl₃ at 1.55 ppm].

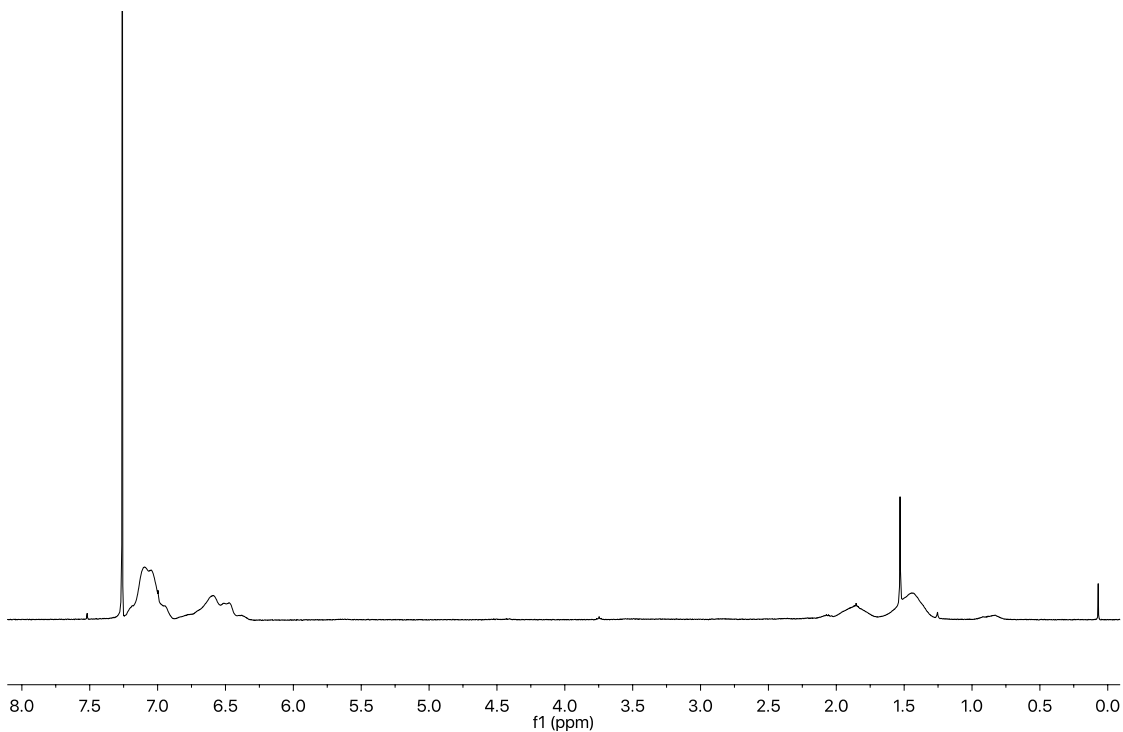


Figure 5.20. Isolated and representative poly(NBI-PS) (polymer shown $M_n = 1.12 \times 10^3$ kg/mol) ^1H NMR (400 MHz, CDCl_3): δ 7.08 (m), 6.62 (m), 1.86 (bs), 1.46 (bs), 0.86 (bs), [Water singlet from CDCl_3 at 1.55 ppm].

Homopolymer Characterization via Gel Permeation – Multi Angle Light Scattering Traces

(GPC-MALS):

Table 5.2. GPC-MALS analysis data of poly(NB-Hep) MW series.

Polymer Sample	GPC M_n (kg/mol)	GPC M_w (kg/mol)	Dispersity (M_w/M_n)	Degree of Polymerization from M_n
p(NB-Hep)-DP107	25.3	25.5	1.01	107
p(NB-Hep)-DP325	76.9	80.6	1.05	325
p(NB-Hep)-DP376	89.0	96.1	1.08	376
p(NB-Hep)-DP437	1.03×10^2	1.18×10^2	1.14	437
p(NB-Hep)-DP465	1.10×10^2	1.45×10^2	1.32	465
p(NB-Hep)-DP721	1.70×10^2	1.94×10^2	1.14	721
p(NB-Hep)-DP996	2.36×10^2	2.58×10^2	1.10	996
p(NB-Hep)-DP1028	2.43×10^2	3.50×10^2	1.44	1,028
p(NB-Hep)-DP1077	2.55×10^2	3.09×10^2	1.21	1,077

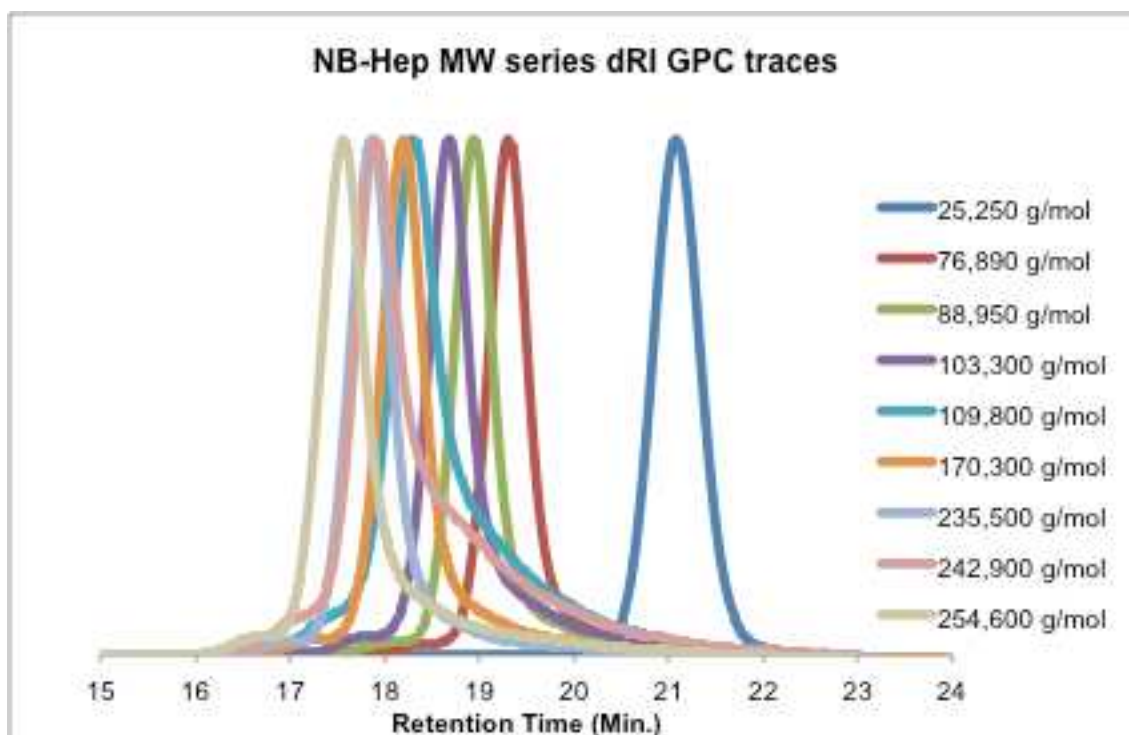


Figure 5.21. Relative Scaling of GPC RI detector traces for p(NB-Hep) MW series.

Table 5.3. GPC-MALS analysis data of poly(NBI-Hep) MW series.

Polymer Sample	GPC M_n (kg/mol)	GPC M_w (kg/mol)	Dispersity (M_w/M_n)	Degree of Polymerization from M_n
p(NBI-Hep)-DP29	9.20	9.49	1.03	29
p(NBI-Hep)-DP75	23.9	24.5	1.02	75
p(NBI-Hep)-DP110	35.4	36.0	1.02	110
p(NBI-Hep)-DP148	47.3	47.8	1.01	148
p(NBI-Hep)-DP260	83.0	84.1	1.01	260
p(NBI-Hep)-DP360	1.15×10^2	1.17×10^2	1.02	360
p(NBI-Hep)-DP454	1.45×10^2	1.48×10^2	1.02	454
p(NBI-Hep)-DP495	1.58×10^2	1.61×10^2	1.02	495
p(NBI-Hep)-DP618	1.98×10^2	2.08×10^2	1.05	618
p(NBI-Hep)-DP621	1.98×10^2	2.04×10^2	1.03	621
p(NBI-Hep)-DP1051	3.36×10^2	3.46×10^2	1.03	1,051
p(NBI-Hep)-DP1135	3.63×10^2	3.73×10^2	1.03	1,135
p(NBI-Hep)-DP1172	3.74×10^2	3.83×10^2	1.02	1,172

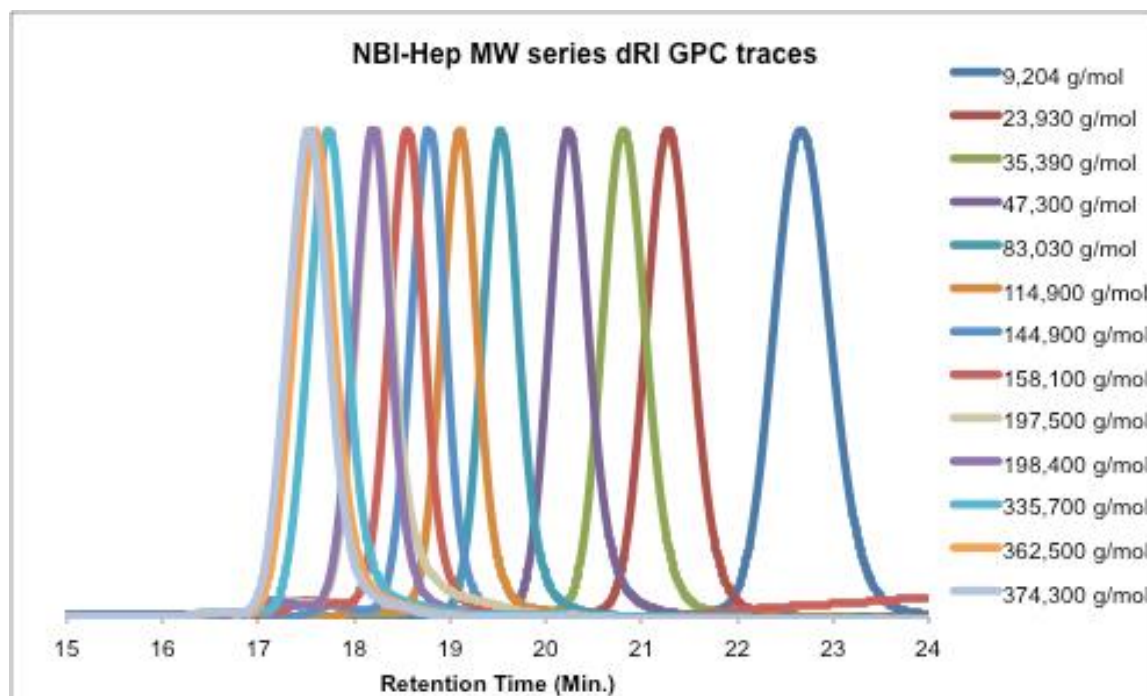


Figure 5.22. Relative Scaling of GPC RI detector traces for p(NBI-Hep) MW series.

Table 5.4. GPC-MALS analysis data of poly(NBI-Dec) MW series.

Polymer Sample	GPC M_n (kg/mol)	GPC M_w (kg/mol)	Dispersity (M_w/M_n)	Degree of Polymerization from M_n
p(NBI-Dec)-DP227	68.8	69.9	1.02	227
p(NBI-Dec)-DP376	1.14×10^2	1.16×10^2	1.02	376
p(NBI-Dec)-DP512	1.56×10^2	1.58×10^2	1.02	512
p(NBI-Dec)-DP863	2.62×10^2	2.69×10^2	1.03	863
p(NBI-Dec)-DP972	2.95×10^2	3.07×10^2	1.04	972
p(NBI-Dec)-DP1575	4.78×10^2	5.48×10^2	1.15	1,575
p(NBI-Dec)-DP2261	6.86×10^2	7.92×10^2	1.15	2,261
p(NBI-Dec)-DP2570	7.80×10^2	9.50×10^2	1.22	2,570

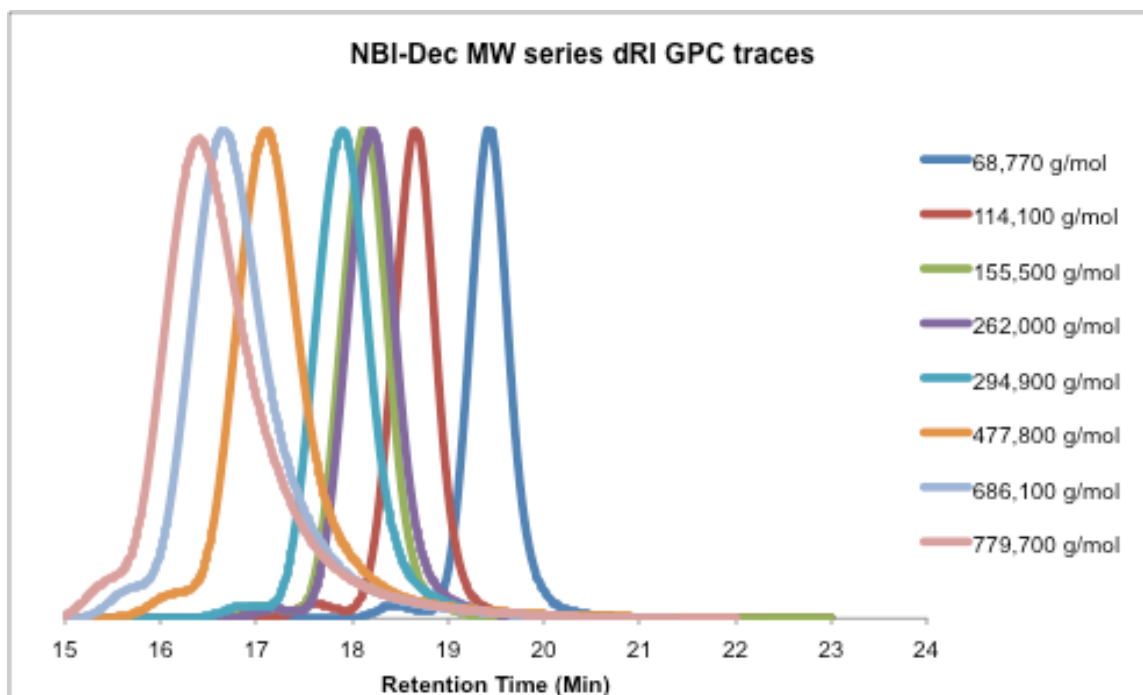


Figure 5.23. Relative Scaling of GPC RI detector traces for p(NBI-Dec) MW series.

Table 5.5. GPC-MALS analysis data of poly(NB-PLA) MW series.

Polymer Sample	GPC M_n (kg/mol)	GPC M_w (kg/mol)	Dispersity (M_w/M_n)	Degree of Polymerization from M_n
p(NB-PLA)-DP14	42.3	43.0	1.02	14
p(NB-PLA)-DP22	68.2	69.9	1.03	22
p(NB-PLA)-DP24	74.7	75.5	1.01	24
p(NB-PLA)-DP68	2.10×10^2	2.12×10^2	1.01	68
p(NB-PLA)-DP69	2.12×10^2	2.16×10^2	1.02	69
p(NB-PLA)-DP95	2.91×10^2	2.99×10^2	1.03	95
p(NB-PLA)-DP147	4.50×10^2	4.65×10^2	1.03	147
p(NB-PLA)-DP184	5.65×10^2	5.79×10^2	1.02	184
p(NB-PLA)-DP298	9.13×10^2	9.50×10^2	1.04	298
p(NB-PLA)-DP442	1.36×10^3	1.53×10^3	1.13	442
p(NB-PLA)-DP510	1.56×10^3	1.88×10^3	1.20	510

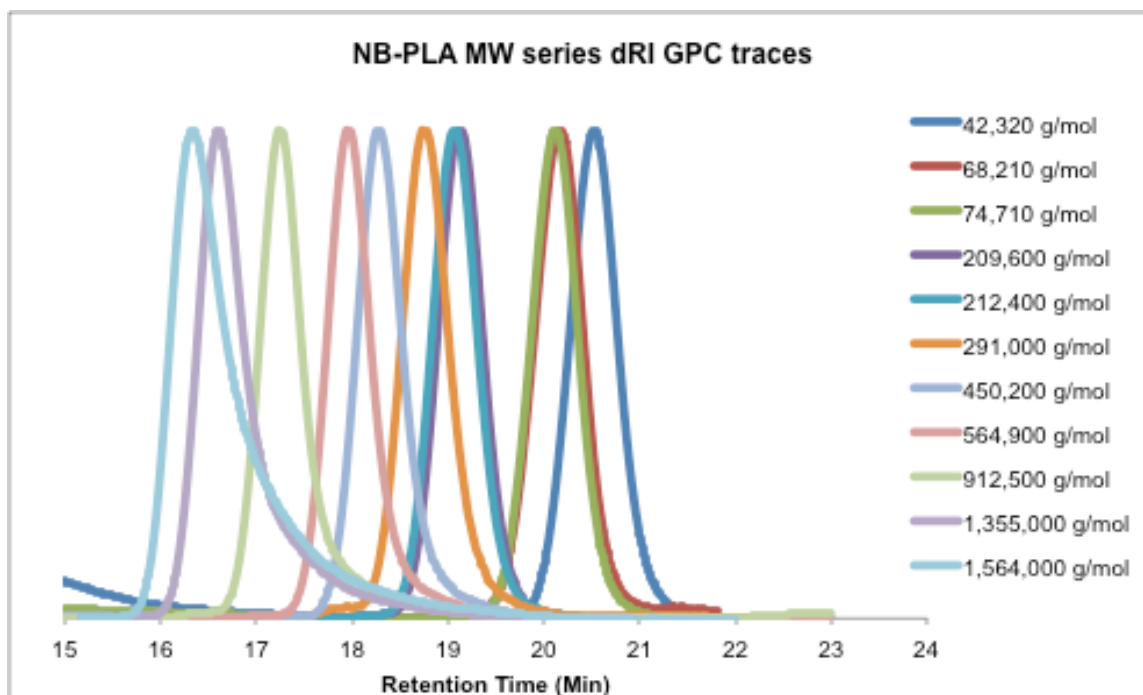


Figure 5.24. Relative Scaling of GPC RI detector traces for p(NB-PLA) MW series.

Table 5.6. GPC-MALS analysis data of poly(NBI-PLA) MW series.

Polymer Sample	GPC M_n (kg/mol)	GPC M_w (kg/mol)	Dispersity (M_w/M_n)	Degree of Polymerization from M_n
p(NBI-PLA)-DP22	69.7	71.0	1.02	22
p(NBI-PLA)-DP67	2.12×10^2	2.19×10^2	1.03	67
p(NBI-PLA)-DP81	2.55×10^2	2.70×10^2	1.06	81
p(NBI-PLA)-DP185	5.84×10^2	5.91×10^2	1.01	185
p(NBI-PLA)-DP339	1.07×10^3	1.12×10^3	1.05	339
p(NBI-PLA)-DP526	1.66×10^3	1.73×10^3	1.05	526
p(NBI-PLA)-DP1135	3.58×10^3	3.77×10^3	1.05	1,135

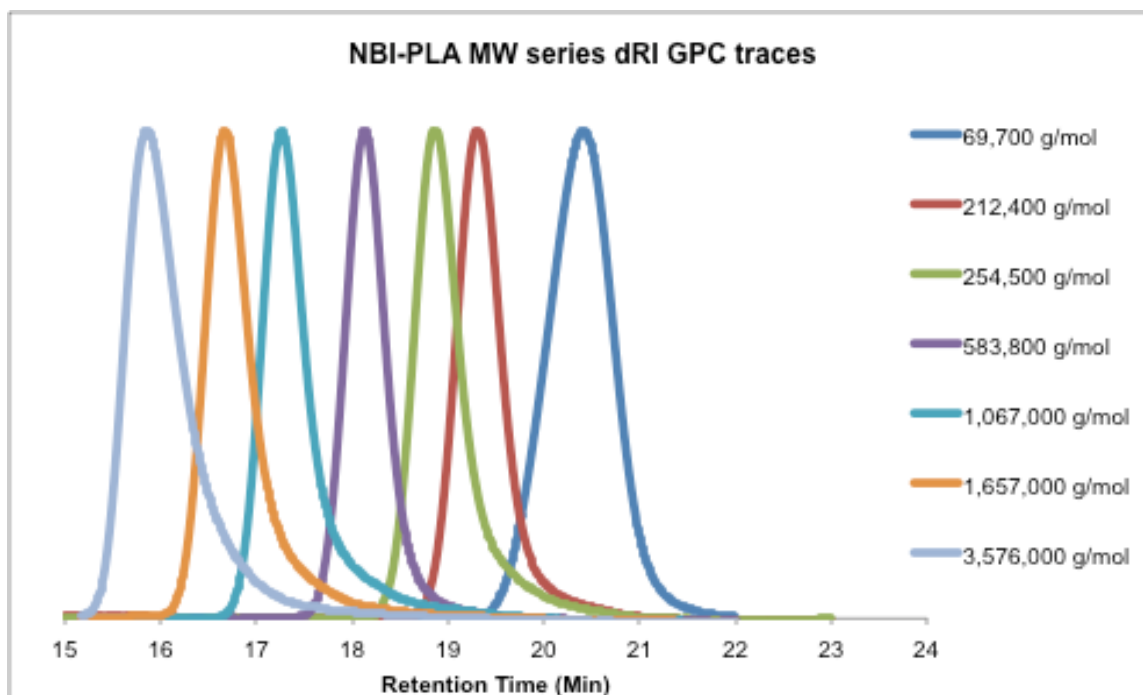


Figure 5.25. Relative Scaling of GPC RI detector traces for p(NBI-PLA) MW series.

Table 5.7. GPC-MALS analysis data of poly(NB-PS) MW series

Polymer Sample	GPC M_n (kg/mol)	GPC M_w (kg/mol)	Dispersity (M_w/M_n)	Degree of Polymerization from M_n
p(NB-PS)-DP61	2.24×10^2	2.28×10^2	1.02	61
p(NB-PS)-DP172	6.26×10^2	6.39×10^2	1.02	172
p(NB-PS)-DP289	1.06×10^3	1.08×10^3	1.02	289
p(NB-PS)-DP340	1.24×10^3	1.33×10^3	1.07	340

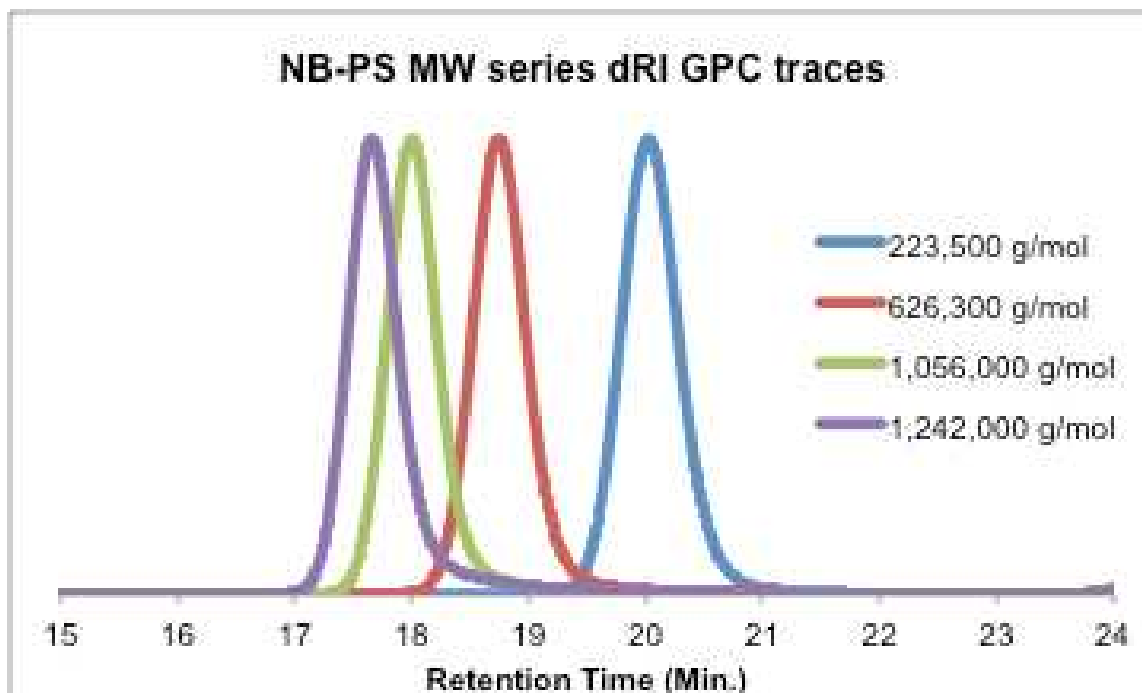


Figure 5.26. Relative Scaling of GPC RI detector traces for p(NB-PS) MW series.

Table 5.8. GPC-MALS analysis data of poly(NBI-PS) MW series.

Polymer Sample	GPC M_n (kg/mol)	GPC M_w (kg/mol)	Dispersity (M_w/M_n)	Degree of Polymerization from M_n
p(NBI-PS)-DP53	1.98×10^2	2.00×10^2	1.01	53
p(NBI-PS)-DP140	5.28×10^2	5.38×10^2	1.02	140
p(NBI-PS)-DP219	8.24×10^2	8.41×10^2	1.02	219
p(NBI-PS)-DP298	1.12×10^3	1.16×10^3	1.04	298

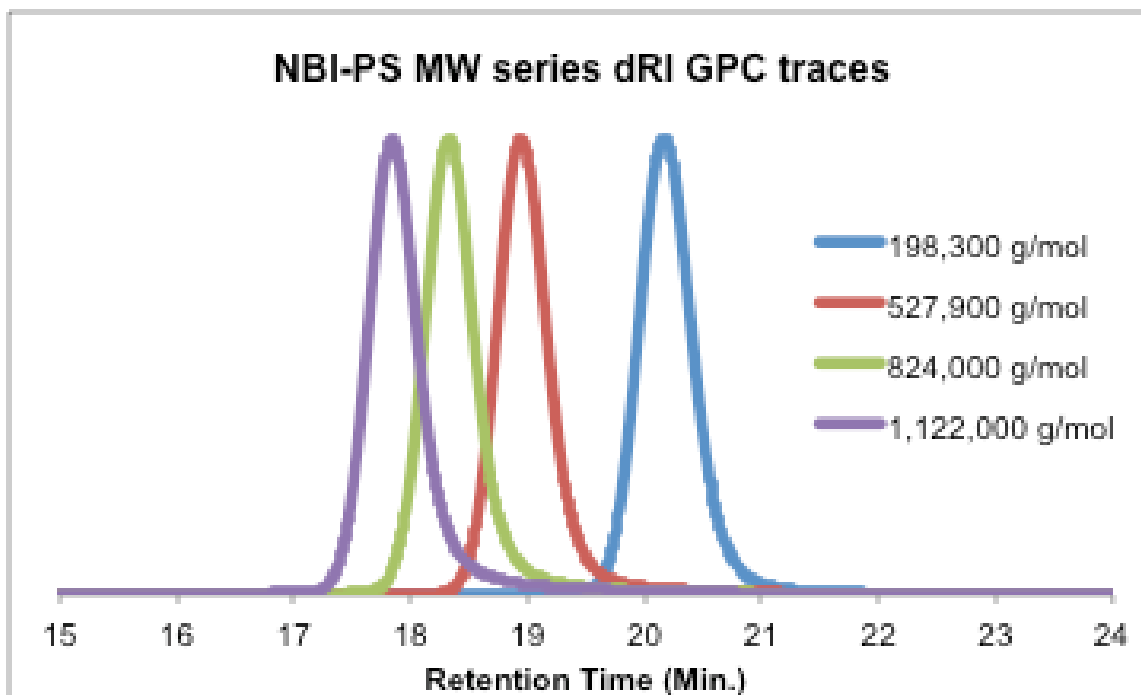


Figure 5.27. Relative Scaling of GPC RI detector traces for p(NBI-PS) MW series (MM used for this series had an $M_n = 3,768$ g/mol and a PDI of 1.01).

Characterization of Linear Homopolymer Molecular Conformation from GPC-MALS:

Table 5.9. Poly(NB-Hep) MW series data obtained from GPC-MALS for the M_n and the Radius of gyration measured with static light scattering (R_z) as long as the polymer was larger than 10 nm in diameter in THF.

Polymer Sample	GPC M_n (kg/mol)	R_z from GPC MALS (nm)	Log M_n	Log R_z
p(NB-Hep)-DP325	76.9	11	4.89	1.0
p(NB-Hep)-DP376	89.0	13	4.95	1.1
p(NB-Hep)-DP437	1.03×10^2	15	5.01	1.2
p(NB-Hep)-DP465	1.10×10^2	18	5.04	1.2
p(NB-Hep)-DP721	1.70×10^2	18	5.23	1.3
p(NB-Hep)-DP996	2.36×10^2	21	5.37	1.3
p(NB-Hep)-DP1028	2.43×10^2	21	5.39	1.3
p(NB-Hep)-DP1077	2.55×10^2	25	5.41	1.4

Table 5.10. Poly(NBI-Hep) MW series data obtained from GPC-MALS for the M_n and the Radius of gyration measured with static light scattering (R_z) as long as the polymer was larger than 10 nm in diameter in THF.

Polymer Sample	GPC M_n (kg/mol)	R_z from GPC MALS (nm)	Log M_n	Log R_z
p(NBI-Hep)-DP360	1.15x10 ²	11	5.06	1.0
p(NBI-Hep)-DP454	1.45x10 ²	15	5.16	1.2
p(NBI-Hep)-DP495	1.58x10 ²	16	5.20	1.2
p(NBI-Hep)-DP618	1.98x10 ²	19	5.30	1.3
p(NBI-Hep)-DP621	1.98x10 ²	20	5.30	1.3
p(NBI-Hep)-DP1051	3.36x10 ²	22	5.53	1.4
p(NBI-Hep)-DP1135	3.63x10 ²	24	5.56	1.4
p(NBI-Hep)-DP1172	3.74x10 ²	25	5.57	1.4

Table 5.11. Poly(NBI-Dec) MW series data obtained from GPC-MALS for the M_n and the Radius of gyration measured with static light scattering (R_z) as long as the polymer was larger than 10 nm in diameter in THF.

Polymer Sample	GPC M_n (kg/mol)	R_z from GPC MALS (nm)	Log M_n	Log R_z
p(NBI-Dec)-DP376	1.14x10 ²	16	5.06	1.2
p(NBI-Dec)-DP512	1.56x10 ²	20	5.19	1.3
p(NBI-Dec)-DP863	2.62x10 ²	21	5.42	1.3
p(NBI-Dec)-DP972	2.95x10 ²	24	5.47	1.4
p(NBI-Dec)-DP1575	4.78x10 ²	37	5.68	1.6
p(NBI-Dec)-DP2261	6.86x10 ²	48	5.84	1.7
p(NBI-Dec)-DP2570	7.80x10 ²	56	5.89	1.8

Static Light Scattering Scaling Relationship:

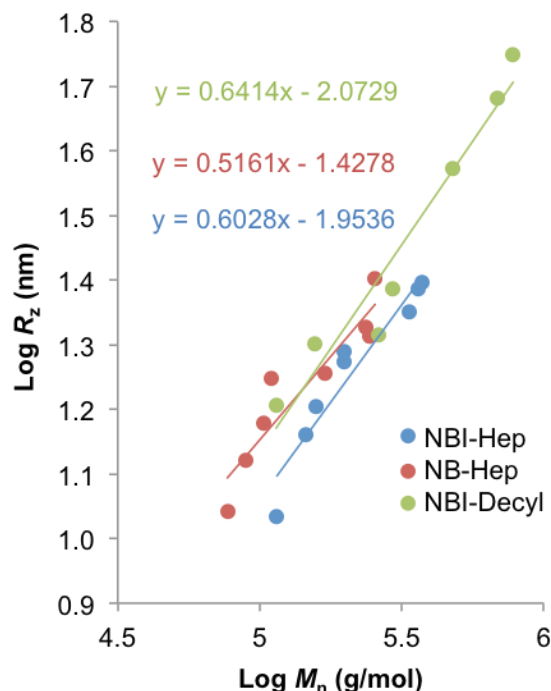


Figure 5.28. A graph of the z-average radius of gyration of the linear polymers in tetrahydrofuran vs. the number average molecular weight of the polymers (scaling factor = 0.64 for NBI-Decyl, 0.52 for NB-Hep, and 0.60 for NBI-Hep).

General Block Copolymer Synthesis

In a nitrogen-filled glovebox, a 20 mL vial was charged with a stir bar and 0.1 g of PLA macromonomer that was then diluted to 0.05 M with anhydrous THF. With rapid stirring, the appropriate amount of G3 catalyst completely dissolved in THF was quickly added via syringe. As conversion stopped determined by GPC, the molar equivalent amount of PS macromonomer at a concentration of 0.05 M in anhydrous THF was added quickly. Also dissolved in the second block mixture was pyridine (20 mM for the BBCPs with the NB-PS MM or 30 mM for the BBCPs with the NBI-PS MM). After 3 hours (for the NB-PS containing BBCPs) or 20 hours (for the NBI-PS containing BBCPs) from the addition of the 2nd block, the polymerization was quenched by the addition of 0.5 mL of ethyl vinyl ether. The polymer was precipitated out into

20 mL of methanol at room temperature, after which the polymer was isolated, washed with excess methanol, and dried under reduced pressure at 70 °C to a constant weight. Yield is recorded below with the GPC-MALS data.

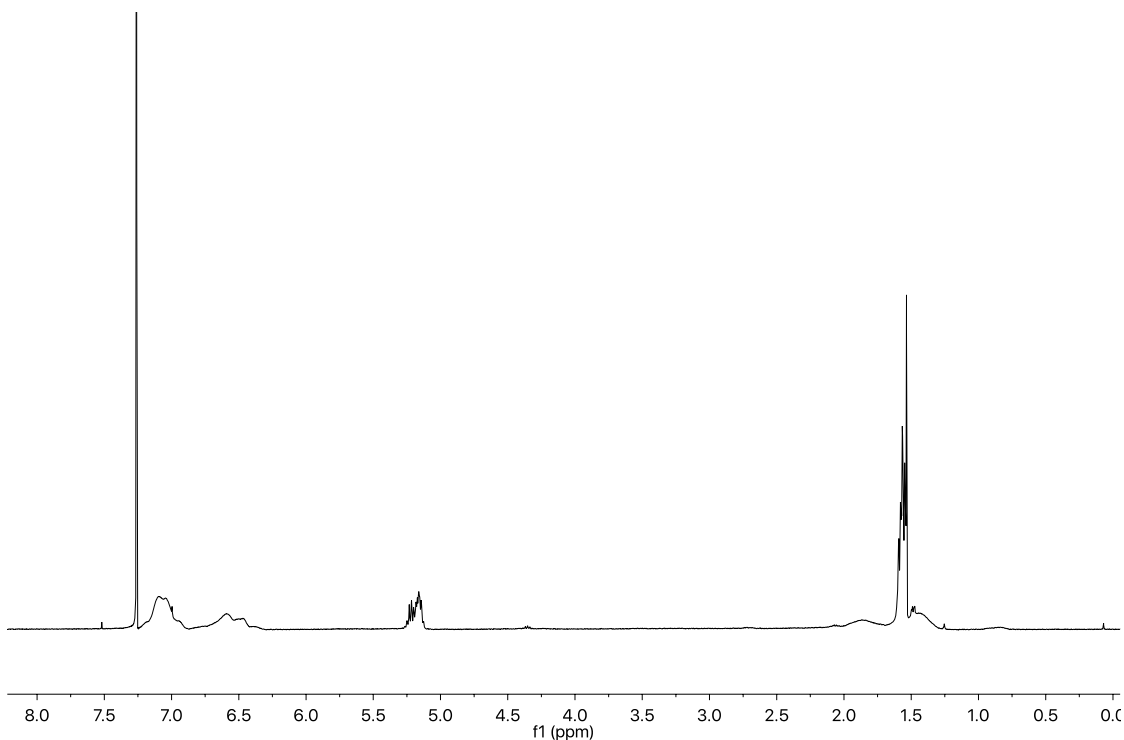


Figure 5.29. Isolated and representative p(NBI-PLA)-*b*-p(NBI-PS) (polymer shown $M_n = 1.56 \times 10^3$ kg/mol) ^1H NMR (400 MHz, CDCl_3): δ 7.08 (m), 6.58 (m), 5.17 (m), 4.35 (m), 1.88 (bs), 1.53 (m), 1.26 (s), 0.91 (bs), [Water singlet from CDCl_3 at 1.55 ppm].

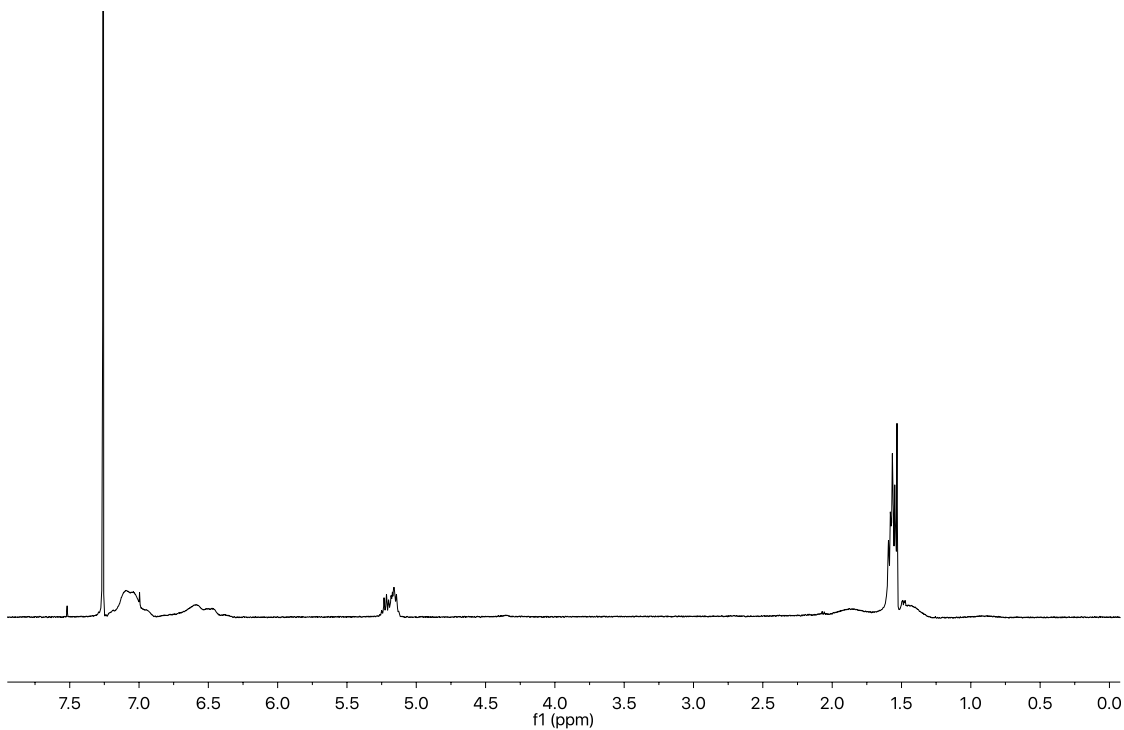


Figure 5.30. Isolated and representative p(NBI-PLA)-*b*-p(NB-PS) (polymer shown $M_n = 2.60 \times 10^3$ kg/mol) ^1H NMR (400 MHz, CDCl_3): δ 7.08 (m), 6.58 (m), 5.17 (m), 4.35 (m), 1.88 (bs), 1.53 (m), 1.26 (s), 0.91 (bs), 0.71 (m) [Water singlet from CDCl_3 at 1.55 ppm].

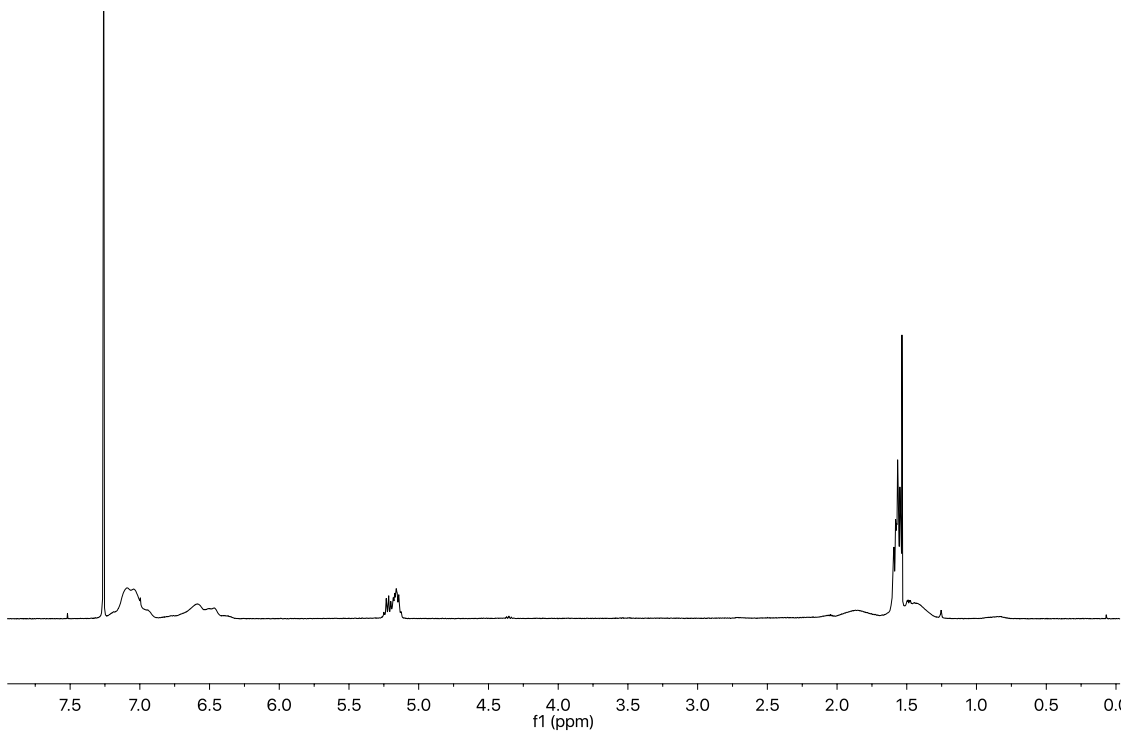


Figure 5.31. Isolated and representative p(NB-PLA)-*b*-p(NBI-PS) (polymer shown $M_n = 2.13 \times 10^3$ kg/mol) ^1H NMR (400 MHz, CDCl_3): δ 7.08 (m), 6.58 (m), 5.17 (m), 4.35 (m), 1.88 (bs), 1.53 (m), 1.26 (s), 0.91 (bs) [Water singlet from CDCl_3 at 1.55 ppm].

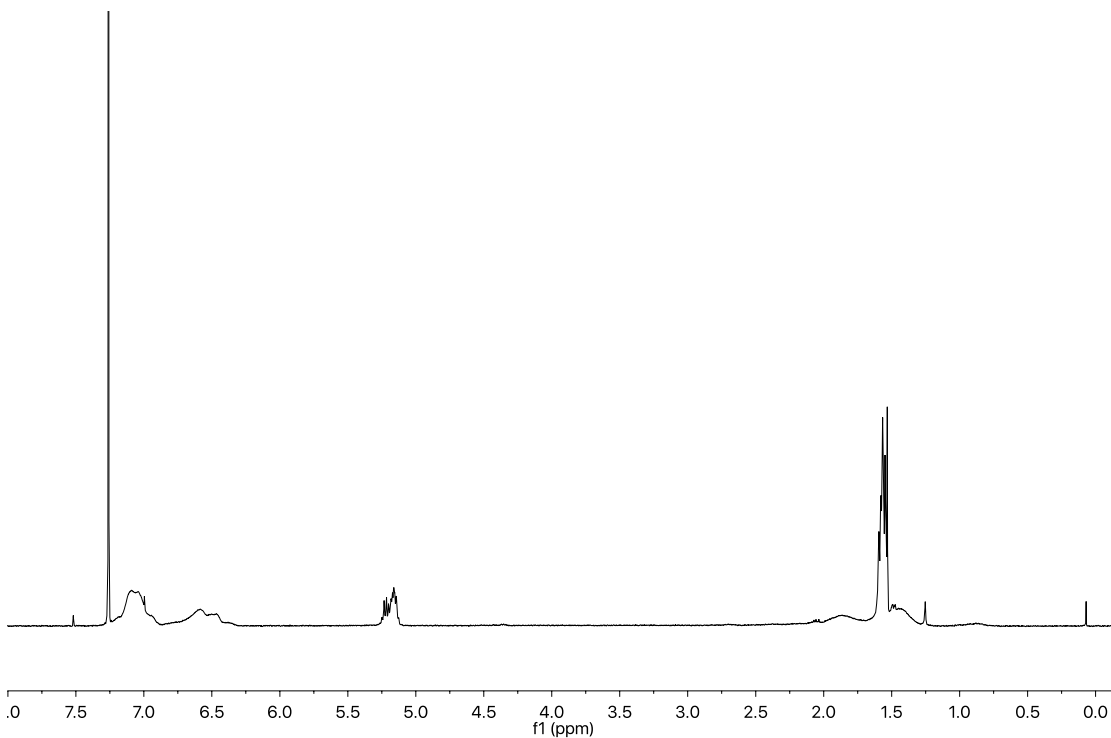


Figure 5.32. Isolated and representative p(NB-PLA)-*b*-p(NB-PS) (polymer shown $M_n = 2.30 \times 10^3$ kg/mol) ^1H NMR (400 MHz, CDCl_3): δ 7.08 (m), 6.58 (m), 5.17 (m), 4.35 (m), 1.88 (bs), 1.53 (m), 1.26 (s), 0.91 (bs), 0.71 (m) [Water singlet from CDCl_3 at 1.55 ppm].

Block Copolymer Characterization via Gel Permeation – Multi Angle Light Scattering Traces (GPC-MALS) and Isolated Yield:

Table 5.12. p(NBI-PLA)-*b*-p(NBI-PS) MW series data obtained from GPC-MALS and isolated yield.

p(NBI-PLA)- <i>b</i> -p(NBI-PS) Sample	M_n (kg/mol)	M_w (kg/mol)	Dispersity (M_w/M_n)	Isolated Yield (%)
1	4.55×10^2	5.02×10^2	1.10	69
2	5.20×10^2	5.38×10^2	1.03	67
3	8.50×10^2	1.02×10^3	1.20	76
4	1.31×10^3	1.47×10^3	1.12	72
5	1.42×10^3	1.74×10^3	1.22	81
6	1.43×10^3	1.89×10^3	1.31	77
7	1.56×10^3	1.96×10^3	1.25	76

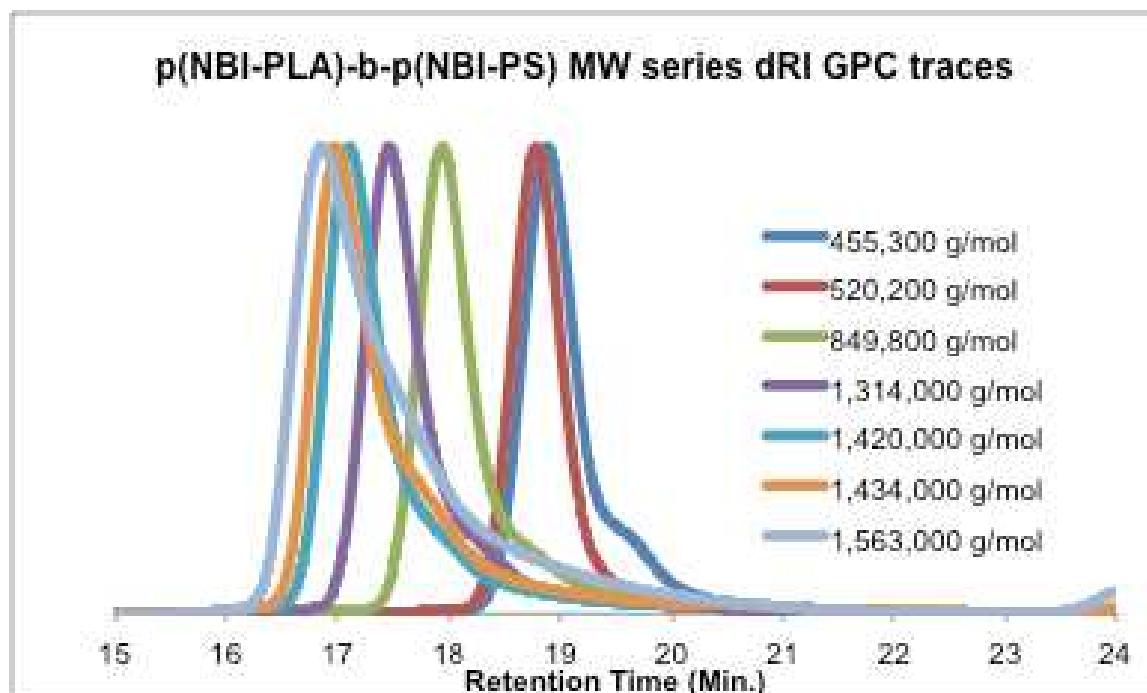


Figure 5.33. Relative Scaling of GPC RI detector traces for p(NBI-PLA)-b-p(NBI-PS) MW series.

Table 5.13. p(NBI-PLA)-b-p(NB-PS) MW series data obtained from GPC-MALS and isolated yield.

p(NBI-PLA)-b-p(NB-PS) Sample	M_n (kg/mol)	M_w (kg/mol)	Dispersity (M_w/M_n)	Isolated Yield (%)
1	6.13×10^2	6.61×10^2	1.08	74
2	7.66×10^2	7.95×10^2	1.04	72
3	1.11×10^3	1.18×10^3	1.07	83
4	1.52×10^3	1.61×10^3	1.05	76
5	1.66×10^3	1.70×10^3	1.03	77
6	2.60×10^3	2.71×10^3	1.04	74

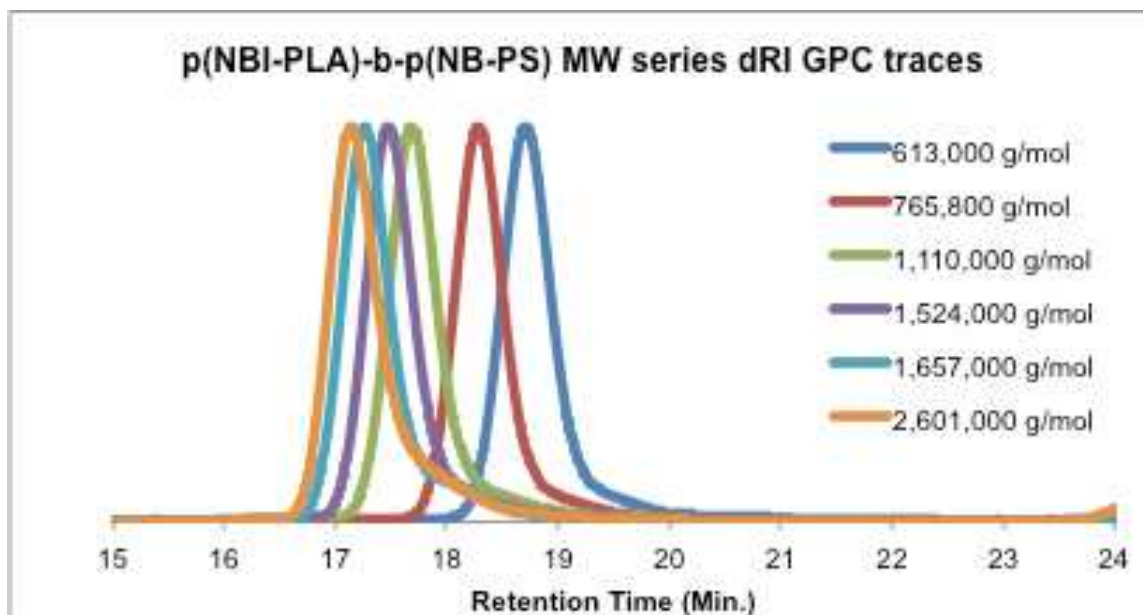


Figure 5.34. Relative Scaling of GPC RI detector traces for p(NBI-PLA)-b-p(NB-PS) MW series.

Table 5.14. p(NB-PLA)-b-p(NBI-PS) MW series data obtained from GPC-MALS and isolated yield.

p(NB-PLA)-b-p(NBI-PS) Sample	M_n (kg/mol)	M_w (kg/mol)	Dispersity (M_w/M_n)	Isolated Yield (%)
1	5.24×10^2	5.40×10^2	1.03	81
2	9.18×10^2	9.69×10^2	1.06	79
3	1.44×10^3	1.52×10^3	1.06	83
4	1.88×10^3	1.97×10^3	1.05	83
5	1.90×10^3	2.03×10^3	1.07	78
6	2.13×10^3	2.42×10^3	1.14	82

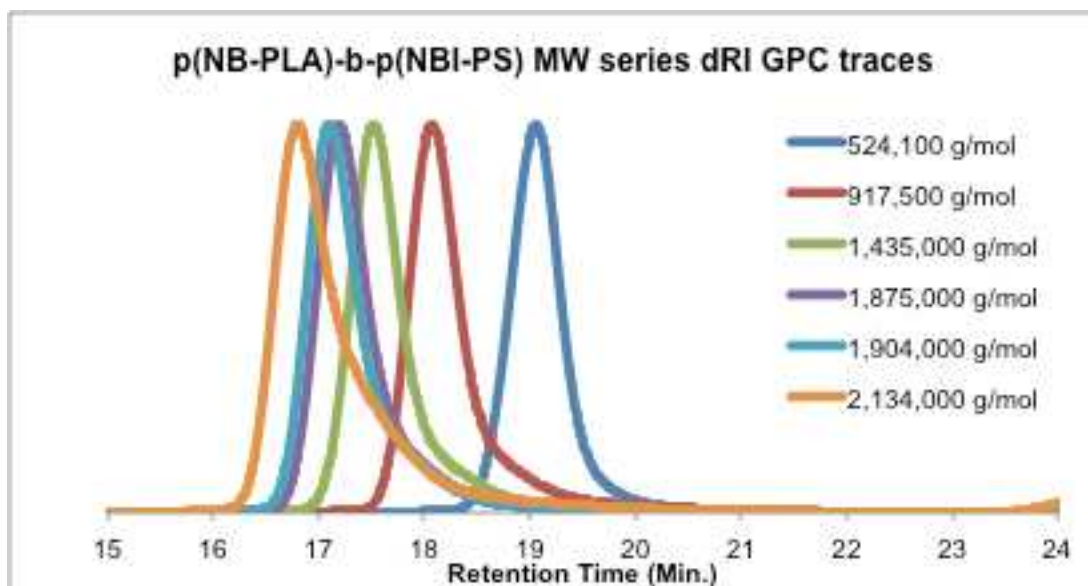


Figure 5.35. Relative Scaling of GPC RI detector traces for p(NB-PLA)-b-p(NBI-PS) MW series.

Table 5.15. p(NB-PLA)-b-p(NB-PS) MW series data obtained from GPC-MALS and isolated yield.

p(NB-PLA)-b-p(NB-PS) Sample	M_n (kg/mol)	M_w (kg/mol)	Dispersity (M_w/M_n)	Isolated Yield (%)
1	4.14×10^2	4.20×10^2	1.02	63
2	7.87×10^2	8.04×10^2	1.02	69
3	1.31×10^3	1.34×10^3	1.03	73
4	1.73×10^3	1.80×10^3	1.04	82
5	1.70×10^3	1.75×10^3	1.03	82
6	2.30×10^3	2.40×10^3	1.04	75

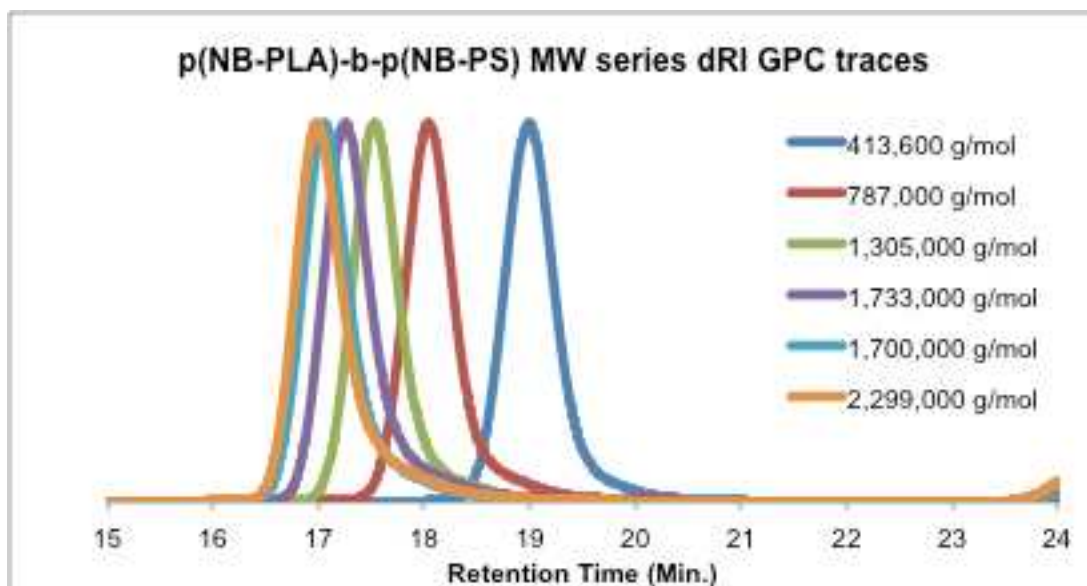


Figure 5.36. Relative Scaling of GPC RI detector traces for p(NB-PLA)-b-p(NB-PS) MW series.

Characterization of Block Copolymer Composition by NMR:

^1H NMR spectroscopy was conducted on each brush block copolymer to observe the degree of polymerization of each block in each of the copolymers. The molar ratios of the styrene repeat unit to the lactide repeat unit were estimated from the integration value of the peak at δ 6.29-7.25 ppm (for styrene) and δ 5.03-5.25 ppm (for lactide). The styrene peaks were integrated to a value of 1 and divided by 5 to produce a molar ratio of 0.2 for styrene in the BBCP. The lactide peak was then integrated and the resulting integration value was divided by 2 to provide the molar amount of lactide in the BBCP.

Then, using the experimentally measured M_n from the GPC for the macromonomer used in the copolymer, the norbornene chain-end group was subtracted out to be able to calculate the number of moles using the MW of each repeat unit of either styrene or lactide within a macromonomer.

With both sets of molar ratios calculated above, it was then possible to divide the respective BBCP molar ratio by the amount of moles of the styrene or lactide within a

macromonomer repeat unit to get an empirical value of the respective macromonomer degree of polymerization in the BBCP. Using these empirical values, a percent of the styrene or lactide macromonomer was calculated based on the sum of the two empirical values. This percent was then used to multiply into the GPC-derived M_n value for the BBCP. The resulting MW value was then divided by the respective experimentally measured M_n of the macromonomer to get an estimate of the degree of polymerization of each macromonomer within a block. The results of the above calculations are shown in the following table below.

Table 5.16. Summary of block degree of polymerization calculations and data obtained from GPC-MALS and NMR.

	BBCP M_n (kg/mol)	NMR Molar ratio (styrene : lactide)	Moles of Sty./ MM unit	Moles of Lac./ MM unit	Empirical MM ratio (sty. MM : lac. MM)	% Sty. in BBCP	% Lac. in BBCP	DP of Sty. Block	DP of Lac. Block
p(NBI-PLA)-b-p(NBI-PS)									
1	5.20x10 ²	0.2 : 0.17	0.0305	0.0447	6.55 : 3.69	64	36	88	55
2	8.50x10 ²	0.2 : 0.14	0.0256	0.0447	7.81 : 3.13	71	29	136	72
3	1.31x10 ³	0.2 : 0.13	0.0256	0.0447	7.81 : 2.91	73	27	217	104
4	1.42x10 ³	0.2 : 0.15	0.0256	0.0447	7.81 : 3.24	71	29	228	120
5	1.43x10 ³	0.2 : 0.14	0.0256	0.0447	7.81 : 3.02	72	28	235	117
6	1.56x10 ³	0.2 : 0.14	0.0256	0.0447	7.81 : 3.13	71	29	251	132
p(NBI-PLA)-b-p(NB-PS)									
1	6.13x10 ²	0.2 : 0.16	0.0309	0.0447	6.48 : 3.47	65	35	109	63
2	7.66x10 ²	0.2 : 0.15	0.0309	0.0447	6.48 : 3.24	67	33	140	74
3	1.11x10 ³	0.2 : 0.13	0.0309	0.0447	6.48 : 2.91	69	31	210	100
4	1.52x10 ³	0.2 : 0.15	0.0309	0.0447	6.48 : 3.36	66	34	276	151
5	1.66x10 ³	0.2 : 0.14	0.0309	0.0447	6.48 : 3.02	68	32	309	155
6	2.60x10 ³	0.2 : 0.14	0.0309	0.0447	6.48 : 3.02	68	32	485	243
p(NB-PLA)-b-p(NBI-PS)									
1	5.24x10 ²	0.2 : 0.13	0.0256	0.0460	7.81 : 2.72	74	26	88	42
2	9.18x10 ²	0.2 : 0.13	0.0256	0.0460	7.81 : 2.72	74	26	154	73
3	1.44x10 ³	0.2 : 0.12	0.0256	0.0460	7.81 : 2.61	75	25	243	110
4	1.88x10 ³	0.2 : 0.11	0.0256	0.0460	7.81 : 2.39	77	23	325	135
5	1.90x10 ³	0.2 : 0.13	0.0256	0.0460	7.81 : 2.72	74	26	319	152
6	2.13x10 ³	0.2 : 0.12	0.0256	0.0460	7.81 : 2.50	76	24	367	158
p(NB-PLA)-b-p(NB-PS)									
1	4.14x10 ²	0.2 : 0.16	0.0309	0.0460	6.48 : 3.48	65	35	74	45
2	7.87x10 ²	0.2 : 0.14	0.0309	0.0460	6.48 : 2.93	69	31	149	75
3	1.31x10 ³	0.2 : 0.14	0.0309	0.0460	6.48 : 2.93	69	31	247	124
4	1.73x10 ³	0.2 : 0.13	0.0309	0.0460	6.48 : 2.82	70	30	332	160
5	1.70x10 ³	0.2 : 0.15	0.0309	0.0460	6.48 : 3.26	66	34	308	178
6	2.30x10 ³	0.2 : 0.13	0.0309	0.0460	6.48 : 2.82	70	30	441	212

Photographs of BBCP Films:

p(NBI-PLA)-b-p(NBI-PS)

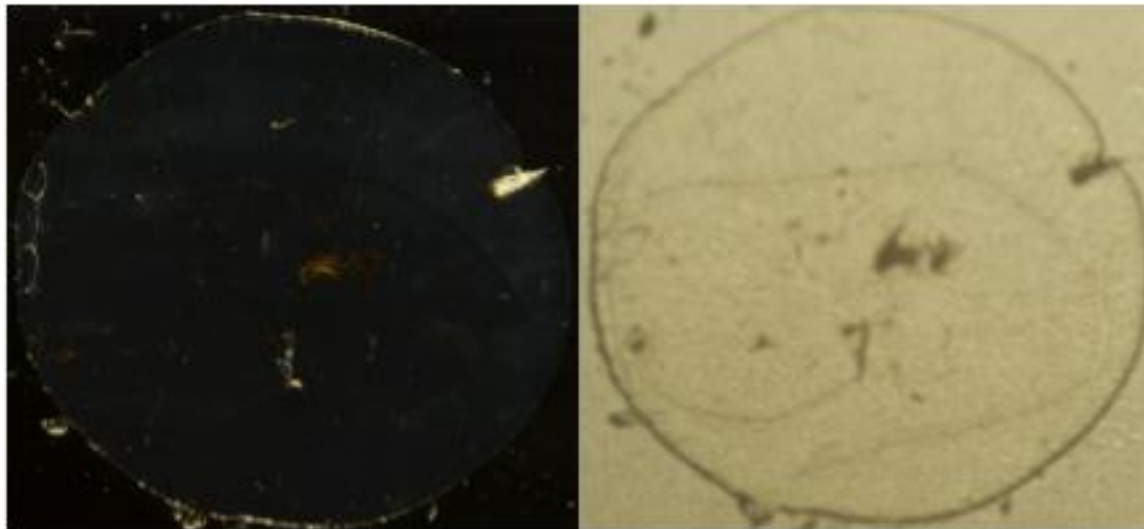


Figure 5.37. Photographs of the reflection (left) and transmission (right) of the *p(NBI-PLA)-b-p(NBI-PS)* ($M_n = 455,300$ g/mol) film.

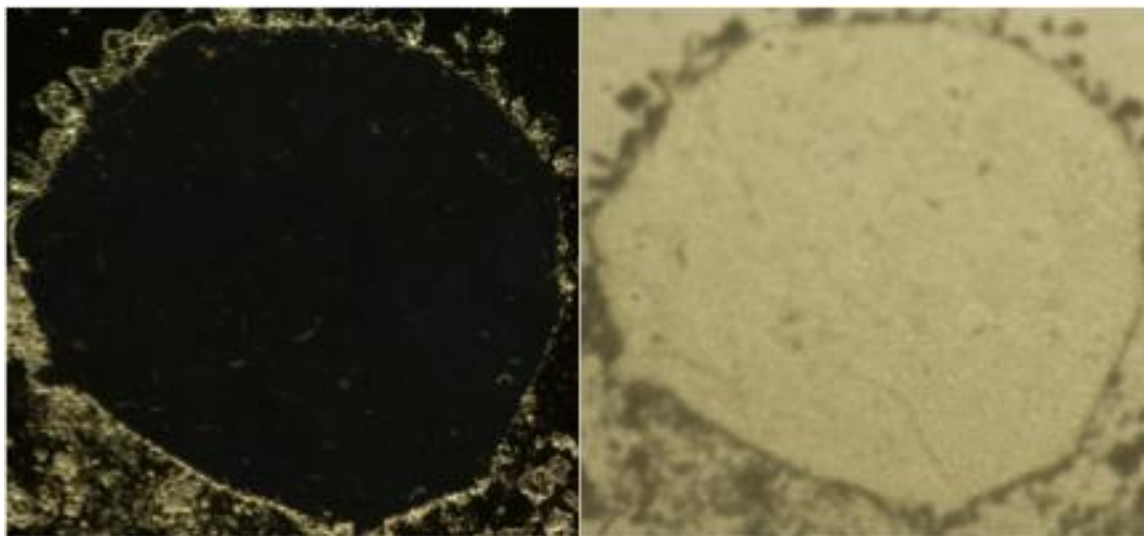


Figure 5.38. Photographs of the reflection (left) and transmission (right) of the *p(NBI-PLA)-b-p(NBI-PS)* ($M_n = 520,200$ g/mol) film.

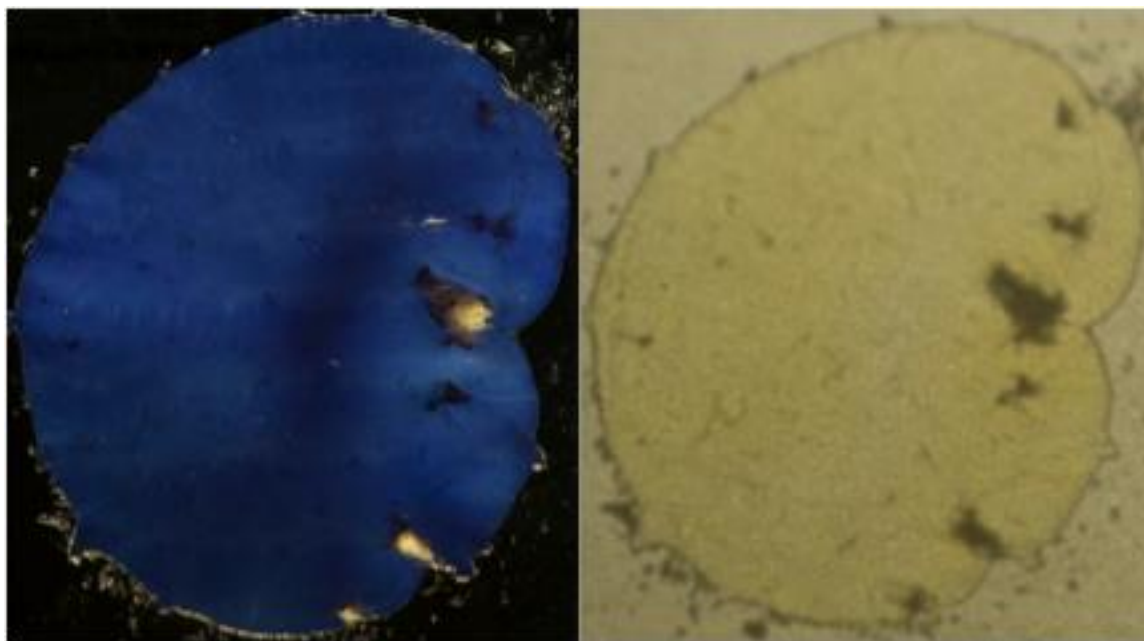


Figure 5.39. Photographs of the reflection (left) and transmission (right) of the p(NBI-PLA)-b-p(NBI-PS) ($M_n = 849,800$ g/mol) film.

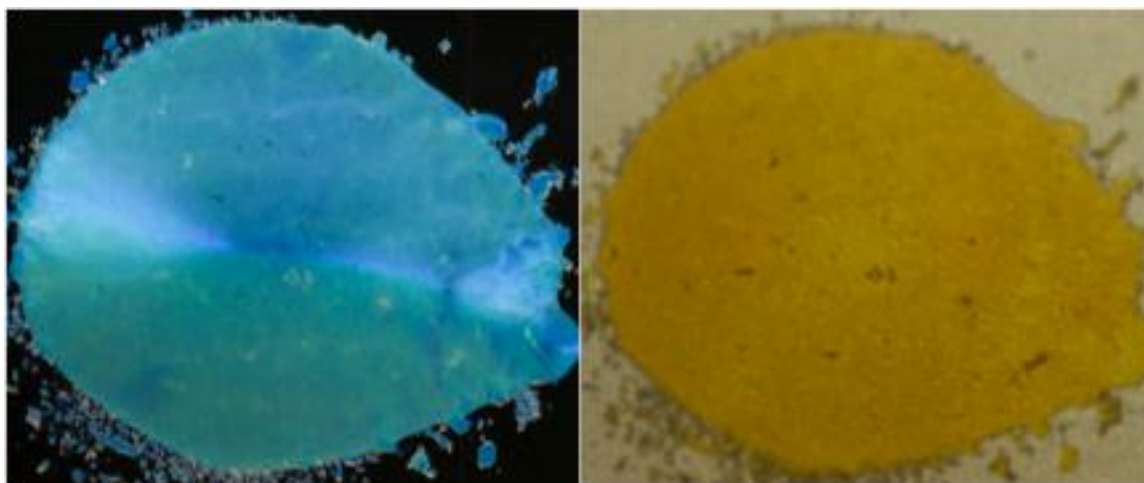


Figure 5.40. Photographs of the reflection (left) and transmission (right) of the p(NBI-PLA)-b-p(NBI-PS) ($M_n = 1,314,000$ g/mol) film.

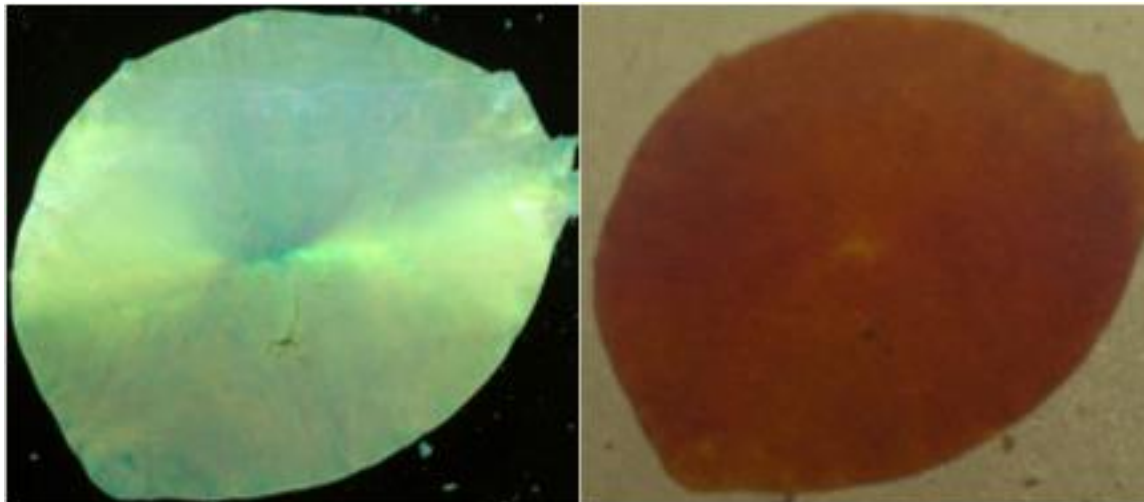


Figure 5.41. Photographs of the reflection (left) and transmission (right) of the p(NBI-PLA)-b-p(NBI-PS) ($M_n = 1,420,000$ g/mol) film.

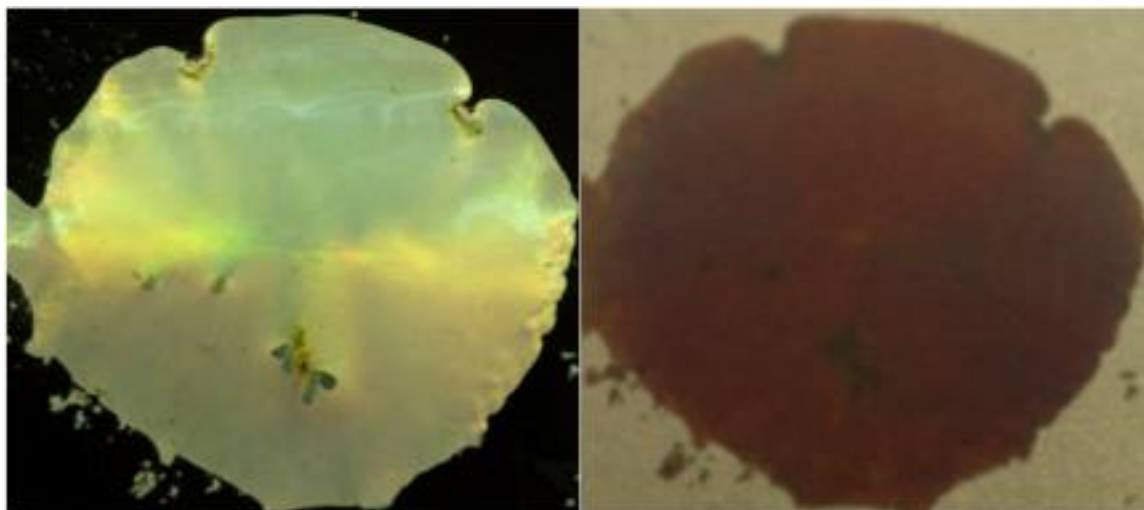


Figure 5.42. Photographs of the reflection (left) and transmission (right) of the p(NBI-PLA)-b-p(NBI-PS) ($M_n = 1,434,000$ g/mol) film.

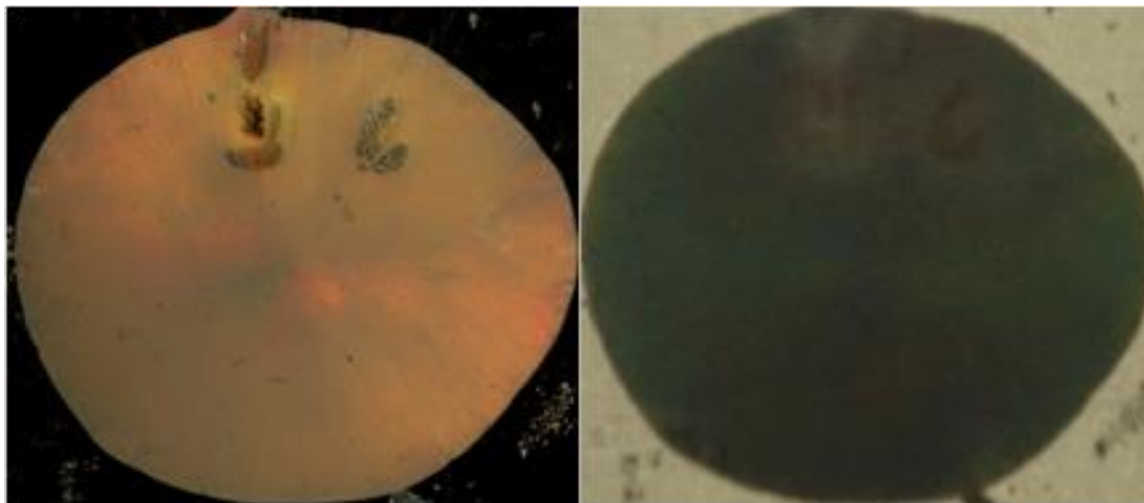


Figure 5.43. Photographs of the reflection (left) and transmission (right) of the p(NBI-PLA)-b-p(NBI-PS) ($M_n = 1,563,000$ g/mol) film.

p(NBI-PLA)-b-p(NB-PS):

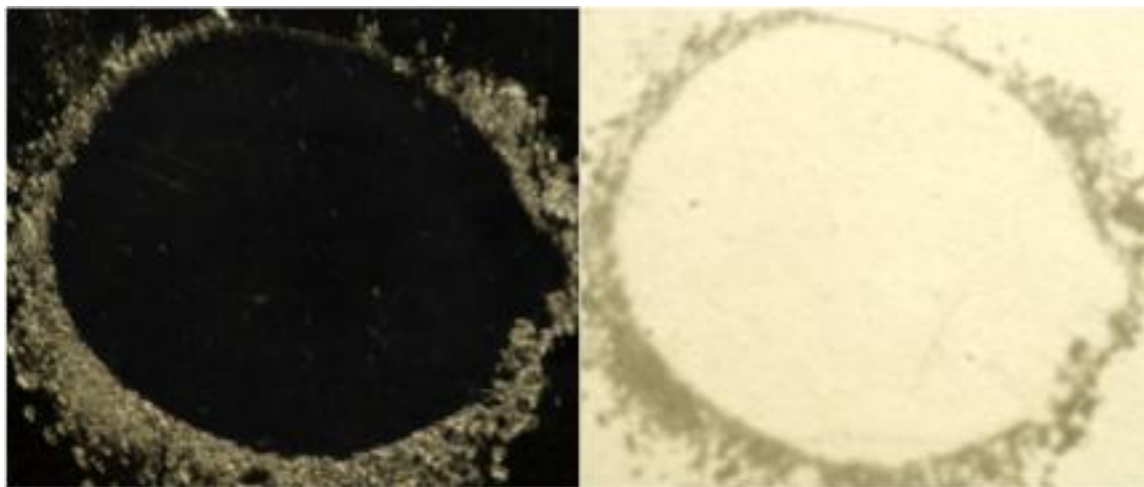


Figure 5.44. Photographs of the reflection (left) and transmission (right) of the p(NBI-PLA)-b-p(NB-PS) ($M_n = 613,000$ g/mol) film.

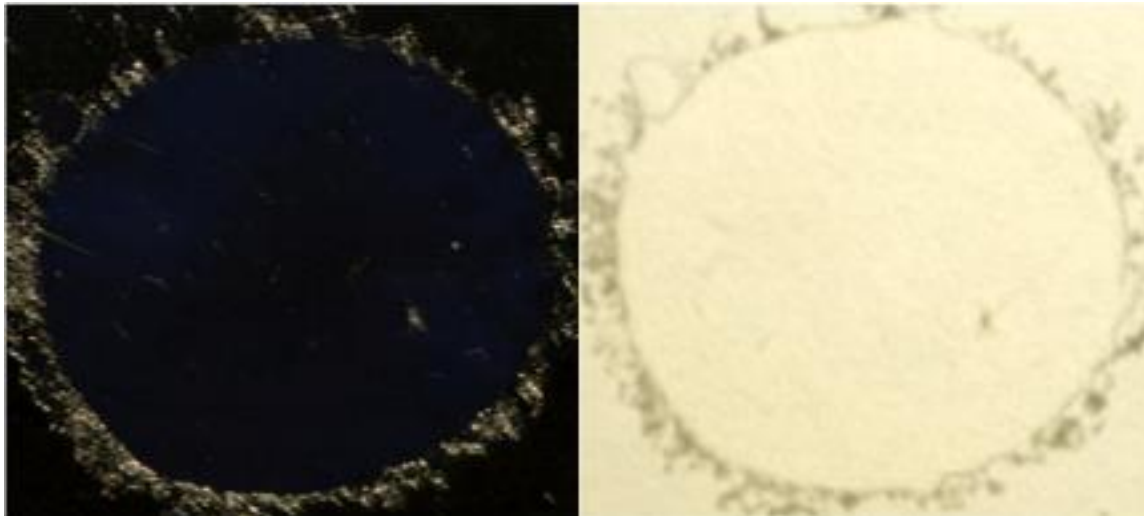


Figure 5.45. Photographs of the reflection (left) and transmission (right) of the p(NBI-PLA)-b-p(NB-PS) ($M_n = 765,800$ g/mol) film.

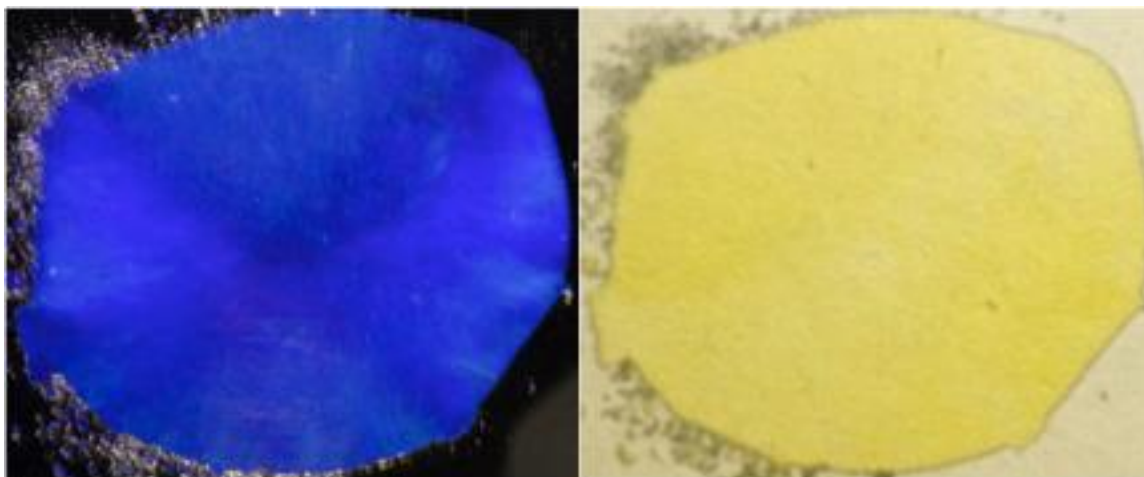


Figure 5.46. Photographs of the reflection (left) and transmission (right) of the p(NBI-PLA)-b-p(NB-PS) ($M_n = 1,110,000$ g/mol) film.

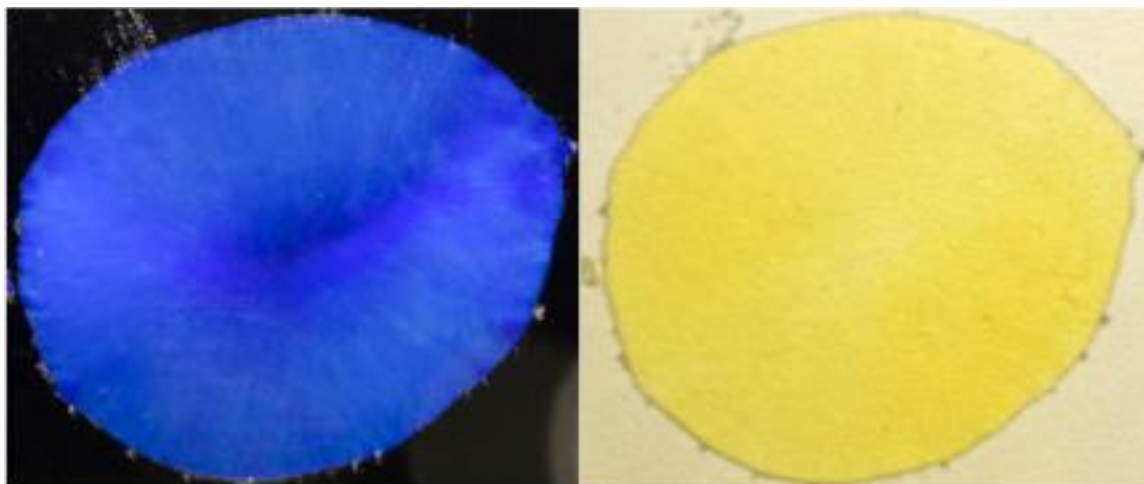


Figure 5.47. Photographs of the reflection (left) and transmission (right) of the p(NBI-PLA)-b-p(NB-PS) ($M_n = 1,524,000$ g/mol) film.

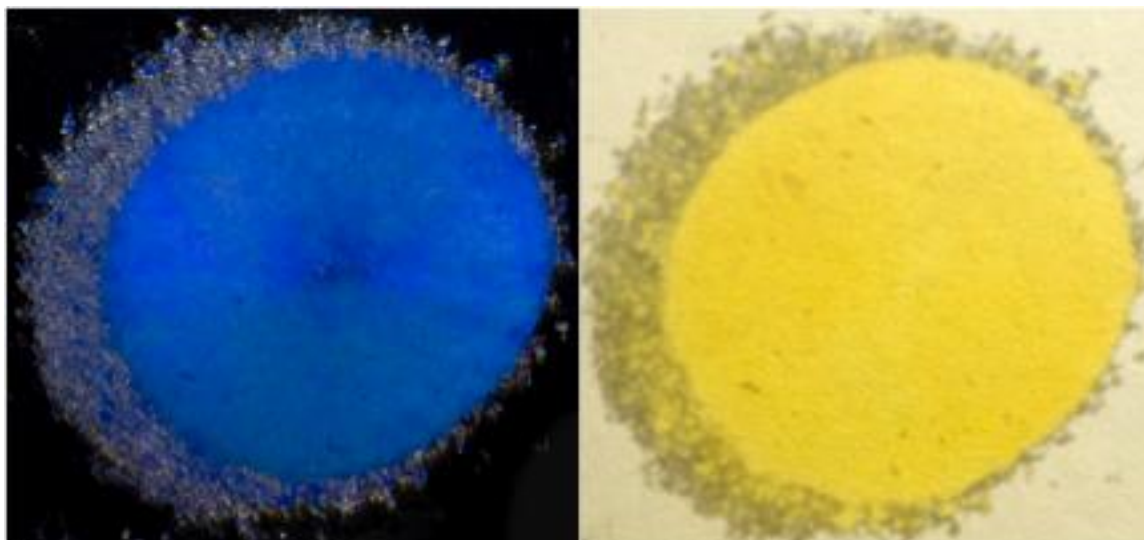


Figure 5.48. Photographs of the reflection (left) and transmission (right) of the p(NBI-PLA)-b-p(NB-PS) ($M_n = 1,657,000$ g/mol) film.

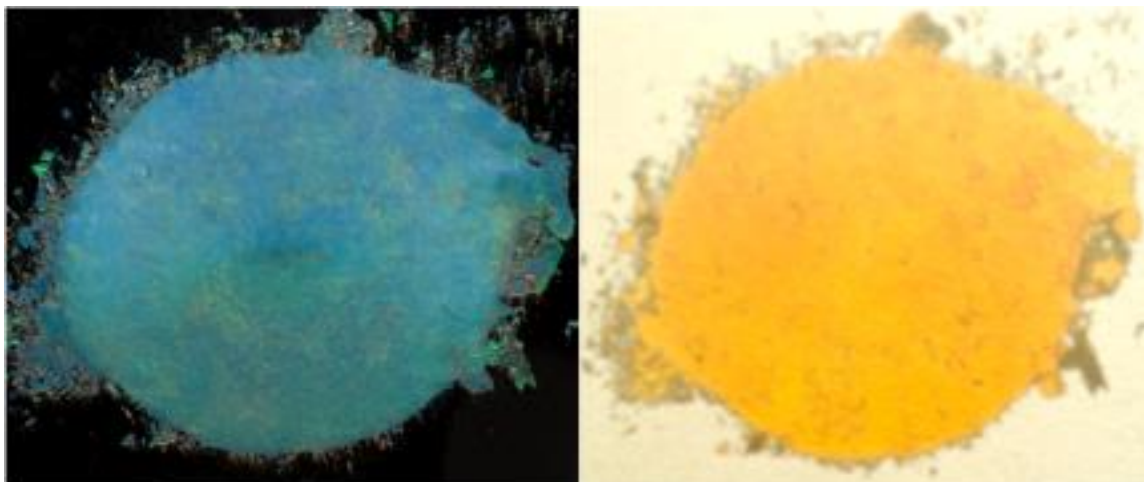


Figure 5.49. Photographs of the reflection (left) and transmission (right) of the p(NBI-PLA)-b-p(NB-PS) ($M_n = 2,601,000$ g/mol) film.

p(NB-PLA)-b-p(NBI-PS)

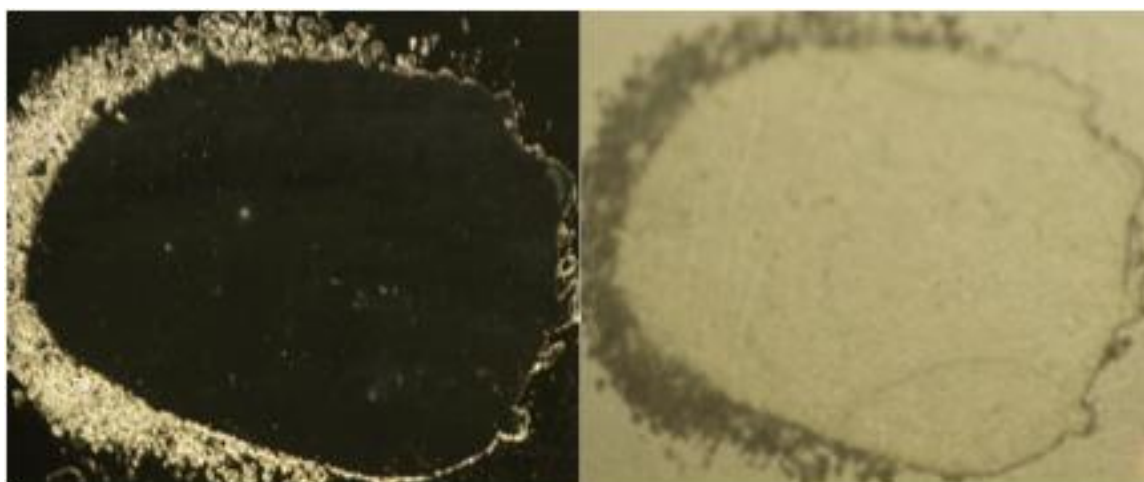


Figure 5.50. Photographs of the reflection (left) and transmission (right) of the p(NB-PLA)-b-p(NBI-PS) ($M_n = 524,100$ g/mol) film.

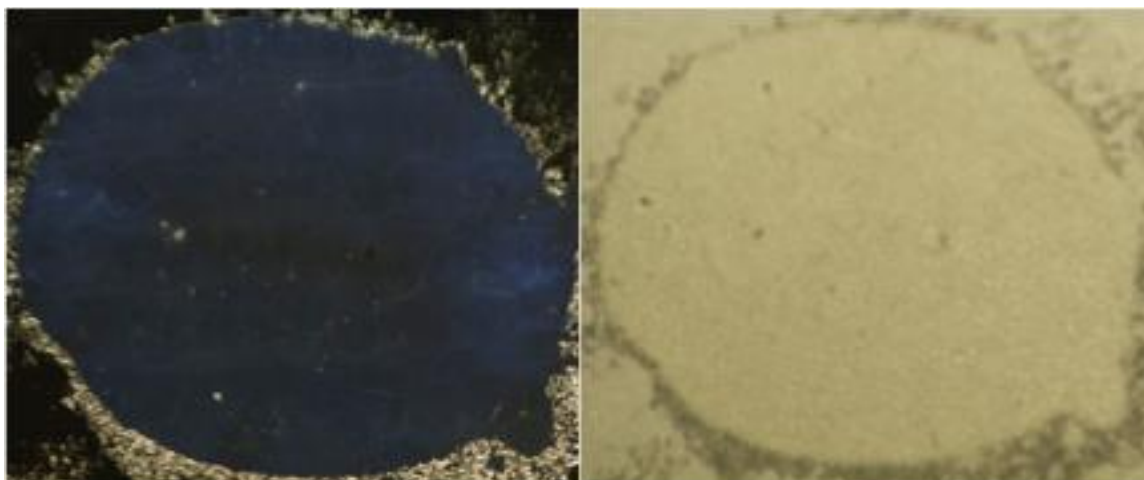


Figure 5.51. Photographs of the reflection (left) and transmission (right) of the p(NB-PLA)-b-p(NBI-PS) ($M_n = 917,500$ g/mol) film.

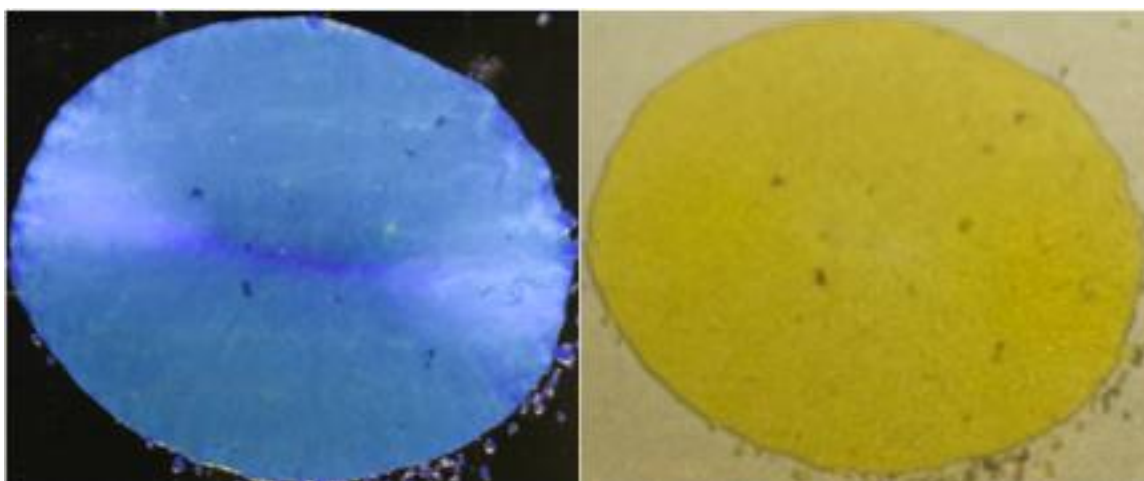


Figure 5.52. Photographs of the reflection (left) and transmission (right) of the p(NB-PLA)-b-p(NBI-PS) ($M_n = 1,435,000$ g/mol) film.

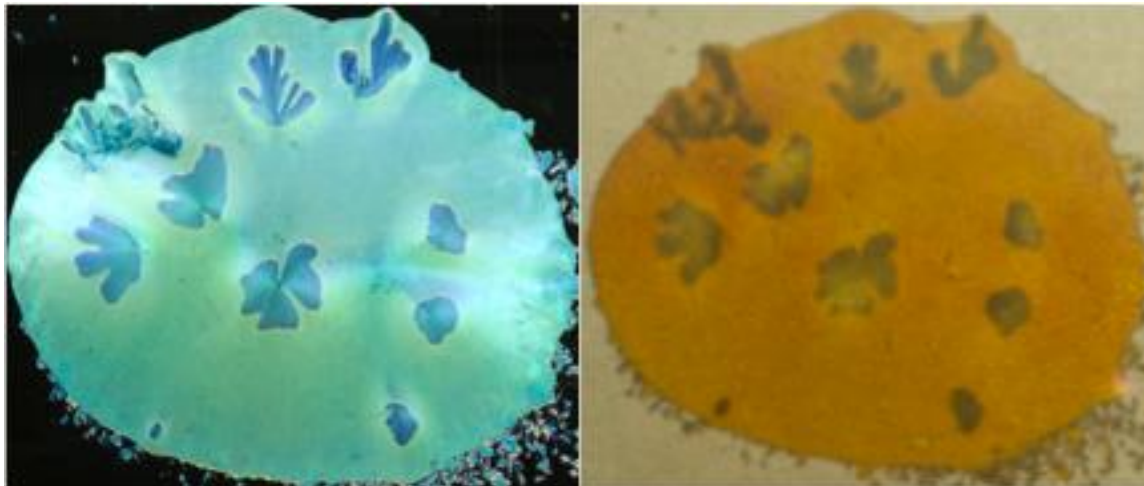


Figure 5.53. Photographs of the reflection (left) and transmission (right) of the p(NB-PLA)-b-p(NBI-PS) ($M_n = 1,875,000$ g/mol) film.

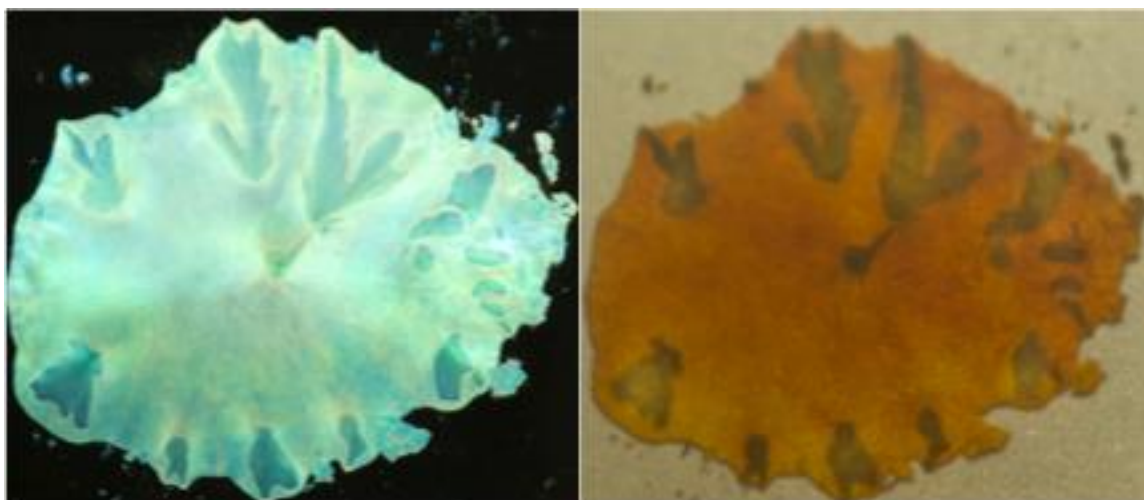


Figure 5.54. Photographs of the reflection (left) and transmission (right) of the p(NB-PLA)-b-p(NBI-PS) ($M_n = 1,904,000$ g/mol) film.

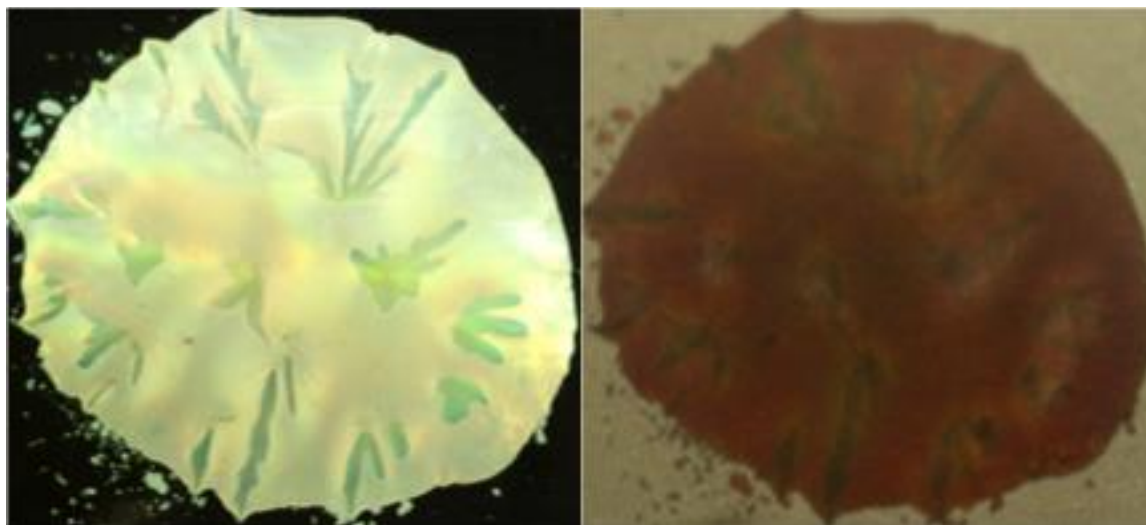


Figure 5.55. Photographs of the reflection (left) and transmission (right) of the p(NB-PLA)-b-p(NBI-PS) ($M_n = 2,134,000$ g/mol) film.

p(NB-PLA)-b-p(NB-PS)

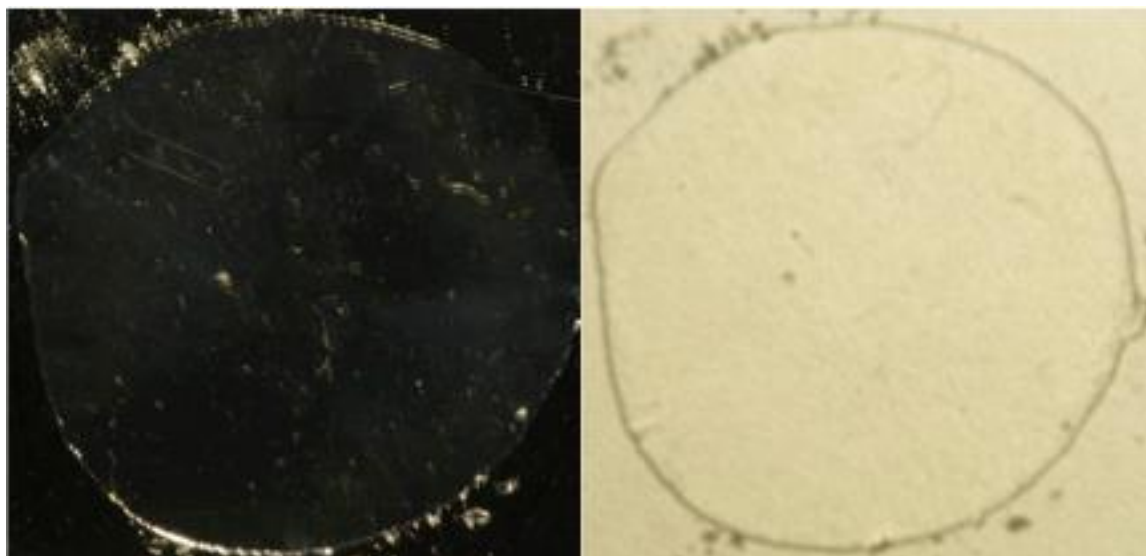


Figure 5.56. Photographs of the reflection (left) and transmission (right) of the p(NB-PLA)-b-p(NB-PS) ($M_n = 413,600$ g/mol) film.

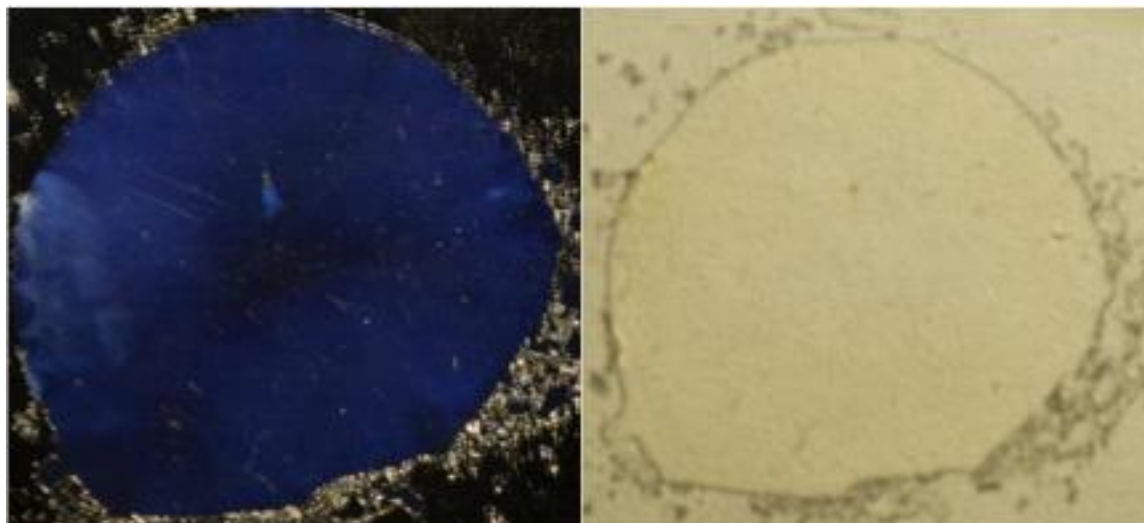


Figure 5.57. Photographs of the reflection (left) and transmission (right) of the p(NB-PLA)-b-p(NB-PS) ($M_n = 787,000$ g/mol) film.

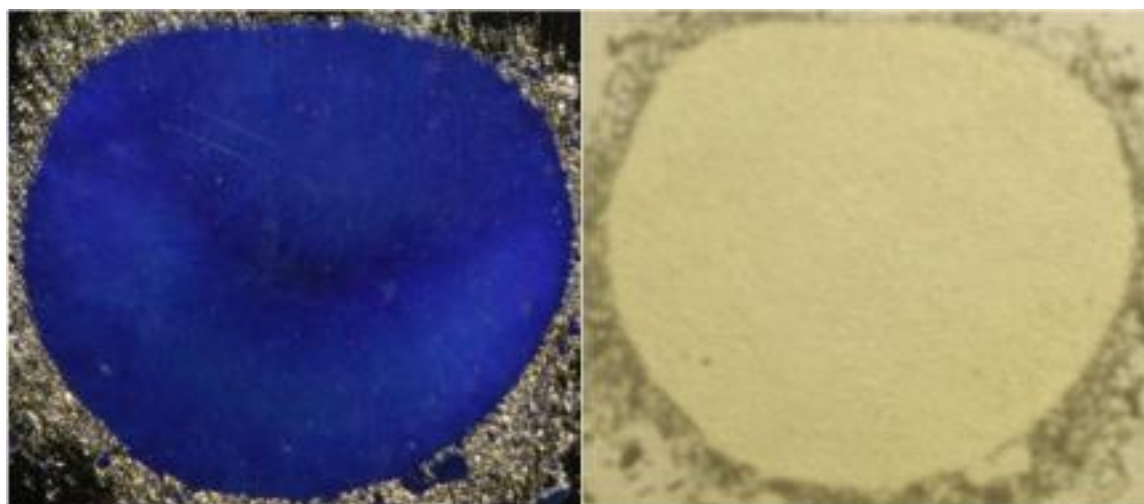


Figure 5.58. Photographs of the reflection (left) and transmission (right) of the p(NB-PLA)-b-p(NB-PS) ($M_n = 1,305,000$ g/mol) film.

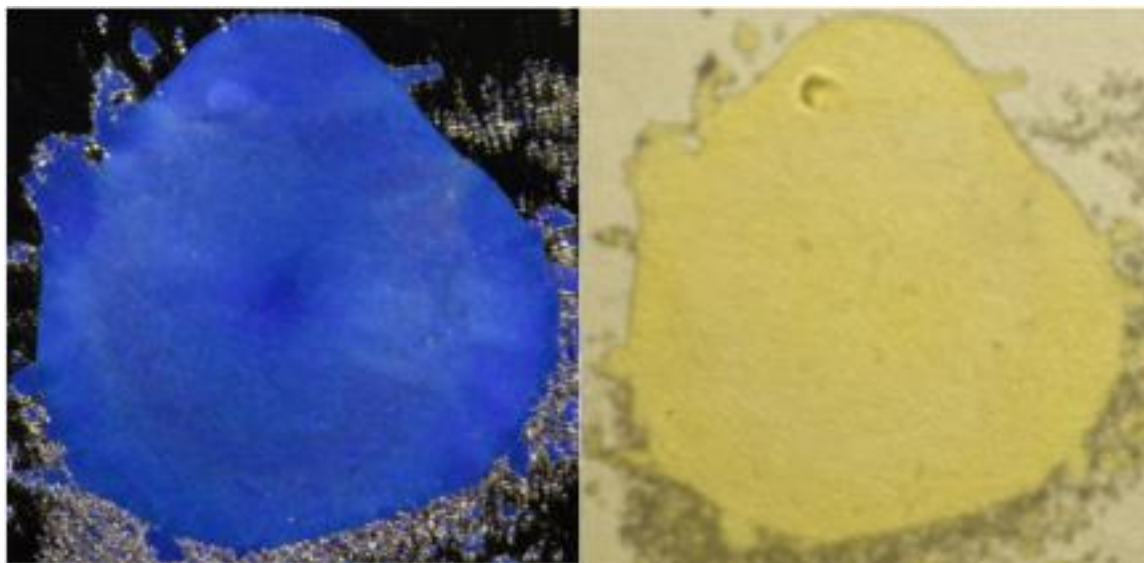


Figure 5.59. Photographs of the reflection (left) and transmission (right) of the p(NB-PLA)-b-p(NB-PS) ($M_n = 1,733,000$ g/mol) film.

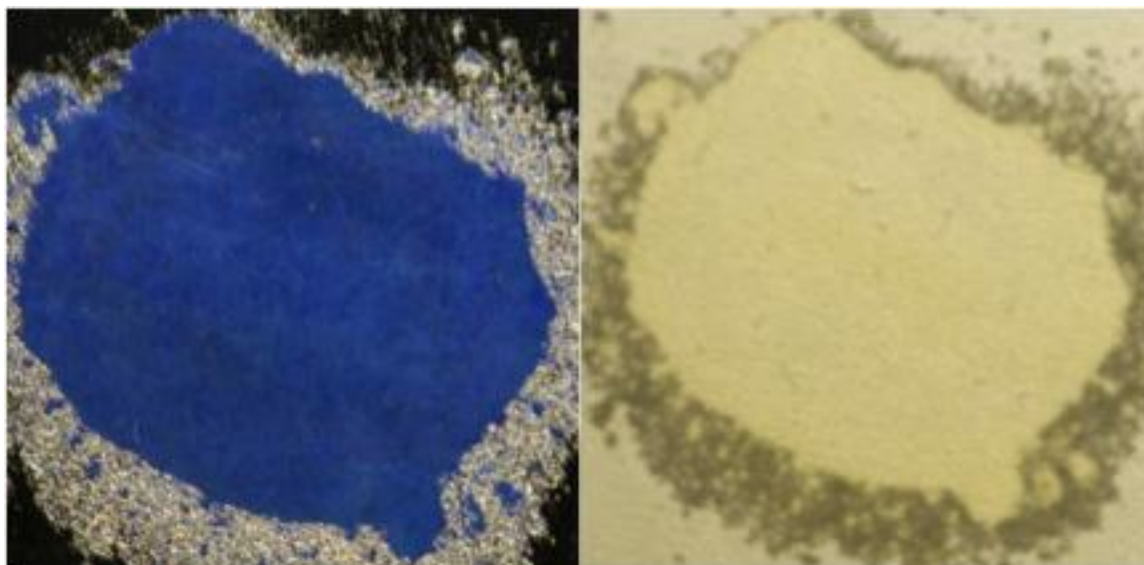


Figure 5.60. Photographs of the reflection (left) and transmission (right) of the p(NB-PLA)-b-p(NB-PS) ($M_n = 1,700,000$ g/mol) film.

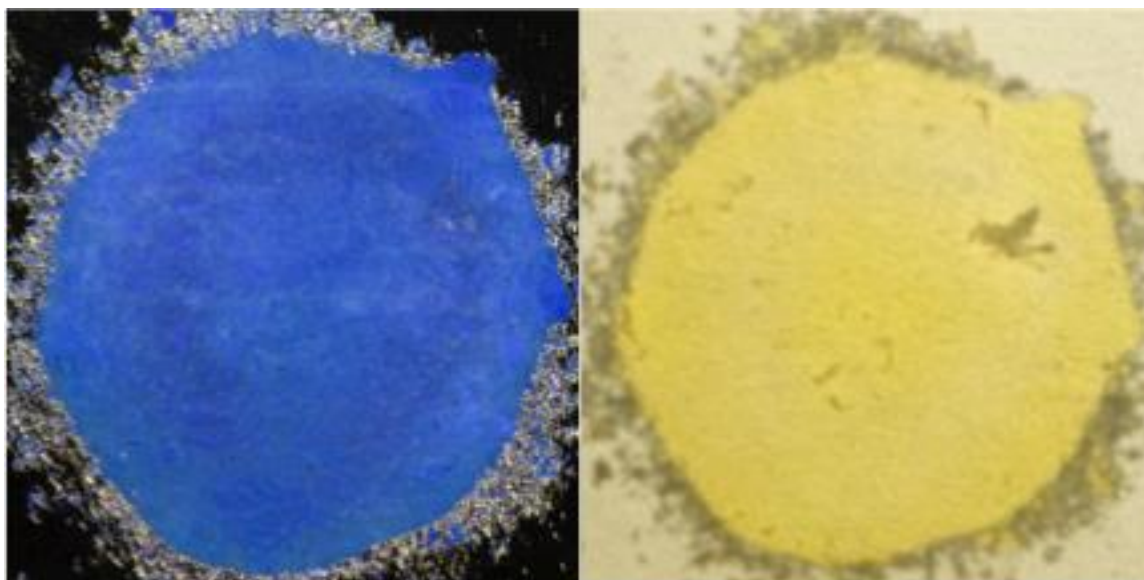


Figure 5.61. Photographs of the reflection (left) and transmission (right) of the p(NB-PLA)-b-p(NB-PS) ($M_n = 2,299,000$ g/mol) film.

UV-Vis DRA Reflection Traces:

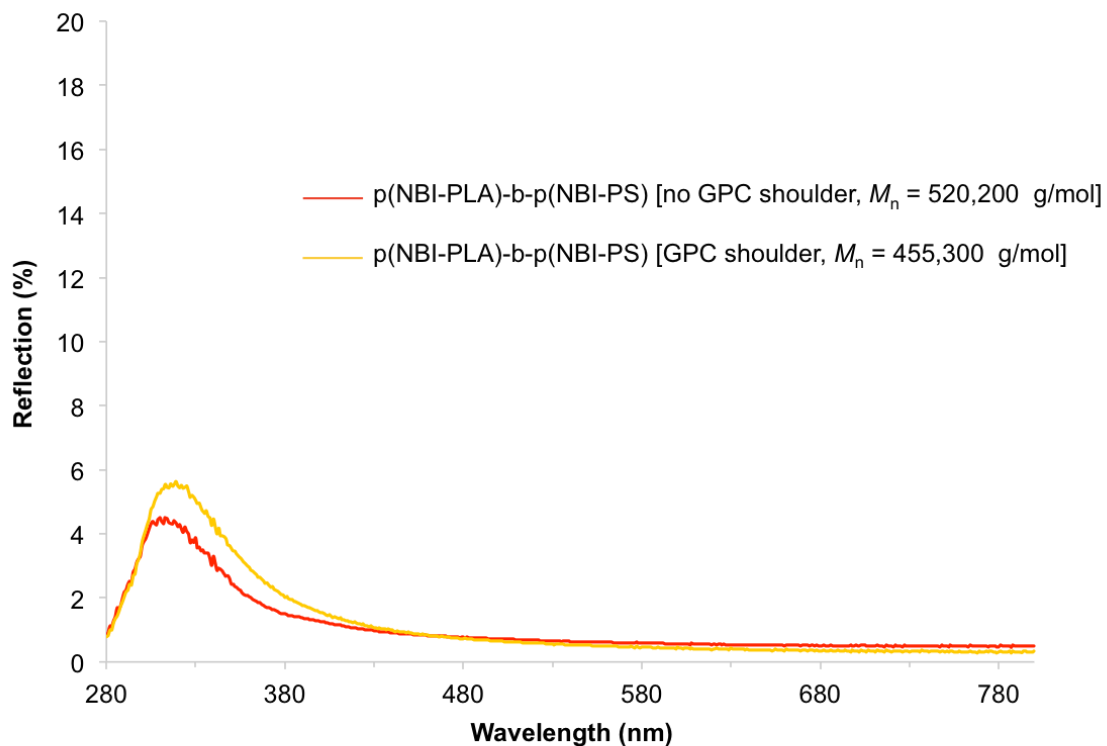


Figure 5.62. Reflection traces of 2 thin films of similar MW (with and without a small MW shoulder in GPC trace) between two glass slides on a UV-Vis diffuse reflectance accessory.

SEM Micrographs of BBCP Films:

p(NBI-PLA)-b-p(NBI-PS)



Figure 5.63. Representative SEM micrograph of the *p(NBI-PLA)-b-p(NBI-PS)* ($M_n = 455,300$ g/mol) film.



Figure 5.64. Representative SEM micrograph of the p(NBI-PLA)-b-p(NBI-PS) ($M_n = 520,200$ g/mol) film.

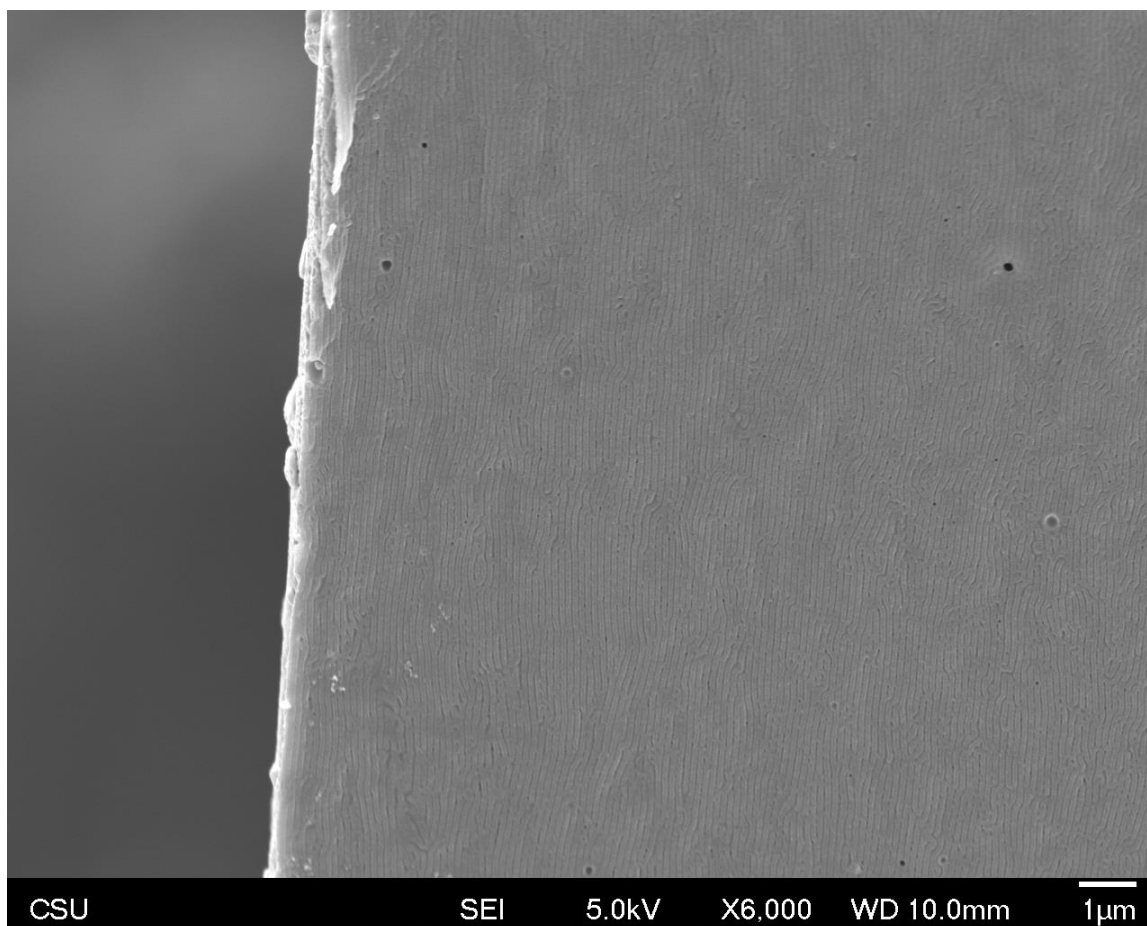


Figure 5.65. Representative SEM micrograph of the p(NBI-PLA)-b-p(NBI-PS) ($M_n = 849,800$ g/mol) film.

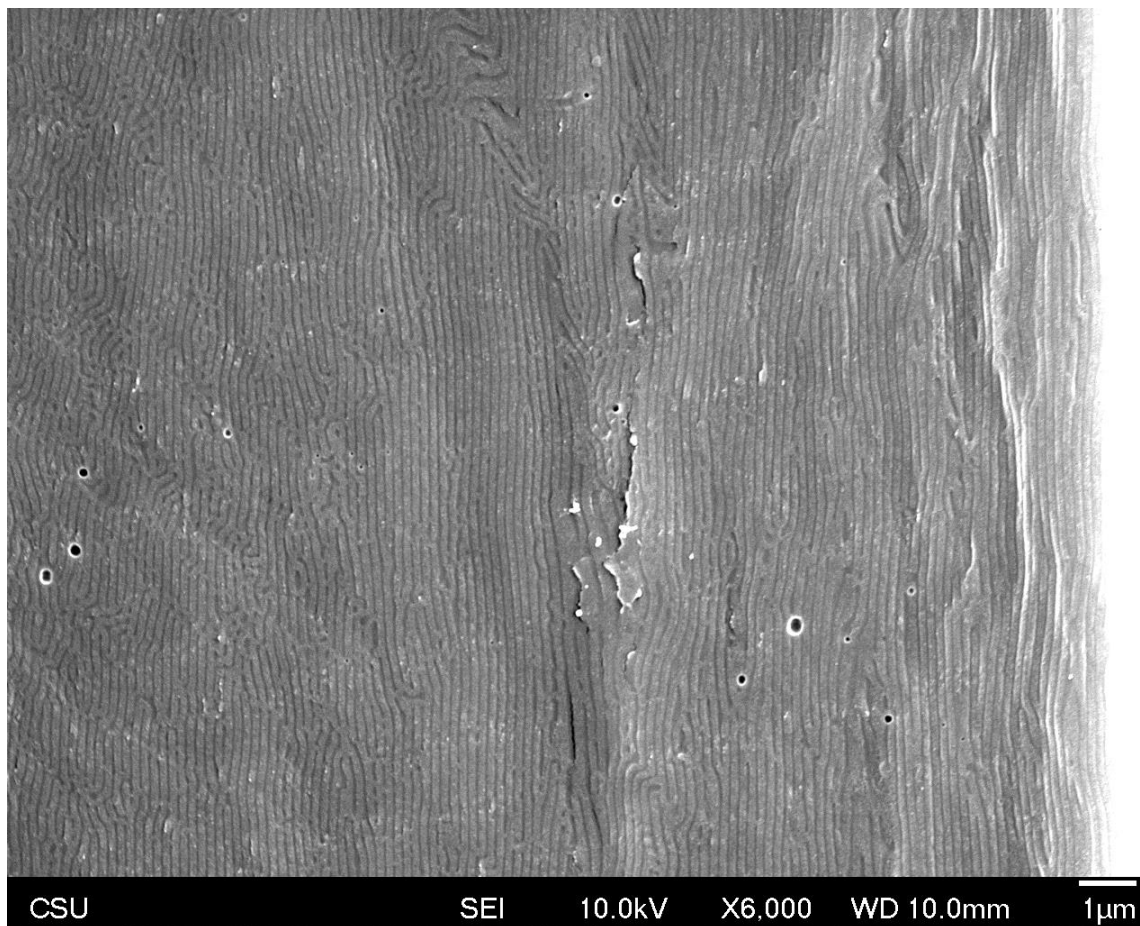


Figure 5.66. Representative SEM micrograph of the p(NBI-PLA)-b-p(NBI-PS) ($M_n = 1,314,000$ g/mol) film.

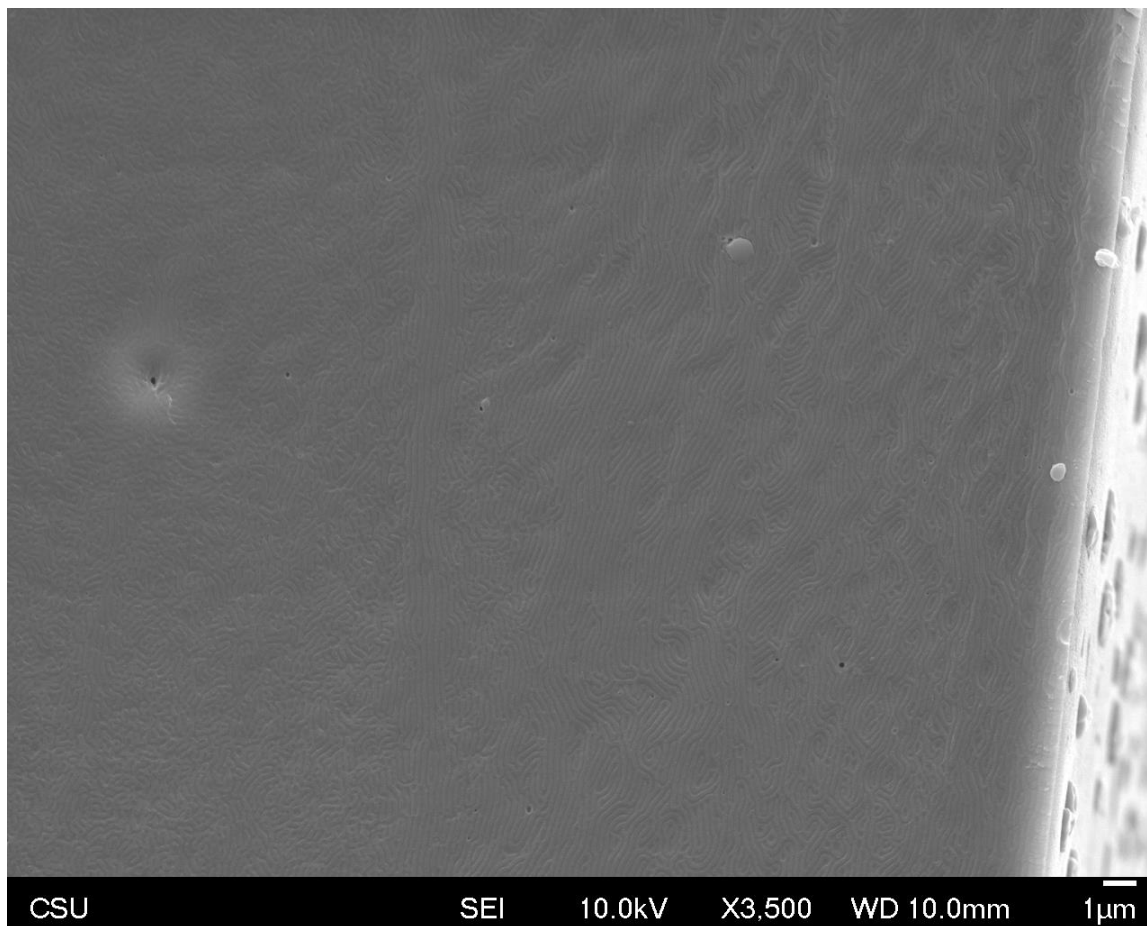


Figure 5.67. Representative SEM micrograph of the p(NBI-PLA)-b-p(NBI-PS) ($M_n = 1,420,000$ g/mol) film.

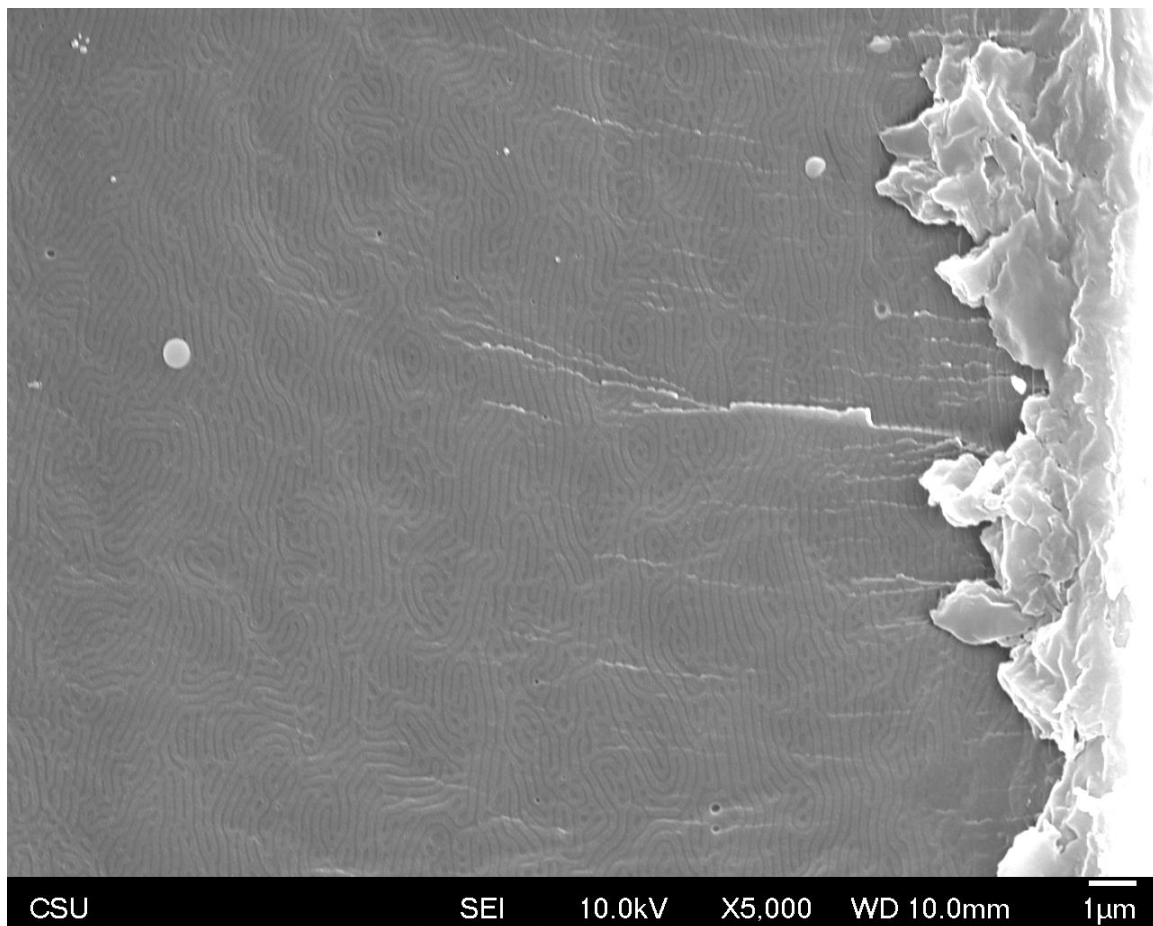


Figure 5.68. Representative SEM micrograph of the p(NBI-PLA)-b-p(NBI-PS) ($M_n = 1,434,000$ g/mol) film.

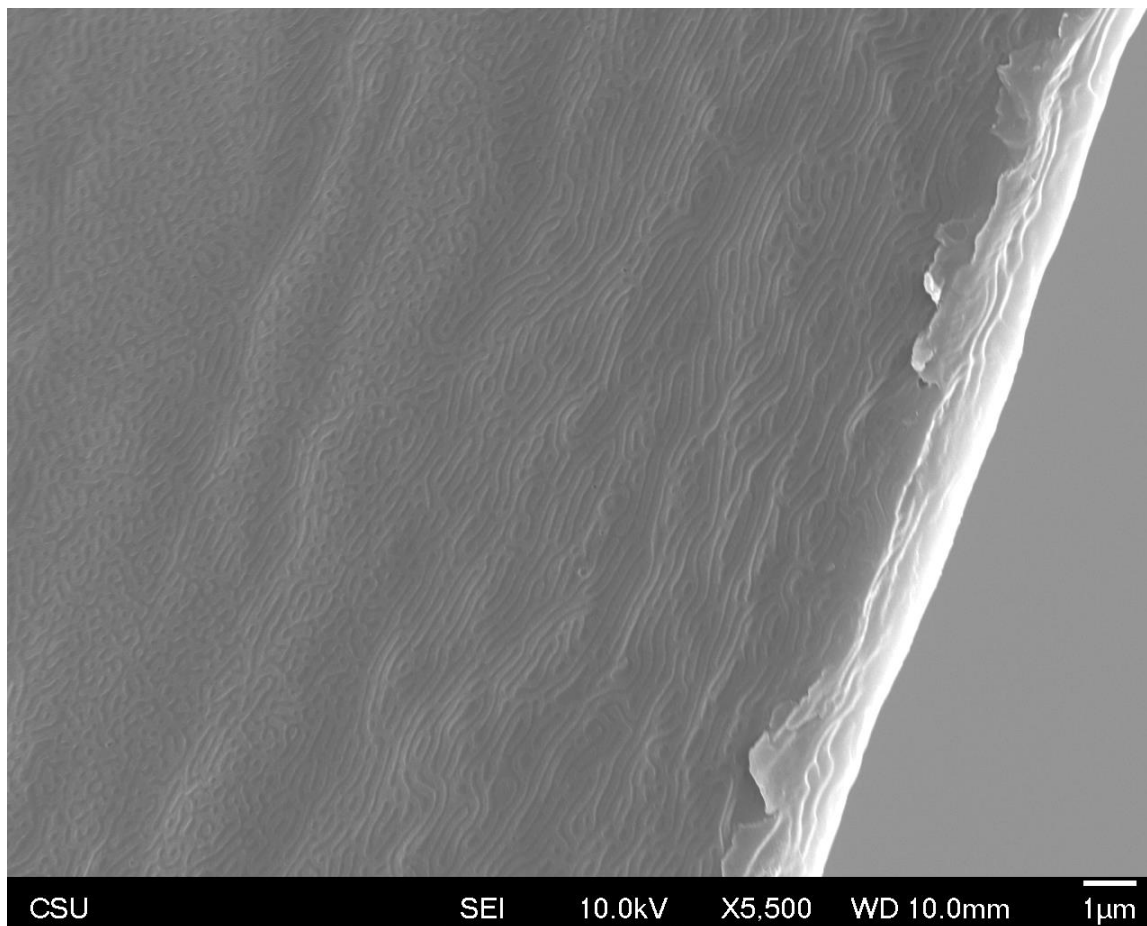


Figure 5.69. Representative SEM micrograph of the p(NBI-PLA)-b-p(NBI-PS) ($M_n = 1,563,000$ g/mol) film.

p(NBI-PLA)-b-p(NB-PS)

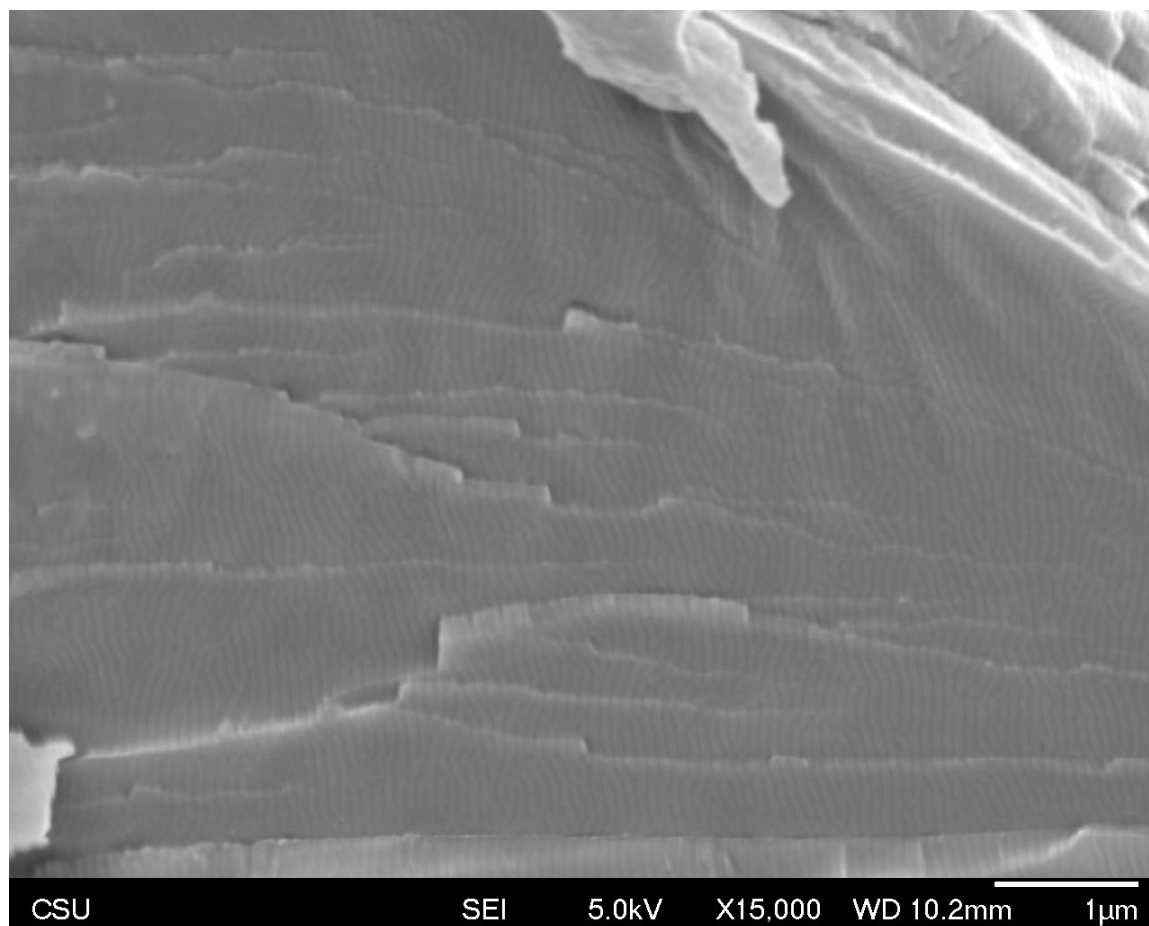


Figure 5.70. Representative SEM micrograph of the p(NBI-PLA)-b-p(NB-PS) ($M_n = 613,000$ g/mol) film.



Figure 5.71. Representative SEM micrograph of the p(NBI-PLA)-b-p(NB-PS) ($M_n = 765,800$ g/mol) film.

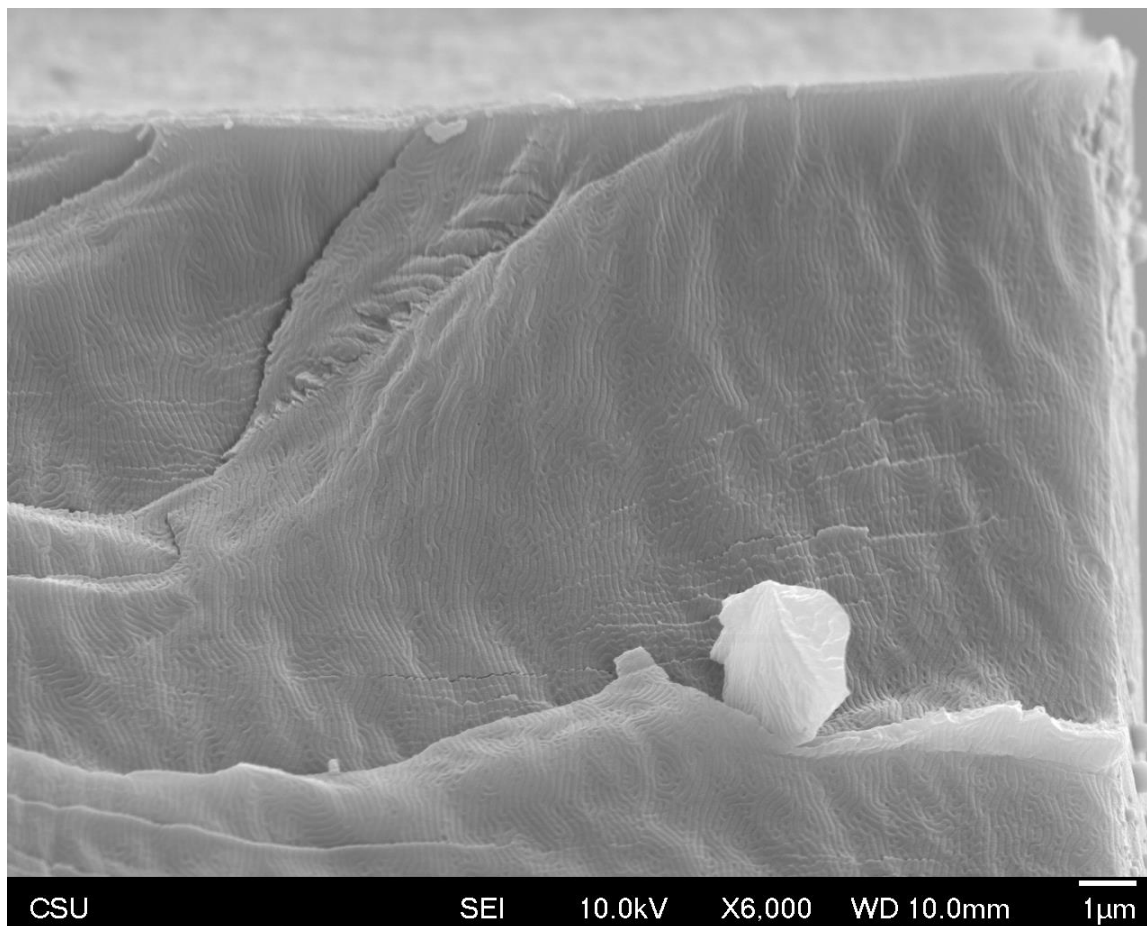


Figure 5.72. Representative SEM micrograph of the p(NBI-PLA)-b-p(NB-PS) ($M_n = 1,110,000$ g/mol) film.

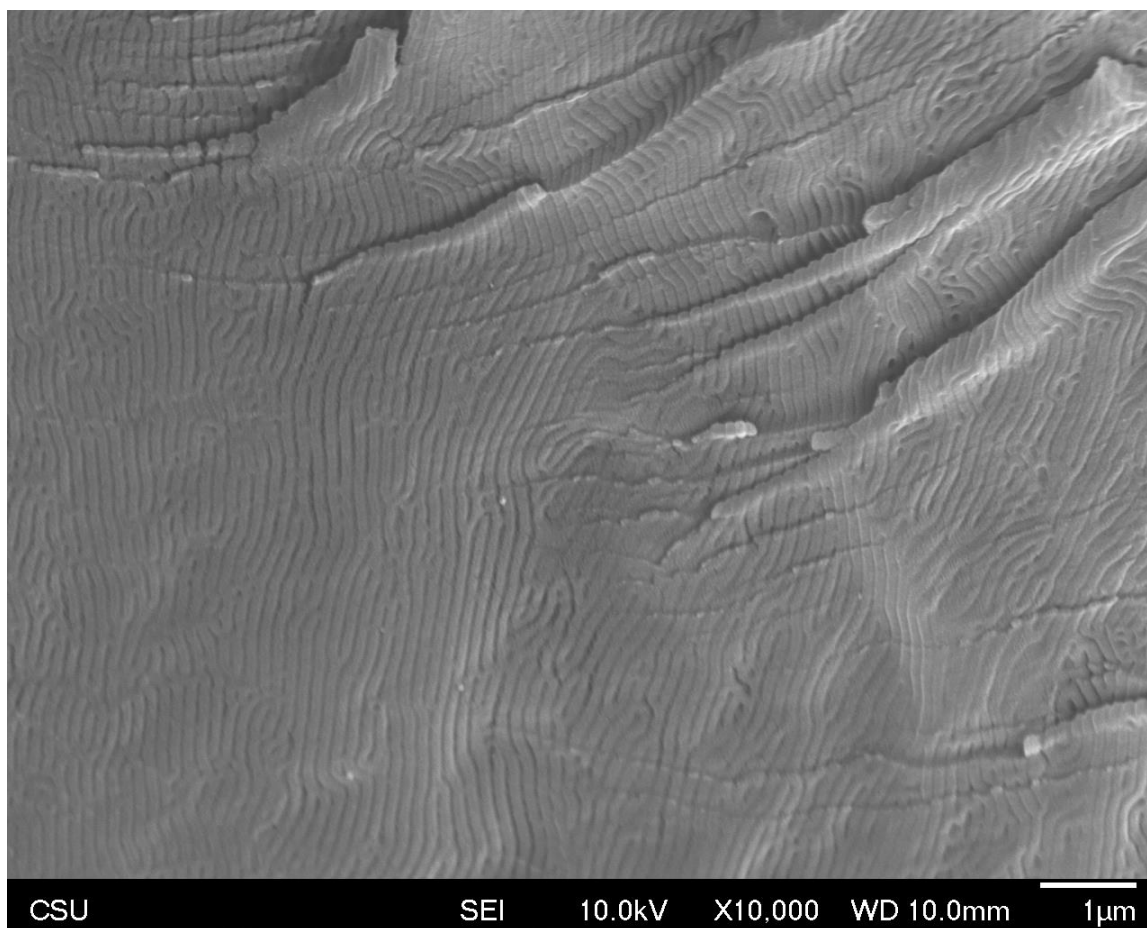


Figure 5.73. Representative SEM micrograph of the p(NBI-PLA)-b-p(NB-PS) ($M_n = 1,524,000$ g/mol) film.

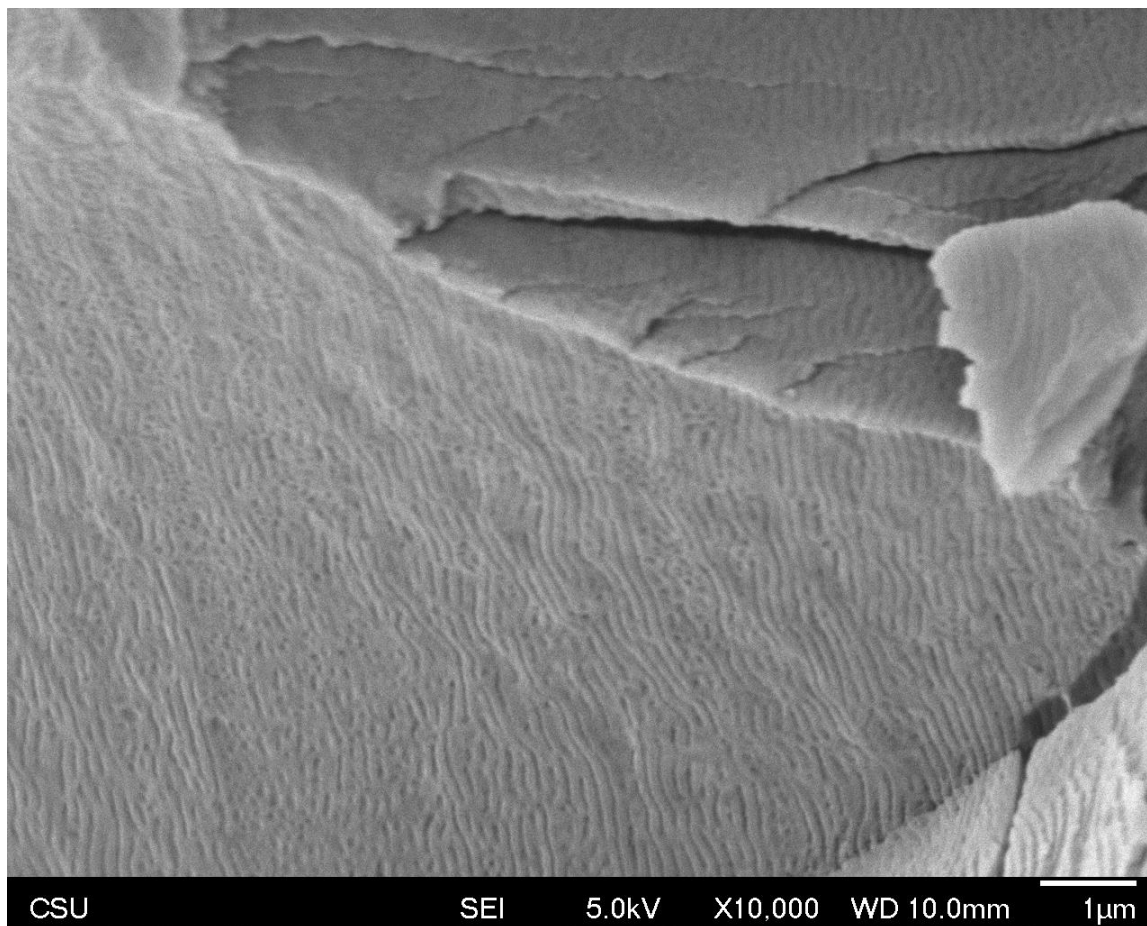


Figure 5.74. Representative SEM micrograph of the p(NBI-PLA)-b-p(NB-PS) ($M_n = 1,657,000$ g/mol) film.

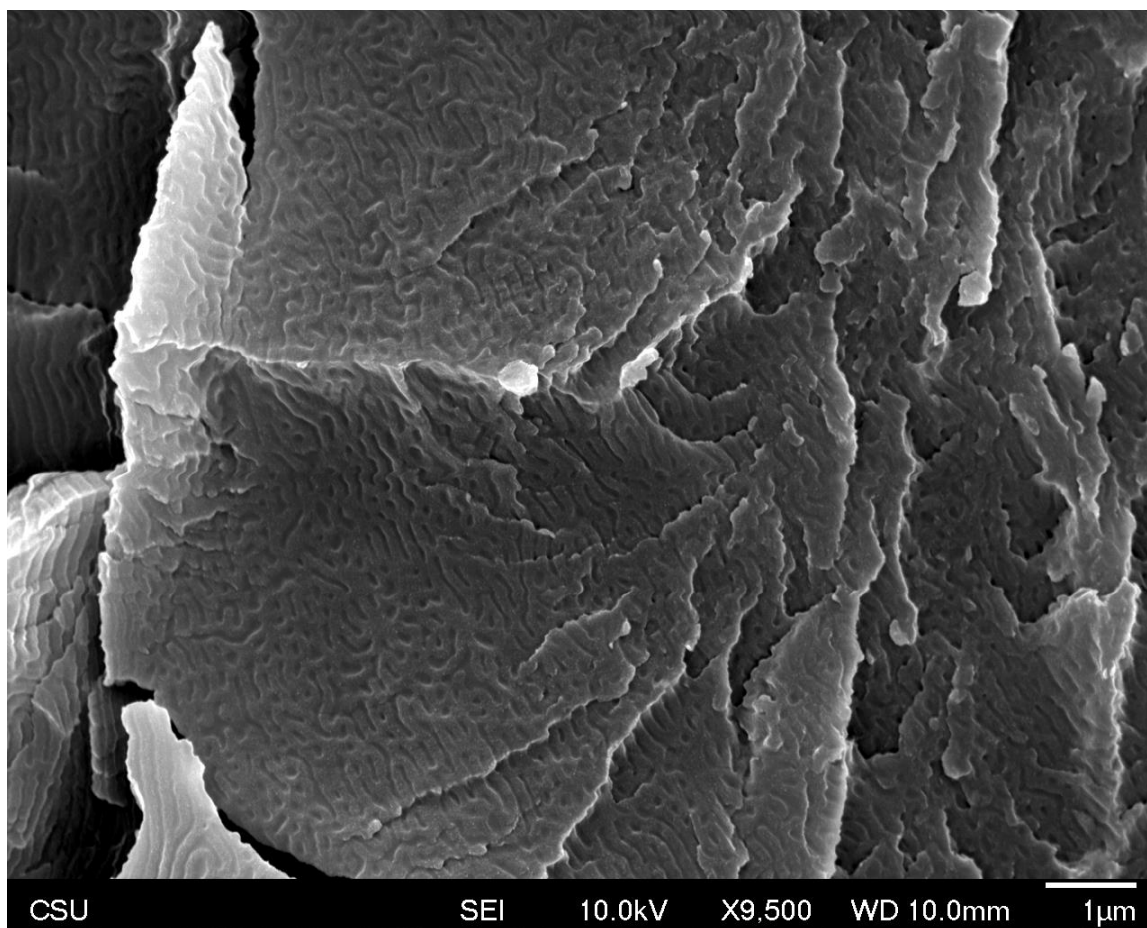


Figure 5.75. Representative SEM micrograph of the p(NBI-PLA)-b-p(NB-PS) ($M_n = 2,601,000$ g/mol) film.

p(NB-PLA)-b-p(NBI-PS)

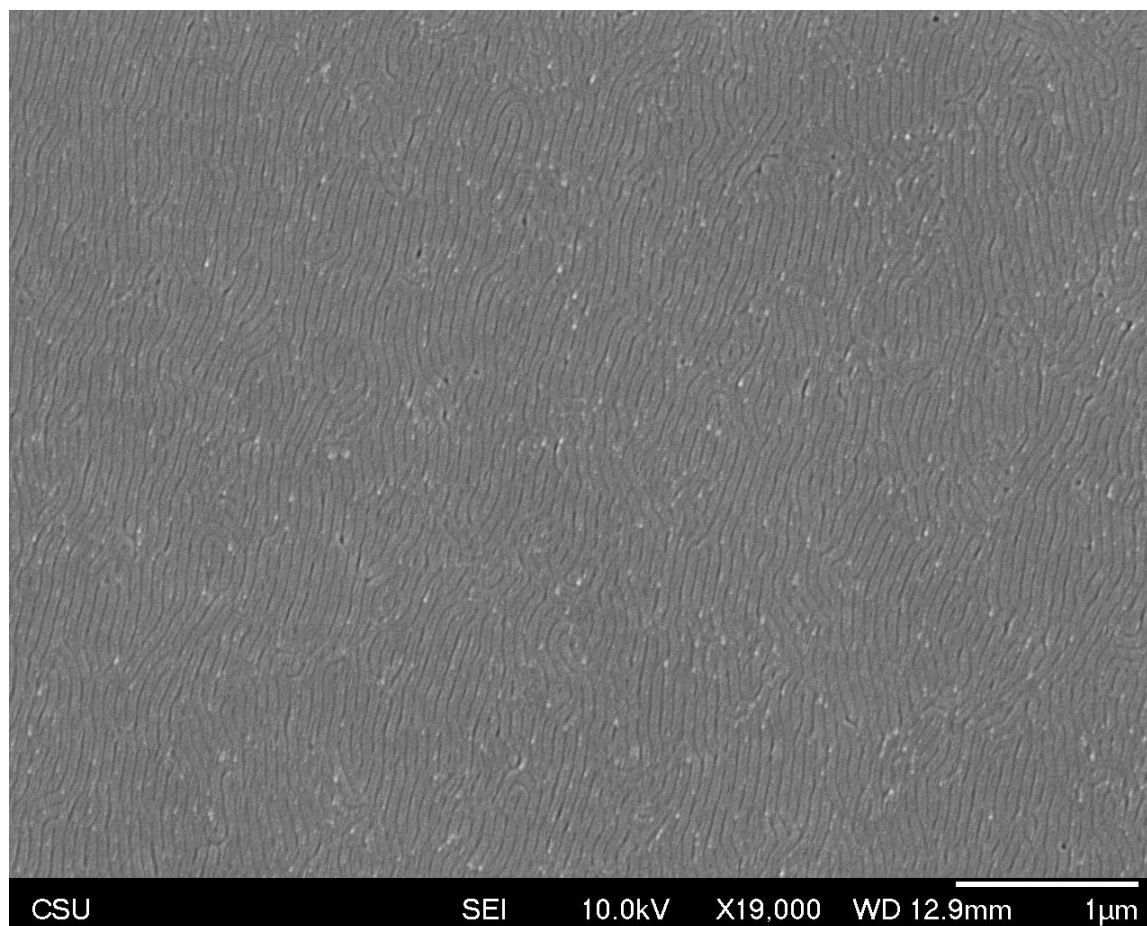


Figure 5.76. Representative SEM micrograph of the *p(NB-PLA)-b-p(NBI-PS)* ($M_n = 524,100$ g/mol) film.

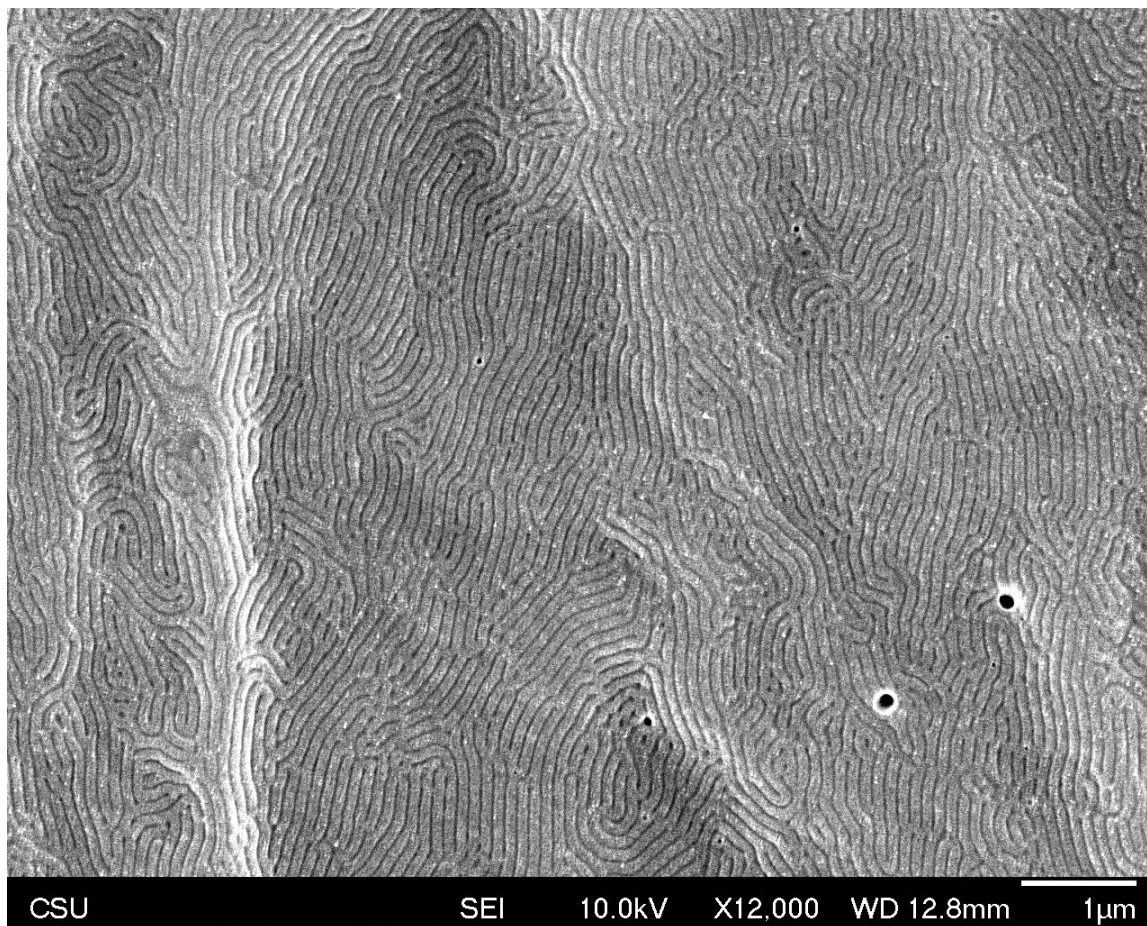


Figure 5.77. Representative SEM micrograph of the p(NB-PLA)-b-p(NBI-PS) ($M_n = 917,500$ g/mol) film.

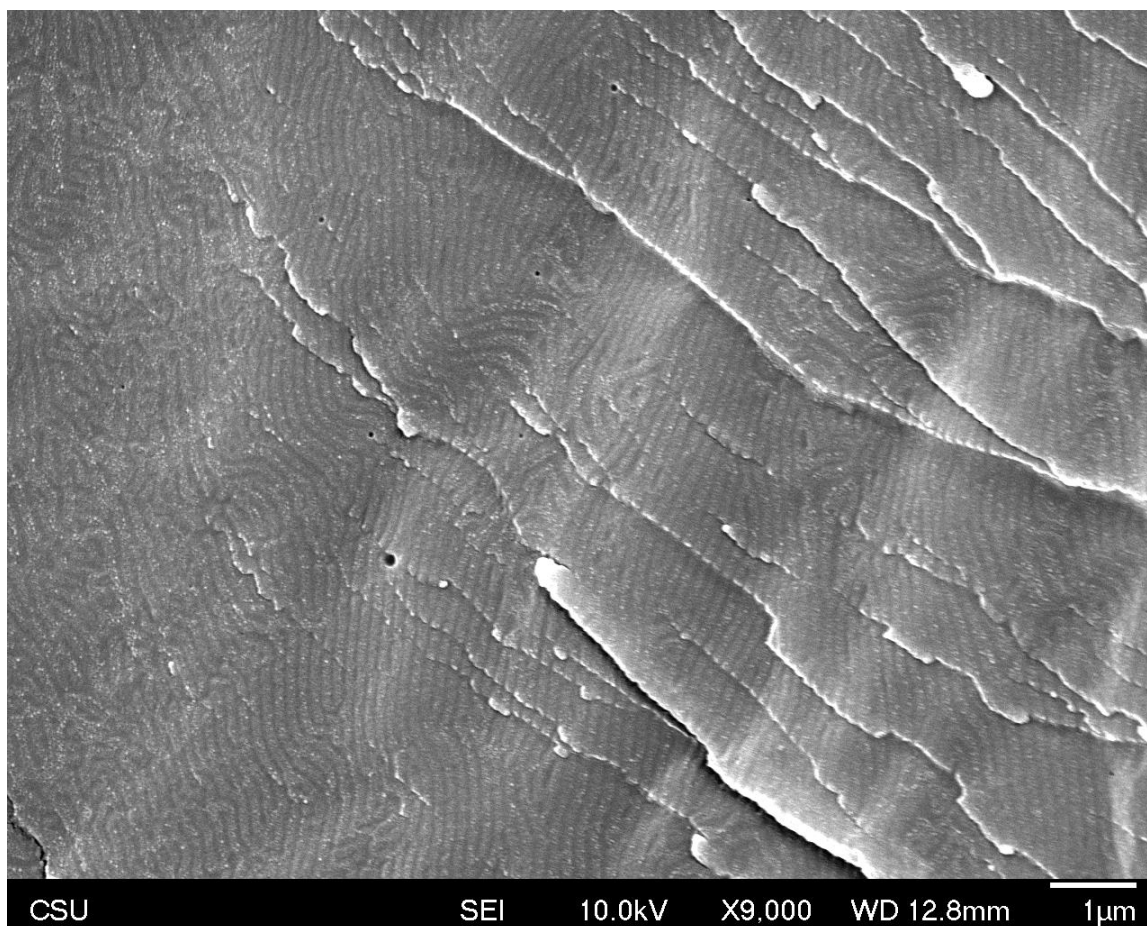


Figure 5.78. Representative SEM micrograph of the p(NB-PLA)-b-p(NBI-PS) ($M_n = 1,435,000$ g/mol) film.

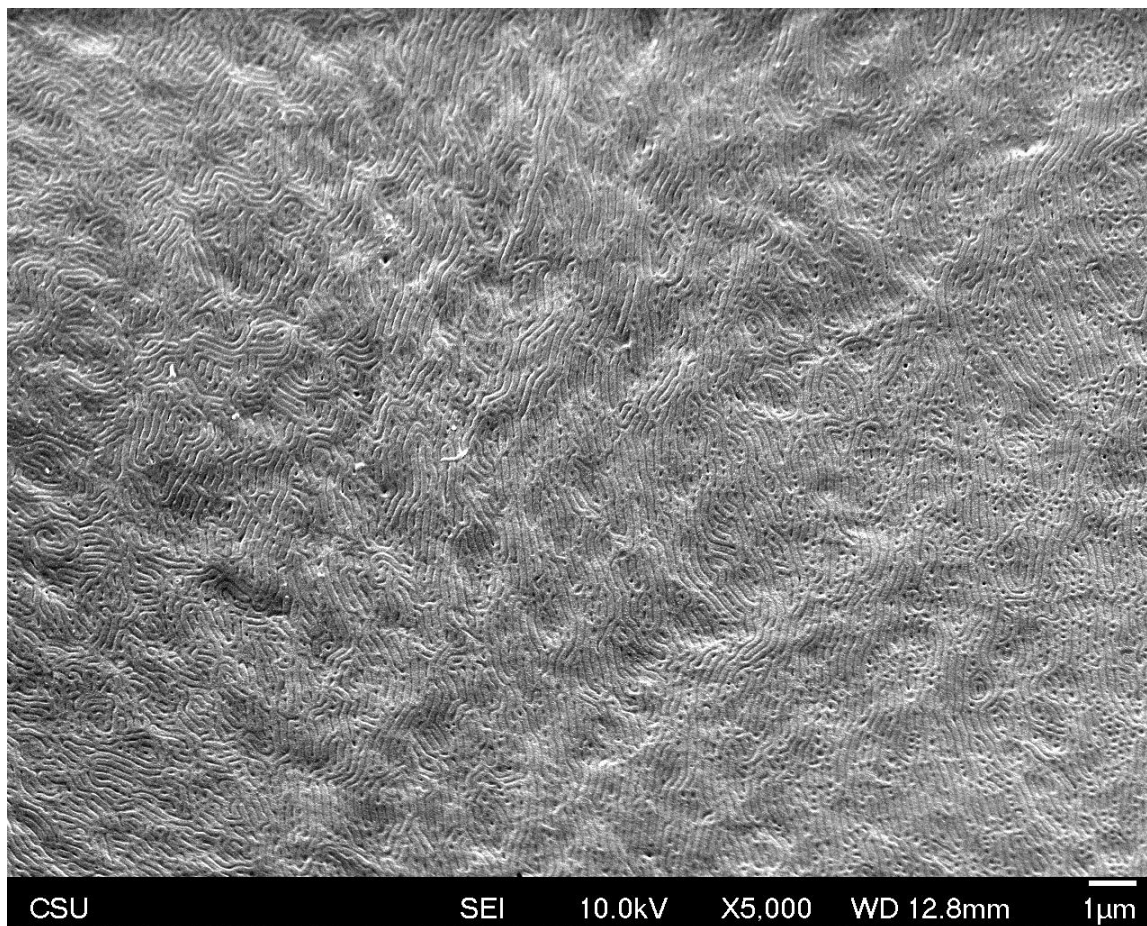


Figure 5.79. Representative SEM micrograph of the p(NB-PLA)-b-p(NBI-PS) ($M_n = 1,875,000$ g/mol) film.

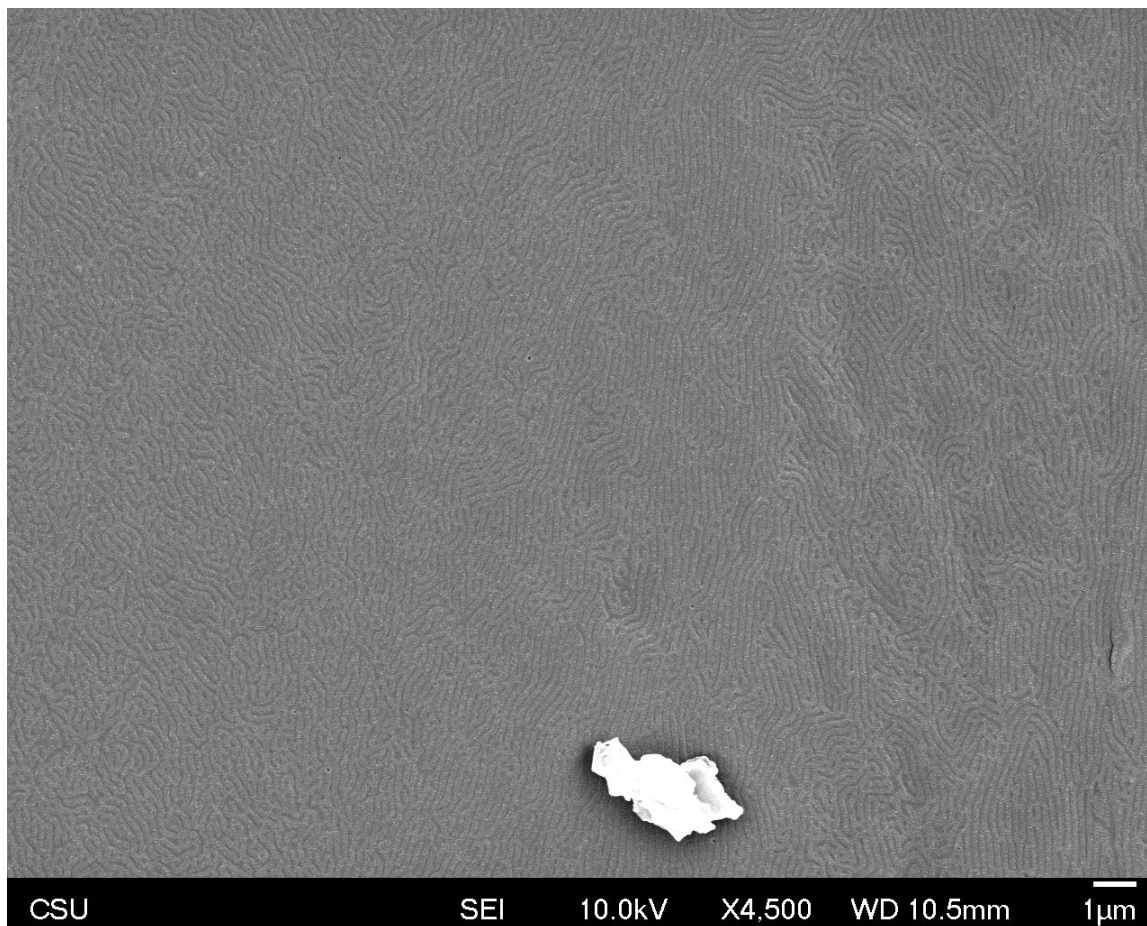


Figure 5.80. Representative SEM micrograph of the p(NB-PLA)-b-p(NBI-PS) ($M_n = 1,904,000$ g/mol) film.

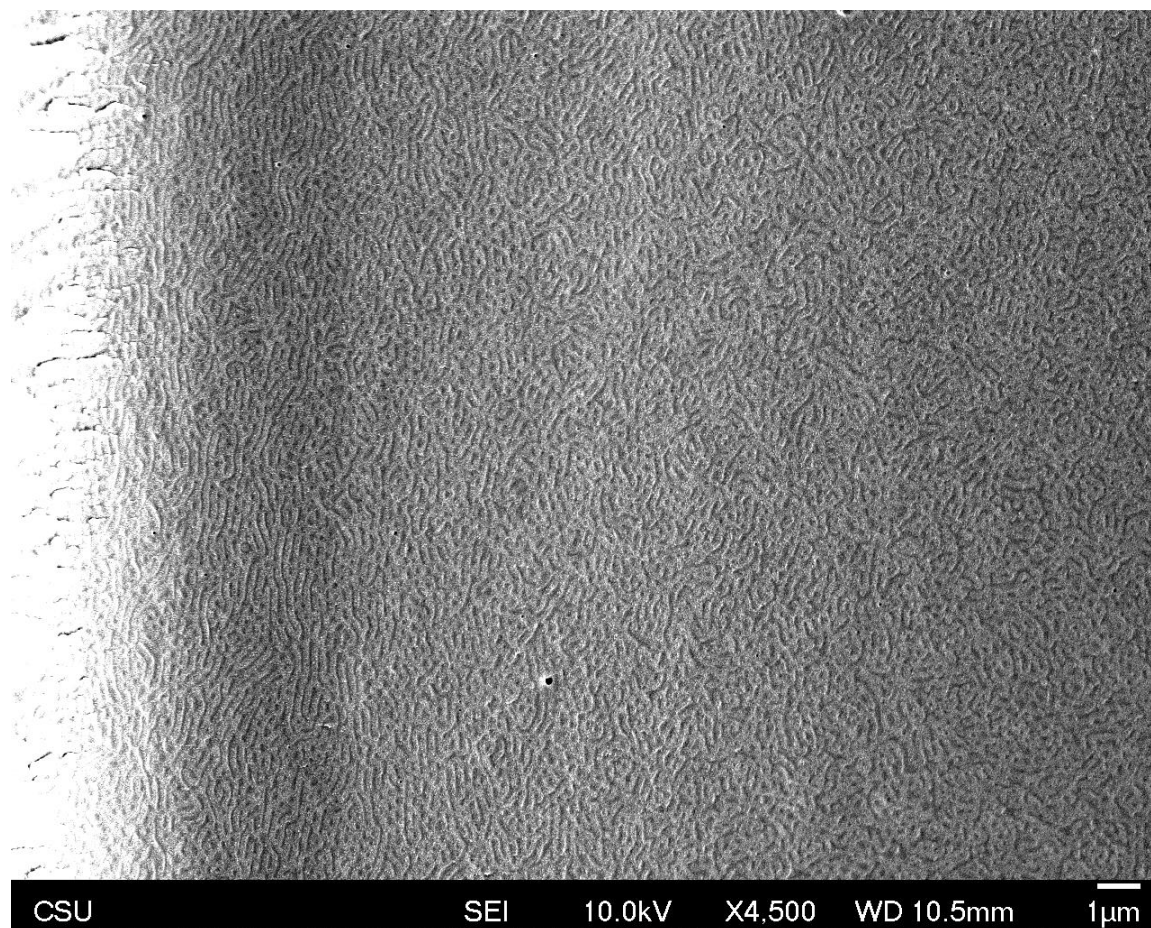


Figure 5.81. Representative SEM micrograph of the p(NB-PLA)-b-p(NBI-PS) ($M_n = 2,134,000$ g/mol) film.

p(NB-PLA)-b-p(NB-PS)



Figure 5.82. Representative SEM micrograph of the *p(NB-PLA)-b-p(NB-PS)* ($M_n = 413,600$ g/mol) film.

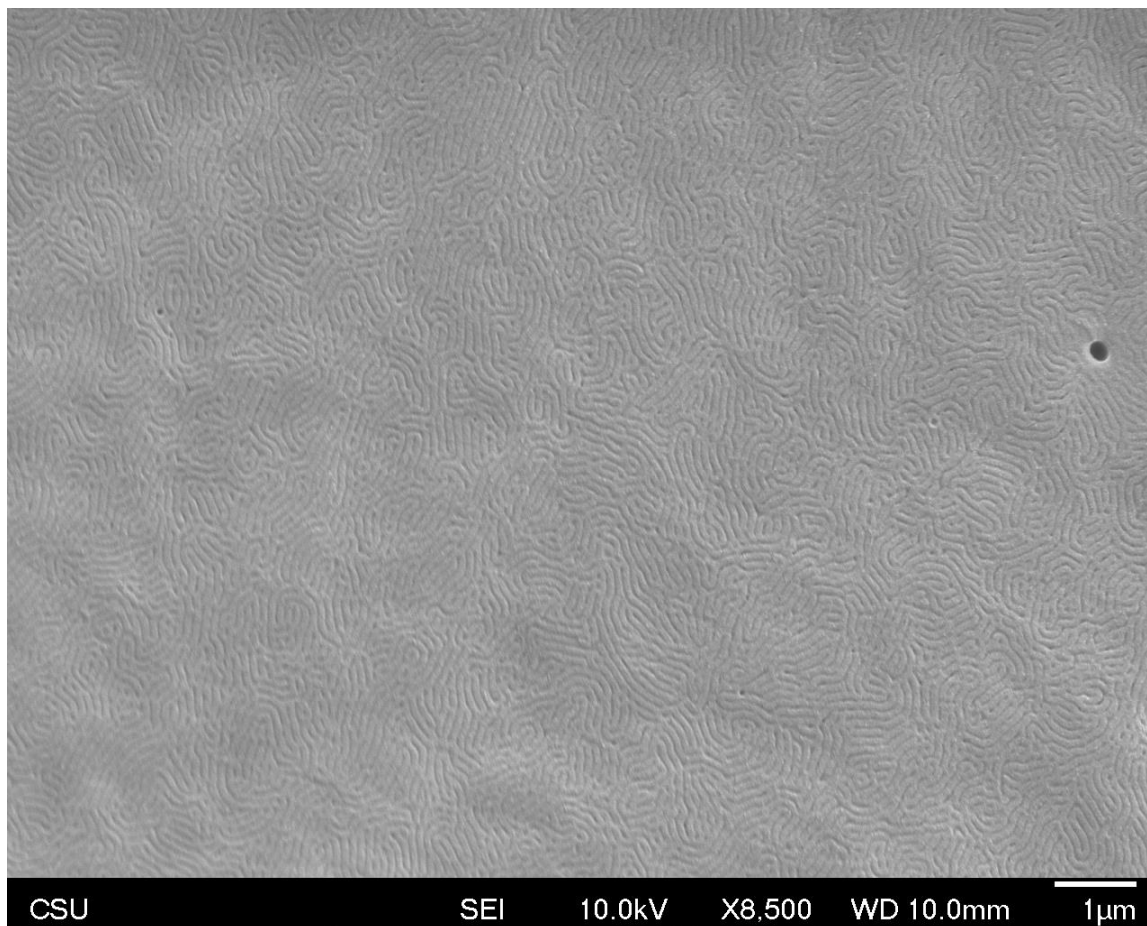


Figure 5.83. Representative SEM micrograph of the p(NB-PLA)-b-p(NB-PS) ($M_n = 787,000$ g/mol) film.

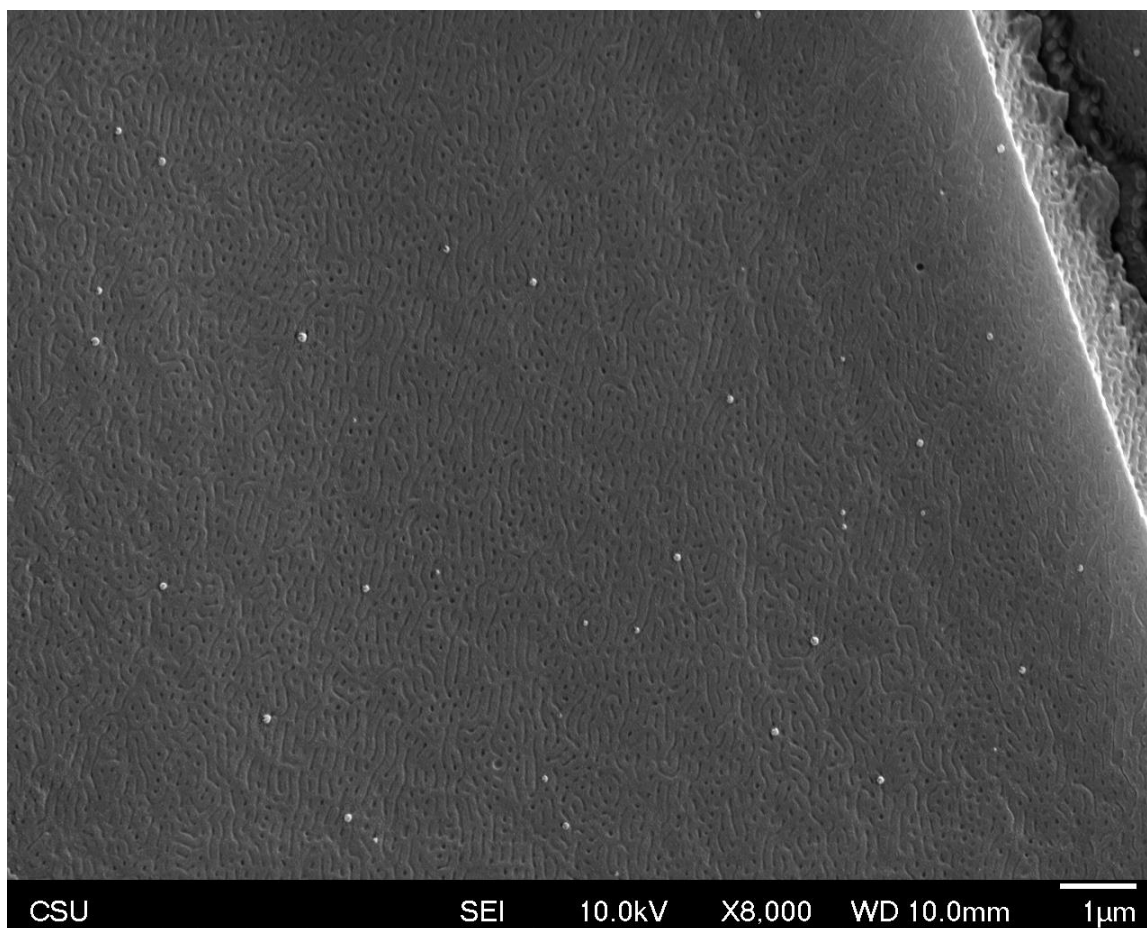


Figure 5.84. Representative SEM micrograph of the p(NB-PLA)-b-p(NB-PS) ($M_n = 1,305,000$ g/mol) film.

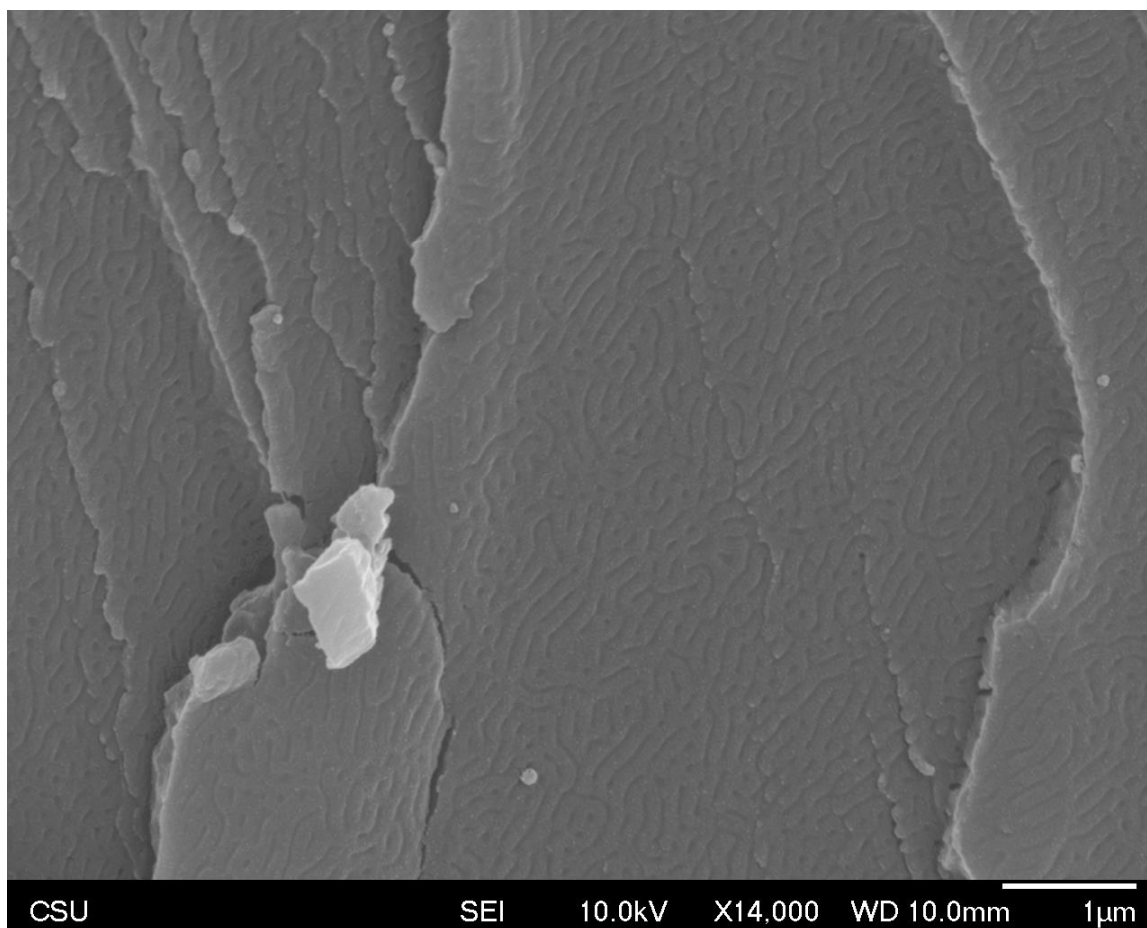


Figure 5.85. Representative SEM micrograph of the p(NB-PLA)-b-p(NB-PS) ($M_n = 1,733,000$ g/mol) film.

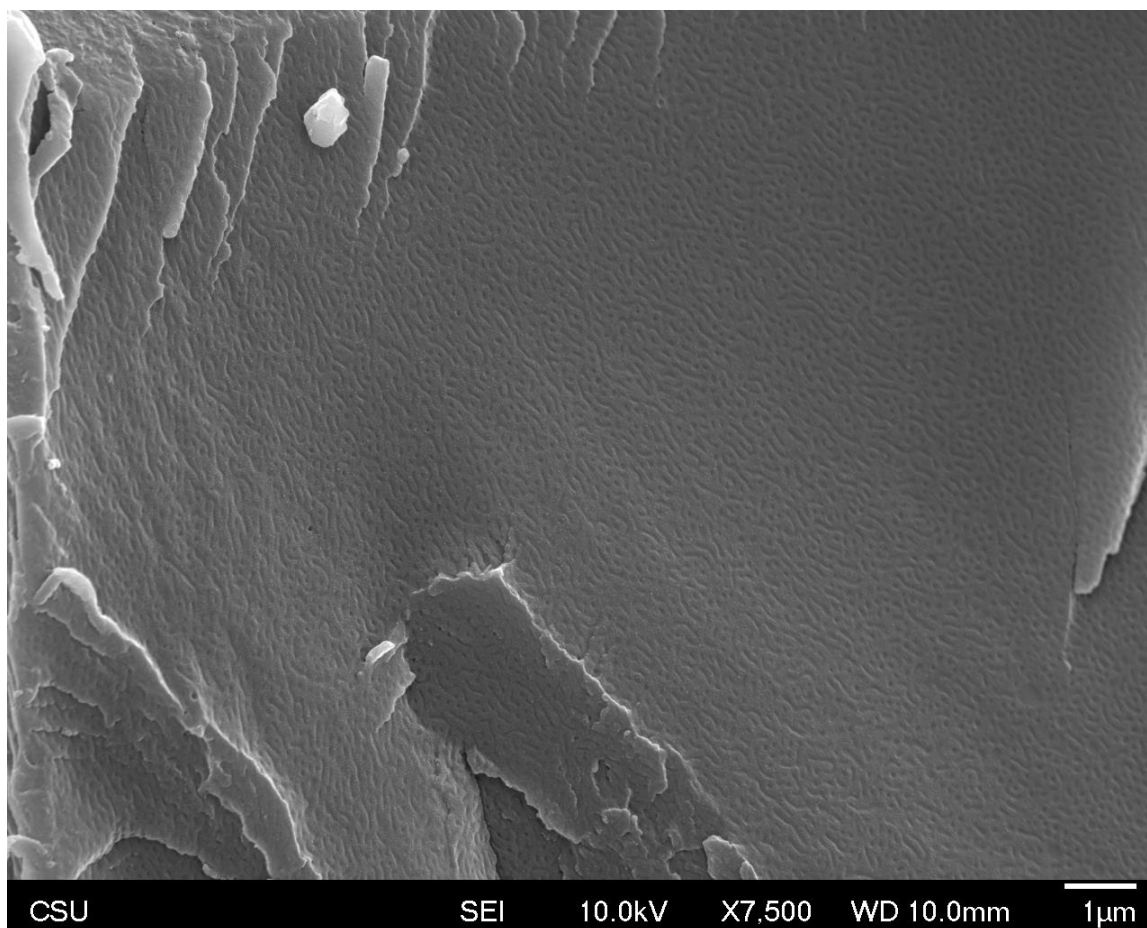


Figure 5.86. Representative SEM micrograph of the p(NB-PLA)-b-p(NB-PS) ($M_n = 1,700,000$ g/mol) film.

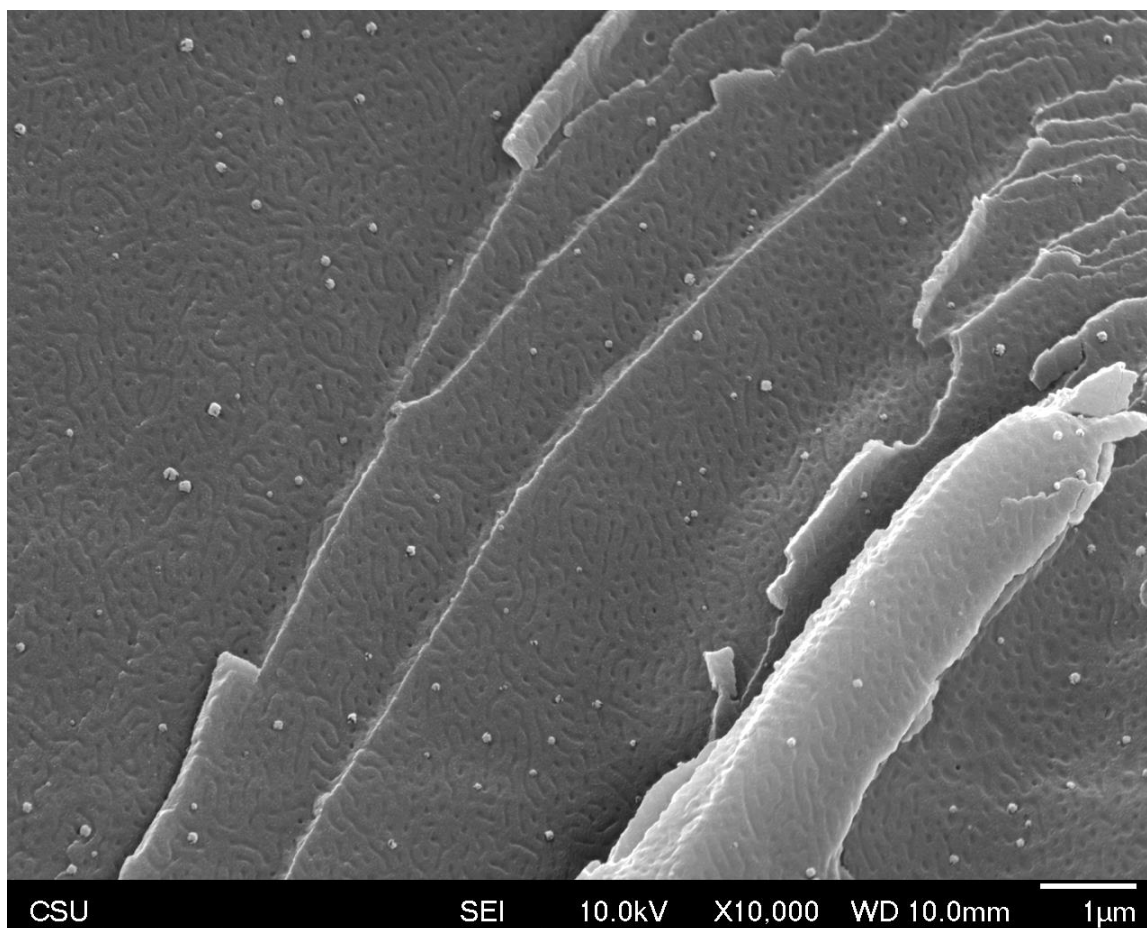


Figure 5.87. Representative SEM micrograph of the p(NB-PLA)-b-p(NB-PS) ($M_n = 2,299,000$ g/mol) film.

Thermal Properties

Thermal Gravimetric Analysis (TGA)

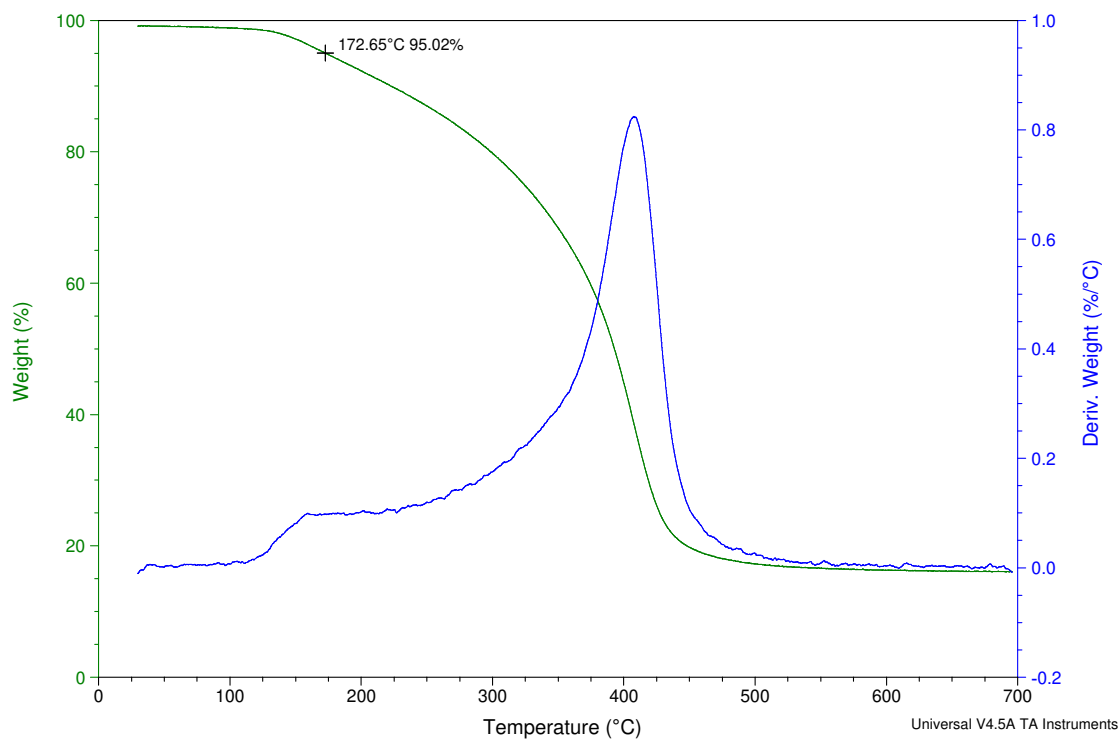


Figure 5.88. TGA trace of p(NB-Hep) ($M_n = 242,900$ g/mol). Decomposition temperature at 5% weight loss is 172.7 °C.

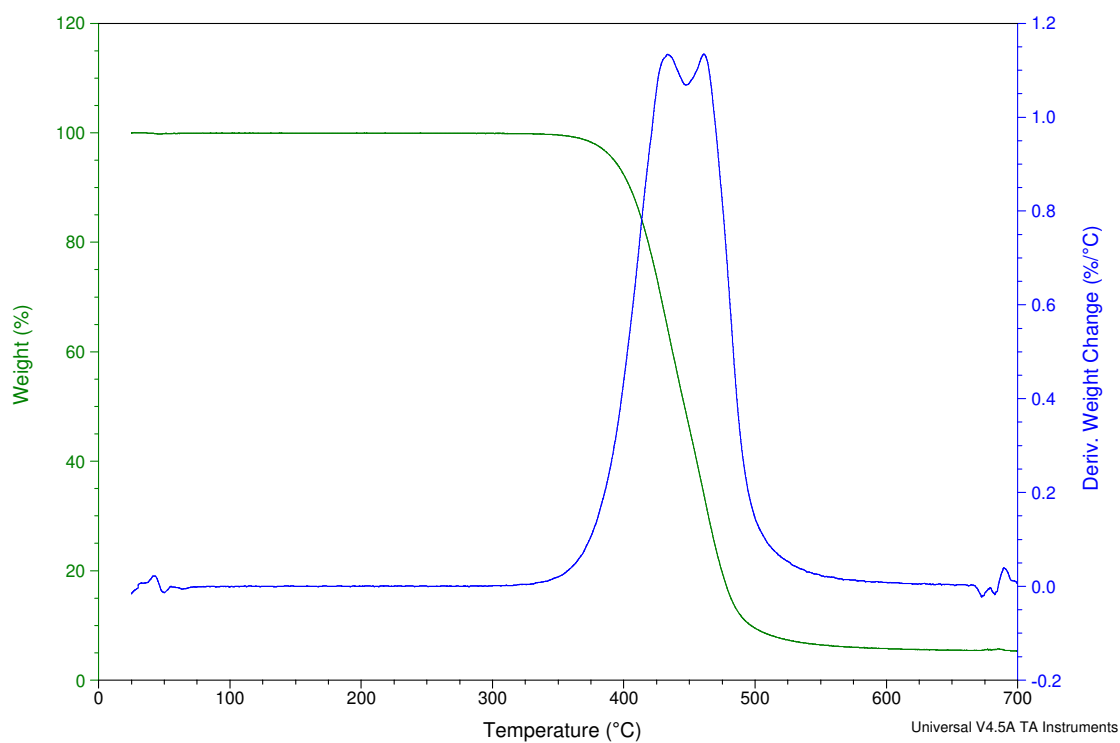


Figure 5.89. TGA trace of p(NBI-Hep) ($M_n = 114,900$ g/mol). Decomposition temperature at 5% weight loss is 392.7 °C.

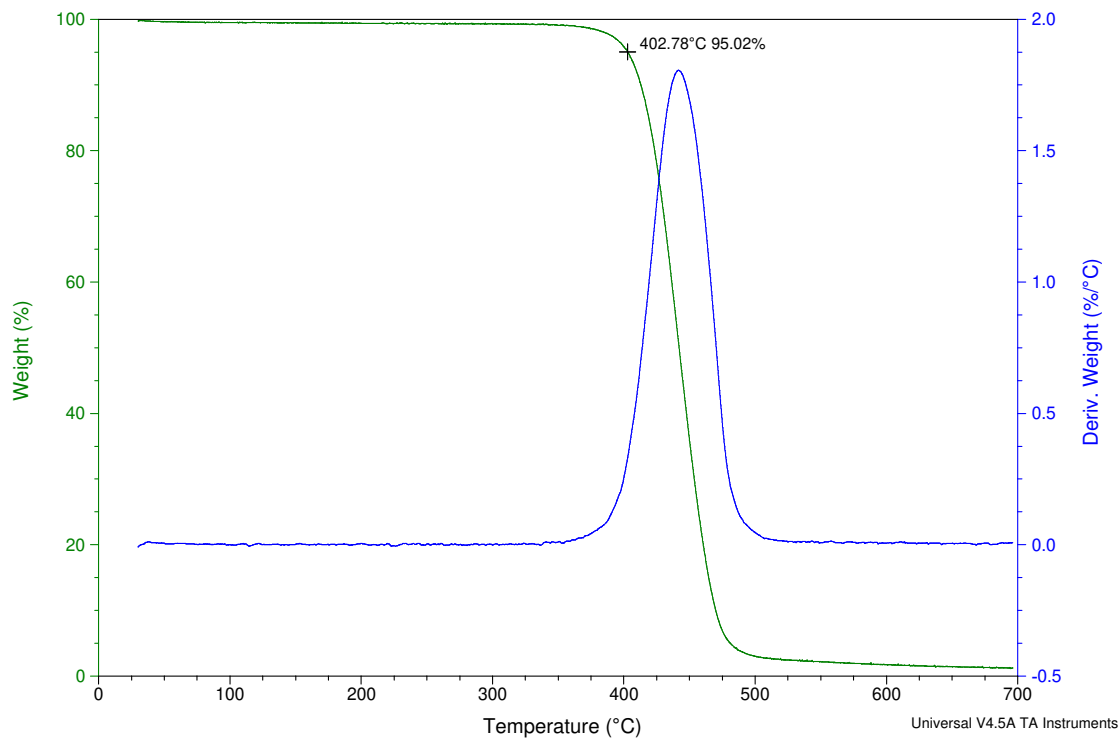


Figure 5.90. TGA trace of p(NBI-Dec) ($M_n = 779,700$ g/mol). Decomposition temperature at 5% weight loss is 402.78 °C.

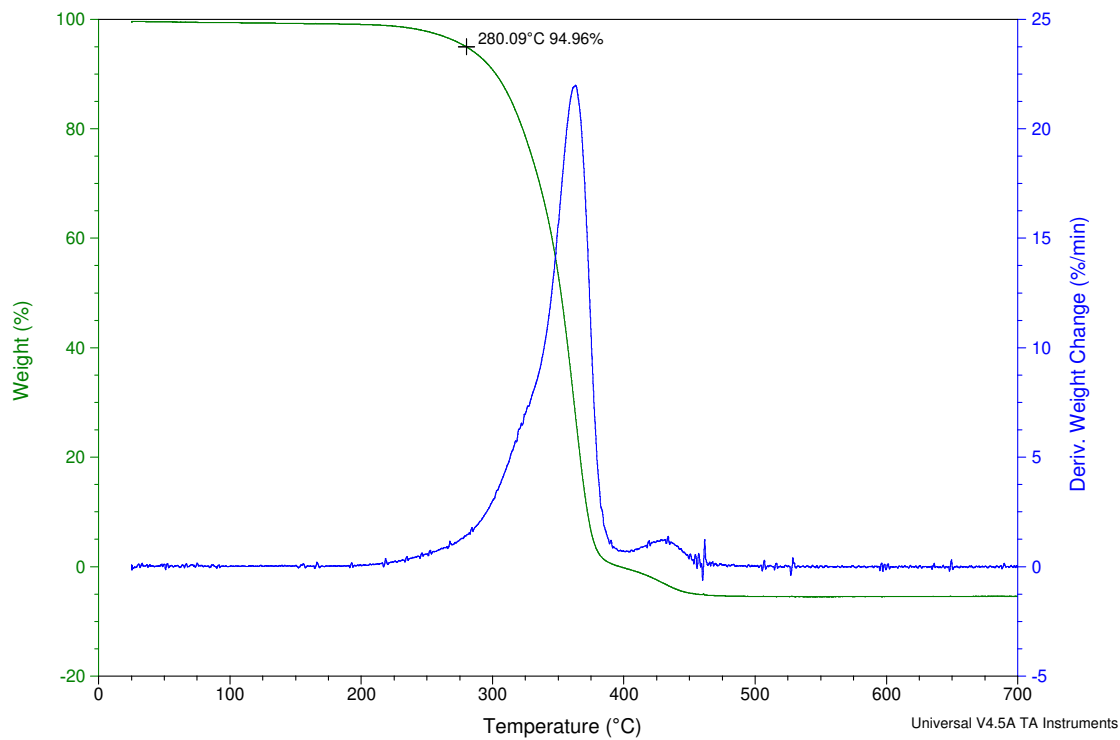


Figure 5.91. TGA trace of p(NB-PLA) ($M_n = 209,600$ g/mol). Decomposition temperature at 5% weight loss is 280.0 °C.

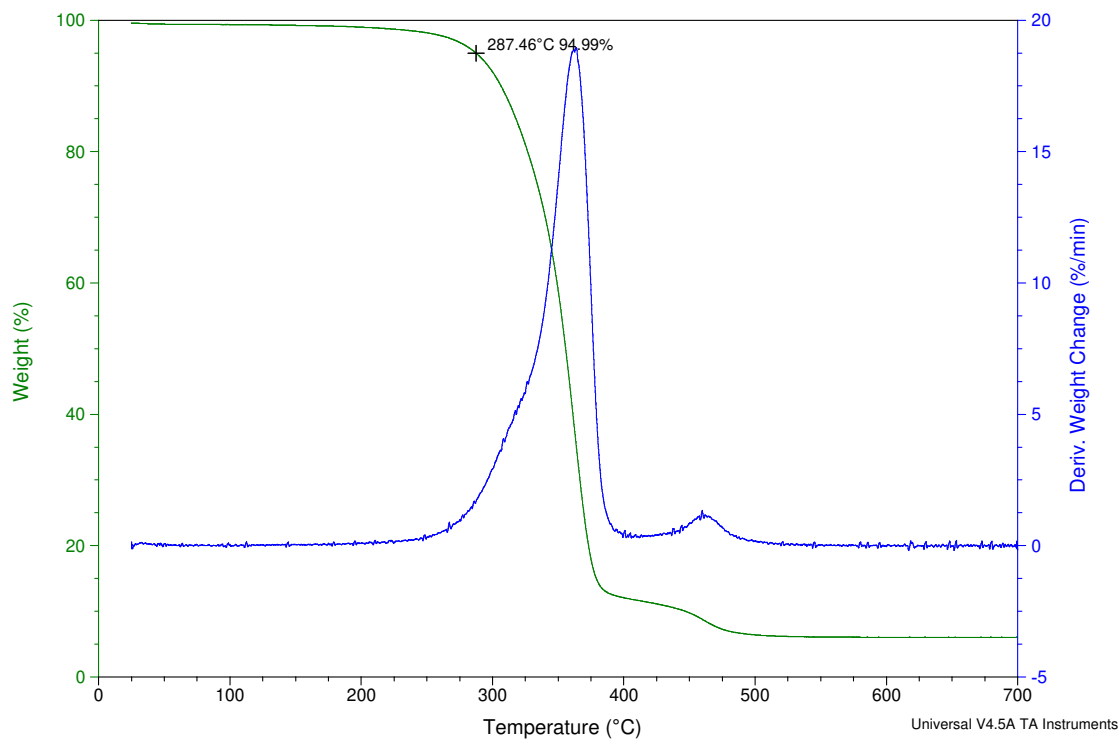


Figure 5.92. TGA trace of p(NBI-PLA) ($M_n = 254,500$ g/mol). Decomposition temperature at 5% weight loss is 287.5 °C.

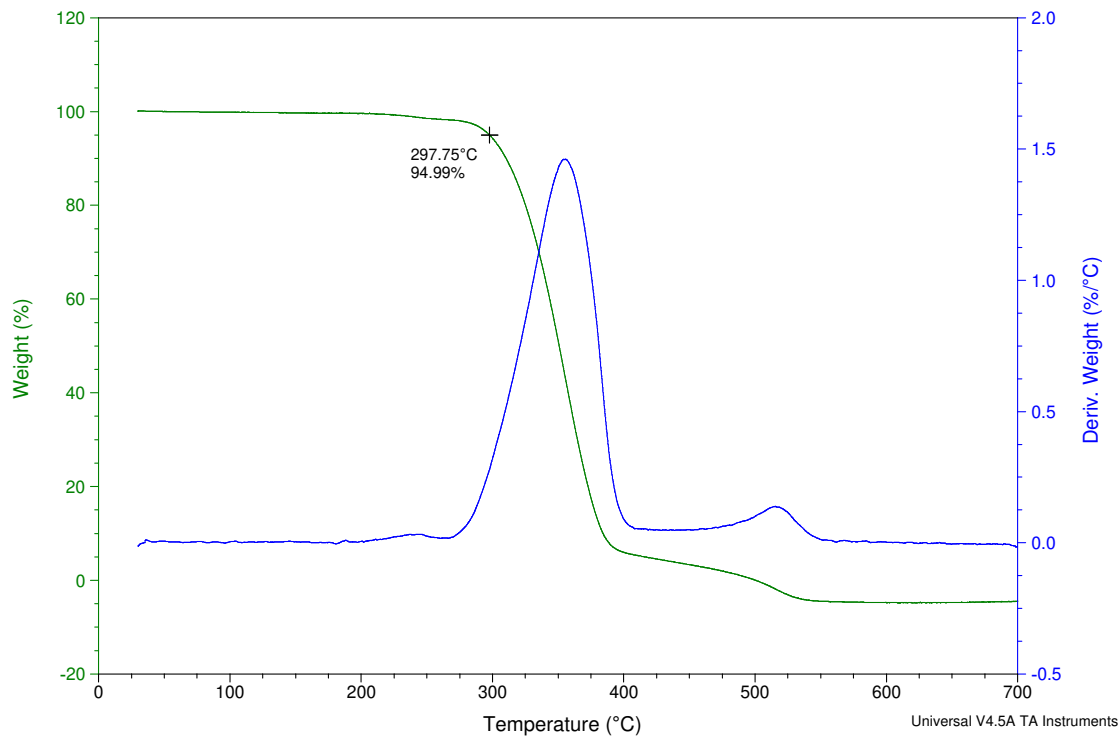


Figure 5.93. TGA trace of p(NB-PS) ($M_n = 1,242,000$ g/mol). Decomposition temperature at 5% weight loss is 297.8 °C.

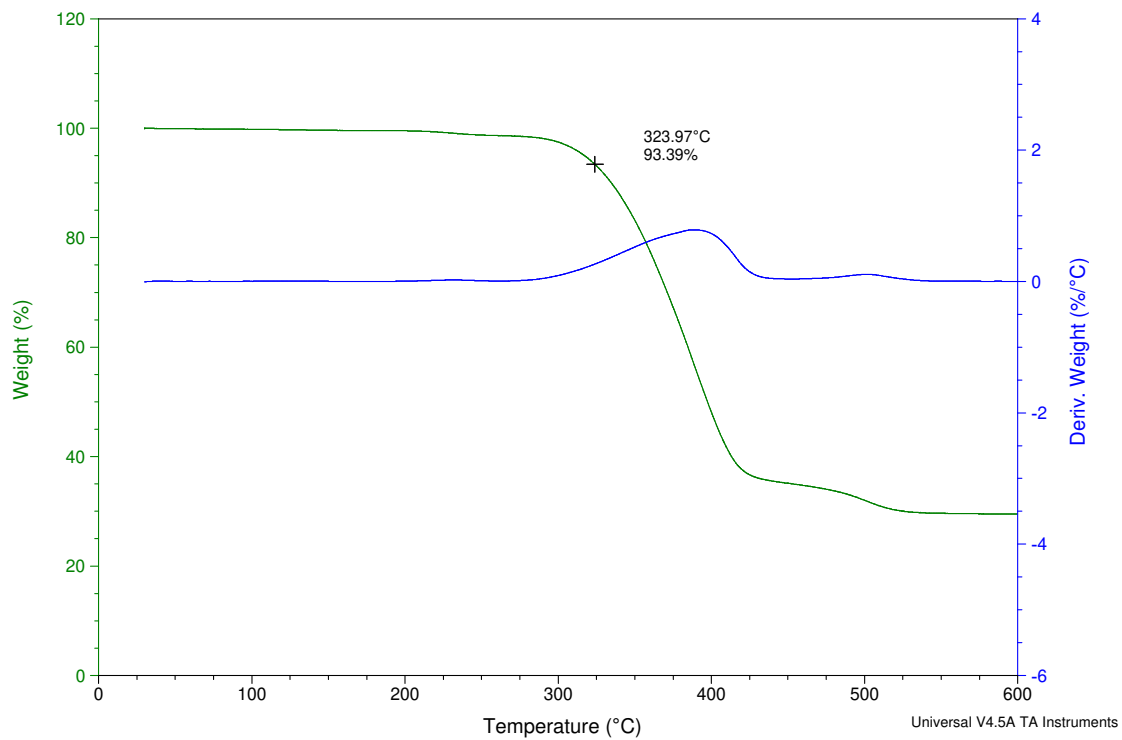


Figure 5.94. TGA trace of p(NBI-PS) ($M_n = 1,122,000$ g/mol). Decomposition temperature at 5% weight loss is 324 °C.

Differential Scanning Calorimetry (DSC)

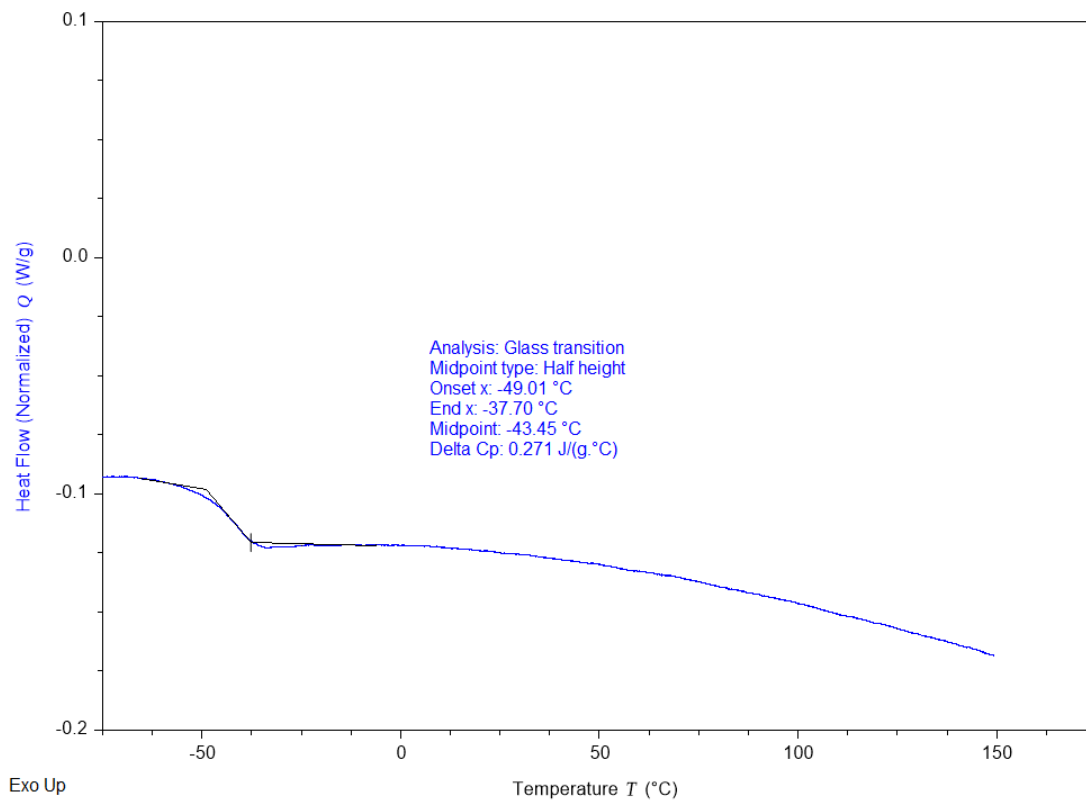


Figure 5.95. Representative and isolated DSC 2nd heat trace for p(NB-Hep) ($M_n = 242,900$ g/mol).

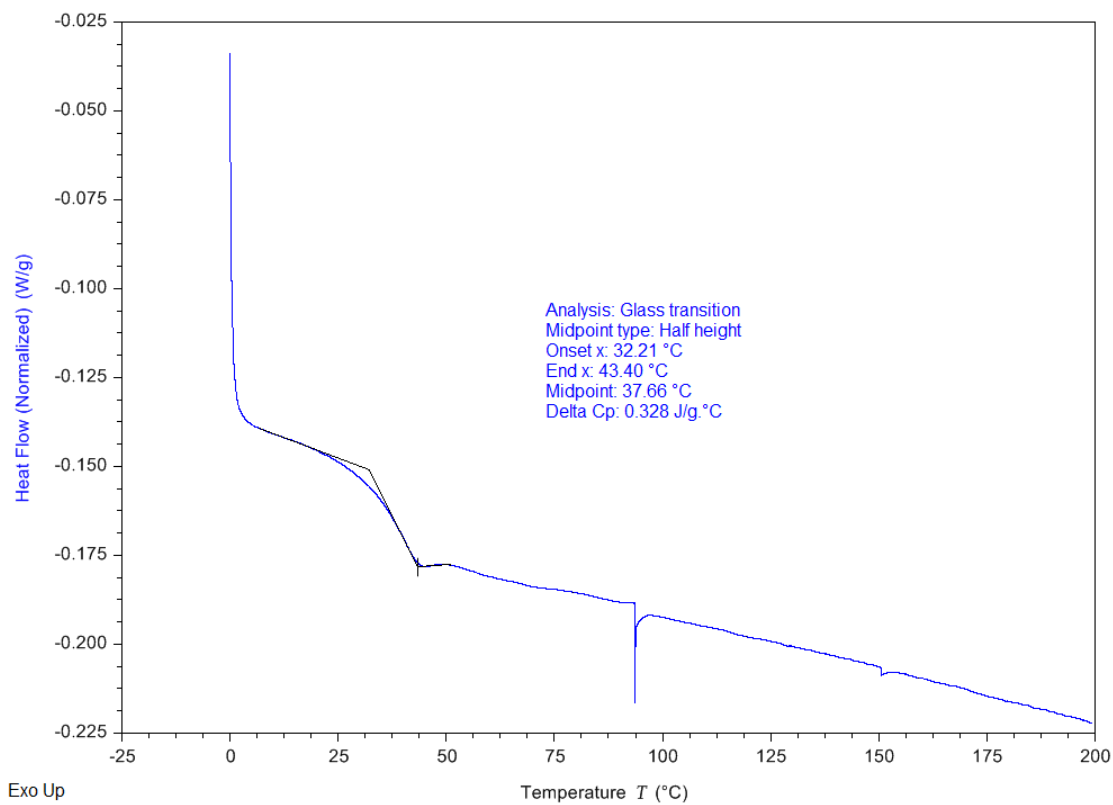


Figure 5.96. Representative and isolated DSC 2nd heat trace for p(NBI-Hep) ($M_n = 114,900$ g/mol).

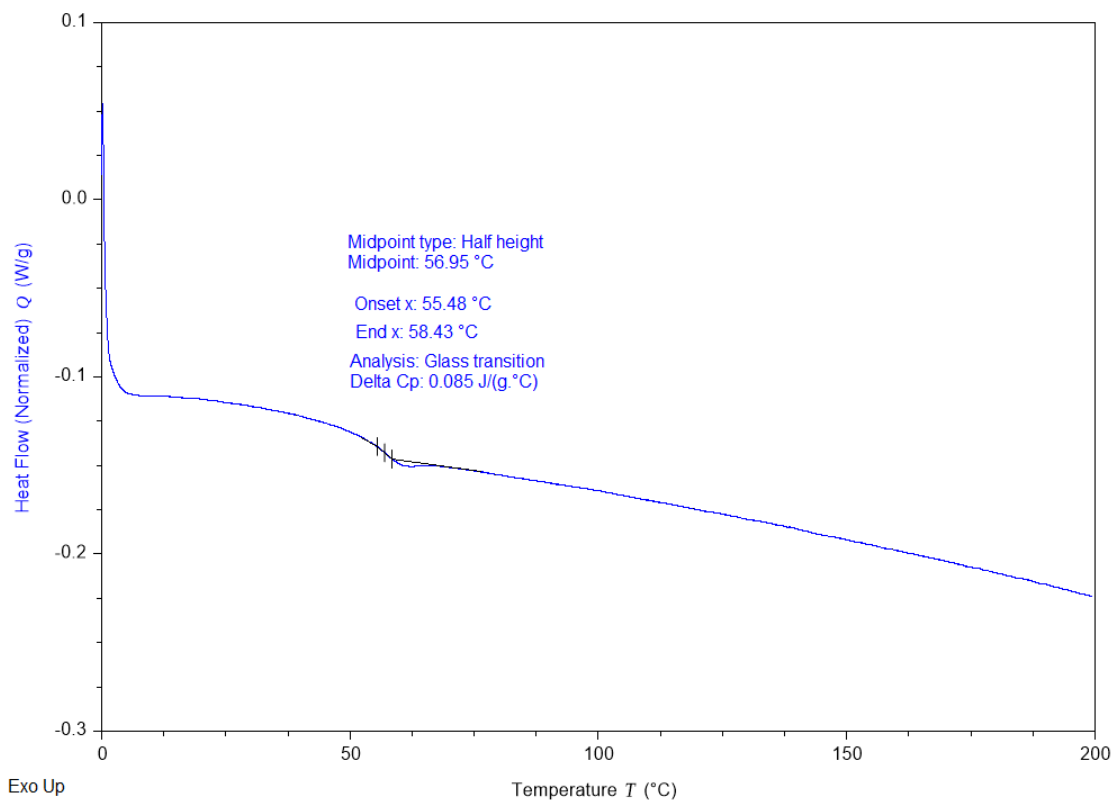


Figure 5.97. Representative and isolated DSC 2nd heat trace for p(NBI-Dec) ($M_n = 779,700$ g/mol).

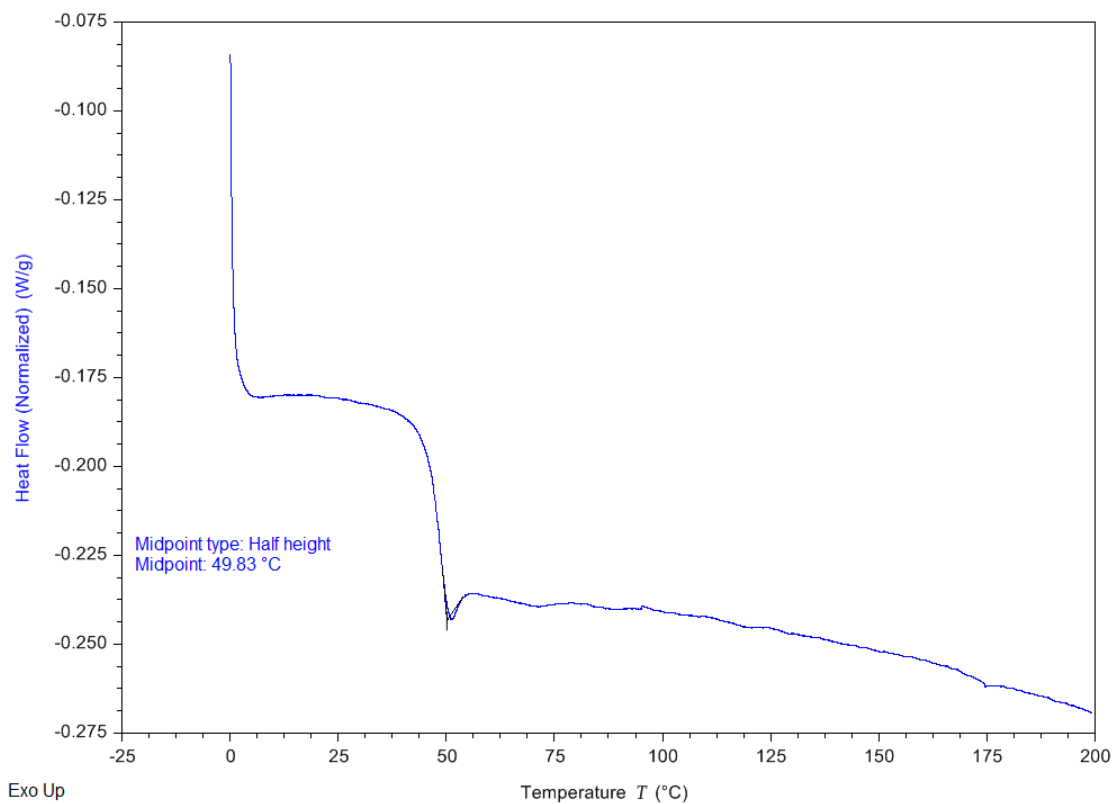


Figure 5.98. Representative and isolated DSC 2nd heat trace for p(NB-PLA) ($M_n = 209,600$ g/mol).

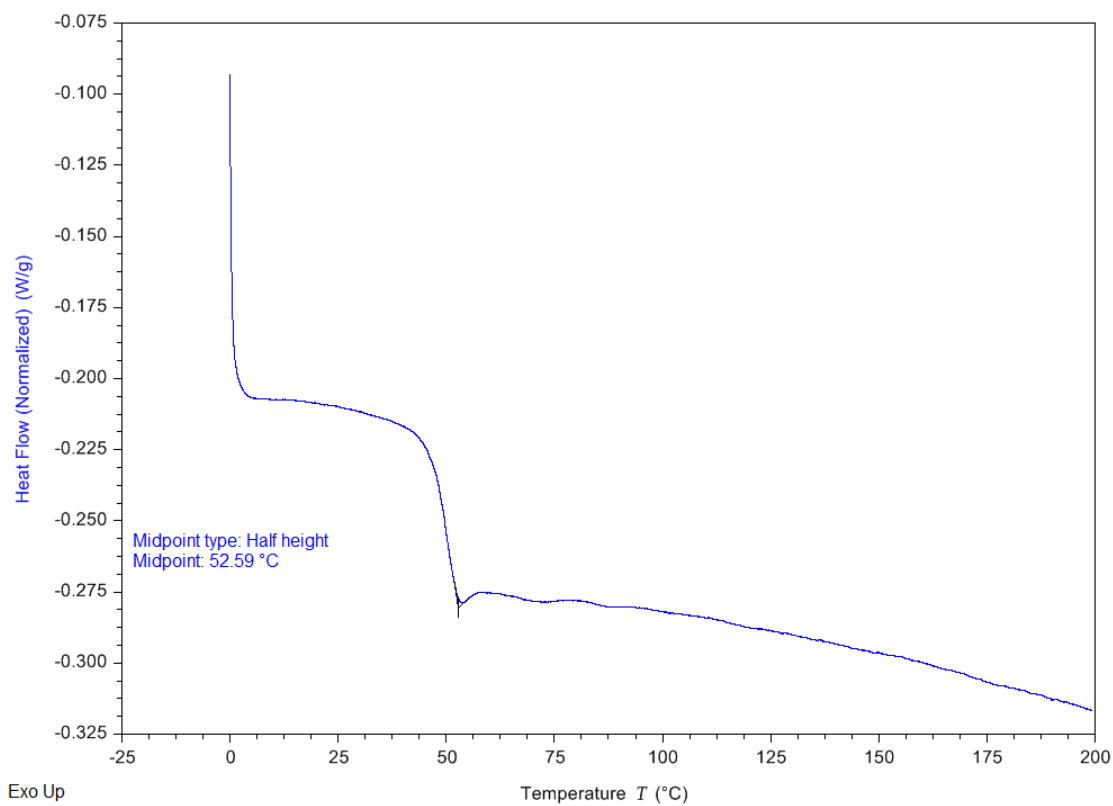


Figure 5.99. Representative and isolated DSC 2nd heat trace for p(NBI-PLA) ($M_n = 254,500$ g/mol).

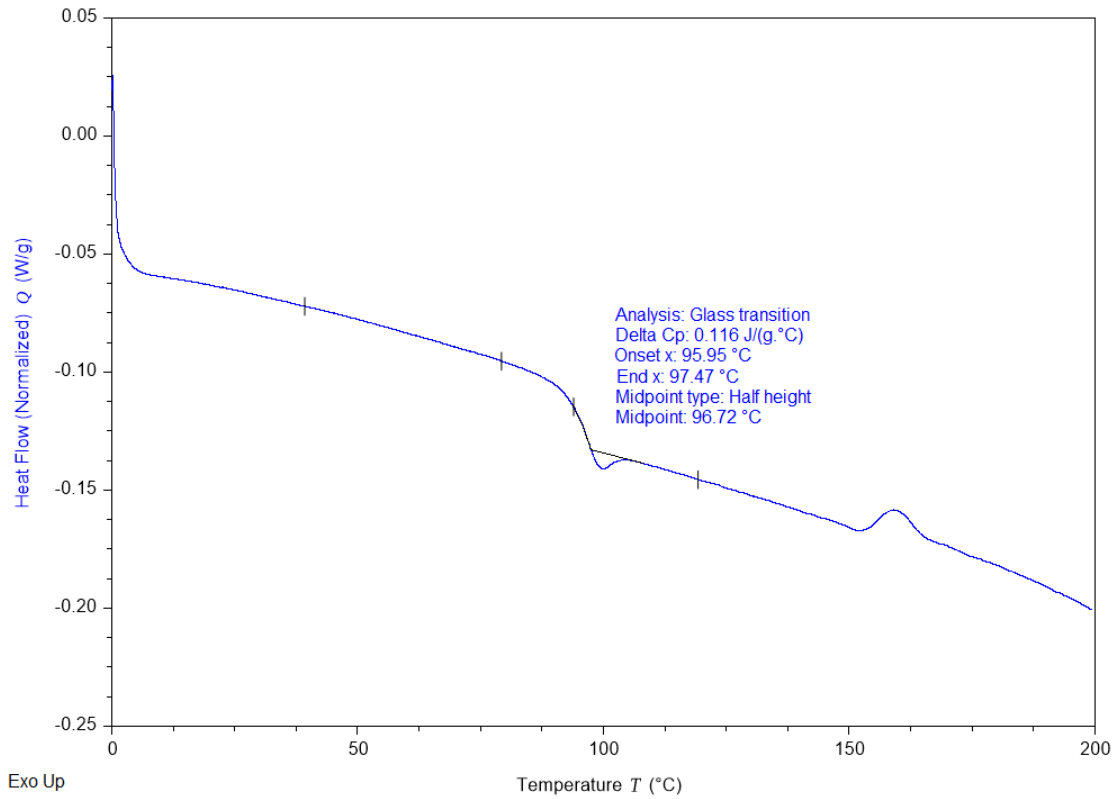


Figure 5.100. Representative and isolated DSC 2nd heat trace for p(NB-PS) ($M_n = 1,242,000$ g/mol) .

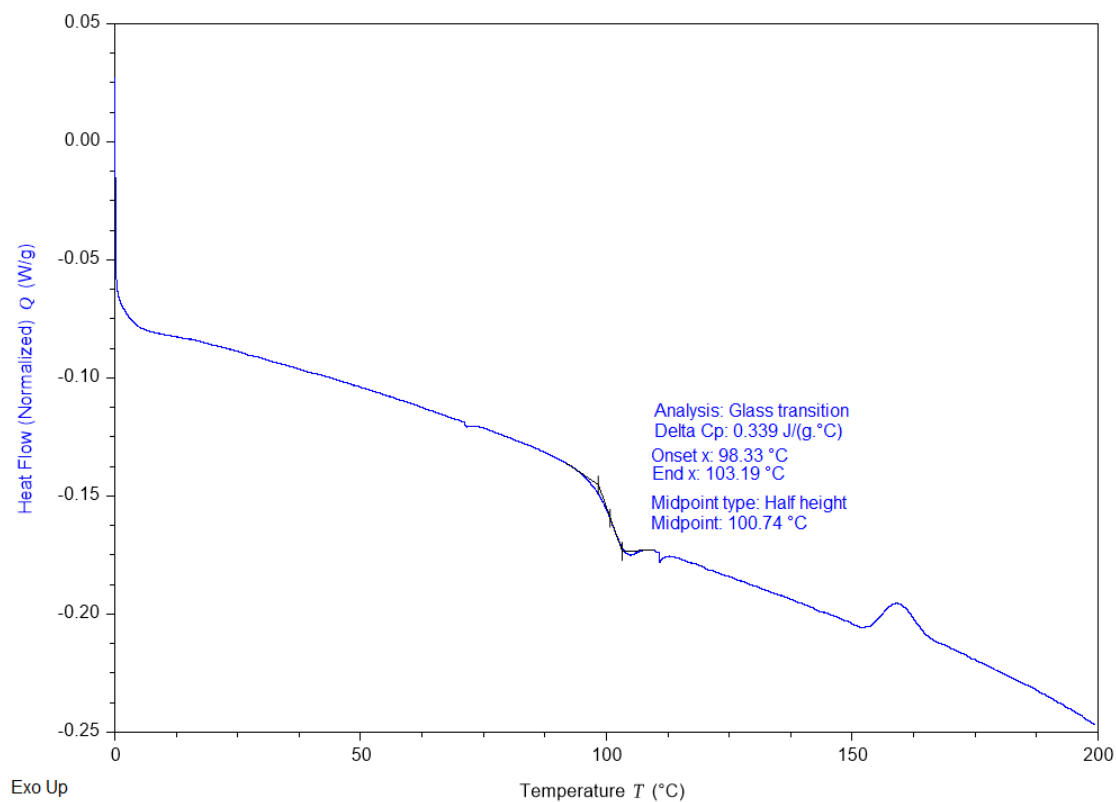


Figure 5.101. Representative and isolated DSC 2nd heat trace for p(NBI-PS) ($M_n = 1,122,000$ g/mol).

Rheological Properties:

Homopolymer MW Series Mastercurves:

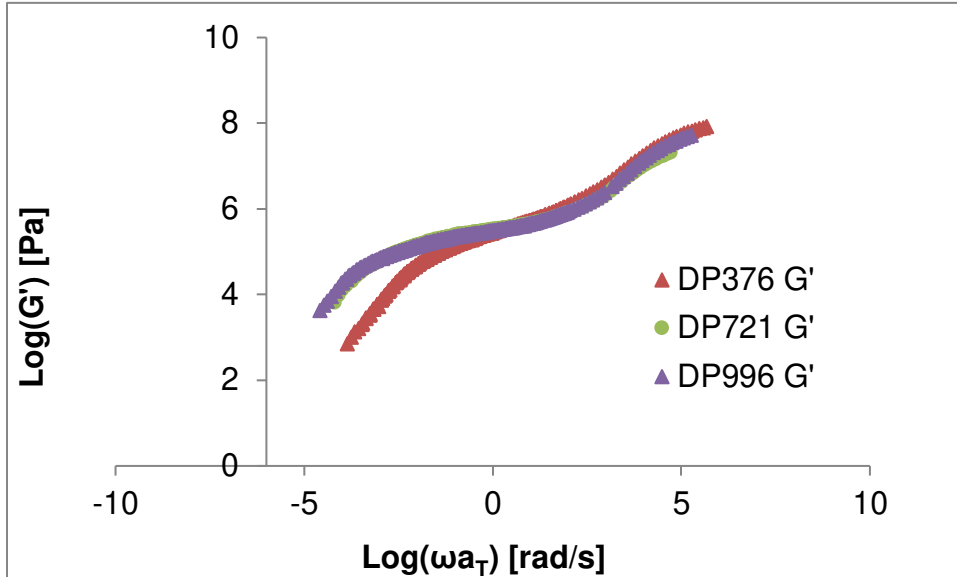


Figure 5.102. Storage modulus mastercurves for 3 of the p(NB-Hep) MW series at $T_{\text{ref}} = T_g + 40$ °C.

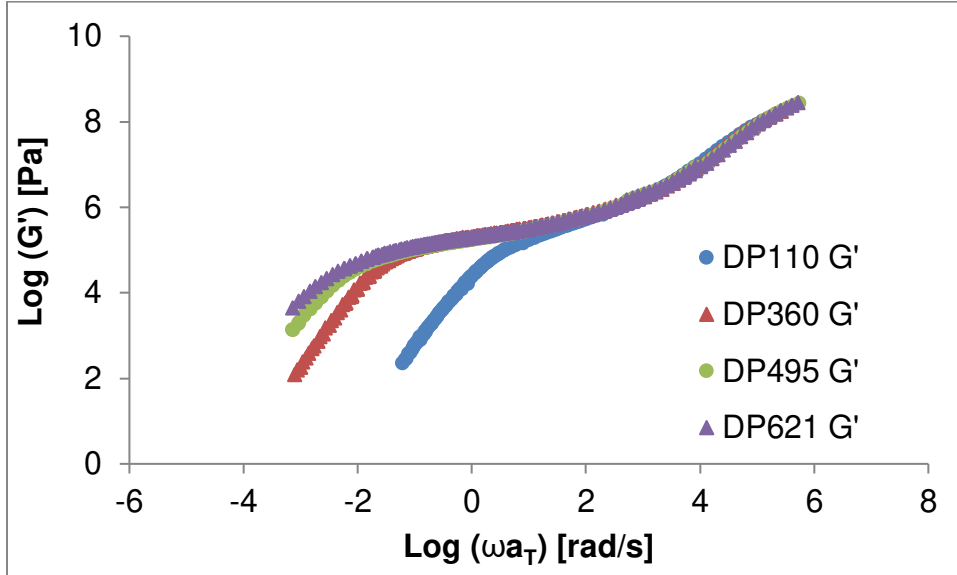


Figure 5.103. Storage modulus mastercurves for 4 of the p(NBI-Hep) MW series at $T_{\text{ref}} = T_g + 40$ °C.

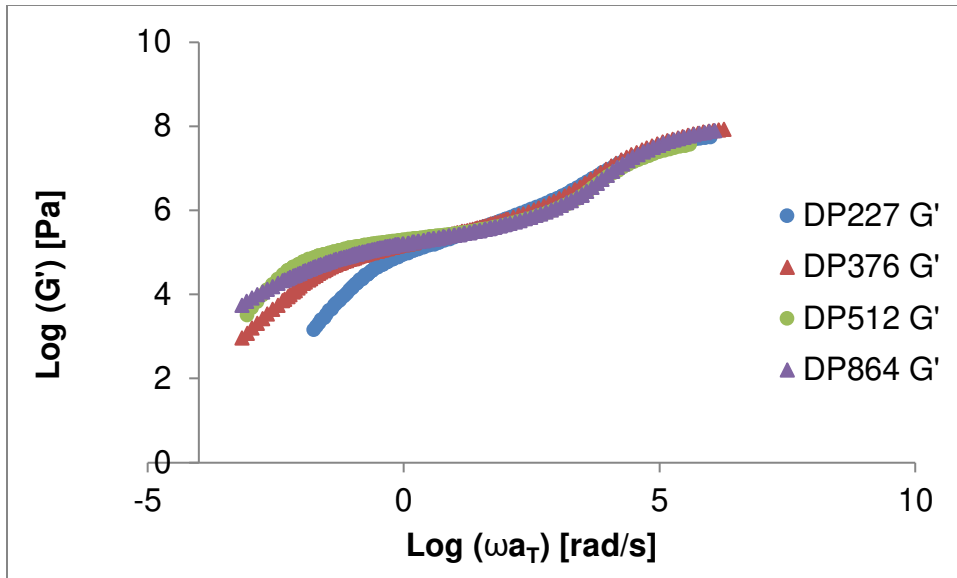


Figure 5.104. Storage modulus mastercurves for 4 of the p(NBI-Dec) MW series at $T_{\text{ref}} = T_g + 40$ °C.

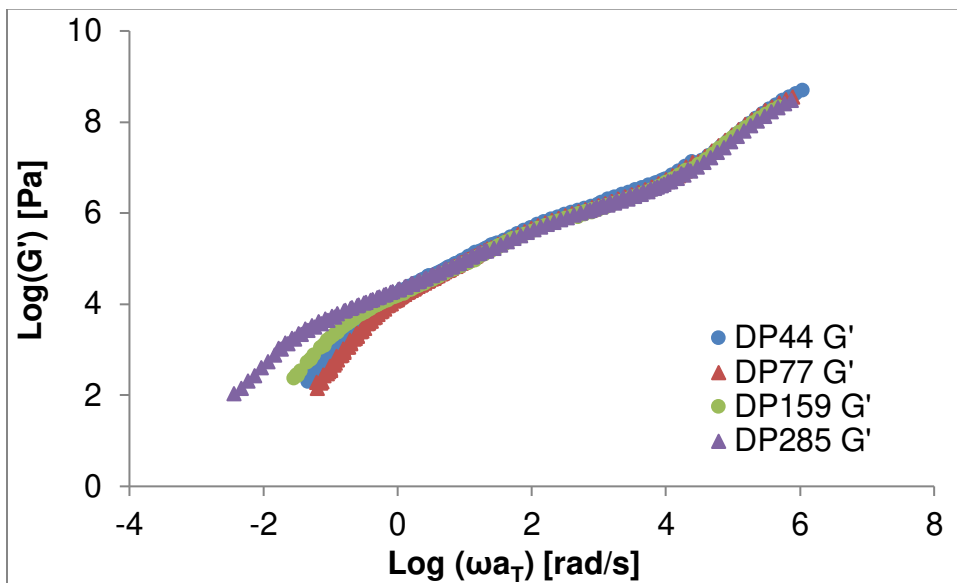


Figure 5.105. Storage modulus mastercurves for 4 of the p(NB-PLA) MW series at $T_{\text{ref}} = T_g + 30$ °C.

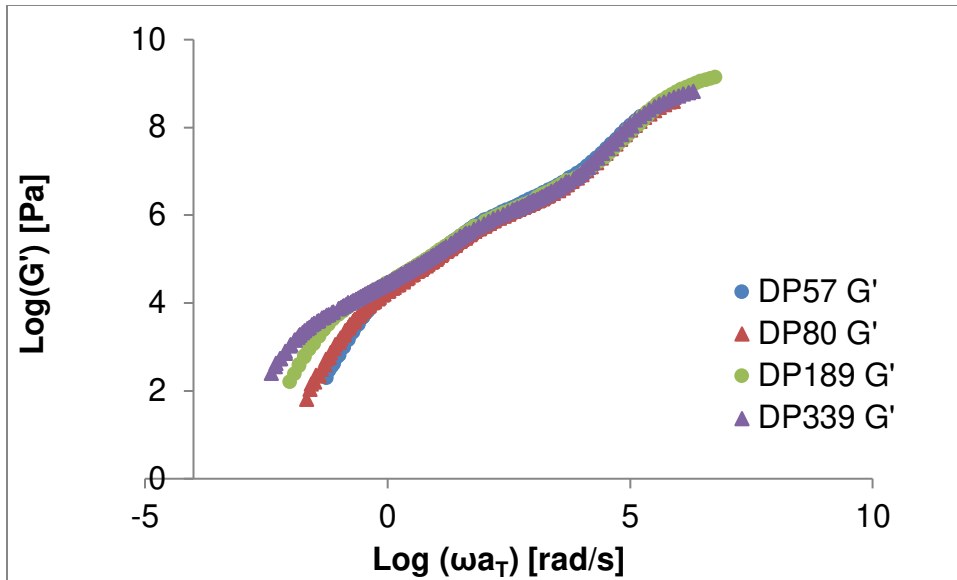


Figure 5.106. Storage modulus mastercurves for 4 of the p(NBI-PLA) MW series at $T_{\text{ref}} = T_g + 30$ °C.

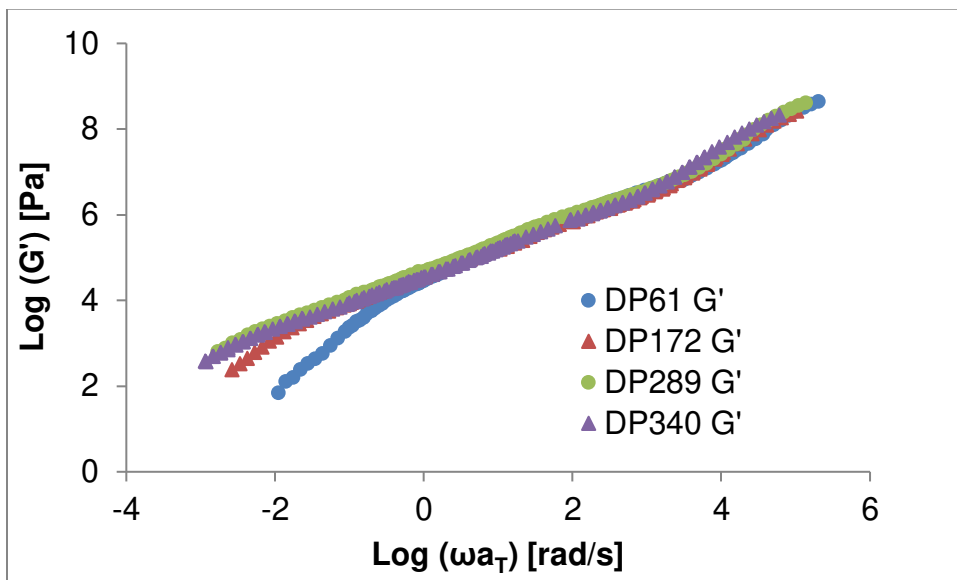


Figure 5.107. Storage modulus mastercurves for 4 of the p(NB-PS) MW series at $T_{\text{ref}} = T_g + 30$ °C.

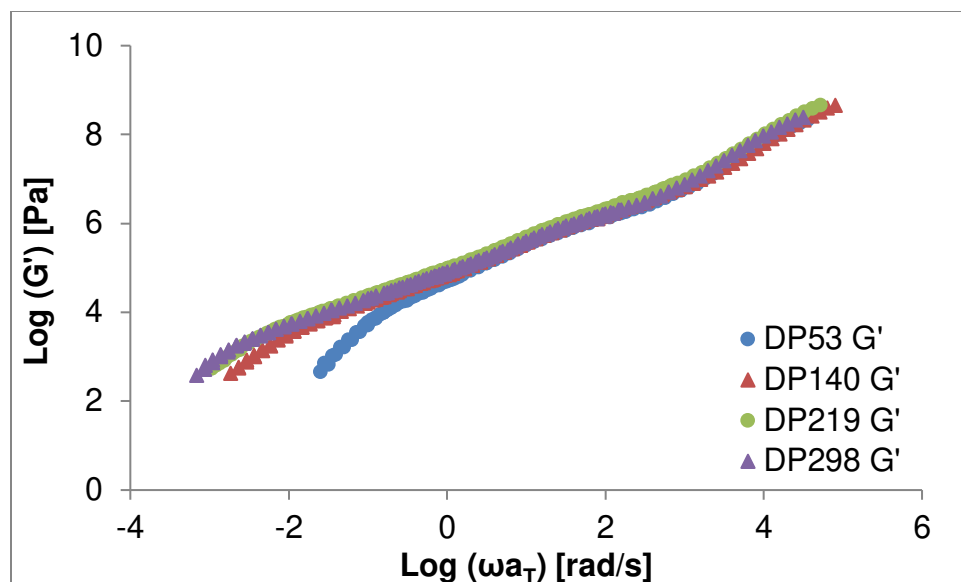


Figure 5.108. Storage modulus mastercurves for 4 of the p(NBI-PS) MW series at $T_{\text{ref}} = T_g + 30$ °C.

Homopolymer Van Gorp-Palmen Plots:

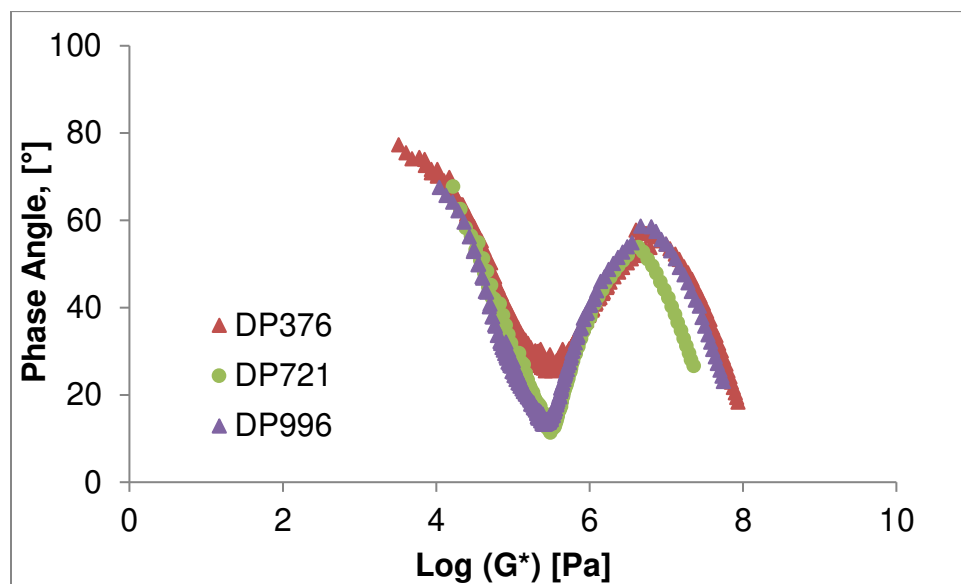


Figure 5.109. The Van Gorp-Palmen plots for 3 of the p(NB-Hep) MW series mastercurves at $T_{\text{ref}} = T_g + 40$ °C.

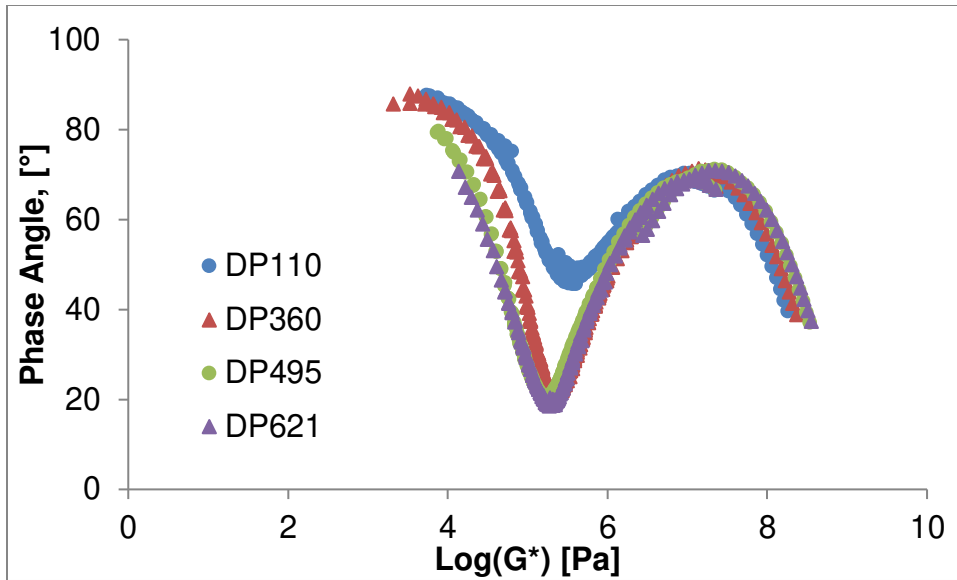


Figure 5.110. The Van Gorp-Palmen plots for 4 of the p(NBI-Hep) MW series mastercurves at $T_{ref} = T_g + 40 \text{ }^\circ\text{C}$.

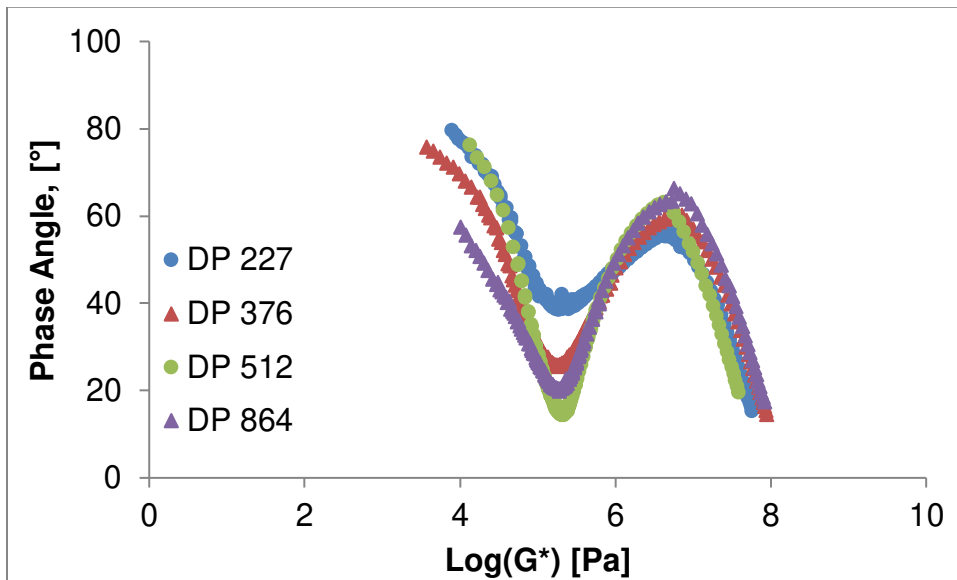


Figure 5.111. The Van Gorp-Palmen plots for 4 of the p(NBI-Dec) MW series mastercurves at $T_{ref} = T_g + 40 \text{ }^\circ\text{C}$.

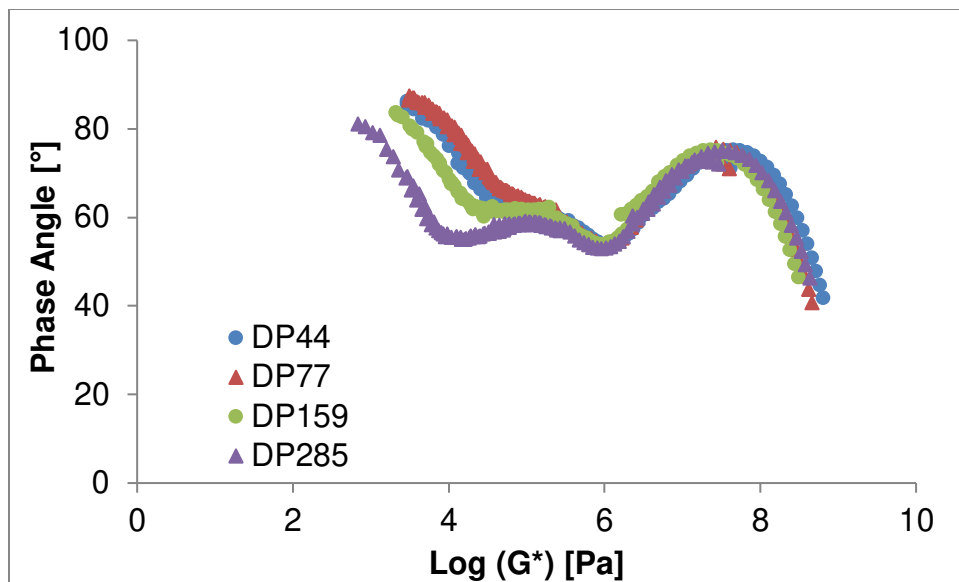


Figure 5.112. The Van Gorp-Palmen plots for 4 of the p(NB-PLA) MW series mastercurves at $T_{\text{ref}} = T_g + 30 \text{ }^\circ\text{C}$

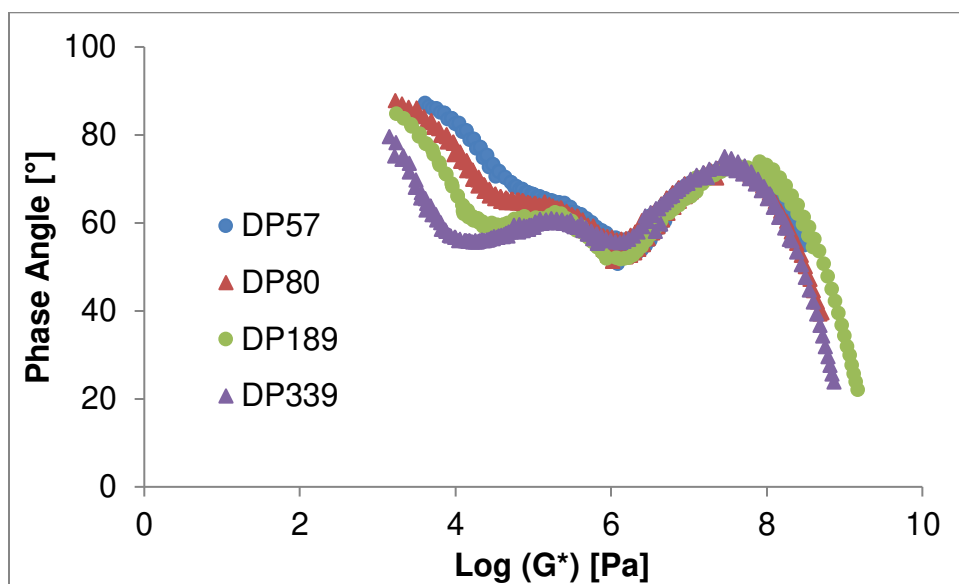


Figure 5.113. The Van Gorp-Palmen plots for 4 of the p(NBI-PLA) MW series mastercurves at $T_{\text{ref}} = T_g + 30 \text{ }^\circ\text{C}$

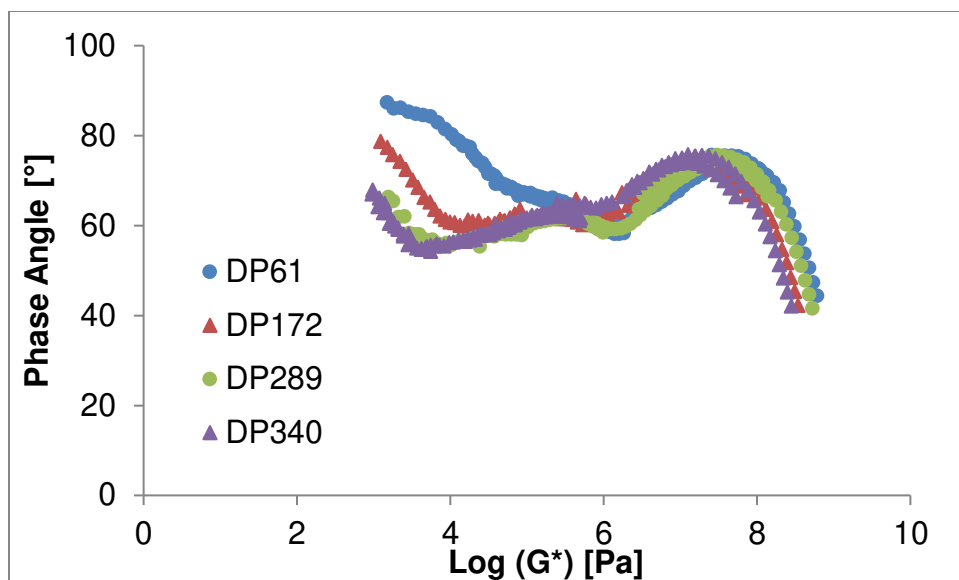


Figure 5.114. The Van Gorp-Palmen plots for 4 of the p(NB-PS) MW series mastercurves at $T_{\text{ref}} = T_g + 30 \text{ }^\circ\text{C}$.

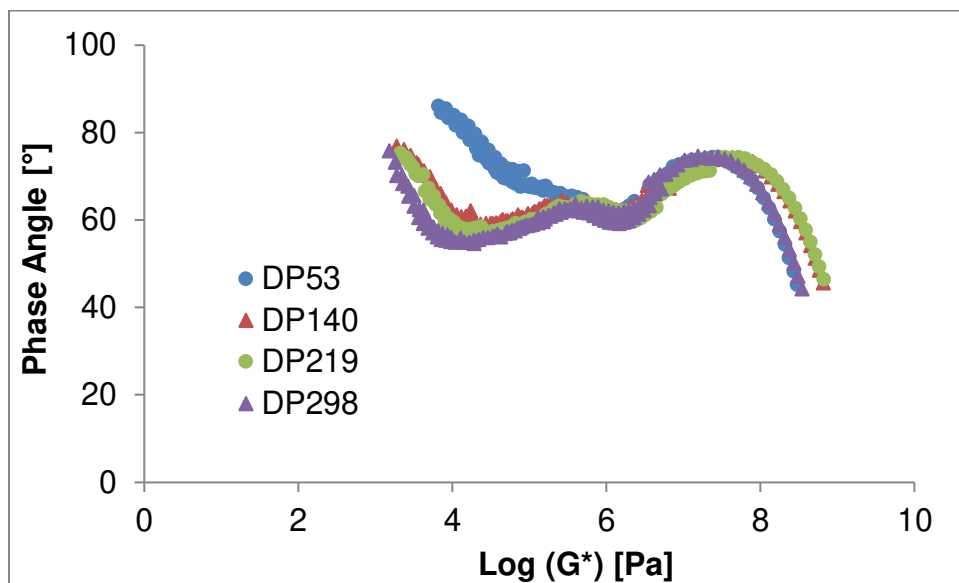


Figure 5.115. The Van Gorp-Palmen plots for 4 of the p(NBI-PS) MW series mastercurves at $T_{\text{ref}} = T_g + 30 \text{ }^\circ\text{C}$.

Linear Homopolymer Williams-Landel-Ferry (WLF) Shift Factor Relationship:

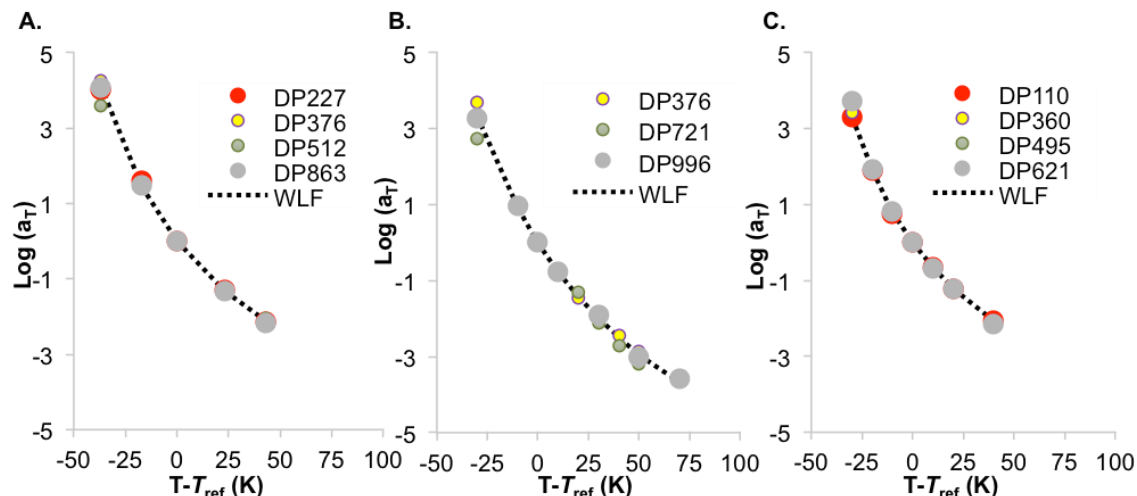


Figure 5.116. WLF graphs of all of the mastercurve shift factors from the time-temperature superposition for the p(NBI-Dec) MW series (A.), the p(NB-Hep) MW series (B.), and the p(NBI-Hep) MW series.

References

- (1) Yablonovitch, E. Photonic Crystals: Semiconductors of Light *Sci. Am.* **2001**, 285, 46-55.
- (2) Joannopoulos, J. D.; Johnson, S. G.; Winn, J. N.; Meade, R. D. *Photonic Crystals: Molding the Flow of Light*, 2nd Ed.; Princeton University Press: Princeton, NJ, **2008**.
- (3) Abouraddy, A. F.; Bayindir, M.; Benoit, G.; Hart, S. D.; Kuriki, K.; Orf, N.; Shapira, O.; Sorin, F.; Temelkuran, B.; Fink, Y. Towards Multimaterial Multifunctional Fibres that See, Hear, Sense and Communicate *Nat. Mater.* **2007**, 6, 336-347.
- (4) Sorin, F.; Abouraddy, A. F.; Orf, N.; Shapira, O.; Viens, J.; Arnold, J.; Joannopoulos, J. D.; Fink, Y. Multimaterial Photodetecting Fibers: A Geometric and Structural Study *Adv. Mater.* **2007**, 19, 3872-3877.
- (5) Schrenk, W. J.; Lewis, R. A.; Wheatley, J. A.; Arends, C. B. Coextruded Infrared Reflecting Films *Int. Polym. Process* **1991**, 6, 255-256

- (6) Boyle, B. M.; French, T. A.; Pearson, R. M.; McCarthy, B. G.; Miyake, G. M. Structural Color for Additive Manufacturing: 3D-Printed Photonic Crystals from Block Copolymers *ACS Nano* **2017**, 11, 3052-3058.
- (7) Bates, F. S.; Hillmyer, M. A.; Lodge, T. P.; Bates, C. M.; Delaney, K. T.; Fredrickson, G. H. Multiblock Polymers: Panacea or Pandora's Box? *Science* **2012**, 336, 434-440.
- (8) Edrington, A. C.; Urbas, A. M.; DeRege, A. C.; Chen, C. X.; Swager, T. M.; Hadjichristidis, N.; Xenidou, M.; Fetters, L. J.; Joannopoulos, J. D.; Fink, Y.; Thomas, E. L. Polymer-Based Photonic Crystals *Adv. Mater.* **2001**, 13, 421-425.
- (9) Fink, Y.; Urbas, A. M.; Bawendi, M. G.; Joannopoulos, J. D.; Thomas, E. L. Block Copolymers as Photonic Bandgap Materials *J. Lightwave Technol.* **1999**, 17, 1963-1969.
- (10) Galisteo-López, J. F.; Ibisate, M.; Sapienza, R.; Froufe-Pérez, L. S.; Blanco, Á.; López, C. Self-Assembled Photonic Structures *Adv. Mater.* **2011**, 23, 30-69.
- (11) Appold, M.; Grune, E.; Frey, H.; Gallei, M. One-Step Anionic Copolymerization Enables Formation of Linear Ultrahigh-Molecular-Weight Block Copolymer Films Featuring Vivid Structural Colors in the Bulk State *ACS Appl. Mater. Interfaces* **2018**, 10, 18202-18212.
- (12) Piunova, V. A.; Miyake, G. M.; Daeffler, C. S.; Weitekamp, R. A.; Grubbs, R. H. Highly Ordered Dielectric Mirrors via the Self-Assembly of Dendronized Block Copolymers *J. Am. Chem. Soc.* **2013**, 135, 15609-15616.
- (13) Sveinbjornsson, B. R.; Weitekamp, R. A.; Miyake, G. M.; Xia, Y.; Atwater, H. A.; Grubbs, R. H. Rapid Self-Assembly of Brush Block Copolymers to Photonic Crystals *Proc. Natl. Acad. Sci. U. S. A.* **2012**, 109, 14332-14336.

- (14) Chang, A. B.; Bates, C. M.; Lee, B.; Garland, C. M.; Jones, S. C.; Spencer, R. K. W.; Matsen, M. W.; Grubbs, R. H. Manipulating the ABCs of self-assembly via low-X block polymer design *Proc. Natl. Acad. Sci. U. S. A.* **2017**, 114, 6462-6467.
- (15) Bates, F. S.; Fredrickson, G. H. Block Copolymers-Designer Soft Materials *Phys. Today* **1999**, 52, 32-38
- (16) Bates, C. M.; Bates, F. S. 50th Anniversary Perspective: Block Polymers – Pure Potential *Macromolecules* **2017**, 50, 3- 22
- (17) Hustad, P. D.; Marchand, G. R.; Garcia-Meitin, E. I.; Roberts, P. L.; Weinhold, J. D. Photonic Polyethylene from Self-Assembled Mesophases of Polydisperse Olefin Block Copolymers *Macromolecules* **2009**, 42, 3788-3794.
- (18) Boyle, B. M.; Heinz, O.; Miyake, G. M.; Ding, Y. Impact of the Pendant Group on the Chain Conformation and Bulk Properties of Norbornene Imide-Based Polymers *Macromolecules* **2019**, 52, 3426-3434.
- (19) Qian, Z.; Koh, Y. P.; Madhusudhan, R. P.; Chang, A. B.; Lin, T.-P.; Guzmán, P. E.; Grubbs, R. H.; Simon, S. L.; McKenna, G. B. Linear Rheology of a Series of Second-Generation Dendronized Wedge Polymers *Macromolecules* **2019**, 52, 2063-2074
- (20) Dutertre, F.; Bang, K.-T.; Vereroudakis, E.; Loppinet, B.; Yang, S.; Kang, S.-Y.; Fytas, G.; Choi, T.-L. Conformation of Tunable Nanocylinders: Up to Sixth-Generation Dendronized Polymers via Graft-Through Approach by ROMP *Macromolecules* **2019**, 52, 3342-3350
- (21) Miyake, G. M.; Weitekamp, R. A.; Piunova, V. A.; Grubbs, R. H. Synthesis of Isocyanate-Based Brush Block Copolymers and Their Rapid Self-Assembly to Infrared-Reflecting Photonic Crystals *J. Am. Chem. Soc.* **2012**, 134, 14249-14254

- (22) Xia, Y.; Olsen, B. D.; Kornfield, J. A.; Grubbs, R. H. Efficient Synthesis of Narrowly Dispersed Brush Copolymers and Study of their Assemblies: The Importance of Side Chain Arrangement *J. Am. Chem. Soc.* **2009**, 131, 18525-18532
- (23) Miyake, G. M.; Piunova, V. A.; Weitekamp, R. A.; Grubbs, R. H. Precisely Tunable Photonic Crystals from Rapidly Self-Assembling Brush Block Copolymer Blends *Angew. Chem. Int. Ed.* **2012**, 51, 11246-11248
- (24) Macfarlane, R. J.; Kim, B.; Lee, B.; Weitekamp, R. A.; Bates, C. M.; Siu, F. L.; Chain, A. B.; Delaney, K. T.; Fredrickson, G. H.; Atwater, H. A.; Grubbs, R. H. Improving Brush Polymer Infrared One-Dimensional Photonic Crystals via Linear Polymer Additives *J. Am. Chem. Soc.* **2014**, 136, 17374-17377
- (25) Verduzco, R.; Li, X.; Pesek, S. L.; Stein, G. E. Structure, Function, Self-assembly, and applications of Bottlebrush Copolymers *Chem. Soc. Rev.* **2015**, 44,2405.
- (26) Dalsin, S. J.; Rions-Maehren, T. G.; Beam, M. D.; Bates, F. S.; Hillmyer, M. A.; Matsen, M. W. Bottlebrush Block Polymers: Quantitative Theory and Experiments *ACS Nano* **2015**, 9, 12233-12245.
- (27) Gu, W.; Huh, J.; Hong, S. W.; Sveinbjornsson, B. R.; Park, C.; Grubbs, R. H.; Russell, T. P. Self-Assembly of Symmetric Brush Diblock Copolymers *ACS Nano* **2013**, 7, 2551-2558.
- (28) Daniel, W. F. M.; Burdynska, J.; Vatankhah-Varnoosfaderani, M.; Matyjaszewski, K.; Paturej, J.; Rubinstein, M.; Dobrynin, A. V.; Sheiko, S. S. Solvent-free, supersoft and superelastic bottlebrush melts and networks. *Nat. Mater.* **2016**, 15, 183-190.
- (29) Dalsin, S. J.; Hillmyer, M. A.; Bates, F. S. Linear Rheology of Polyolefin-Based Bottlebrush Polymers. *Macromolecules* **2015**, 48, 4680-4691.

- (30) Hu, M.; Xia, Y.; McKenna, G. B.; Kornfield, J. A.; Grubbs, R. H. Linear Rheological Response of a Series of Densely Branched Brush Polymers. *Macromolecules* **2015**, *44*, 6935-6943.
- (31) Haugan, I. N.; Maher, M. J.; Chang, A. B.; Lin, T.-P.; Grubbs, R. H.; Hillmyer, H. A.; Bates, F. S. Consequences of Grafting Density on the Linear Viscoelastic Behavior of Graft Polymers, *ACS Macro Lett.* **2018**, *7*, 525-530.
- (32) Rathgeber, S.; Pakula, T.; Wilk, A.; Matyjaszewski, K.; Beers, K. L. On the Shape of Bottle-brush Macromolecules: Systematic Variation of Architectural Parameters *J. Chem. Phys.* **2005**, *122*, 124904.
- (33) Dutta, S.; Wade, M. A.; Walsh, D. J.; Guironnet, D.; Rogers, S. A.; Sing, C. E. Dilute solution structure of bottlebrush polymers *Soft Matter* **2019**, *15*, 2928.
- (34) Paturej, J.; Kreer, T. Hierarchical excluded volume screening in solutions of bottlebrush polymers *Soft Matter* **2017**, *13*, 8534.
- (35) Saito, Y.; Kikuchi, M.; Jinbo, Y.; Narumi, A.; Kawaguchi, S. Determination of the Chain Stiffness Parameter of Molecular Rod Brushes Consisting of a Polymethacrylate Main Chain and Poly(n-hexyl isocyanate) Side Chains *Macromolecules* **2015**, *48*, 8971-8979.
- (36) Saito, Y.; Lien, L. T. N.; Jinbo, Y.; Kumaki, J.; Narumi, A.; Kawaguchi, S. Influence of the primary structure of the main chain on backbone stiffness of cylindrical rod brushes *Polym. J.* **2013**, *45*, 193-201.
- (37) Iwawaki, H.; Urakawa, O.; Inoue, T.; Nakamura, Y. Rheo-Optical Study on Dynamics of Bottlebrush-Like Polymacromonomer Consisting of Polystyrene. II. Side Chain Length Dependence on Dynamical Stiffness of Main Chain *Macromolecules* **2012**, *45*, 4801-4808.

- (38) Nakamura, Y.; Norisuye, T. Backbone Stiffness of Comb-Branched Polymers *Polym. J.* **2001**, 33 (11), 874 – 878.
- (39) Sheiko, S. S.; Sumerlin, B. S.; Matyjaszewski, K. Cylindrical Molecular Brushes: Synthesis, Characterization, and Properties. *Prog. Polym. Sci.* **2008**, 33, 759-785.
- (40) Rzaev, J. Molecular Bottlebrushes: New Opportunities in Nanomaterials Fabrication *ACS Macro Lett.* **2012**, 1, 1146-1149
- (41) Walsh, D. J.; Dutta, S.; Sing, C. E.; Guironnet, D. Engineering of Molecular Geometry in Bottlebrush Polymers *Macromolecules* **2019**, 52, 4847-4857.
- (42) Yavitt, B. M.; Fei, H.-F.; Kopanati, G. N.; Winter, H. H.; Watkins, J. J. Power Law Relaxations in Lamellae Forming Brush Block Copolymers with Asymmetric Molecular Shape *Macromolecules* **2019**, 52, 1557-1566
- (43) Fei, H.-F.; Yavitt, B. M.; Hu, X.; Kopanati, G.; Ribbe, A.; Watkins, J. J. Influence of Molecular Architecture and Chain Flexibility on the Phase Map of Polystyrene-block-poly(dimethylsiloxane) Brush Block Copolymers *Macromolecules* **2019**, 52, 6449-6457
- (44) Sunthar, P. In *Rheology of Complex Fluids*; Deshpande, A. P.; Krishnan, J. M.; Kumar, S., Eds.; Springer: New York, **2010**.
- (45) Kisliuk, A.; Ding, Y.; Hwang, J.; Lee, J. S.; Annis, B. K.; Foster, M. D.; Sokolov, A. P. Influence of Molecular Architecture on Fast and Segmental Dynamics and the Glass Transition in Polybutadiene *J. Polym. Sci., Part B: Polym. Phys.* **2002**, 40, 2431-2439
- (46) van Gorp, M.; Palmen, J. Time-Temperature Superposition for Polymeric Blends. *Rheol. Bull.* **1998**, 67, 5-8
- (47) Trinkle, S.; Friedrich, C. Van Gorp-Palmen-Plot: a way to characterize polydispersity of linear polymers. *Rheol. Acta* **2001**, 40, 322-328

- (48) Ngai, K. L.; Paluch, M. Classification of Secondary Relaxation in Glass-Formers based on Dynamic Properties *J. Chem. Phys.* **2004**, 120, 857
- (49) Williams, M. L.; Landel, R. F.; Ferry, J. D. The Temperature Dependence of Relaxation Mechanisms in Amorphous Polymers and Other Glass-Forming Liquids *J. Am. Chem. Soc.* **1955**, 77, 3701-3707
- (50) Ferry, J. D. In *Viscoelastic Properties of Polymers*, 3rd Ed.; Ferry, J. D., Ed; John Wiley & Sons: New York, **1980**; p 304
- (51) Ding, Y.; Sokolov, A. P. Breakdown of Time-Temperature Superposition Principle and Universality of Chain Dynamics in Polymers *Macromolecules* **2006**, 39, 3322-3326
- (52) Kunal, K.; Robertson, C. G.; Pawlus, S.; Hahn, S. F.; Sokolov, A. P. Role of Chemical Structure in Fragility of Polymers: A Qualitative Picture *Macromolecules* **2008**, 41, 7232-7238
- (53) Ngai, K. L.; Roland, C. M. Chemical Structure and Intermolecular Cooperativity: Dielectric Relaxation Results *Macromolecules* **1993**, 26, 6824-6830
- (54) Love J. A.; Morgan J. P.; Trnka T. M.; Grubbs R. H. A Practical and Highly Active Ruthenium-Based Catalyst that Effects the Cross Metathesis of Acrylonitrile *Angew. Chem., Int. Ed.* **2002**, 41, 4035-4037.
- (55) Radzinski S.C.; Foster J.C.; Chapleski R.C.; Troya D.; Matson J.B. Bottlebrush Polymer Synthesis by Ring-Opening Metathesis Polymerization: The Significance of the Anchor Group. *J. Am. Chem. Soc.* **2016**, 138, 22, 6998-7004
- (56) Matson J. B.; Grubbs R. H. Synthesis of Fluorine-18 Functionalized Nanoparticles for use as in vivo Molecular Imaging Agents. *J. Am. Chem. Soc.* **2008**, 130, 6731-6733.

- (57) Whitfield, R.; Anastasaki, A.; Nikolaou, V.; Jones, G.R.; Engelis, N.G.; Discekici, E.H.; Fleischmann, C.; Willenbacher, J.; Hawker, C.J.; Haddleton, D.M. Universal Conditions for the Controlled Polymerization of Acrylates, Methacrylates, and Styrene via Cu(0)-RDRP. *J. Am. Chem. Soc.* **2017**, 139, 1003-1010.
- (58) Radzinski, S.C.; Foster, J.C.; Scannelli, S.J.; Weaver, J.R.; Arrington, K.J.; Matson, J.B. Tapered Bottlebrush Polymers: Cone-Shaped Nanostructures by Sequential Addition of Macromonomers. *ACS Macro Lett.* **2017**, 6, 1175-1179.

CHAPTER 6 – SUMMARY

The work presented in this dissertation provides insight into the polymer synthesis, characterization, and self-assembly of dendritic block copolymers (DBCP) and bottlebrush block copolymers (BBCP), as well as the application of these polymer architectures in photonic crystal (PC) materials. DBCPs were shown to possess many characteristics similar to those of bottlebrush polymers such as a rod-like conformation, a reduced capability for chain entanglement, and lower glassy moduli compared to non-rigid, linear polymers. Further, DBCP PCs represented the first example of 3D printing structural color. To better facilitate 3D printing structural color and other novel thermoplastic materials in the future, the first demonstration of powder melt extrusion (PME) additive manufacturing was shown in this dissertation. For BBCPs, the backbone composition's effect on the global BBCP conformation and in modulating self-assembly processes was shown to dramatically shift the wavelength of reflection of the PC material at similar molecular weights as well as improve the fidelity of the nanostructure morphology as the molecular weight increases from 50 kg/mol to 2,000 kg/mol.

The polymer structure-property relationships illuminated by this dissertation have laid the groundwork for new research efforts into engineering BCPs for novel PC applications. The ability to directly tailor the BCP architecture to modulate the dynamics, self-assembly, and application of PC materials creates a promising future for engineering better polymeric PC materials. By engineering more efficient polymeric PC materials, the creation of color can start to be re-invented in a more sustainable way.

Lastly, as presented in this dissertation, the incorporation of structural color into additive manufacturing and the broadening of the capabilities of 3D printing to incorporate less than ideal

but novel build materials with PME will have significant impacts on the future of the additive manufacturing field. Not only does 3D printing structural color promise more sustainable color in plastic parts and the potential to build selective optical filters and guides of unlimited geometries, but also, as demonstrated in Chapter 2, the research presented expands the scope of structural color beyond academia and industry into the public's use. This is due to being able to 3D print structural color on a sub \$1,000 fused filament fabrication printer as the global media company, 3D Printing Industry (3DPI), highlighted in the article titled, "Natural Inspiration for 3D Printing with Color Uses Photonic Crystals and Sub \$1000 3D Printer" (Figure 6.1).¹ This article focused on the research presented in Chapter 2 of this dissertation. PME has also sown the seeds of innovation as other academic research groups at the University of Wisconsin have reached out to us as they begin to investigate PME's use for their own applications within the additive manufacturing field.

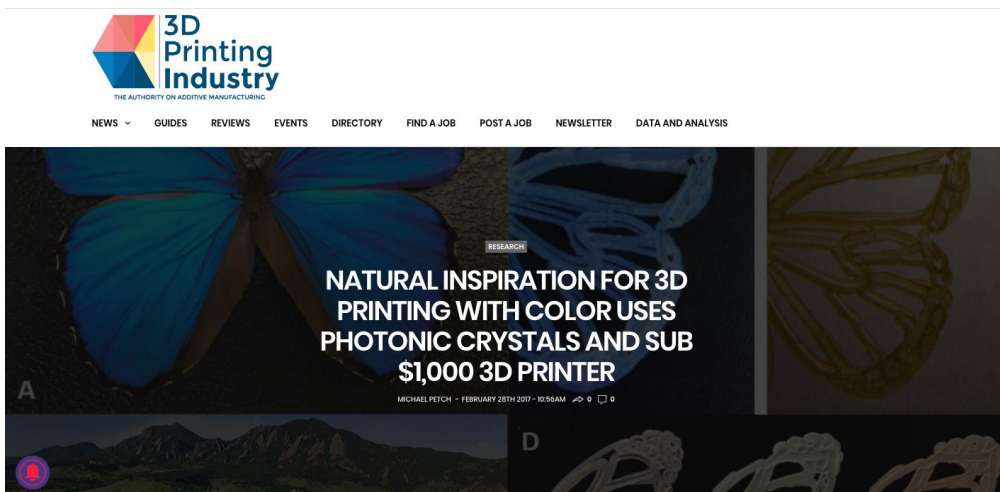


Figure 6.1. A picture of the Natural Inspiration for 3D Printing with Color Uses Photonic Crystals and Sub \$1000 3D Printer article's page on 3DPI's website.

References

- (1) 3D Printing Industry, Natural Inspiration for 3D Printing with Color Uses Photonic Crystals and Sub \$1000 3D Printer (Accessed 18 March, 2020), <https://3dprintingindustry.com/news/natural-inspiration-3d-printing-color-uses-photonic-crystals-sub-1000-3d-printer-106729/>

APPENDIX I

List of Publications by Bret Michael Boyle (August 2015- April 2020)

6. Boyle, B. M.; Collins, J. L.; Mensch, T. E.; Ryan, M. D.; Newell, B. S.; Miyake, G. M. Impact of Backbone Composition on Homopolymer Dynamics and Brush Block Copolymer Self-Assembly *To Be Submitted* **2020**
5. Chen, D-F; Boyle, B.; McCarthy, B.; Lim, C-H; Miyake, G.M. Controlling Polymer Composition in Organocatalyzed Photoredox Radical Ring-Opening Polymerization of Vinylcyclopropanes *J. Am. Chem. Soc.*, **2019**, 141, 33, 13268-13277.
4. Boyle, B.M.;[†] Xiong, P.T.;[†] Mensch, T; Werder, T.J.; Miyake, G.M. Powder Melt Extrusion 3D Printing *Addit. Manuf.*, **2019**, 29, 100811.
3. Boyle, B.M.;[†] Heinz, O.;[†] Miyake, G.M.; Ding, Y. The Impact of the Pendant Group on the Chain Conformation and Bulk Properties of Norbornene Imide-Based Polymers *Macromolecules*, **2019**, 52, 9, 3426-3434.
2. Loranger, S; Bassett, C.; Cole, J.P.; Boyle, B.M.; Weber, T.C. Acoustically Relevant Properties of Four Crude Oils at Oceanographic Temperatures and Pressures *The Journal of the Acoustical Society of America*, **2018**, 144, 2926.
1. Boyle, B.M.;[†] French, T.F.;[†] Pearson, R.M.; McCarthy, B.G.; Miyake, G.M. Structural Color for Additive Manufacturing: 3D-Printed Photonic Crystals from Block Copolymers *ACS Nano*, **2017**, 11 (3), 3052–3058.